TAL
TECH

DOCTORAL THESIS

Spin-Waves in Magnetoelectric Materials with Strong Single-Ion Anisotropy

Laur Peedu

Spin-Waves in Magnetoelectric Materials with Strong Single-Ion Anisotropy

LAUR PEEDU

TAL
TECH
PRESS

TALLINN UNIVERSITY OF TECHNOLOGY
School of Science
Department of Cybernetics

The dissertation was accepted for the defence of the degree of Doctor of Philosophy (Applied Physics) on 14 November 2022

Supervisor: PhD Toomas Rõõm,
National Institute of Chemical Physics and Biophysics,
Tallinn, Estonia

Co-supervisor: PhD Urmas Nagel,
National Institute of Chemical Physics and Biophysics,
Tallinn, Estonia

Opponents: PhD Alexey B. Kuzmenko,
University of Geneva,
Genève, Switzerland

PhD Rasmus Toft-Petersen,
Technical University of Denmark,
Kongens Lyngby, Denmark

Defence of the thesis: 13 December 2022, Tallinn

Declaration:
Hereby I declare that this doctoral thesis, my original investigation and achievement, submitted for the doctoral degree at Tallinn University of Technology, has not been submitted for any academic degree elsewhere.

Laur Peedu

_____
signature

Spinn-lained tugeva anisotroopiaga magnetelektrilistes materjalides

LAUR PEEDU

TAL TECH KIRJASTUS

Contents

List of publications

The present Ph.D. thesis is based on the following publications that are referred to in the text by Roman numbers.

I L. Peedu, V. Kocsis, D. Szaller, J. Viirok, U. Nagel, T. Rõõm, D. G. Farkas, S. Bordács, D. L. Kamenskyi, U. Zeitler, Y. Tokunaga, Y. Taguchi, Y. Tokura and I. Kézsmárki, "Spin excitations of magnetoelectric LiNiPO$_4$ in multiple magnetic phases," *Phys. Rev. B*, vol. 100, p. 024406, Apr 2019.

II J. Vit, J. Viirok, L. Peedu, T. Rõõm, U. Nagel, V. Kocsis, Y. Tokunaga, Y. Taguchi, Y. Tokura, I. Kézsmárki, P. Balla, K. Penc, J. Romhányi, S. Bordács, "In situ electric-field control of THz nonreciprocal directional dichroism in the multiferroic Ba$_2$CoGe$_2$O$_7$," *Phys. Rev. L*, vol. 127, p. 157201, July 2021.

III L. Peedu, V. Kocsis, D. Szaller, B. Forrai, S. Bordács, I. Kézsmárki, J. Viirok, U. Nagel, B. Bernáth, D. L. Kamenskyi, A. Miyata, O. Portugall, Y. Tokunaga, Y. Tokura, Y. Taguchi and T. Rõõm, "THz spectroscopy of spin excitations in magnetoelectric LiFePO$_4$ in high magnetic fields," *Phys. Rev. B*, vol. 106, p. 134413, Oct 2022.

Author's contributions to the publications

I In I, I carried out the THz spectroscopy experiments of $LiNiPO_4$ in KBFI and in HFML. I analysed the results, prepared the figures, planned and organized the work needed, wrote the manuscript and included theory results obtained by David Szaller.

II In II, I modified the TeslaFIR rotational Voigt probe for electric field measurements and helped to carry out the experiments. Additionally I reviewed the manuscript and recommended changes.

III In III, I modified TeslaFIR setup to reduce the heat load from the sample on the bolometer. I conducted the THz spectroscopy experiments of $LiFePO_4$ in KBFI and HFML. I analysed the experimental results, prepared the figures for publication, wrote the manuscript and included theory results obtained by David Szaller.

Approbation

I presented the results of the thesis at the following conferences:

1. **L. Peedu**, T. Rõõm, J. Viirok, U. Nagel, D. Szaller, S. Bordács, I. Kézsmárki, D. L. Kamenskyi, V. Kocsis, Y. Tokunaga, Y. Taguchi, Y. Tokura. "THz spectroscopy of spin waves in multiferroic LiNiPO$_4$ in high magnetic fields," APS March Meeting: 13–18 March 2017, New Orleans, LA, USA.

2. **L. Peedu**, J. Viirok, U. Nagel, T. Rõõm, D. Szaller, S. Bordács, I. Kézsmárki, D. L. Kamenskyi, H. Engelkamp, U. Zeitler, V. Kocsis, Y. Tokunaga, Y. Taguchi, Y. Tokura. "Optical spin-wave excitations of multiferroic LiNiPO$_4$ in high magnetic fields," 3rd Grandmaster PhD Workshop in Physics: 19–23 February 2018, Vienna, Austria.

3. **L. Peedu**, J. Viirok, U. Nagel, T. Rõõm, S. Bordács, I. Kézsmárki, B. Bernáth, D. L. Kamenskyi, V. Kocsis, Y. Tokunaga, Y. Taguchi, Y. Tokura. "THz spectroscopy of spin waves in multiferroic LiFePO$_4$ in high magnetic fields," APS March Meeting: 5–9 March 2018, Los Angeles, CA, USA.

4. **L. Peedu**, T. Rõõm, J. Viirok, U. Nagel, D. Szaller, S. Bordács, I. Kézsmárki, D. L. Kamenskyi, V. Kocsis, Y. Tokunaga, Y. Taguchi, Y. Tokura. "THz spectroscopy of spin waves in multiferroic LiNiPO$_4$ in high magnetic fields," GSFMT scientific conference, 4–5 February 2019, Tartu, Estonia.

5. **L. Peedu**, J. Viirok, U. Nagel, T. Rõõm, D. Szaller, S. Bordács, I. Kézsmárki, D. L. Kamenskyi, V. Kocsis, Y. Tokunaga, Y. Taguchi, Y. Tokura. "THz spectroscopy of Spin Waves in Multiferroic LiNiPO$_4$ in High Magnetic Fields," APS March Meeting: 4–8 March 2019, Boston, MA, USA.

6. **L. Peedu**, J. Viirok, U. Nagel, T. Rõõm, S. Bordács, I. Kézsmárki, B. Bernáth, D. L. Kamenskyi, H. Engelkamp, U. Zeitler, V. Kocsis, Y. Tokunaga, Y. Taguchi, Y. Tokura. "THz spectroscopy of spin waves in magnetoelectric LiFePO$_4$ in high magnetic fields," 4th Grandmaster PhD Workshop in Physics: 1–7 September 2019, Split, Croatia.

Abbreviations

AC	Alternating Current
AFM	Anti-Ferromagnetic
BMS	Beamsplitter
DC	Direct Current
EM	Electromagnetic
ESR	Electron Spin Resonance
FFT	Fast Fourier transform
FIR	Far Infrared
FM	Ferromagnetic
HFML	High Field Magnet Laboratory
IFFT	Inverse Fast Fourier Transform
INS	Inelastic Neutron Scattering
KBFI	National Institute of Chemical Physics and Biophysics (Keemilise ja Bioloogilise Füüsika Instituut)
ME	Magnetoelectric
MF	Multiferroic
NDD	Nonreciprocal Directional Dichroism
RM	Roof Mirror
THz	Terahertz, $1\,\mathrm{THz} = 10^{12}\,\mathrm{Hz}$
SIBS	Single-Ion Bound State
ZPD	Zero Path Difference of interferometer

Symbols

ε_0	Vacuum permittivity
μ_0	Vacuum permeability
μ_{B}	Bohr magneton
$\hbar$	Reduced Planck constant
c_0	Speed of light in vacuum, $c_0 = (\varepsilon_0 \mu_0)^{-1/2}$
k_{B}	Boltzmann constant
f	Frequency
ω	Angular frequency, $\omega = 2\pi f$
$\mathscr{E}$	Energy, $\mathscr{E} = \hbar \omega$
λ	Wavelength of electromagnetic radiation
$\mathbf{k}$	Wavevector, $|k| = 2\pi/\lambda$
$\bar{\omega}$	Wavenumber, $\bar{\omega} = \lambda^{-1}$
$\langle\,\rangle$	Ensemble average
T	Temperature
T_{N}	Néel temperature
T_{C}	Curie temperature
g	Electron g factor
Λ	Single-ion anisotropy parameter, $H_{\mathrm{sia}} = \Lambda\, S_i^\alpha S_i^\beta, \quad \alpha, \beta = x, y, z$
J	Heisenberg exchange interaction parameter, $H_{\mathrm{exc}} = J\, \mathbf{S}_i \cdot \mathbf{S}_j$
$\mathbf{D}$	Dzyaloshinskii-Moriya interaction parameter, $H_{\mathrm{DM}} = \mathbf{D} \cdot [\mathbf{S}_i \times \mathbf{S}_j]$
E^ω	Electric-field amplitude of electromagnetic radiation
H^ω	Magnetic-field amplitude of electromagnetic radiation
R	Reflectance

Units

$[f] = \mathsf{THz}$
$[\bar{\omega}] = \mathsf{cm}^{-1}$
$[\mathscr{E}] = \mathsf{meV}$

$1\,\mathsf{THz} = 10^{12}\,\mathsf{Hz} = 33\ \mathsf{cm}^{-1} = 4.1\,\mathsf{meV}$
$1\ \mathsf{cm}^{-1} = 0.03\,\mathsf{THz} = 0.12\,\mathsf{meV}$
$1\,\mathsf{meV} = 0.24\,\mathsf{THz} = 8\ \mathsf{cm}^{-1}$

Introduction

The progress in modern technology is based on the discovery of new materials and physical interactions that increase the efficiency and functionality of devices. One particularly interesting functionality stems from the coupling between the magnetic and electric degrees of freedom, called magnetoelectric effect. Magnetoelectric effect allows to control magnetism with electric field and charge order with magnetic field. This effect has drawn enormous interest because it is believed to be the key to achieving cross-control of electromagnetic properties in solids with minute energy dissipation [1–3]. Variety of possible applications of magnetoelectric materials are to be found in spintronics, optics, sensing, data storage and computing [4–10]. Unfortunately, most of the multiferroics show their functionality substantially below room temperatures where magnetic and charge order develops. A rare example is $BiFeO_3$ where the control of magnetism has been achieved through the use of an electric field at room temperature [11, 12].

The magnetoelectric effect is linked to the ordering of magnetic and electric dipoles, hence revealing itself in materials with coexisting ferro-electric and -magnetic orders, termed as multiferroics. The ordered magnetic moments produce wavelike motion throughout the solid. Such a wave was first predicted by F. Bloch in 1929 [13] and is named the spin wave, a collective excitation of electron spins. Since spins carry a magnetic moment they interact with magnetic field and with other magnetic moments. In magnetoelectric materials the spins also interact with electric field. This lead to the discovery of the electric-dipole active spin wave termed electromagnon [14] and soon after that to the discovery of the simultaneously electric- and magnetic-dipole active spin wave, the magnetoelectric resonance [15, 16].

One of the most interesting optical effects is directional optical anisotropy, where the counter-propagating unpolarized light beams passing through a medium can experience different indices of refraction [17]. This effect was found to be exceptionally large in multiferroic materials at THz frequencies [15] leading to almost one-way transparency [18]. From the unidirectional nature, the optical diodes were realized where the direction of transparency for the THz radiation can be switched by magnetic fields [15, 18–23], electric fields [24–26] or both [27].

Magnetoelectric materials with low symmetry exhibit anisotropic distribution of charge and magnetization. Anisotropic exchange interactions between the spins shift the magnon spectrum from zero to finite frequency [28]. These magnons in general can be detected by electron spin resonance, THz and INS. If $S > 1/2$, spin excitations in addition to magnons are present. These additional spin excitations are invisible to electron spin resonance, THz and INS, but they gain magnetic dipole activity if there is a strong single-ion anisotropy [29] or anisotropic exchange interaction [30, 31] and therefore can be probed by these techniques. Furthermore, if the inversion symmetry is broken, magnons and new modes may gain electric dipole activity [29]. Thus, materials with strong anisotropy and with broken inversion symmetry should exhibit dynamic magnetoelectric effect of spin excitations, it is magnetoelectric spin resonances.

THz absorption spectroscopy combined with magnetic field is an excellent probe to investigate magnetoelectric properties of materials. Firstly, the spin-wave frequencies and their evolution in magnetic field tell us about the interactions between the spins. This is a valuable input to spin models from where the exchange interaction and anisotropies are determined. Secondly, THz spectroscopy with polarized radiation can reveal selection rules for spin excitations, whether they couple to the magnetic, electric or to both fields of radiation. For example, inelastic neutron scattering is a powerful tool to study spin waves but neutrons scatter off from magnetic moments and are insensitive to elec-

tric dipoles. Because of the electric field of the electromagnetic wave, THz spectroscopy can also access more exotic spin excitations carrying the electric dipole moment what can be expressed in terms of spin-quadrupolar operators [29, 30]. Thus, the information obtained with THz spectroscopy is vital in the process of understanding the magnetoelectric effect and designing new magnetoelectric materials. In the National Institute of Chemical Physics and Biophysics (KBFI), we employed the THz absorption spectroscopy technique at low temperature in frequency range between 3 and 200 cm^{-1}, and in magnetic fields up to 17 T. Using the facilities of the High Field Magnet Laboratory in Nijmegen, Netherlands, the magnetic field range was extended up to 32 T.

This thesis is about the THz spectroscopic study of two orthophosphate compounds and demonstrates the switching of non-reciprocal directional dichroism in the $Ba_2CoGe_2O_7$ crystal. They are all magnetoelectric materials with strong single-ion anisotropy, $\Lambda >> J$.

The first goal of this PhD thesis was to measure the THz absorption spectra and their magnetic field dependence and to determine the selection rules for observed absorption lines in orthophosphates $LiNiPO_4$ and $LiFePO_4$. Earlier works where the spin excitations were studied include Raman [32–34] and electron spin resonance [35, 36] spectroscopy studies. More detailed information came from inelastic neutron scattering studies [37–42]. However, the magnetoelectric nature of spin excitations was not revealed. It is important because $LiNiPO_4$ and $LiFePO_4$ are sister compounds to $LiCoPO_4$, where the directional dichroism at spin wave resonances and its switching with applied electric and magnetic fields has been demonstrated [43]. Based on the similarities of crystal lattices and magnetic structures, magnetoelectric resonances are also expected to be present in $LiNiPO_4$ and $LiFePO_4$. Both compounds show magnetic-field-induced abrupt changes of their spin structure [44, 45]. Therefore, the measurements were extended to magnetic fields as high as 32 T.

The second goal was to demonstrate experimentally the electric field control of THz non-reciprocal directional dichroism in the multiferroic $Ba_2CoGe_2O_7$. While the magnetic field and simultaneously magnetic- and electric-field control of THz light switching is shown in several magnetoelectric materials [15, 18–23, 27], compounds where the control of non-reciprocal directional dichroism is achieved by electric field alone are sparse [24, 46].

This thesis begins with the description of the magnetoelectric effect, spin excitations and the relation between these two, Sec. 1. Then, in Sec. 2 the detailed overview of the THz spectroscopy technique, including the mathematical background of the interferometric method, is presented. The handling of measured THz spectra is described in Sec. 3. Sec. 4 presents the results together with the discussion.

1 Theoretical principles

1.1 Multiferroic and magnetoelectric materials

Multiferroics are materials in which two or more primary ferroic orders (ferromagnetism, ferroelectricity, ferroelasticity and ferrotoridicity) coexist simultaneously in the same phase [47]. The ferroic orders have an order parameter that can be switched by its conjugate field, meaning that the magnetization $\mathbf{M}$ created by ferromagnetic order can be switched by applying magnetic field $\mathbf{H}$, electric polarization $\mathbf{P}$ in ferroelectrics by electric field $\mathbf{E}$, strain ε in ferroelastics by stress ρ and the magnetic whirls in ferrotoroidal order by applying crossed electric and magnetic field $\mathbf{E} \times \mathbf{H}$ [48, 49]. From here on we will use the term multiferroic (MF) for materials which have simultaneously (anti-)ferroelectric and (anti-)ferromagnetic order. Many multiferroic materials also exhibit the magnetoelectric (ME) effect where the cross coupling of electric and magnetic degrees of freedom allow the control of $\mathbf{P}$ with $\mathbf{H}$ and $\mathbf{M}$ with $\mathbf{E}$ [1, 6, 50], see Fig. 1. The ME coupling has been the main center of research interest in multiferroics as it has high potential for future applications [51–57]. Compared to multiferroics where at least two primary ferroic orders are needed, the magnetoelectric materials are not restricted to ferroic orders [49, 58]. Quite often the magnetoelectrics still possess ferromagnetism, but lack a transition temperature for electric order and by definition then the ferroelectric order. The electric polarization can be magnetically driven through distorted structure around the magnetic atoms, discussed further in Sec. 1.2.2.

Although the ordering is natural there are only a few strong magnetoelectric multiferroics. While magnetic materials can be simultaneously insulating or conductive, ferroelectric materials can be solely insulating as otherwise the electric field would induce electric current rather than switch the ferroelectric domains. Furthermore, the ferromagnetic order originates from the localized electrons that in case of rare-earth ions and transition metals comes from a partially filled d or f electronic orbitals. In ferroelectrics, for example with ABO_3 pervoskite structure, the electric polarization is induced from the off-centre shift of the B-cation inside the oxygen cage. This shift breaks the centrosymmetry and creates an electric dipole. But to minimize the Coulumbian electrostatic repulsion of the surrounding oxygen anions the B-cation has to have d^0 electron configuration, e.g. empty d orbitals [59]. Therefore it is usual that in multiferroic materials ferroelectric and ferromagnetic orders have different origin [60].

Macroscopic orders act differently under spatial inversion and time reversal operations, see Fig. 2. On time reversal operation magnetic moments change direction, but not upon spatial inversion. At the same time electric dipoles are invariant under time reversal but reversed under spatial inversion. Thus ferroelectrics have broken inversion symmetry and ferromagnetics have broken time reversal symmetry.

1.2 Classification of magnetoelectric multiferroic materials

Magnetoelectric multiferroic materials can be classified as type-I and type-II [60]. In type-I multiferroic materials magnetism and ferroelectricity rely on independent mechanisms to occur. In this group it is usual that the ferroelectric transition takes place at a higher temperature while magnetic moments order at lower temperatures. As the ordering occurs at different temperatures, the domains accompanied by ferroic orders can exist independently from each other. In type-II multiferroic materials the ordering of magnetic moments breaks the inversion symmetry and by that induces the ferroelectric order. This allows stronger coupling between magnetism and ferroelectric polarization than in type-I MF materials. Magnetically-driven magnetoelectric materials, i. e. type-II, allow easy
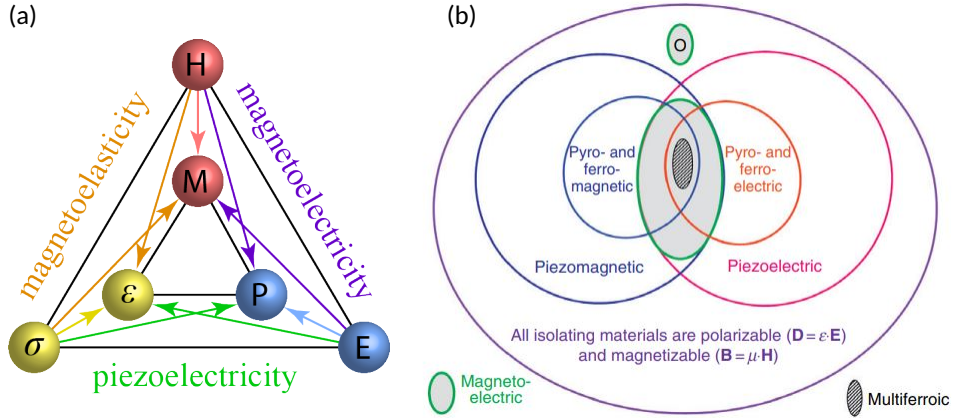
*Figure 1: (a) Primary order parameters magnetization **M**, polarization **P** and strain ε with their conjugate fields: magnetic field **H**, electric field **E** and stress ρ. In multiferroics different parameters and conjugate fields can be cross coupled leading to magnetoelasticity, piezoelectricity and magnetoelectricity. This panel is reproduced based on Ref. [61]. (b) Venn diagram for electromagnetic insulators. Ferroic materials that are magnetically and electrically polarizable are multiferroics. The magnetoelectric effect can exist in materials with ferroic orders or in materials that are electrically and magnetically polarizable. Panel (b) is reproduced based on Fig. 3.11 in Ref. [62].*

manipulation of magnetization by electric field that is essential for applications. Major mechanisms for type-I and type-II multiferroic materials are described in the next sections. It is important to note that the main mechanisms can coexist in materials. $LiNiPO_4$, $LiFePO_4$ and $Ba_2CoGe_2O_7$ samples discussed in this thesis are type-II ME materials. While in $LiNiPO_4$ and $LiFePO_4$ the magnetoelectric effect arises from the connection between superexchange, Dzyaloshinskii-Moriya interaction or elastic distortions [41, 45, 64, 65], the electric polarization in $Ba_2CoGe_2O_7$ is created through the p-d hybridization mechanism [66].

1.2.1 Type-I multiferroic materials

The magnetoelectric mechanisms in type-I multiferroics can be classified, depending on how the ferroelectric polarization emerges.

Lone-pair mechanism

The lone-pair mechanism is based on the violation of the inversion symmetry by valence electrons that do not participate in chemical bonds [60]. These lone pair electrons are highly polarizable and can produce a local electric polarization. The lone pairs are nearly spherically distributed in the absence of the bond, but if surrounded by the oxygen anions they shift away from the centrosymmetric positions because of electrostatic repulsion and form a lobe-like localized distribution. If the local electric dipoles order they produce a ferroelectric order. This mechanism can result in a very large electric polarization with transition temperature well above room temperature. The most famous room temperature multiferroic compound with lone-pair mechanism is $BiFeO_3$. $BiFeO_3$ has an electric polarization of 100 $\mu C/cm^2$ [70] and a ferroelectric transition temperature of 1100K [71]. The G-type antiferromagnetic order of **B** sets in below T_N = 640K [72]. In $BiFeO_3$ the electric polarization is from the lone-pair 6s electrons of Bi^{3+}, while the mag-
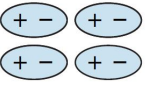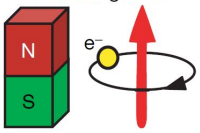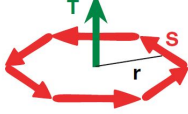
	Space Invariant	Space Change
Time Invariant	Ferroelastic	Ferroelectric
Time Change	Ferromagnetic	Ferrotoroidic

Figure 2: Ferroelastic, ferroelectric, ferromagnetic and ferrotoridic orders under spatial inversion and time reversal symmetry operation. This illustration is reproduced based on Fig. 2 in Ref. [63].

a Lone-pair mechanism **b** Geometric ferroelectricity **c** Charge ordering

O^{2-} Bi^{3+} Fe^{2+} Fe^{3+} Rare-earth ion Mn^{3+}
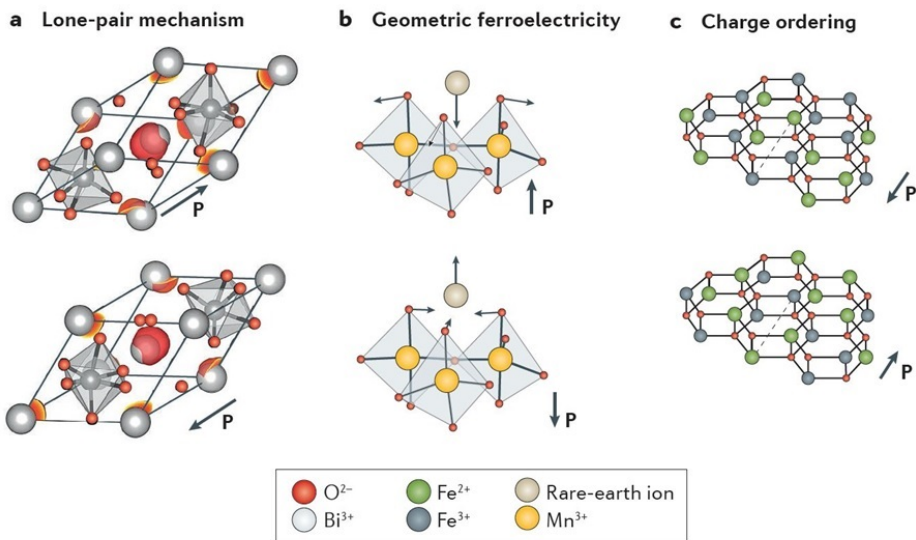
Figure 3: Mechanisms for coexisting magnetic and electric long-range order in Type I multiferroic compounds. (a) The lone-pair mechanism for electric polarization in $BiFeO_3$. The lone pair shown as red isosurface of the electron localized function originates from two electrons that shift away from Bi^{3+} ion toward the FeO_6 octahedra. This lone pair shift induces a electric polarization **P** in the [111] direction. (b) The geometric ferroelectricity in h-$RMnO_3$. The shift of the R-ions originates from the movement of the MnO_5 bipyramids which leads to a ferroelectric polarization **P** along the [001] axis [67]. (c) The ferroelectricity from charge ordering in $LuFe_2O_3$. The alternating layers with the Fe^{2+} and Fe^{3+} ions with ratios 2:1 and 1:2 results in the spontaneous ferroelectric polarization [68]. This illustration is produced based on Fig. 1 in Ref. [69].

netism is from the $Fe^{3+}d^5$ ions. The lone-pair effect of $BiFeO_3$ is illustrated in Fig. 3(a).

Geometric ferroelectricity model

Geometric restriction can result in the distortion of the crystal lattice that produces polar distortions and by that the geometric ferroelectricity, see Fig. 3(b). Structurally the polar distortion is often produced by the rotation of oxygen polyhedra like bipyramids that have rare-earth ions inside.

The rotation of trigonal bipyramids is responsible for ferroelectricity in the family of hexagonal rare-earth manganites h-RMnO$_3$ where R is a rare-earth ion in range of Ho-Lu and Y [67]. This family of geometric ferroelectrics has a high Curie point, $T_C \leq 1200$ K, while antiferromagnetic order sets in below room temperature at $T_N = 120$ K [73, 74].

Another example of geometric ferroelectricity is the family of layered barium transition metal fluorides BaMF$_4$ with $M =$ Mg, Mn, Fe, Co, Ni or Zn, which develop ferroelectric order around $T_C \leq 1000$ K [75]. Not all members of this family have a magnetically ordered phase at low temperature. Members with $M =$ Mn, Fe, Co, or Ni order antiferromagnetically with T_N in range from 20 to 70 K [76, 77]. This family is interesting because of its very small electric polarization ($\approx 0.01\ \mu$ C/cm^{-2}) that is coupled to a weak ferromagnetic moment, allowing an easy reversal of the magnetic moment with electric field.

Charge ordering model

When localized valence electrons distribute unevenly around their host ions they can generate a periodic sequence of differently charged ions that results in ferroelectric polarization. This mechanism has been proposed in several compounds, including organics, LuFe$_2$O$_4$ [78, 79], Fe$_3$O$_4$, Pr$_{1-x}$Ca$_x$MnO$_3$ [80] and RNiO$_3$. LuFe$_2$O$_4$ was the first compound where the charge ordering mechanism of creating ferroelectricity was proposed. In this compound the alternating ions of Fe^{2+} and Fe^{3+} produce a charge order at 330 K, see Fig. 3(c). Because the ions creating ferroelectric order in these materials are magnetic, like Fe in LuFe$_2$O$_4$, they exhibit the magnetic order at low temperature and are multiferroic. Although the charge ordering concept is believed to exist, many compounds in which it was initially proposed have been later questioned [81, 82].

1.2.2 Type-II multiferroic materials

The electric polarization in the type-II magnetoelectric multiferroics is induced by the long-range magnetic order. In this class the electric and magnetic degrees of freedom are strongly coupled although the induced electric polarization is much smaller than in type-I magnetoelectric multiferroic materials. The three main mechanisms for type-II multiferroics are discussed next.

Exchange striction model

The exchange striction model is based on the alternating chain of magnetic ions, M_A and M_B, that in the magnetically ordered state break the inversion symmetry as discussed next. When different magnetic ions order, they can shift closer in pairs to minimize the exchange energy, illustrated in the first column of Fig. 4 . This shifting introduces alternating bond lengths, $M_A - M_B$, that break the inversion symmetry and allow electric polarization. It should be noted that this mechanism is independent from relativistic spin-orbit coupling [83]. The exchange interaction model permits stronger ME coupling
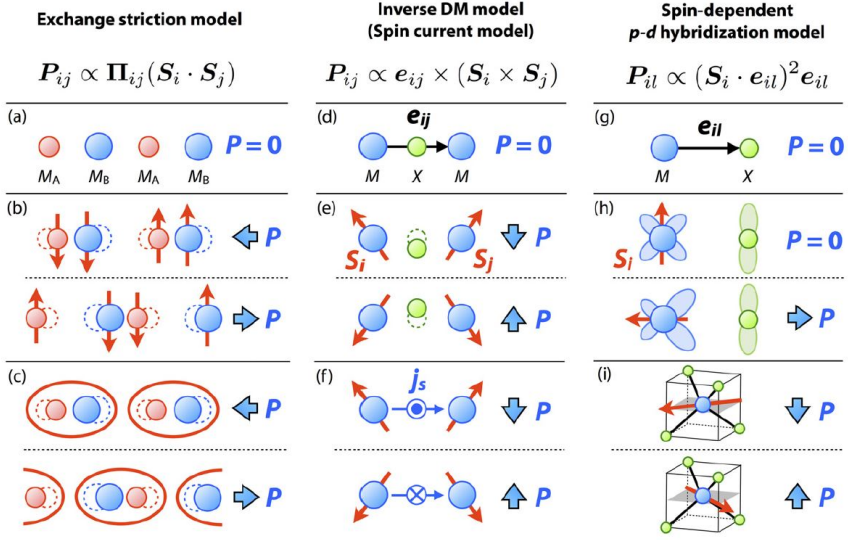
Figure 4: *The three major mechanisms of spin induced electric polarization in type-II magnetoelectric multiferroics. The (a)-(c) illustrate the exchange striction model which arises from symmetric exchange interaction, (d)-(f) show the inversed Dzyaloshinskii-Moriya model also known as spin current model that is governed by the antisymmetric spin exchange interaction and (g)-(i) illustrate the spin-dependent $p-d$ hybridization model. The $\mathbf{P}$ is the electric polarization and the blue arrow next to it indicates the expected direction, the Π_{ij}, $\mathbf{e}_{ij}$ and $\mathbf{e}_{il}$ are the unit vectors connecting the magnetic M ion sites or magnetic to ligand X ion sites. Each column illustrates the examples depending on whether the ferroelectric polarization is generated or absent for a given model. This illustration is reproduced from Ref. [2].*

than magnetism-driven polarization that relies on the spin-orbit coupling effects or on the Dzyaloshinskii-Moriya mechanisms (described in next paragraph) [84].

The electric polarization induced by exchange striction model for a spin pair $\mathbf{S}_i$ and $\mathbf{S}_j$ along crystallographic direction Π_{ij} is

$$\mathbf{P}_{ij} \approx \Pi_{ij} \left(\mathbf{S}_i \cdot \mathbf{S}_j \right). \tag{1}$$

The exchange striction mechanism is mainly responsible for the macroscopic ferroelectric polarization in the perovskite-type manganites $R\mathrm{MnO}_3$ (R = Ho, Er, Tm, Yb, and Lu) [85], the manganese oxides $R\mathrm{Mn}_2\mathrm{O}_5$ (R = Y, Yb, Ho, Er, and Tm) [86] and in the $\mathrm{CaBaCo}_4\mathrm{O}_7$ [87].

Inverse Dzyaloshinskii-Moriya model

Ferroelectric polarization created by the inverse Dzyaloshinskii-Moriya model is described as

$$\mathbf{P} \approx \mathbf{e}_{ij} \times \left(\mathbf{S}_i \times \mathbf{S}_j \right), \tag{2}$$

where the $\mathbf{S}_i$ and $\mathbf{S}_j$ are spins on different sites and $\mathbf{e}_{ij}$ is the unit vector connecting the two sites.

The perquisite for this mechanism is that the crystal has to have a non-collinear magnetic structure. There are two distinct models which can be used to derive the Eq. (2). In the first model, the ferroelectric polarization is created due to the symmetry requirements of Dzyaloshinskii-Moriya interaction which forces the ligand X to be displaced from the vector connecting the two magnetic ions [68]. In this model the ferroelectric polarization is parallel to the ligand displacement direction, see Fig. 4(e). In the second model, the ferroelectric polarization is created by the spin currents through the electronic orbitals without the deformation of lattice, see Fig. 4(f) [88]. As both these mechanisms reach the same description of $\mathbf{P}$ the inverse Dzyaloshinskii-Moriya model is often referred as the spin current mechanism.

A good example is the perovskite BiFeO_3. Its spontaneous polarization in the spin-cycloid phase can be described by the spin-current mechanism [22]. In other perovskite type manganites, $R\mathrm{MnO}_3$ (R = Tb, Dy), the ferroelectric polarization can be described with the Dzyaloshinskii-Moriya model [89–91].

Spin-dependent p-d hybridization model

The spin-dependent p-d hybridization model is based on an polar bond that can be modulated by the spin direction dependent hybridization through spin-orbit coupling, see the last column of Fig. 4. The electric polarization is created on a single spin site and is independent of the neighboring spins. The direction of the electric polarization depends on the direction of the spin compared to the direction of the ligand bond, see Fig. 4(h). The $p-d$ hybridization induced electric polarization of the polar bond $\mathbf{e}_{il}$ that connects spin site i to a ligand site l is

$$\mathbf{P} \approx \left(\mathbf{S}_i \cdot \mathbf{e}_{il} \right)^2 \mathbf{e}_{il}. \tag{3}$$

This model is used to explain the multiferroic properties of different compounds in the åkermanite family, $\mathrm{Ba}_2X\mathrm{Ge}_2\mathrm{O}_7$ (where X = Mn, Co and Cu) [66] and $A_2\mathrm{CoGe}_2\mathrm{O}_7$ (where A = Ca and Sr) [92, 93]. In $\mathrm{Ba}_2\mathrm{CoGe}_2\mathrm{O}_7$ it was also shown that this mechanism combined with magnetic field can induce electric polarization in the paramagnetic phase where the long range spin order is absent [94, 95]. The magnetoelectric spectroscopy results of $\mathrm{Ba}_2\mathrm{CoGe}_2\mathrm{O}_7$ are discussed in the Sec. 4.2.

1.3 Magnetoelectric effect

1.3.1 Static magnetoelectric effect

The intrinsic ME effect, predicted by symmetry arguments in 1894 by Pierre Curie [96], is defined as any coupling between the magnetic and electric properties of material. The effect was experimentally demonstrated on Cr_2O_3 in 1960s [97]. Although the ME effect got rigorous attention in 60s and 70s it only reached wider audience at the start of 21st century with the realization of its advantages for applications [98].

Thermodynamically, the ME effect is traditionally described in Landau theory and can be expressed by the expansion of the free energy of a material [1, 6, 58]. The free energy in dc limit using the Einstein summation convention is

$$
\begin{aligned}
F(\mathbf{E}, \mathbf{H}) = & F_0 - P_i^S E_i - M_i^S \mu_0 H_i - \frac{1}{2}\varepsilon_0 \chi_{ij}^{ee} E_i E_j - \frac{1}{2}\mu_0 \chi_{ij}^{mm} H_i H_j \\
& - \sqrt{\varepsilon_0 \mu_0}\chi_{ji}^{me} E_i H_j - \sqrt{\varepsilon_0 \mu_0}\chi_{ji}^{em} E_j H_i \\
& - \frac{1}{2}\beta_{ijk}E_i H_j H_k - \frac{1}{2}\gamma_{ijk}H_i E_j E_k - \cdots,
\end{aligned}
\tag{4}
$$

where subscripts (i, j, k) refer to the three components of a variable in spatial coordinates, $\mathbf{E}$ is the electric field with components $\{E_i, E_j, E_k\}$, $\mathbf{H}$ is the magnetic field with components $\{H_i, H_j, H_k\}$, M_i^S and P_i^S are the components of spontaneous magnetization $\mathbf{M}^S$ and polarization $\mathbf{P}^S$, F_0 is the ground state free energy without applied fields, ε_0 and μ_0 are the dielectric and magnetic susceptibilities of vacuum, χ_{ij}^{ee} and χ_{ij}^{mm} denote the dielectric and magnetic susceptibilities, β_{ijk} and γ_{ijk} are the third-order tensors of dielectric and magnetic susceptibilities. The third-order tensors describe the magnetic and electric quadrupolar effects. The χ_{ji}^{me} is the component of the dimensionless tensor $\hat{\chi}^{me}$ which accounts for the magnetization induced by electric field. The electric polarization created by applied magnetic field is described with the dimensionless tensor $\hat{\chi}^{em}$ with the components of χ_{ij}^{em}. From the free energy we can get the magnetization with derivative of F in $\mathbf{H}$ as $\mathbf{M} = -\frac{1}{\mu_0}\frac{\partial F}{\partial \mathbf{H}}$ and electric polarization with derivative of F in $\mathbf{E}$ as $\mathbf{P} = -\frac{\partial F}{\partial \mathbf{E}}$ [58, 99]:

$$
\begin{aligned}
M_i(\mathbf{E}, \mathbf{H}) = & M_i^S + \chi_{ij}^{mm}H_j + \sqrt{\frac{\varepsilon_0}{\mu_0}}\chi_{ij}^{me}E_j + \beta_{ijk}E_i H_j + \frac{1}{2}\gamma_{ijk}E_j E_k + \cdots, \\
P_i(\mathbf{E}, \mathbf{H}) = & P_i^S + \varepsilon_0 \chi_{ij}^{ee}E_j + \sqrt{\varepsilon_0 \mu_0}\chi_{ij}^{em}H_j + \frac{1}{2}\beta_{ijk}H_j H_k + \gamma_{ijk}H_i E_j + \cdots
\end{aligned}
\tag{5}
$$

Higher order terms β_{ijk} and γ_{ijk} are often neglected as their contribution is usually small compared to the $\hat{\chi}^{me}$ and $\hat{\chi}^{em}$, which define the linear ME effect,

$$
\begin{aligned}
\mu_0 \mathbf{M} &= \hat{\chi}^{me}\mathbf{E}, \\
\mathbf{P} &= \hat{\chi}^{em}\mathbf{H}.
\end{aligned}
\tag{6}
$$

The $\hat{\chi}^{me}$ and $\hat{\chi}^{em}$ tensors are interconnected in the static limit, $\omega = 0$, through the Kubo formula, see Sec. 1.3.4, with the relation $\hat{\chi}^{em} = (\hat{\chi}^{me})^T$, where T is the matrix transpose operator. According to the Neumann's principle the magnetoelectric tensor should reflect the ground-state symmetry of the magnetic crystal. Defining that the linear energy $\mathscr{E} = \hat{\chi}^{em}\mathbf{E}\mathbf{H}$ should not change by applying a symmetry operation, i.e space inversion operation acts as $\hat{I}\mathscr{E} = \mathscr{E}$. The space inversion reverses $\mathbf{E}$ while leaves $\mathbf{H}$ preserved, acting on energy as $\hat{I}\mathscr{E} = \hat{\chi}^{em}(-\mathbf{E})\mathbf{H}$, and because the $\mathscr{E}$ should not change we get $\hat{\chi}^{em} = -\hat{\chi}^{em}$ which is only possible if $\hat{\chi}^{em} = 0$. The same can be shown for time reversal $\hat{T}$, which reverses $\mathbf{H}$ while leaves $\mathbf{E}$ intact. In conclusion, the ME tensor has non-zero elements only

if the time-reversal and space-inversion symmetry are simultaneously broken, as then the $\mathscr{E}$ is preserved.

From Eq. (5) it is imminent that for the ME effect the material doesn't have to have simultaneous (anti-)ferromagnetic or (anti-)ferroelectric orders. Also large values of $\hat{\chi}^{\text{em}}$ and $\hat{\chi}^{\text{me}}$ are not a prerequisite for the material to be (anti-)ferroelectric or (anti-)ferromagnetic. However, materials that exhibits ferroic orders are liable for a strong linear magnetoelectric effect, as they often possess large susceptibilities which define the thermodynamic limit for $\hat{\chi}^{\text{me}}$ as [1]

$$\chi_{ji}^{\text{me}} < \sqrt{\chi_{ii}^{\text{ee}} \chi_{jj}^{\text{mm}}}. \tag{7}$$

1.3.2 Dynamic response of linear magnetoelectric effect

To understand the light propagation in magnetoelectric materials and the optical ME effect we first have to describe the dynamic ME effect. For simplification we cover the linear ME regime, neglecting the higher order terms of Eq. (5). The dynamic response of polarization and magnetization reads as

$$\mathbf{P}^{\omega} = \varepsilon_0 \hat{\chi}^{\text{ee}}(\omega)\mathbf{E}^{\omega} + \sqrt{\varepsilon_0 \mu_0}\hat{\chi}^{\text{em}}(\omega)\mathbf{H}^{\omega},$$
$$\mathbf{M}^{\omega} = \hat{\chi}^{\text{mm}}(\omega)\mathbf{H}^{\omega} + \sqrt{\frac{\varepsilon_0}{\mu_0}}\hat{\chi}^{\text{me}}(\omega)\mathbf{E}^{\omega}. \tag{8}$$

where frequency-dependent susceptibilities can be found as

$$\hat{\chi}^{\text{ee}}(\omega) = \left.\frac{\partial \mathbf{P}^{\omega}}{\partial \mathbf{E}^{\omega}}\right|_{\mathbf{E}^{\omega}=0}, \quad \hat{\chi}^{\text{mm}}(\omega) = \left.\frac{\partial \mathbf{M}^{\omega}}{\partial \mathbf{H}^{\omega}}\right|_{\mathbf{H}^{\omega}=0},$$
$$\hat{\chi}^{\text{em}}(\omega) = \left.\frac{\partial \mathbf{P}^{\omega}}{\partial \mathbf{H}^{\omega}}\right|_{\mathbf{H}^{\omega}=0}, \quad \hat{\chi}^{\text{me}}(\omega) = \left.\frac{\partial \mathbf{M}^{\omega}}{\partial \mathbf{E}^{\omega}}\right|_{\mathbf{E}^{\omega}=0}. \tag{9}$$

From here on the susceptibilities are written without the frequency, ω, dependence. The electric displacement $\mathbf{D}^{\omega}$ and magnetic induction $\mathbf{B}^{\omega}$ are defined as

$$\mathbf{D}^{\omega} = \varepsilon_0 \mathbf{E}^{\omega} + \mathbf{P}^{\omega},$$
$$\mathbf{B}^{\omega} = \mu_0 \left(\mathbf{H}^{\omega} + \mathbf{M}^{\omega}\right). \tag{10}$$

Using the Eq. (8) and Eq. (10) we get

$$\mathbf{D}^{\omega} = \varepsilon_0 \mathbf{E}^{\omega} \left(1 + \hat{\chi}^{\text{ee}}\right) + \sqrt{\varepsilon_0 \mu_0}\hat{\chi}^{\text{em}}\mathbf{H}^{\omega},$$
$$\mathbf{B}^{\omega} = \mu_0 \mathbf{H}^{\omega} \left(1 + \hat{\chi}^{\text{mm}}\right) + \sqrt{\mu_0 \varepsilon_0}\hat{\chi}^{\text{me}}\mathbf{E}^{\omega}. \tag{11}$$

The last equation could be simplified by using the relations of dielectric permittivity,

$$\hat{\varepsilon} = 1 + \hat{\chi}^{\text{ee}}, \tag{12}$$

and the magnetic permeability,

$$\hat{\mu} = \frac{1}{1 - \hat{\chi}^{\text{mm}}}, \tag{13}$$

in form,

$$\hat{\mu} \approx 1 + \hat{\chi}^{\text{mm}}, \tag{14}$$

where it is assumed that the effect of magnetization is small compared to the applied field, $\hat{\chi}^{\text{mm}} \ll 1$.

1.3.3 Nonreciprocal directional dichroism

In the following analysis we consider a plane wave at location $\mathbf{r}$ with frequency ω as

$$
\begin{aligned}
\mathbf{E}^{\omega}(\mathbf{r},t) &= \mathbf{E}_0^{\omega} e^{-i\omega t} e^{i\mathbf{k}\cdot\mathbf{r}} \\
\mathbf{H}^{\omega}(\mathbf{r},t) &= \mathbf{H}_0^{\omega} e^{-i\omega t} e^{i\mathbf{k}\cdot\mathbf{r}},
\end{aligned}
\tag{15}
$$

where $\mathbf{k}$ is the wavevector and t is time. The propagation of these waves is described by the following Maxwell equations in the insulating medium,

$$
\begin{aligned}
\mathbf{k}\cdot\mathbf{D}^{\omega} = 0, \quad \mathbf{k}\times\mathbf{E}^{\omega} = \omega\mathbf{B}^{\omega}, \\
\mathbf{k}\cdot\mathbf{B}^{\omega} = 0, \quad \mathbf{k}\times\mathbf{H}^{\omega} = -\omega\mathbf{D}^{\omega}.
\end{aligned}
\tag{16}
$$

By substituting the Eq. (11) into the right hand column of Eq. (16) we get

$$
\begin{aligned}
\mathbf{k}\times\mathbf{E}^{\omega} &= \omega\left[\mu_0\mathbf{H}^{\omega}(1+\hat{\chi}^{\mathrm{mm}})+\sqrt{\mu_0\varepsilon_0}\hat{\chi}^{\mathrm{me}}\mathbf{E}^{\omega}\right], \\
\mathbf{k}\times\mathbf{H}^{\omega} &= -\omega\left[\varepsilon_0\mathbf{E}^{\omega}(1+\hat{\chi}^{\mathrm{ee}})+\sqrt{\varepsilon_0\mu_0}\hat{\chi}^{\mathrm{em}}\mathbf{H}^{\omega}\right].
\end{aligned}
\tag{17}
$$

The refractive index N is introduced as

$$
N = \frac{c}{\omega}|\mathbf{k}| = \frac{|\mathbf{k}|}{\omega\sqrt{\varepsilon_0\mu_0}},
\tag{18}
$$

where c is the speed of light in vacuum and $N = |\mathbf{N}|$. The refractive index is a complex function $N = n + ik$ where n is the index of refraction and k is the extinction coefficient. In non-ME materials $\hat{\chi}^{\mathrm{me}} = \hat{\chi}^{\mathrm{em}} = 0$, and in isotropic materials Eq. (17) gives $N = \sqrt{\hat{\varepsilon}\hat{\mu}}$.

It is convenient to show Eq. (17) in matrix form with the relations of Eq. (12) and Eq. (14),

$$
\omega\begin{bmatrix} -\varepsilon_0\hat{\varepsilon} & -\sqrt{\varepsilon_0\mu_0}\hat{\chi}^{\mathrm{em}}-\hat{\mathbf{k}}_{\times} \\ \sqrt{\varepsilon_0\mu_0}\hat{\chi}^{\mathrm{me}}-\hat{\mathbf{k}}_{\times} & \mu_0\hat{\mu} \end{bmatrix}\begin{pmatrix} \mathbf{E}^{\omega} \\ \mathbf{H}^{\omega} \end{pmatrix} = \omega A(\hat{\mathbf{k}}_{\times})\begin{pmatrix} \mathbf{E}^{\omega} \\ \mathbf{H}^{\omega} \end{pmatrix} = 0, \tag{19}
$$

where $\hat{\mathbf{k}}_{\times} \equiv \mathbf{k}\times$ is the cross product operator. This equation has non-trivial solutions for Eq. (18) if the determinant of the matrix $A(\hat{\mathbf{k}}_{\times})$ is zero. However, the low symmetry of MF materials can make that a tedious calculation, as the quartic equations for the index of refraction are hard to solve analytically. One workaround is to define a magnetic symmetry and to determine the non-zero susceptibility tensors components from symmetry principles. Then the solutions of refractive index can be derived depending on the light propagation direction [18]. The solution of Eq. (19) for Eq. (18) yields a refractive index for individual polarizations E_{δ}^{ω} and H_{γ}^{ω}, where $\delta \neq \gamma$, in $+\mathbf{k}$ and $-\mathbf{k}$ directions.

If linearly polarized light is travelling through a thin sample where the light polarization is almost preserved, the index of refraction can be approximated by

$$
N_{\delta,\gamma}^{\pm}(\omega) \approx \sqrt{\varepsilon_{\delta\delta}(\omega)\mu_{\gamma\gamma}(\omega)} \pm \frac{1}{2}\left[\chi_{\delta\gamma}^{\mathrm{em}}(\omega)+\chi_{\gamma\delta}^{\mathrm{me}}(\omega)\right],
\tag{20}
$$

where the indices $\{\gamma,\delta\}$ define the directions of oscillating fields $\{\mathbf{H}^{\omega},\mathbf{E}^{\omega}\}$, respectively and the $\pm$ defines the direction of light propagation. The term $\pm\frac{1}{2}\left[\chi_{\delta\gamma}^{\mathrm{em}}(\omega)+\chi_{\gamma\delta}^{\mathrm{me}}(\omega)\right]$ determines whether the refractive index is different for oppositely travelling waves. In this equation the off-diagonal elements of tensors $\hat{\varepsilon}$ and $\hat{\mu}$ are neglected as the diagonal components dominate over them in leading order of refraction index.

The absorption coefficient is related to the imaginary part of the refractive index as,

$$
\alpha_{\delta,\gamma}^{\pm\mathbf{k}}(\omega) = 2\frac{\omega}{c}\Im N_{\delta,\gamma}^{\pm\mathbf{k}}(\omega).
\tag{21}
$$

Table 1: The optical effects of spin-waves arising from the dynamic susceptibility tensor elements that are related to the linear ME effect. The indexes $\alpha, \beta = x, y, z$ where $\alpha \neq \beta$. The table is reproduced from Ref. [101].

Optical effects	Susceptibility
Magnetoactive absorption	$\chi_{\alpha\alpha}^{mm}$
Electroactive absorption	$\chi_{\alpha\alpha}^{ee}$
Faraday rotation	$\chi_{\alpha\beta}^{mm} - \chi_{\beta\alpha}^{mm}, \chi_{\alpha\beta}^{ee} - \chi_{\beta\alpha}^{ee}$
Natural circular dichroism (NCD)	$\chi_{\alpha\alpha}^{me} - \chi_{\alpha\alpha}^{em}$
Nonreciprocal directional dichroism (NDD)	$\chi_{\alpha\beta}^{me} + \chi_{\beta\alpha}^{em}$

The nonreciprocal directional dichroism is defined as the difference of absorption by counter propagating waves [100] as

$$\Delta\alpha_{\gamma,\delta}^{\pm\mathbf{k}}(\omega) = \alpha_{\gamma,\delta}^{+\mathbf{k}}(\omega) - \alpha_{\gamma,\delta}^{-\mathbf{k}}(\omega) = 2\frac{\omega}{c}\Im\left[\chi_{\gamma\delta}^{em}(\omega) + \chi_{\delta\gamma}^{me}(\omega)\right]. \tag{22}$$

NDD is only one of the optical effects that arises from the dynamic susceptibilities. Other optical effects and their relation to the dynamic susceptibilities are summarized in Table 1.

1.3.4 Magnetoelectric susceptibilities derived from Kubo formula

The microscopic description of the ME effect is governed by the Kubo formula, that defines the linear response of a quantum system to a time-dependent small perturbation [102]. Here the perturbation is an electromagnetic field where the electric and magnetic field components are oscillating at frequency ω. According to the Kubo formula optical susceptibilities at finite temperature are [100, 103]

$$\chi_{\gamma\delta}^{ee}(z) = -\frac{V_c}{\varepsilon_0\hbar}\sum_{m,n}\frac{e^{-\beta\hbar\omega_n} - e^{-\beta\hbar\omega_m}}{\sum_i e^{-\beta\hbar\omega_i}} \times \frac{\langle n|P_\gamma|m\rangle\langle m|P_\delta|n\rangle}{z - \omega_m + \omega_n}, \tag{23}$$

$$\chi_{\gamma\delta}^{mm}(z) = -\frac{\mu_0 V_c}{\hbar}\sum_{m,n}\frac{e^{-\beta\hbar\omega_n} - e^{-\beta\hbar\omega_m}}{\sum_i e^{-\beta\hbar\omega_i}} \times \frac{\langle n|M_\gamma|m\rangle\langle m|M_\delta|n\rangle}{z - \omega_m + \omega_n}, \tag{24}$$

$$\chi_{\gamma\delta}^{me}(z) = -\frac{V_c}{\hbar}\sqrt{\frac{\mu_0}{\varepsilon_0}}\sum_{m,n}\frac{e^{-\beta\hbar\omega_n} - e^{-\beta\hbar\omega_m}}{\sum_i e^{-\beta\hbar\omega_i}} \times \frac{\langle n|M_\gamma|m\rangle\langle m|P_\delta|n\rangle}{z - \omega_m + \omega_n}, \tag{25}$$

$$\chi_{\delta\gamma}^{em}(z) = -\frac{V_c}{\hbar}\sqrt{\frac{\mu_0}{\varepsilon_0}}\sum_{m,n}\frac{e^{-\beta\hbar\omega_n} - e^{-\beta\hbar\omega_m}}{\sum_i e^{-\beta\hbar\omega_i}} \times \frac{\langle n|P_\delta|m\rangle\langle m|M_\gamma|n\rangle}{z - \omega_m + \omega_n}, \tag{26}$$

where $z = \omega + i\varepsilon$ is complex frequency, $\varepsilon \to 0+$; $|n\rangle$ and $|m\rangle$ are eigenstates with energies $\hbar\omega_n$ and $\hbar\omega_m$, respectively. M_γ and P_δ are the operators of the magnetic and electric dipole density, V_c is the volume of the unit cell and $\beta = (k_BT)^{-1}$ is the inverse temperature. If the transition matrix element $\langle m|P_\gamma|n\rangle$ is finite then the transition $|n\rangle \to |m\rangle$ is electric dipole active and the charge susceptibility $\chi_{\gamma\delta}^{ee}(z)$ is non-zero. Similarly, when the transition matrix element $\langle m|M_\delta|n\rangle \neq 0$, then the magnetic dipole active transition is allowed and the susceptibility $\chi_{\gamma\delta}^{mm}(z)$ is non-zero. ME susceptibilities $\chi_{\gamma\delta}^{me}(z)$ and $\chi_{\delta\gamma}^{em}(z)$ for the transition $|n\rangle \to |m\rangle$ are non-zero if both matrix elements, $\langle m|M_\delta|n\rangle$ and $\langle m|P_\gamma|n\rangle$, are finite, it is $|n\rangle \to |m\rangle$ is simultaneously magnetic-dipole and electric-dipole active.

At zero-temperature limit the excitations are from the ground state $|0\rangle$ and $\frac{e^{-\beta\hbar\omega_0}}{\sum_i e^{-\beta\hbar\omega_i}} = 1$. Then the Eq. (25) has the form

$$\chi_{\gamma\delta}^{\text{me}}(z) = -\frac{V_c}{\hbar}\sqrt{\frac{\mu_0}{\varepsilon_0}}\sum_m\left[\frac{\langle 0|M_\gamma|m\rangle\langle m|P_\delta|0\rangle}{z-\omega_m} - \frac{\langle m|M_\gamma|0\rangle\langle 0|P_\delta|m\rangle}{z+\omega_m}\right]. \tag{27}$$

For simplification we introduce a notation $MP \equiv \langle 0|M_\gamma|m\rangle\langle m|P_\delta|0\rangle$ and separate the transition matrix elements to real and imaginary part as

$$\langle 0|M_\gamma|m\rangle\langle m|P_\delta|0\rangle = \Re(MP) + i\Im(MP). \tag{28}$$

Since M_γ and P_δ are Hermitian,

$$\langle m|M_\gamma|0\rangle\langle 0|P_\delta|m\rangle = \left(\langle 0|M_\gamma|m\rangle\langle m|P_\delta|0\rangle\right)^* = \Re(MP) - i\Im(MP). \tag{29}$$

By using these relations we can rewrite the Eq. (27) as

$$\begin{aligned}
\chi_{\gamma\delta}^{\text{me}}(z) &= -\frac{V_c}{\hbar}\sqrt{\frac{\mu_0}{\varepsilon_0}}\sum_m\left[\frac{\Re(MP)+i\Im(MP)}{z-\omega_m} - \frac{\Re(MP)-i\Im(MP)}{z+\omega_m}\right]\\
&= -\frac{V_c}{\hbar}\sqrt{\frac{\mu_0}{\varepsilon_0}}\sum_m\left[\Re(MP)\left(\frac{1}{z-\omega_m}-\frac{1}{z+\omega_m}\right) + i\Im(MP)\left(\frac{1}{z-\omega_m}+\frac{1}{z+\omega_m}\right)\right].
\end{aligned} \tag{30}$$

In the limit of vanishing imaginary part of complex frequency, $z = \omega + i\varepsilon$, we have

$$\lim_{\varepsilon\to 0}\frac{1}{\omega+i\varepsilon\pm\omega_m} = \frac{1}{\omega\pm\omega_m} - i\pi\delta(\omega\pm\omega_m), \tag{31}$$

where the imaginary part follows from the definition of delta-function,

$$\delta(x) = \frac{1}{\pi}\lim_{\varepsilon\to 0}\frac{\varepsilon}{x^2+\varepsilon^2}. \tag{32}$$

Making these substitutions the zero-temperature ME susceptibility, Eq. (30), becomes

$$\begin{aligned}
\chi_{\gamma\delta}^{\text{me}}(\omega) = -\frac{V_c}{\hbar}\sqrt{\frac{\mu_0}{\varepsilon_0}}\sum_m\Big\{&\Re(MP)\frac{2\omega_m}{\omega^2-\omega_m^2} - i\pi\Re(MP)\left[\delta(\omega-\omega_m)-\delta(\omega+\omega_m)\right]\\
&+ i\Im(MP)\frac{2\omega}{\omega^2-\omega_m^2} + \pi\Im(MP)\left[\delta(\omega-\omega_m)+\delta(\omega+\omega_m)\right]\Big\}.
\end{aligned} \tag{33}$$

From this equation the imaginary and real parts of $\chi_{\gamma\delta}^{\text{me}}(\omega)$ can be separated,

$$\Re\chi_{\gamma\delta}^{\text{me}}(\omega) = -\frac{V_c}{\hbar}\sqrt{\frac{\mu_0}{\varepsilon_0}}\sum_m\left\{\Re(MP)\frac{2\omega_m}{\omega^2-\omega_m^2} + \pi\Im(MP)\left[\delta(\omega-\omega_m)+\delta(\omega+\omega_m)\right]\right\}, \tag{34}$$

$$\Im\chi_{\gamma\delta}^{\text{me}}(\omega) = -\frac{V_c}{\hbar}\sqrt{\frac{\mu_0}{\varepsilon_0}}\sum_m\left\{\Im(MP)\frac{2\omega}{\omega^2-\omega_m^2} - \pi\Re(MP)\left[\delta(\omega-\omega_m)-\delta(\omega+\omega_m)\right]\right\}. \tag{35}$$

For the time-reversal even operator, $(P_\alpha)' = P_\alpha$, and time-reversal odd operator, $(M_\alpha)' = -M_\alpha$, it holds [104, p. 219]

$$\begin{aligned}
\left(\langle m|P_\alpha|n\rangle\right)' &= +\langle n|P_\alpha|m\rangle, \tag{36}\\
\left(\langle m|M_\alpha|n\rangle\right)' &= -\langle n|M_\alpha|m\rangle, \tag{37}
\end{aligned}$$

where $(\dots)'$ is the time-reversal operation. Therefore, the real part of the transition matrix element product, $MP = \langle 0|M_\gamma|m\rangle\langle m|P_\delta|0\rangle$, is antisymmetric under the time reversal while the imaginary part is symmetric. By that the ME tensors, Eqs. (34) and (35), are connected by the time reversal symmetry as $(\chi_{\gamma\delta}^{\mathrm{me}})' = -\chi_{\delta\gamma}^{\mathrm{em}}$. In the zero-frequency limit ME susceptibility is real and if $\omega_m > 0$ only the real part of the matrix element product $\langle 0|M_\gamma|m\rangle\langle m|P_\delta|0\rangle$ contributes to the static ME susceptibility:

$$\chi_{\gamma\delta}^{\mathrm{me}}(0) = \frac{2V_c}{\hbar}\sqrt{\frac{\mu_0}{\varepsilon_0}}\sum_m \frac{\Re\left(\langle 0|M_\gamma|m\rangle\langle m|P_\delta|0\rangle\right)}{\omega_m}. \tag{38}$$

1.3.5 Magnetoelectric sum rule

The NDD of spin-wave excitation is connected to the static ME effect through the ME sum rule [100]. While it can be derived through Kramers-Kronig relations, it can also be obtained from Kubo formulas, Eqs. (22) and (38), as described in the Supplemental Material of Ref. [100]. The ME sum rule connects the directional dichroism spectra of magneto-electric excitations to the linear ME susceptibility as

$$\chi_{\gamma\delta}^{\mathrm{me}}(0) = \frac{c}{2\pi}\mathscr{P}\int_0^\infty \frac{\Delta\alpha(\omega)}{\omega^2}\,\mathrm{d}\omega, \tag{39}$$

where $\mathscr{P}$ stands for the Cauchy principal value integral.

According to this sum rule, the main contribution to the static ME effect comes from low energy ME excitations as the absorption difference, $\Delta\alpha$ is suppressed by the ω^2 in the denominator. The sum rule defines the importance of the characterization of dynamic ME excitations in order to obtain additional information about magnetoelectric effect that is not possible with the static experimental techniques.

1.4 Spin precession dynamics

Fundamentally, magnetic materials contain atoms with net magnetic moments μ that strongly interact with each other. However, it is convenient to ignore the atomic nature and characterize the dynamics of magnetic moments through a vector field. Here the vector field is the magnetization, i.e magnetic moment per unit volume. This micromagnetic description of magnetization was first formulated by Landau and Lifshitz [105] for an arbitrary body with preferred direction of magnetization. They were interested how regions of magnetic domains are created inside the material and how the domains change in time in response to the external magnetic field. In this Section we will derive the Landau-Lifshitz equation and show how it leads to the dynamic magnetic susceptibility what describes the THz absorption spectrum of spin-waves.

1.4.1 Landau-Lifshitz equation

To derive Landau-Lifshitz equation we have to understand the precession of magnetic moments. Electron, in addition to orbital angular momentum, $\mathbf{L}$, has internal angular momentum, spin $\mathbf{S}$, making the total angular momentum,

$$\mathbf{J} = \mathbf{L} + \mathbf{S}. \tag{40}$$

From the classical mechanics it is known that the time evolution of angular momentum equals to the torque that is applied to the body:

$$\frac{d\mathbf{J}}{dt} = \boldsymbol{\tau}. \tag{41}$$

The total angular momentum is related to magnetic moment $\boldsymbol{\mu}$ through the gyromagnetic ratio γ as

$$\boldsymbol{\mu} = -\gamma \mathbf{J}, \tag{42}$$

with the minus from the electron's negative charge. The gyromagnetic ratio is defined as

$$\gamma = g\frac{|e|}{2m_e}, \tag{43}$$

where g is the Landé g factor, e is the electron charge and m_e is the electron mass. The magnetization of body $\mathbf{M}$ is equal to the sum of all magnetic moments per volume unit:

$$\mathbf{M} = \frac{N\boldsymbol{\mu}}{V}, \tag{44}$$

where N is the number of magnetic moments and V is the volume of the sample. Lets assume there is an effective magnetic field, $\mu_0 \mathbf{H}^{\mathrm{eff}} = \mathbf{B}^{\mathrm{eff}}$, acting on electron. $\mathbf{B}^{\mathrm{eff}}$ induces a torque on the magnetic moment [106],

$$\boldsymbol{\tau} = \boldsymbol{\mu} \times \mathbf{B}^{\mathrm{eff}}, \tag{45}$$

which can be rewritten through Eq. (44) as

$$\boldsymbol{\tau} = \frac{V}{N}\mathbf{M} \times \mathbf{B}^{\mathrm{eff}}. \tag{46}$$

We can derive the $\mathbf{J}$ through Eqs. (42,44) as

$$\mathbf{J} = -\frac{\boldsymbol{\mu}}{\gamma} = -\frac{V\mathbf{M}}{\gamma N}. \tag{47}$$

Using the last two equations and Eqs. (41), we derive the Landau-Lifshitz equation which describes the motion of magnetization in the magnetic field:

$$\frac{d\mathbf{M}}{dt} = -\gamma \mathbf{M} \times \mathbf{B}^{\mathrm{eff}}. \tag{48}$$

Thus, in a magnetically ordered body the effective field $\mathbf{B}^{\mathrm{eff}}$ induces a precession of local magnetization $\mathbf{M}(\mathbf{r}, t)$ whereas the γ determines the precession rate. To describe the dynamics of a a discrete set of magnetic moments $\mathbf{M}_i$, where $i = 1, 2, ..n$, the equation of motion can be written as

$$\frac{d\mathbf{M}_i}{dt} = -\gamma \mathbf{M}_i \times \mathbf{B}_i^{\mathrm{eff}}. \tag{49}$$

Please note, because we explicitly assume that the gyromagnetic ratio is negative, see Eq. (42), there is a minus sign on the right hand side of Eq. (49).

The effective field, $\mathbf{B}_i^{\mathrm{eff}}$, producing torque on $\mathbf{M}_i$ consists of applied magnetic field and magnetic field generated by nearby magnetic moments $\mathbf{M}_j$ and by the orbital motion of nearby electrons. The $\mathbf{B}_i^{\mathrm{eff}}$ is the change of energy, $U(\mathbf{M}) \equiv U(\mathbf{M}_1, \mathbf{M}_2, \ldots, \mathbf{M}_n)$, by the work done when rotating $\mathbf{M}_i$ against $\mathbf{B}_i^{\mathrm{eff}}$ forces [106] as

$$\mathbf{B}_i^{\mathrm{eff}} = -\left[\mathbf{x}\frac{\partial U(\mathbf{M})}{\partial M_{ix}} + \mathbf{y}\frac{\partial U(\mathbf{M})}{\partial M_{iy}} + \mathbf{z}\frac{\partial U(\mathbf{M})}{\partial M_{iz}}\right] \equiv -\frac{\partial U(\mathbf{M})}{\partial \mathbf{M}_i}, \tag{50}$$

where M_{ix}, M_{iy} and M_{iz} are the components of the i-th magnetic moment $\mathbf{M}_i$.

In Ref. I, the Landau-Lifshitz equation (48) is rewritten for the spin system using $\mathbf{M} = -\gamma\hbar\mathbf{S}$ and spin Hamiltonian $\mathscr{H}$ as energy,

$$\dot{\mathbf{S}}_i \equiv \frac{d\mathbf{S}_i}{dt} = -\frac{1}{\hbar}\mathbf{S}_i \times \frac{\partial \mathscr{H}}{\partial \mathbf{S}_i}. \tag{51}$$

1.4.2 Resonance frequencies of magnons

To get the resonance frequencies of magnon modes, we have to solve the Eq. (51). Since we are interested in the absorption of long-wavelength radiation, the excited magnons are in the Γ point. Then it is sufficient to solve Eq. (51) for one magnetic unit cell for N spins, where N is the number of spins in the unit cell. We assume that deviations $\delta \mathbf{S}_i$ from equilibrium positions $\mathbf{S}_i^0$ are small, i.e $\mathbf{S}_i = \mathbf{S}_i^0 + \delta \mathbf{S}_i$. If we multiply the Eq. (51) with $\mathbf{S}_i$ then the right hand side equals to zero, because $\mathbf{S}_i$ and the right hand side of Eq. (51) are perpendicular vectors. Therefore

$$\frac{d\,|\mathbf{S}_i|^2}{dt} = 0, \tag{52}$$

from where it follows that the spin length is constant in the first order of $\delta \mathbf{S}_i$. If we insert $\mathbf{S}_i$ into Eq. (51) and keep only the terms linear in $\delta \mathbf{S_i}$ we get

$$\delta \dot{\mathbf{S}}_i = -\frac{1}{\hbar} \mathbf{S}_i^0 \times \frac{\partial \mathcal{H}_\delta}{\partial \mathbf{S}_i}, \tag{53}$$

where the effective field is

$$\frac{\partial \mathcal{H}_\delta}{\partial \mathbf{S}_i} = \frac{\partial \mathcal{H}}{\partial \mathbf{S}_i}\bigg|_{\{\mathbf{S}^0\}+\{\delta\mathbf{S}\}}. \tag{54}$$

The equilibrium spin configuration $\{\mathbf{S}^0\}$ is found by minimizing the energy, $\mathcal{H}$, with respect to the orientation of each spin; spins are treated as classical vectors with constant length. The correct equilibrium spin configuration must satisfy

$$\frac{\partial \mathcal{H}}{\partial \mathbf{S}_i}\bigg|_{\{\mathbf{S}^0\}} = 0. \tag{55}$$

Energies of magnon modes, $\hbar\omega$, are calculated from the Eq. (53) by assuming a harmonic time dependence:

$$\delta \mathbf{S}_i(t) = e^{i\omega t} \delta \mathbf{S}_i^0, \tag{56}$$

where $\delta \mathbf{S}_i^0$ is the amplitude of the i-th spin in the magnon mode.

1.4.3 Damping effect of magnetization

In Eq. (51) spins would undergo an endless precession motion around the effective field. However, from experiments it is known that this motion decays in a finite time because of microscopic thermal motion that is induced by the local magnetization field [106]. This damping occurs because of the coupling of the magnetization to spin waves, eddy currents, lattice vibrations, strains and defects. The damping term cannot be derived theoretically and therefore has to be introduced empirically. There are two main approaches to describe the damping of magnetization, the Gilbert equation and the Landau-Lifshitz-Gilbert equation. Next, we analyse how the Landau-Lifshitz-Gilbert and the Gilbert equations are related.

The Gilbert damping equation originates from Eq. (49) where Gilbert introduced a phenomenological damping term η [107, p. 181] as

$$\frac{d\mathbf{M}_i}{dt} = -\gamma \mathbf{M}_i \times \left(\mathbf{B}_i^{\text{eff}} - \eta \frac{d\mathbf{M}_i}{dt} \right), \tag{57}$$

$$= -\gamma \mathbf{M}_i \times \mathbf{B}_i^{\text{eff}} + \eta\,\gamma \mathbf{M}_i \times \frac{d\mathbf{M}_i}{dt}. \tag{58}$$

From this equation we can derive the Landau-Lifshitz-Gilbert equation, first by applying a vector product by $\mathbf{M}_i$ to both sides:

$$\mathbf{M}_i \times \frac{d\mathbf{M}_i}{dt} = -\gamma\mathbf{M}_i \times \left(\mathbf{M}_i \times \mathbf{B}_i^{\text{eff}}\right) + \eta\,\gamma\mathbf{M}_i \times \left(\mathbf{M}_i \times \frac{d\mathbf{M}_i}{dt}\right). \tag{59}$$

This can be simplified by using $\mathbf{A} \times \mathbf{B} \times \mathbf{C} = \mathbf{B}(\mathbf{A}\cdot\mathbf{C}) - \mathbf{C}(\mathbf{A}\cdot\mathbf{B})$ for the damping term, $\mathbf{M}_i \times \left(\mathbf{M}_i \times \frac{d\mathbf{M}_i}{dt}\right) = \mathbf{M}_i\left(\mathbf{M}_i \cdot \frac{d\mathbf{M}_i}{dt}\right) - \frac{d\mathbf{M}_i}{dt}(\mathbf{M}_i \cdot \mathbf{M}_i) = -M_i^2\frac{d\mathbf{M}_i}{dt}$ where we used $\mathbf{M}_i \cdot \frac{d\mathbf{M}_i}{dt} = 0$. That leads to the relation

$$\mathbf{M}_i \times \frac{d\mathbf{M}_i}{dt} = -\gamma\mathbf{M}_i \times \left(\mathbf{M}_i \times \mathbf{B}_i^{\text{eff}}\right) - \eta\gamma M_i^2 \frac{d\mathbf{M}_i}{dt}. \tag{60}$$

From Eq. (60) and Eq. (58) we get

$$\frac{d\mathbf{M}_i}{dt} = -\gamma\mathbf{M}_i \times \mathbf{B}_i^{\text{eff}} + \eta\gamma\left[-\gamma\mathbf{M}_i \times \left(\mathbf{M}_i \times \mathbf{B}_i^{\text{eff}}\right) - \eta\gamma M_i^2 \frac{d\mathbf{M}_i}{dt}\right], \tag{61}$$

which after rearrangements equals to the Landau-Lifshitz-Gilbert equation,

$$\frac{d\mathbf{M}_i}{dt} = -\beta\mathbf{M}_i \times \mathbf{B}_i^{\text{eff}} - \lambda\mathbf{M}_i \times \left(\mathbf{M}_i \times \mathbf{B}_i^{\text{eff}}\right), \tag{62}$$

where constants β and λ are defined as

$$\beta = \frac{\gamma}{1 + \gamma^2\eta^2 M_i^2} \quad \text{and} \quad \lambda = \frac{\gamma^2\eta}{1 + \gamma^2\eta^2 M_i^2}. \tag{63}$$

Equations. (62) and (58) are equivalent if the constants are defined as in Eq. (63). From practical aspects described in Ref. [108], for high damping systems Eq. (62) should not be used while Eq. (58) is plausible for all values of damping.

The assumption, $\gamma^2\eta^2 M_i^2 \ll 1$ is made often in literature to simplify Eq. (61):

$$\frac{d\mathbf{M}_i}{dt} = -\gamma\mathbf{M}_i \times \mathbf{B}_i^{\text{eff}} - \eta\gamma^2\mathbf{M}_i \times \left(\mathbf{M}_i \times \mathbf{B}_i^{\text{eff}}\right). \tag{64}$$

Using a dimensionless damping constant $\alpha = \gamma\eta M$ [106], we rewrite the Landau-Lifshitz-Gilbert equation as

$$\frac{d\mathbf{M}_i}{dt} = -\gamma\mathbf{M}_i \times \mathbf{B}_i^{\text{eff}} - \frac{\alpha\gamma}{M_i}\mathbf{M}_i \times \left(\mathbf{M}_i \times \mathbf{B}_i^{\text{eff}}\right). \tag{65}$$

This equation can be rewritten for a spin system with relation $\mathbf{M}_i = -\gamma\hbar\mathbf{S}_i$ and by Hamiltonian $\mathcal{H}(\mathbf{S}_1, \mathbf{S}_2, \ldots, \mathbf{S}_n)$, that describes the energy change of the system, as

$$\frac{d\mathbf{S}_i}{dt} = -\frac{1}{\hbar}\mathbf{S}_i \times \frac{\partial\mathcal{H}}{\partial\mathbf{S}_i} + \frac{\alpha}{\hbar S_i}\mathbf{S}_i \times \left(\mathbf{S}_i \times \frac{\partial\mathcal{H}}{\partial\mathbf{S}_i}\right). \tag{66}$$

In the Ref. I and Ref. III we used the Landau-Lifshitz-Gilbert equation in order to calculate the absorption spectrum of THz radiation by spin wave modes as described in the next section.

1.4.4 Absorption coefficient and Landau-Lifshitz-Gilbert equation

The absorption coefficient is proportional to the imaginary part of the refractive index, already defined by Eq. (21). The refractive index for ME materials was defined in Eq. (20). From here on we assume only a small polarization rotation and negligible linear magneto-electric susceptibilities. If the polarization of incident radiation is (E_k^ω, H_l^ω) where k and l are x, y, or z, then the refractive index simplifies to

$$N_{k,l} = \sqrt{\varepsilon_{kk}\mu_{ll}}, \tag{67}$$

where ε_{kk} is the background dielectric permittivity and μ_{ll} is the magnetic permittivity defined by Eq. (13). By assuming that $\chi_{ll}^{mm} \ll 1$ in Eq. (13), we can define

$$\sqrt{\mu_{ll}} = \sqrt{\frac{1}{1-\chi_{ll}^{mm}}} \approx 1 + \frac{1}{2}\chi_{ll}^{mm}. \tag{68}$$

Using Eq. (68) for dynamic magnetic permeability $\chi_{ll}(\omega)$ in Eq. (67) we get

$$N_{k,l} \approx \sqrt{\varepsilon_{kk}}\left(1 + \frac{\chi_{ll}^{mm}(\omega)}{2}\right). \tag{69}$$

If we assume that ε_{kk} is constant and real at low frequencies, then the absorption coefficient which is proportional to the imaginary part of the refractive index, is

$$\alpha_{k,l}(\omega) = \frac{2\omega}{c}\sqrt{\varepsilon_{kk}}\,\Im\,\chi_{ll}^{mm}(\omega). \tag{70}$$

Note that although the alternating magnetic field interacts with the spins, the absorption of radiation depends on the dielectric properties of material, ε_{kk}.

The susceptibility $\chi_{ll}^{mm}(\omega)$ is obtained by summing all the magnetic moments in the unit cell, $\mathbf{M} = \gamma\hbar\sum_{i=1}^{N}\mathbf{S}_i$. Then

$$\gamma\hbar\left[\sum_{i=1}^{M}\delta\mathbf{S}_i(t)\right] = \chi_{ll}^{mm}(\omega)\mu_0\mathbf{H}^\omega(t), \tag{71}$$

where the time-dependent magnetization, left side, is induced by the time-dependent magnetic field through the frequency-dependent magnetic susceptibility χ_{ll}^{mm}, right side. To get the relationship Eq. (71), we rewrite Eq. (66) using $\mathbf{A}\times\mathbf{B}\times\mathbf{C} = \mathbf{B}(\mathbf{A}\cdot\mathbf{C}) - \mathbf{C}(\mathbf{A}\cdot\mathbf{B})$,

$$\frac{d\mathbf{S}_i}{dt} = -\frac{1}{\hbar}\mathbf{S}_i\times\frac{\partial\mathcal{H}}{\partial\mathbf{S}_i} + \mathbf{S}_i\left(\frac{\alpha}{\hbar S_i}\mathbf{S}_i\cdot\frac{\partial\mathcal{H}}{\partial\mathbf{S}_i}\right) - \frac{\partial\mathcal{H}}{\partial\mathbf{S}_i}\left(\frac{\alpha}{\hbar S_i}\mathbf{S}_i\cdot\mathbf{S}_i\right). \tag{72}$$

The harmonic alternating magnetic field of electromagnetic waves is introduced by adding the $\mathbf{H}^\omega(t) = \mathbf{H}^\omega\exp(i\omega t)$ to the effective field, and to the equation of motion, by keeping only terms linear in $\delta\mathbf{S}_i$ and $\mathbf{H}^\omega$, is

$$
\begin{aligned}
\delta\dot{\mathbf{S}}_i = \quad & -\frac{1}{\hbar}\mathbf{S}_i^0\times\left[\frac{\partial\mathcal{H}_\delta}{\partial\mathbf{S}_i} - \mu_0\mathbf{H}^\omega(t)\right] \\
& + \frac{\alpha}{\hbar}\frac{\mathbf{S}_i^0}{S_i^0}\mathbf{S}_i^0\cdot\left[\frac{\partial\mathcal{H}_\delta}{\partial\mathbf{S}_i} - \mu_0\mathbf{H}^\omega(t)\right] \\
& - \frac{\alpha}{\hbar}S_i^0\left[\frac{\partial\mathcal{H}_\delta}{\partial\mathbf{S}_i} - \mu_0\mathbf{H}^\omega(t)\right].
\end{aligned}
\tag{73}
$$

Using $\delta\mathbf{S}_i(t) = \delta\mathbf{S}_i^0\exp(i\omega t)$ and Eq. (71) the magnetic susceptibility χ_{ll}^{mm} is obtained from Eq. (73). Keep in mind that here the derivative of the Hamiltonian is calculated at $\{\mathbf{S}^0 + \delta\mathbf{S}\}$ as defined by Eq. (54).

1.5 Spin excitations

In magnetically ordered materials, THz electromagnetic radiation can force electron spins to deviate slightly from their ground state to excite a wavelike behaviour throughout the solid, i.e. excite magnetic waves named spin waves including magnons [13,109]. While the term spin wave is describing all long range spin excitations, a magnon is a spin wave quasi-particle, described with quantum-mechanical operators. In magnetoelectric compounds exotic magnetic fluctuations can emerge from the mixed dipolar and quadrupolar orders. These excitations arise from anisotropic exchange interactions that hybridize fluctuations which carry a fundamentally different quantum number. In the following sections we will describe magnon, multi-spin and quadrupolar excitation processes, discuss how they become observable for THz spectroscopy and how their spin projection state defines the magnetic field dependence of these modes.

1.5.1 Magnons

The term magnon comes from linear spin-wave theory with the assumption that the spin length of each individual spin is constant. Magnon is a spin-wave quasiparticle with angular momentum of $1\hbar$, magnetic moment of $1g\mu_B$ and it has spin one. A magnon is created by the magnetic dipole interaction between the spin and the magnetic vector of light [110, 111]. The corresponding particle of light is photon that has almost zero momentum and from the momentum conservation law it follows that if photon excites a magnon, it has to have zero linear momentum, i.e magnons are excited in the centre of the Brillouin zone where $\mathbf{k} = 0$. Magnons are often the strongest low energy spin-wave excitations. By the spin-wave theory the maximum number of allowed magnon excitations equals the number of spins N in the unit cell [112]. If the fixed spin length condition is relaxed and there exists an anisotropic distribution of charge and magnetization, then there can be many more collective lattice excitations that arise from multipolar degrees of freedom [30]. This is discussed in the following paragraph. For an easier understanding of the different spin waves, please see Fig. 5.

In materials which have a strong spin-orbit coupling spins can be excited by the electric component of light [111]. Compared to the magnetic excitation where spin projection state changes by $\Delta m_s = 1$ in the electric transition $\Delta m_s = 2$. If a magnon is excited by electric field its named electromagnon [14] and when by both components of electromagnetic radiation the term ME resonance is used [15, 16]. There are no sharp borderlines between the magnon, electromagnon and ME resonance. The terms used to describe spin waves depends on the fields they are excited by as well as which theory is used. The electric dipole activity in magnetoelectric materials is closely related to strong single-ion anisotropy which can mix energy levels with different spin-projections m_s states [27,42]. In these systems magnons can be excited between the same energy levels simultaneously by $\Delta m_s = 1$ or $\Delta m_s = 2$. Although the electric dipole activity is not captured by the spin-wave theory, it can describe these excitations reasonably well and reveal the spin dynamics of the material, see Ref. I and III.

1.5.2 Multi-spin excitations and bound-states

In strongly interacting magnetic materials, where $\Lambda >> J$, a single absorbed photon can excite oppositely polarized spin waves at nearby sites, i.e create a two-magnon excitation [113]. The two individual spin waves are propagating in correlated manner and are created on a single magnon dispersion curve with wavevectors $\mathbf{k_1} + \mathbf{k_2} = 0$ [111, 114]. While it is possible to excite two-magnon excitations at every point of the Brillouin zone, only those which originate from the regions with the highest density of states gain enough strength

to be detected [115]. The highest density of states, if neglecting the zone centre, is at the edges of Brillouin zone. The magnetic component of light can only excite excitations in the centre of Brillouin zone ($k = (0,0,0)$), to access the edges the process has to go through the electric component of light or be mediated by another excitation like phonon. One possibility how spins can be directly excited by the E^ω is through spin-orbit coupling [115].

To illustrate possible two-magnon excitations, we consider a two-sublattice antiferromagnet with two magnon excitations with frequencies $\omega^\pm(\mathbf{k})$. As one magnon induces a spin projection change $\Delta m_s = 1$, a two-magnon excitation can have $\Delta m_s = \{-2, 0, +2\}$. When Δm_s increases by one, let the state function be $|\mathbf{k}, +\rangle$ and if it decreases then $|\mathbf{k}, -\rangle$. There can be four different two-magnon states, see Table 2 [116]. In the case of a ferromagnet where all spins are pointing in the same direction we can only create two-magnon excitations by flipping two spins to the opposite, the state $|\mathbf{d}\rangle$ in Table 2. The situation gets more complicated when we have an antiferromagnet, as then we can also have $\Delta m_s = \{0, +2\}$, states $|\mathbf{a}\rangle$, $|\mathbf{b}\rangle$ and $|\mathbf{c}\rangle$ in Table 2. The magnons in the states $|\mathbf{a}\rangle$ and $|\mathbf{d}\rangle$ where $\Delta m_s = \{-2, +2\}$ are excited on same sublattices, but the states $|\mathbf{b}\rangle$ and $|\mathbf{c}\rangle$ where $\Delta m_s = 0$ the magnons are created on different sublattices [117]. Because of different nature of these two, $|\mathbf{a}\rangle$ and $|\mathbf{d}\rangle$ are named as two-magnon bound states and $|\mathbf{b}\rangle$ and $|\mathbf{c}\rangle$ two-magnon excitations. The four states have different parity relations, where odd parity means that the flipping of spacial coordinates can change the original system, which is neglected for even parity. The parity relation depends on the symmetry of the material. If we assume that the magnetic ions are in the centre of the inversion symmetry then the $\Delta m_s = 0$ states have different parity. For example, the Raman scattering technique can only probe positive parity states and by that can not see the state $|\mathbf{c}\rangle$ in Table 2. The parity defines which activity the two-magnon excitation has, odd parity indicates that the excitation can also be electric-dipole active, while even refers to magnetic-dipole activity. The spectral shape of the excitations is also different, the absorption of the states $|\mathbf{a}\rangle$ and $|\mathbf{d}\rangle$ looks like wide peaks, while the $|\mathbf{b}\rangle$ and $|\mathbf{c}\rangle$ are rather absorption bands [114, I]. The four states act differently in applied magnetic field. This can be used to distinguish the type of two-magnon excitations, Ref. I. In applied magnetic field the $|\mathbf{a}\rangle$, $|\mathbf{d}\rangle$ states are moving linearly in magnetic field appropriate to the $\Delta m_s = \{-2, +2\}$ while the $|\mathbf{b}\rangle$, $|\mathbf{c}\rangle$ states are insensitive to magnetic field [115].

Another class of multipolar excitations called quadrupolar excitations emerge in low symmetry materials with $S > 1/2$ and strong single-ion anisotropy. These originate from oscillating magnetic dipole and quadrupole moments and can be described with a multi-boson theory, [27, 29, 118] and [119, Ch. 8.3]. In multi-boson theory the fixed spin length condition, used in spin-wave theory, is relaxed and the expected number of excitations increases from N to $2NS$. For example, a four spin system $N = 4$, where $S = 2$, the expected number of excitations based on the spin-wave theory would be 4 and based on multi-boson theory 16. Therefore, the multi-boson theory can describe 12 more excitations than the spin-wave theory. Despite that, the complicated multi-boson theory is often not practised as the spin-wave mean-field theory can predict the magnetic exchange parameters reasonably well.

The family of quadrupolar excitations governs several different excitations, namely the spin-stretching modes and the single-ion bound states. These modes are expected in materials with strong single-ion anisotropy irrespective their crystal structure or magnetic order. In crystals with broken inversion symmetry the electric dipole and the spin quadrupole have the same symmetry, thus they can be excited with the electric field component of light. Peculiarly, in non-centrosymmetric crystals through electric dipole, the quadrupolar excitations become observable even without magnetic anisotropy [29].

Table 2: Possible two-magnon excitation states. The four states are represented as $|\mathbf{a}\rangle \, \Delta m_s$. For parity determination, it is assumed that the magnetic ions are in the centre of inversion symmetry. The odd parity is marked with minus $-$ while even with $+$. The Table is constructed based on [116, Ch. VI] and [115, (38)].

State	Δm_s	Parity
$|\mathbf{a}\rangle = |\mathbf{k}, +\rangle |-\mathbf{k}, +\rangle$	$+2$	$+$
$|\mathbf{b}\rangle = 2^{-\frac{1}{2}} \left[|\mathbf{k}, +\rangle |-\mathbf{k}, -\rangle + |\mathbf{k}, -\rangle |-\mathbf{k}, +\rangle \right]$	0	$+$
$|\mathbf{c}\rangle = 2^{-\frac{1}{2}} \left[|\mathbf{k}, +\rangle |-\mathbf{k}, -\rangle - |\mathbf{k}, -\rangle |-\mathbf{k}, +\rangle \right]$	0	$-$
$|\mathbf{d}\rangle = |\mathbf{k}, -\rangle |-\mathbf{k}, -\rangle$	-2	$+$

Spin-stretching modes arise from the relaxing of the spin length and as the name says, they can be understood as waves of oscillating spin lengths propagating in the lattice. The spin-stretching modes with additional quadrupole excitations were found in $Ba_2CoGe_2O_7$ and described with multi-boson spin wave theory, which allowed to understand the effect of non-zero easy-plane single-ion anisotropy [29]. If $\Lambda = 0$, then the only THz spectroscopy non-silent modes are magnons and by turning on $\Lambda > 0$, quadrupolar excitations become observable. If $\Lambda >> 0$, higher spin-projection states are suppressed and spin-wave spectra corresponding to isolated spins, like single-ion bound states (SIBS), become observable.

Single-ion bound states are $\Delta m_s = \{-2, +2\}$ excitations excited on a single site, see Fig. 5 and can be thought of as packets of reversed spins propagating in the lattice. There can be even larger single-ion bound states than two spin deviations if $S \geq 1$ and $\Lambda >> |J|$ [113, 120]. The SIBS cannot be detected with probes bound by the dipolar selection rule, as dipolar matrix elements vanish because of the operator $S^- = S^x - iS^y$ that must act on a single site twice. However, if the material has hybridization between dipolar and quadrupole fluctuations, the SIBS can be detected by FIR [121, 122], INS [30, 123] and ESR [120, 124]. Localized excitations usually do not have dispersion, but if the exchange interaction along the spins is larger than the transverse exchange interaction, the overlapping bands of magnons and SIBS are hybridized with an energy gap, giving the SIBS a mixed dipolar-quadrupolar dispersive character throughout the Brillouin zone [30]. Compared to the two-magnon bound state, the SIBS can be excited on a lower energy because of neglecting the $2D$ anisotropy of different sites, Fig. 5. This can be used to distinguish the SIBS from other excitations, as the energy can be lower than that of two-magnon excitations and in rare cases also below magnons, while the effective g-factor is twice as large as that of magnons [113, 121]. The SIBS can also exist in the range of the two-magnon continuum [124], which would make it possible to distinguish it [113], although for separating the high energy SIBS from spin-stretching modes or two-magnon bound states a theoretical analysis is needed.

1.5.3 The magnetic field dependence of mixed spin states

ME materials with strong anisotropies or Dzyaloshinskii-Moriya coupling can mix different spin projection states and give a finite electric-dipole moment to $\Delta m_s = \pm 2$, $\Delta m_s = \pm 3$ or even $\Delta m_s = \pm 4$ transitions, making them THz light active. These spin-wave excitations can have an unconventionally steep magnetic field dependence of frequency. In this section the origin of this steep dependence is investigated.

The classical energy of a magnetic moment $\boldsymbol{\mu}$ in magnetic field is $U = -\boldsymbol{\mu} \cdot \mathbf{B}$. The magnetic moment of an electron spin is $\boldsymbol{\mu} = -g\mu_B\mathbf{S}$, where the gyromagnetic ratio g and

Figure 5: Sketches of spin excitations in an easy-axis antiferromagnet with $S = 1$. (a) For an individual spin there are three possible spin projection states, $m_s = +1, 0, -1$, which are represented by up arrow, a dot and a down arrow, respectively. (b) The ground state of an antiferromagnet with spin Hamiltonian, $\mathscr{H} = \sum_{i,j} J_{ij} \mathbf{S}_i \cdot \mathbf{S}_j - D \sum_i \left(S_i^z \right)$, where J_{ij} is Heisenberg exchange interaction between spins and D is easy-axis single-ion anisotropy. We define the exchange interaction between the same sublattice spins as J and for different sublattices as J'. (c) One magnon excitation - the spin projection state changes by 1. The spin in the middle has 4 neighbouring spins from which two are situated at the same sublattice (row) and two are at different sublattice. The energy of this magnon is the sum of the neighbouring spins' exchange interaction $2J + 2J'$ and the single ion anisotropy D. (d) A visualization of the two-magnon excitation, where a single photon creates the spin projection change on two different sub-lattice spin sites, in total by $\Delta m_s = 2$. The energy is equal to the double of the single magnon energy. (e) Single-ion bound state where the spin projection changes by $\Delta m_s = 2$ on a single spin site. The energy of excitation can be lower than the two-magnon excitation. (f) Two-magnon bound state where a single photon creates spin projection states on neighbouring sites, in total by $\Delta m_s = 2$. This figure was inspired by the Fig. 7 in Ref. [125] and Fig. 1 in Ref. [30].
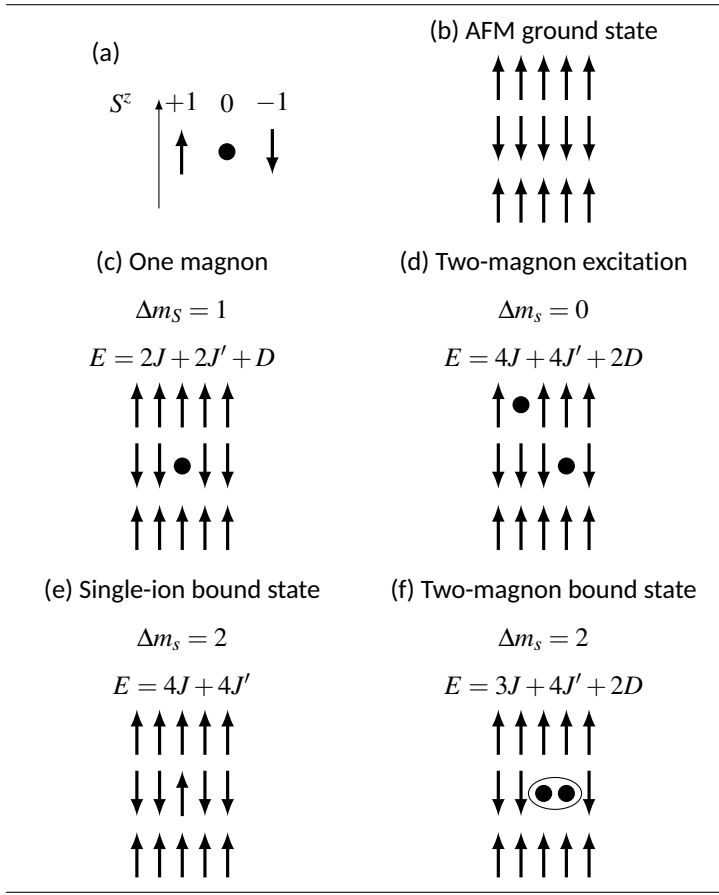
the Bohr magneton $\mu_B = \gamma\hbar$ are positive quantities, see Eq. (43). Thus, the Hamiltonian is

$$\mathcal{H}_z = g\mu_B\mu_0 \mathbf{H} \cdot \mathbf{S}, \tag{74}$$

where μ_0 is the magnetic permeability, $\mu_0\mathbf{H} = \mathbf{B}$ is the applied magnetic field and $\mathbf{S}$ is spin in units of $\hbar$. The projection of $\mathbf{S}$ on the z axis is $S_z|S,m_s\rangle = m_s|S,m_s\rangle$. The quantum number m_s has $2S+1$ values, $m_s \in \{-S, -S+1, \ldots S\}$.

The energy of the spin state $|S,m_s\rangle$ in magnetic field $B = [0,0,B_z]$ is

$$E_{m_s} = \langle m_s| \mathcal{H}_z |m_s\rangle = g\mu_B B_z m_s. \tag{75}$$

We assume mixed spin projection states, m_s and m_s', with mixing coefficients α and β as

$$|S'\rangle = \alpha|S,m_s\rangle + \beta|S,m_s'\rangle, \tag{76}$$

where $|\alpha|^2 + |\beta|^2 = 1$. The matrix elements of Eq. (74) are diagonal in m_s and therefore the energy of the mixed spin state in magnetic field is

$$\langle S'| \mathcal{H}_z |S'\rangle =$$
$$g\mu_B B_z \left(|\alpha|^2 \langle m_s| S_z |m_s\rangle + |\beta|^2 \langle m_s'| S_z |m_s'\rangle\right) =$$
$$g\mu_B B_z \left(|\alpha|^2 m_s + |\beta|^2 m_s'\right). \tag{77}$$

The energy difference of the two states, $E_{m_s^a}$ and $E_{m_s^b}$ defined by Eq. (75), is

$$\Delta E = \Delta m_s g\mu_B B_z, \tag{78}$$

where $\Delta m_s = m_s^a - m_s^b$. The Δm_s in the mixed spin state is calculated as

$$\Delta m_s = \left(|\alpha|^2 m_s^a + |\beta|^2 m_s^{a'}\right) - \left(|\eta|^2 m_s^b + |\xi|^2 m_s^{b'}\right), \tag{79}$$

where $|\eta|^2 + |\xi|^2 = 1$.

The ΔE value in the magnetic field is defined by the difference of the spin projection states Δm_s that results as a multiplier before the Landé g-factor, see Eq. (78). Therefore, for the magnetic-dipole transition $\Delta m_s = 1$ with $g = 2$ and $\mu_B = 0.4668 \mathrm{cm}^{-1}\mathrm{T}^{-1}$ we expect magnetic field dependence of $\Delta E = 0.93$ (cm^{-1}T^{-1}). To compare it with mixed spin states, we consider the mixed spin state wave functions of LiFePO$_4$ from Ref. [42] shown in Table 3. The reader should be warned that the mixed states in Ref. [42] are defined only for one ion in zero magnetic field and as the mixing of spin states changes with the magnetic field the upcoming discussion should not be used for interpreting the the magnetic field dependence of excitations in LiFePO$_4$, Ref. III. There are two $\Delta m_s = 1$ transitions possible between energy levels $n : 0 \to 1$ and $n : 0 \to 4$. The $n : 0 \to 1$ results in $\Delta E = 1.83 - 0.82 = 1.01$ (cm^{-1}T^{-1}) and $n : 0 \to 4$ is $\Delta E = 1.83 - (-0.82) = 2.65$ (cm^{-1}T^{-1}). The $n = 4$ energy level is moving in the opposite direction in magnetic field compared to $n = 0$, resulting in an amplified field dependence of $n : 0 \to 4$ transition. While this field dependence is abnormally high for $\Delta m_s = 1$ excitation, it is reasonable for $\Delta m_s = 3$ transition that is also allowed between $n : 0 \to 4$. The electric-dipole $\Delta m_s = 3$ transition field dependence using Eq. (78) is $\Delta E = 2.8$ (cm^{-1}T^{-1}) that is well in range of the mixed state value $\Delta E = 2.65$ (cm^{-1}T^{-1}). The $n : 0 \to 1$ excitation can be classified as magnon and $n : 0 \to 4$ as quadrupolar ME resonance. In conclusion, the magnetic field dependence of mixed spin state transitions is not well defined and can vary depending on the mixing coefficients and the movement direction of the individual energy level.

Table 3: The LiFePO$_4$ single ion energies and spin states in the magnetically ordered phase from Table II in Ref. [42]. The effective quantum number $\tilde{m}_s = \left(|\alpha|^2 m_s + |\beta|^2 m_s'\right)$ is calculated from the wave function. The spin state energy is calculated using Eq. (77) with $\tilde{m}_s$ and assuming $g = 2$ and $\mu_B = 0.4668 \text{ cm}^{-1}\text{T}^{-1}$.

n	Energy (cm^{-1})	Wave function	$\tilde{m}_s$	$g\mu_B\tilde{m}_s$ (cm^{-1}T^{-1})
0	0	$0.99|2\rangle + 0.12|0\rangle$	1.96	1.83
1	64.5	$0.97|1\rangle + 0.25|-1\rangle$	0.878	0.82
2	102.7	$0.80|0\rangle + 0.60|-2\rangle$	-0.72	-0.67
3	130.7	$0.80|-2\rangle + 0.60|0\rangle$	-1.28	-1.20
4	132.7	$0.97|-1\rangle + 0.25|1\rangle$	-0.878	-0.82

36

2 Experimental details

This chapter covers the two far infrared experimental setups that were used in this work. Firstly, the TeslaFIR with Martin-Puplett type SPS200 spectrometer, which is located in the National Institute of Chemical Physics and Biophysics (KBFI), Tallinn. Secondly, the experimental setup in the High Magnetic Field Laboratory (HFML) in Nijmegen, where the measurements were conducted on a Genzel type Bruker IFS-113 spectrometer.

The chapter starts by introducing the interferometric detection based on the Michelson interferometer. The efficiency shortcomings of this type of a interferometer are also described. Subsequently, descriptions of Genzel and Martin-Puplett interferometers are presented, wherein some of the shortcomings of the Michelson type interferometer have been addressed. Next, a detailed description of interferometric detection realized in Martin-Puplett interferometer is presented and the calculation process of spectra from measured interferograms is outlined. The last two sections are devoted to the overview of the TeslaFIR and Nijmegen setups, including the description of measurement probes and modifications made by the author of this work.

2.1 Michelson interferometer

The most common configuration for interferometric detection is the two-beam Michelson interferometer [126,127], see Fig. 6. The interferometric detection is an experimental method, where light is divided into two beams and recombined after introducing a path difference x between the beams, so that the detected light intensity at the interferometer output becomes a function of path difference, $I(x)$. From this function, the spectra, $I(\omega)$, can be calculated using a Fourier transform [128].
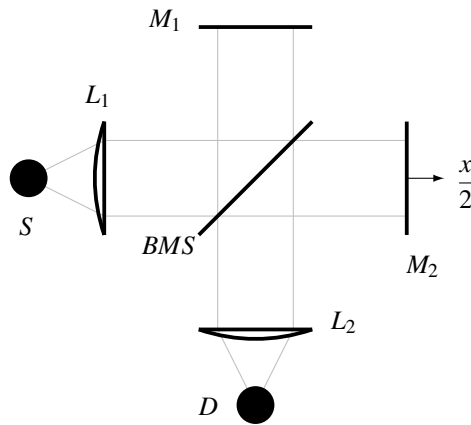

Figure 6: Michelson two-beam interferometer. S – source, D – detector, M_1 – stationary mirror, M_2 – movable mirror, BMS – beamsplitter, L_1 and L_2 – focusing lenses.

The incident monochromatic light from the source S is transformed to a parallel beam by lens L_1. The beamsplitter BMS splits the parallel beam to two components. One of the beams is reflected from mirror M_1, which is at a fixed length, the other beam is reflected from the moving mirror M_2 which introduces a path difference of x. The two reflected beams recombine at the BMS and travel toward the lens L_2 that focuses the two beams to the detector D where they produce an interference pattern. The detected modulated
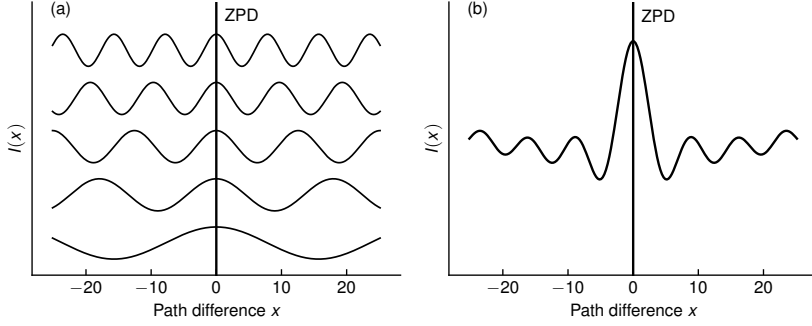
Figure 7: The illustration of interferogram generation with superposition of cosine waves. (a) The interferograms from a monochromatic source at five different frequencies. (b) The interferogram resulting from the sum of the panel (a) interferograms based on Eq. (87), which is the interferogram for a polychromatic source. The maximum of the interferogram is at $x = 0$, the zero path difference (ZPD). At ZPD all monochromatic components sum up constructively.

intensity as a function of the path difference x is

$$I(x) = \frac{I_0}{2} \left[1 + \cos\left(2\pi\bar{\omega}x\right) \right] = \frac{I_0}{2} \left[1 + \cos(\Delta) \right], \tag{80}$$

where $\bar{\omega}$ is the wavenumber defined as inverse of wavelength, $\bar{\omega} = 1/\lambda$, and the incident light intensity is I_0. Eq. (80) has two parts, the constant component $\frac{I_0}{2}$ and the modulated part $\frac{I_0}{2}\cos(\Delta)$, usually referred as interferogram, see Fig. 7.

The Michelson interferometer has several features which hinder its performance. Firstly, at low frequencies the efficiency of dielectric beamsplitters goes to zero as $\bar{\omega}^2/t$, where t is the beamsplitter thickness. Hence, increasing the thickness of the beamsplitter increases efficiency at low frequency. Secondly, although a thicker beamsplitter increases the efficiency at low frequency, it introduces a periodic oscillation of the interferometer output intensity as a function of frequency [129]. For example, for the 6 μm thick Mylar beamsplitter the zero-intensity regions are at $k_n \approx n \times 600$ cm^{-1} and for the 12 μm thick Mylar at $k_n \approx n \times 250$ cm^{-1} where $n = 0, 1, 2, 3, ...$ [130]. Thirdly, the beamsplitter reflectance, which defines the modulated part of intensity, Eq. (80), depends on the refractive index of the dielectric material of the beamsplitter and also varies for s and p polarizations, see Fig. 9 [131]. This reduces the useful modulated intensity as the beamsplitter reflectance R may deviate from the optimal value, $R = 0.5$. As will be shown below, the third feature can be overcome in the Genzel design and first and second in the Martin-Puplett design.

2.2 Genzel interferometer

The Genzel interferometer is a two-beam interferometer and was designed by Ludwig Genzel to overcome some of the Michelson interferometer's problems and to make the design more compact and user-friendly. The Genzel interferometer has been used in Bruker IFS-113, layout shown in Fig. 8. The main difference from the Michelson interferometer is that the incident light from the source is focused on the beamsplitter. The focused beam makes it possible to reduce the beamsplitter diameter and to use a motorized carousel with several beamsplitters. Since the change of the beamsplitters is motorized there is no need to break the vacuum of the instrument when switching between different frequency regions. The small size of the beamsplitter also reduces noise by decreasing
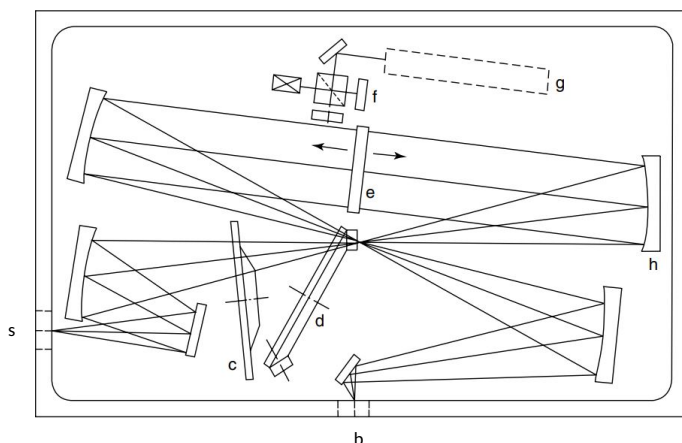
Figure 8: The Genzel interferometer scheme used in Bruker IFS-113 FT-IR spectrometer. s – source port, d – beamsplitter carousel, h – spherical collimating mirror, e – moving two-sided mirror, c – filter wheel, f – moving mirror of the reference interferometer attached to e, g – He-Ne laser light source for the reference interferometer and b – bolometer port. The reference interferometer is for measuring the position of the moving two-sided mirror. The figure is reproduced from Ref. [131].

the drum-head vibrations of the beamsplitter foil. The Genzel design is more compact because the incident radiation angle of a beamsplitter is only 15° compared to the Michelson 45°. The smaller angle reduces the difference of the perpendicular polarizations intensity ratio after the beamsplitter, see Fig. 9, allowing polarization studies without having to re-orient the sample for maximum signal [131]. The equal polarization ratio also increases the efficiency of the beamsplitter. After light is split into two by the beamsplitter, the beams are collimated by spherical mirrors to reflect from different sides of a two-sided moving mirror. This, compared to the Michelson interferometer, creates a two times larger optical path difference for the same mirror displacement. The amplification of path difference by two-sided mirror is seen as a benefit of Genzel interferometer with the downside that it doubles the alignment errors of the moving mirror. In the Bruker IFS-113 spectrometer, the mirror movement is measured very precisely with a small integrated He-Ne laser interferometer, labelled as f and g in Fig. 8.
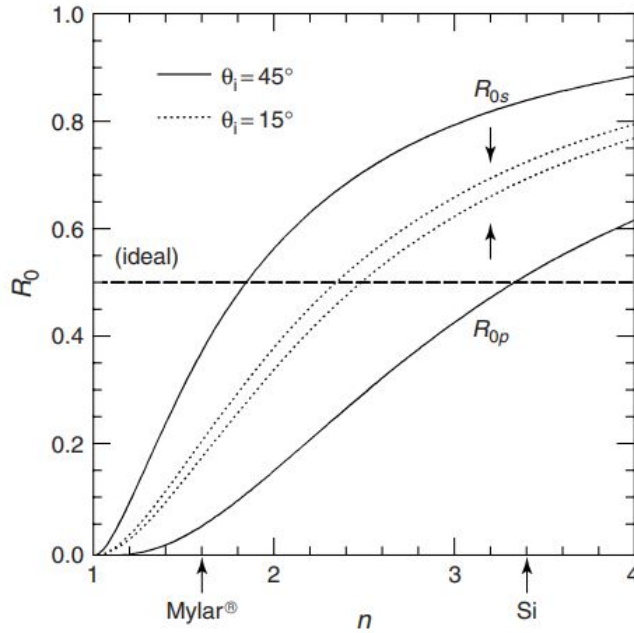
Figure 9: *Dielectric beamsplitter reflectance amplitude (R_0) dependence on the BMS index of refraction (n), radiation polarization and incidence angle (θ_i). The vertical axis is the reflectance amplitude R_0 and the horizontal axis is the refractive index n of the beamsplitter. The electric field polarization parallel (s) and perpendicular (p) to the plane of incidence. The two dotted and solid lines correspond to the 15° and 45° incident radiation of s and p polarizations. The values of refractive index for Mylar and Si are indicated. Note that reflectance values are closer to the ideal value of 0.5 the higher refractive index materials. The difference of s and p polarizations is much smaller at the reduced angle of incidence. The figure is reproduced from Ref. [131].*

2.3 Martin-Puplett interferometer

2.3.1 Basic design

The interferometer with a dielectric beamsplitter has small efficiency at low frequencies. To address this D. H. Martin and E. Puplett proposed a polarizing interferometer [132]. The Martin-Puplett design uses the high efficiency of a wire-grid beamsplitter to separate two orthogonal polarizations of light that will travel different paths in the interferometer.

A wire-grid polarizer consists of thin parallel conducting wires separated by a small distances d. When light enters the wire-grid the electric field that is parallel to the wires will induce a current along the wire. To this component of light, the wires act as metal surface and reflect the light. The electric component of light that is perpendicular to the wires does not introduce any significant currents and therefore the grid is transparent to this polarization of light. Wire-grid polarizers can have reflection and transmission coefficients more than 99.999% at low frequencies, see Fig. 10, if the wavelengths of light is much greater then the wire spacing, $\lambda \gg d$ [133–135].

The layout of the Martin-Puplett interferometer is shown in Fig. 11. The incident light from the source is collimated by the lens L_1. To create a linearly polarized radiation, the collimated beam passes the $[001]$ aligned wire-grid polarizer Pol_1 from which the $[010]$ component of light travels toward similar wire-grid with wires in the $[111]$ direction. Thus, the wire-grid BMS acts as a beamsplitter by dividing the $[010]$ polarization into two beams,
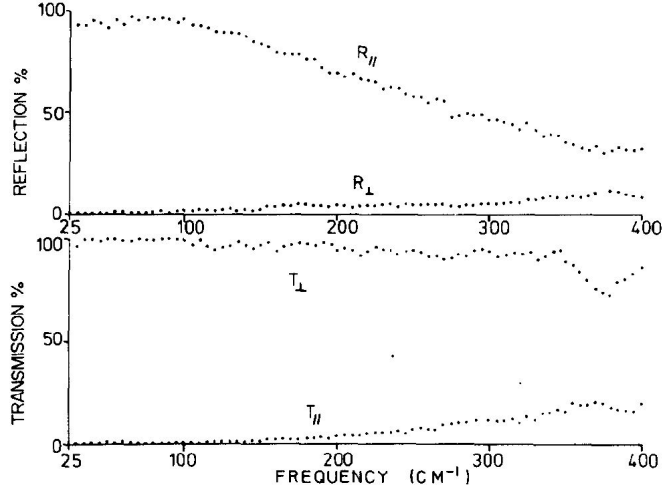
Figure 10: *The reflectance R and transmittance T coefficients of wire-grids made up from 5 μm thick tungsten wire with the spacing of 12.5 μm. The polarization of incident light electric field vector, parallel (∥) or perpendicular (⊥) to the wire-grid, is marked as the subscript of R and T. The figure is reproduced from Ref. [133].*

one $[101]$ and the other $[0\bar{1}1]$ polarized. Half of the incoming intensity is reflected toward fixed roof mirror RM_1 and the other half is transmitted toward the movable roof mirror RM_2. Both beams are linearly polarized with polarizations perpendicular to each other.

The roof-mirror consists of two reflecting perpendicular planes. The crossing of the planes is referred to as ridge line. For example the ridge of RM_2 is the $[001]$ direction. We can separate the incident light that propagates in $[100]$ direction, perpendicular to the ridge, into two components, polarized along the ridge, $[001]$, and perpendicular to the ridge, $[010]$. The polarization component parallel to the ridge does not change direction while the other, perpendicular to the ridge, will be rotated by 180° upon reflection from the two faces, from $[010]$ to $[0\bar{1}0]$. If the incident light polarization is at 45° relative to the ridge line, $[0\bar{1}1]$, then the back-reflected light polarization is rotated by 90° to the $[011]$ direction. Since the roof mirror flips the beam polarization by 90°, the beam reflected initially from the BMS (beam A) will now be transmitted at the BMS and vice versa for the beam B. Hence, both beams are directed to polarizer Pol_2.

The motion of the roof mirror RM_2 in the x direction changes the path difference between the two orthogonally polarized beams A and B. The path difference creates a wavelength ($\lambda = 1/\bar{\omega}$) dependent phase difference $\rho = 2\pi\bar{\omega}x$. Therefore, the light before Pol_2 becomes elliptically polarized with the ellipticity depending on the path difference and wavelength. For a polychromatic light the radiation at Pol_2 contains all polarizations from linear to circular, except at $x = 0$, where it is linearly polarized for any $\bar{\omega}$. The output polarizer Pol_2 provides intensity modulation at the detector. The intensity is at the maximum, if Pol_1 and Pol_2 are parallel, and there is a zero intensity with crossed Pol_1 and Pol_2 at ZPD.
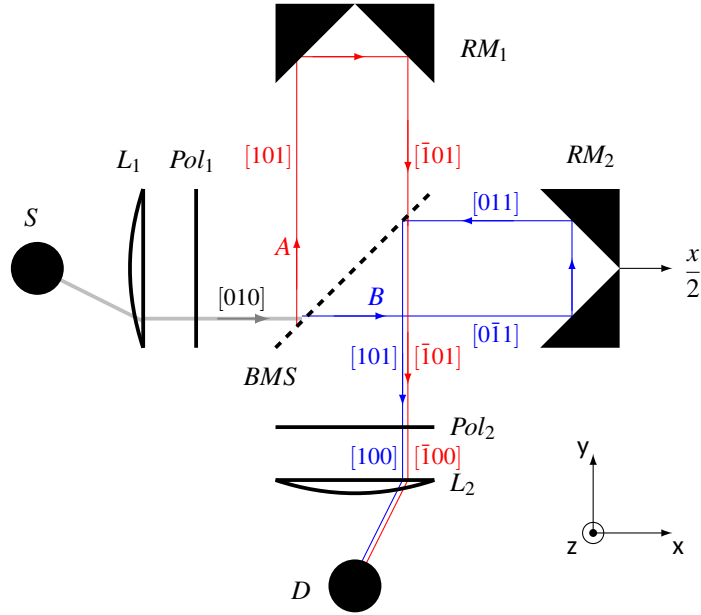
41

Figure 11: Outline of the Martin-Puplett interferometer. S – source, D – detector, RM_1 – stationary roof mirror, RM_2 – movable roof mirror, BMS – beamsplitter, Pol_1 – input polarizer, Pol_2 – output polarizer, L_1 and L_2 – focusing lenses. The solid lines show the beam path in the direction of arrows with polarization state defined in brackets. The light from S is collimated by L_1 with polarization state $[010]$ defined by Pol_1, wires in $[001]$ direction. The beam with polarization along $[010]$ is divided into two beams by BMS, wires in $[111]$ direction. Beam A that is reflected from BMS has polarization $[101]$ and travels toward RM_1 where the light polarization of the back-reflected beam is rotated by 90°, to direction $[\bar{1}01]$. Because of the 90° rotation of the polarization the beam A is now fully transmitted by the BMS in $[\bar{1}01]$ polarization. Beam B that is transmitted through the BMS in the $[0\bar{1}1]$ polarization will be, after back-reflection from the RM_2 and reflection from BMS, in the $[101]$ polarization at Pol_2. By moving the roof mirror RM_2 a path difference between cross-polarized beams A and B is created. The output polarizer assorts the $[001]$ polarization from both beams and focuses the beams by L_2 to the detector, where they interfere.

2.3.2 Description of interferometric detection

To better understand the working principle of the Martin-Puplett interferometer, we investigate how the electric field component of a plane wave changes when travelling through the spectrometer, Fig. 11. The electric field vector after Pol_1 is

$$\mathbf{E}_{\text{in}} = a\hat{p}\cos\omega t, \tag{81}$$

where a is the amplitude of the light, t is time, ω is angular frequency and $\hat{p}$ is a unit vector parallel to the polarization of Pol_1 and Pol_2. Next, the light strikes the beamsplitter which divides it into two beams, A and B. The electric field vector at the BMS is

$$\mathbf{E}_1 = \frac{a}{\sqrt{2}}\hat{n}\cos\omega t + \frac{a}{\sqrt{2}}\hat{t}\cos\omega t, \tag{82}$$

where the $\hat{n}$ and $\hat{t}$ are orthogonal unit vectors rotated $\pm45°$ off from $\hat{p}$ having relation $\hat{p}\cdot\hat{n} = \hat{p}\cdot\hat{t} = \frac{1}{\sqrt{2}}$. We choose an $\hat{n}$ that projects on the direction of BMS wires, [111] in Fig. 11.

Thus, the first part of Eq. (82) is reflected in the direction of beam A and the second part is transmitted in the direction of beam B at the BMS. Both beams are reflected from rooftop mirrors RM_1 and RM_2, and RM_2 can be moved to create a path difference x. The overall phase shift of beam A is Δ_A and beam B is Δ_B with mean of $\overline{\Delta} = \frac{\Delta_A + \Delta_B}{2}$ and difference of $\Delta = \Delta_A - \Delta_B = 2\pi\bar{\omega}x$. The electric field vector after re-combination at BMS is

$$\mathbf{E}_2 = \frac{a}{\sqrt{2}}\hat{n}\cos(\omega t + \Delta_A) + \frac{a}{\sqrt{2}}\hat{\imath}\cos(\omega t + \Delta_B). \tag{83}$$

One can show that the intensity after BMS, $I_2 = \langle \mathbf{E}_2 \cdot \mathbf{E}_2 \rangle$, is independent of the optical path difference x. The modulation of intensity by x can be introduced by adding a linear polarizer Pol_2 in the beam. The light at the output after leaving Pol_2 has the amplitude

$$E_{\text{out}} = \mathbf{E}_2 \cdot \hat{p} = \frac{a}{2}\left[\cos\left(\omega t + \Delta_A\right) + \cos\left(\omega t + \Delta_B\right)\right] = a\cos(\omega t + \overline{\Delta})\cos\frac{\Delta}{2} \tag{84}$$

and the intensity at the output is

$$I_{\text{out}} = \langle E_{\text{out}}^2 \rangle = \frac{a^2}{2}\cos^2\frac{\Delta}{2} = \frac{a^2}{4}(1 + \cos\Delta) = \frac{I_{\text{in}}}{2}(1 + \cos\Delta), \tag{85}$$

where the intensity I_{in} as defined after Pol_1 is

$$I_{\text{in}} = \langle \mathbf{E}_{\text{in}} \cdot \mathbf{E}_{\text{in}} \rangle = \frac{a^2}{2}, \tag{86}$$

$\langle \ldots \rangle$ denotes the time-average and $\mathbf{E}_{\text{in}}$ is given by Eq. (81).

If the source emits at several frequencies, then the interferogram is a sum of interferograms at several $\bar{\omega}_i$,

$$I(x) = \frac{1}{2}\sum_i I_{\bar{\omega}_i}\left[1 + \cos\left(2\pi\bar{\omega}_i x\right)\right]. \tag{87}$$

Real infrared measurement systems operate using the thermal radiation from a heated black body or a synchrotron, the emission of which is a continuous spectrum. In the continuous limit Eq. (87) becomes [136]

$$I(x) = \frac{1}{2}\int_0^\infty d\bar{\omega} S(\bar{\omega})[1 + \cos(2\pi\bar{\omega}x)], \tag{88}$$

where $S(\bar{\omega}) = |E_s(\bar{\omega})|^2$ is the power spectrum of the light source. As we are interested in the modulated intensity, we can leave out the term independent of x. After normalizing the source intensity,

$$I_0 = \int_0^\infty d\bar{\omega} S(\bar{\omega}), \tag{89}$$

the normalized interferogram is

$$\gamma(x) = \frac{1}{2I_0}\int_0^\infty d\bar{\omega} S(\bar{\omega})\cos(2\pi\bar{\omega}x). \tag{90}$$

The inverse complex Fourier transform of the interferogram $\gamma(x)$ is the spectrum $P(\bar{\omega})$,

$$P(\bar{\omega}) = \frac{2}{\pi}\int_{-\infty}^\infty \gamma(x)e^{-i2\pi\bar{\omega}x}dx, \tag{91}$$

where $P(\bar{\omega}) = S(\bar{\omega})/I_0$. The Eq. (91) is only valid for the interferogram $\gamma(x)$ which is symmetrical about $x = 0$.

The interferogram in real systems is recorded based on the movement of the mirror in a limited range,

$$-L_1 \leq x \leq L_2, \quad \text{where} \quad L_2 \geq L_1 > 0. \tag{92}$$

L_1 is called the negative limit and L_2 is the positive limit.

The resolution of the spectrum is determined by the positive limit of the interferogram as

$$\Delta\bar{\omega} = \frac{1}{L_2}. \tag{93}$$

Therefore, in the literature the asymmetric and symmetric interferograms are also called high and low resolution interferograms. From the Eq. (93) it would seem that the highest obtainable resolution is determined only by L_2. In practice, the resolution can be increased up to a certain point and after that further increase of the resolution is limited by the signal to noise ratio [137].

Next, we assume the interferogram is sampled at mirror positions separated by δ. The Nyquist criterion states that at least two data points per one period have to be measured, to still be able to resolve a frequency from the signal. This gives us the high frequency cut-off of the spectrum what can be obtained from the interferogram with the smallest sampling step δ,

$$\bar{\omega}_{\mathrm{max}} = \frac{1}{2\delta}. \tag{94}$$

The interferogram maximum is at ZPD, the mirror position where the optical paths of the two beams are equal, $x = 0$. Because of sampling, it is certain, that the ZPD of the interferogram will be missed by $\varepsilon \leq \delta/2$. This causes a phase error in the complex Fourier transform and distorts the spectrum.

Phase distortions in the interferogram originate from the spectrometer: error of measuring the mirror position, misalignment, or intrinsic asymmetry of interferometer arms and the reaction time of the detector. The result of these distortions is that the interferogram is not completely symmetric on both sides of the ZPD and we must take them properly into account. The phase $\phi(\bar{\omega})$ enters into the interferogram as

$$\gamma(x) = \frac{1}{2I_0} \int_0^\infty d\bar{\omega} S(\bar{\omega}) \cos[2\pi\bar{\omega}x + \phi(\bar{\omega})]. \tag{95}$$

The result of the measured interferogram Fourier transform is

$$P(\bar{\omega})e^{i\phi(\bar{\omega})} = \frac{2}{\pi} \int_{-\infty}^\infty \gamma(x)e^{-i2\pi\bar{\omega}x}dx. \tag{96}$$

The phase distortions can be corrected if we assume that the phase $\phi(\bar{\omega})$ is a slowly varying function of frequency,

$$\phi(\bar{\omega}) = \phi_0 + \beta\bar{\omega}, \tag{97}$$

with β as the coefficient of the linear term in phase and ϕ_0 the genuine phase. The correction term of ZPD is the slope β because the shifted ZPD position is just a linear phase error, $\beta = \varepsilon$, as shown in [136]. If instead of a linear term in the phase, the phase would have a parabolic or a higher order power dependence on $\bar{\omega}$, then it would mean that the ZPD position depends on $\bar{\omega}$ and can not be recovered so easily [138]. β can be calculated from the symmetric part of the interferogram and used to correct the maximum position of the whole asymmetric interferogram. The correction of phase errors in Fourier spectroscopy is analysed in Ref. [136].

The fast Fourier transform (FFT) reduces the calculation time from N^2 to $Nlog(N)$. In order to use FFT the number of interferogram points has to be increased with zero filling to the power of 2 [139]. Zero filling is a method where the end of interferogram is continued by zeros. Zero filling also gives more output points per a spectral resolution element. In case of an asymmetric interferogram the farthest points of the interferogram are included only once while the central symmetric part is used twice. This leads FFT to reduce the resolution of spectra by almost a factor of two. It is possible to avoid this by using a truncation function that weights the symmetric part by half, as shown in Fig. 12(e).

For minimizing the phase error from the abrupt stop of the interferogram tails, the interferogram is multiplied by an apodization function, which gradually tapers the tails to zero. It is important to note here that the apodization function has to be centred exactly at the real ZPD position, otherwise the apodization will introduce an additional phase error. Without apodization the sharp absorption lines have several side lopes with diminishing amplitude, which would make it harder to quantify the absorption line parameters. The side effect of apodization is that the spectral lines are wider in the measured spectra. To suppress the widening, the interferogram has to be measured longer by the factor k_{ap}. The weighting factors $w(x)$ for path difference x and factors k_{ap} are changing depending apodization functions as

$$
\begin{aligned}
w(x)^{\text{boxcar}} &= 1, & k_{ap}^{\text{boxcar}} &= 1.207 \\
w(x)^{\text{triangular}} &= \frac{1}{2}\left[1 - \frac{x}{L_2}\right], & k_{ap}^{\text{triangular}} &= 1.772 \\
w(x)^{\text{Bessel}} &= \frac{1}{2}\left[1 - \left(\frac{x}{L_2}\right)^2\right], & k_{ap}^{\text{Bessel}} &= 1.904 \\
w(x)^{\text{cosine}} &= \frac{1}{2}\left[1 - \cos\left(\frac{\pi x}{L_2}\right)\right], & k_{ap}^{\text{cosine}} &= 2.000.
\end{aligned}
\tag{98}
$$

In SPS we prefer to use the cosine apodization function also known as Hann window.

Next we will discuss the procedure used in TeslaFIR, SPS software to calculate the spectrum. An asymmetric interferogram is shown in Fig. 12(a). The ZPD of interferogram is found by fitting a parabola through the interferogram maximum and points on either side of it, see Fig. 12(a) inset. The distance between the parabola maximum and the interferogram sampled maximum is ε, which is used to shift the interferogram to a new coordinate frame for minimizing the phase error. The phase of the low resolution interferogram used to correct the high resolution interferogram, if both interferograms have the same number of points M, which is done by zero filling the interferograms to 2^M, Fig. 12(b). Before we can use inverse FFT (IFFT), the interferogram has to be apodized, then cut and folded to be suitable for the complex FFT algorithm, what expects real values in the beginning of the array, starting from the ZPD until the last data point followed by the imaginary values from the left side of the interferogram in the reversed order as shown in Fig. 12(c). From the phase one can calculate the β by Eq. (97). The phase of the high resolution interferogram, i.e the ZPD position, is then further corrected by shifting the maximum to the new value by β which determines the range of high resolution interferogram as $-L_1 + \beta \leq x \leq L_2 - \beta$. In this range, we have to introduce truncation in order to give proper weight to those asymmetric interferogram points that were measured twice, the green line in Fig. 12(e). After the truncation, the interferogram is apodized and folded for IFFT, Fig. 12(f). The result of IFFT is the transmission spectra seen in Fig. 12(g).
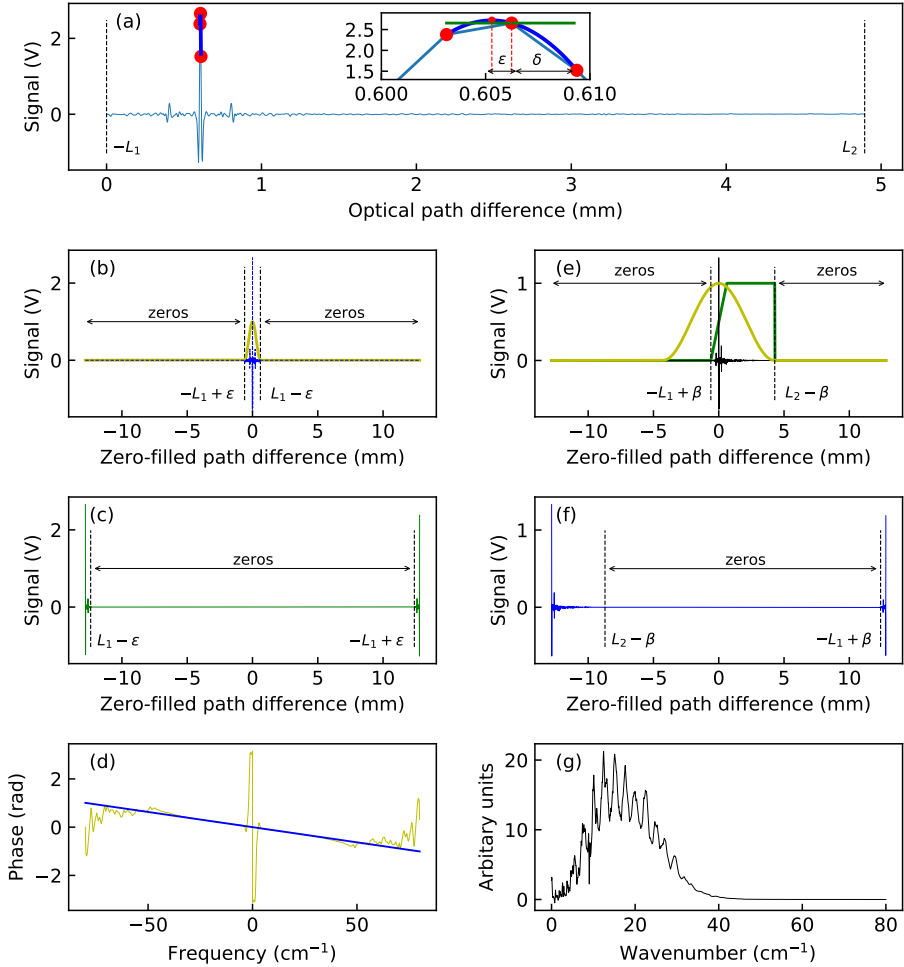
Figure 12: Steps implemented in the SPS software to calculate the spectrum from a measured interferogram. (a) An interferogram measured with the TeslaFIR experimental setup. The interferogram extends from $-L_1$ to L_2, where L_1 and L_2 are the distances from the maximum of the interferogram. The inset shows the fitting of the interferogram maximum with parabola, blue line. The large red circles shows the sampled points with step δ. The maximum of the parabola is marked with small red circle and is at the distance ε from the nearest sampled point. The green horizontal line through sampled point indicates that also the intensity maximum of the interferogram was missed by sampling. (b) The symmetric part of the interferogram from panel (a) which has been shifted by ε to the left and zero filled to 2^M points. The yellow line shows the weight of the cosine-based apodization function. (c) The double sided low resolution interferogram for the complex IFFT that will be used for the phase correction. (d) The phase calculated from the symmetric low resolution interferogram. The slope of the linear fit of the phase, blue line, determines the interferogram ZPD correction β. (e) The zero filled asymmetric interferogram from panel (a) with apodization function, yellow, and ramping truncation function, green. (f) The double sided high resolution interferogram for the complex IFFT. (g) The calculated phase corrected spectrum.

46

2.4 TeslaFIR experimental setup

The main experimental setup used in this thesis is named TeslaFIR and is located in KBFI. The setup consists of a Martin-Puplett interferometer, a ^{4}He cryostat, a 17 T superconducting solenoid and a Si bolometer cooled by the closed ^{3}He system to 0.3 K. The layout of TeslaFIR is shown in Fig. 13. The frequency range of spectrometer extends from 75 GHz up to 6 THz. The sample can be measured in the temperature range of 2.5 K to 400 K. The applicable magnetic field is $-17 \ldots 17$ T and the maximum dc electric field across the sample using electrodes is up to 1 kV / cm. The transmission can be measured in Faraday and Voigt configuration and the reflection in Kerr configuration. The Faraday (Kerr) or Voigt configuration define whether the wavevector $\mathbf{k}$ is parallel or perpendicular, respectively, to the external magnetic field, as shown in Fig. 15.

The cryostat is cooled with a liquid helium (^{4}He) reservoir that is surrounded by a shield cooled by liquid nitrogen (N_2). The maximum field is limited to 15 T if the magnet is at $T = 4.2$ K and to 17 T if the liquid ^{4}He is kept close to the liquid helium superfluid transition temperature, $T_\lambda = 2.17$ K. The helium bath is cooled below 4.2 K by pumping on a λ-helix. The helix is situated above the magnet and is made out of a copper pipe having a motor controlled needle valve toward the main helium bath. The ^{4}He entering the λ-helix has the same temperature as the ^{4}He in main bath, but as the flow is limited by the needle valve, the helium pressure and temperature inside λ-helix are lower, cooling the main bath and therefore the magnet.

The TeslaFIR setup uses a Sciencetech Inc. SPS-200 spectrometer which is be operated in a polarizing Martin-Puplett configuration. SPS-200 uses a wire-grid beamsplitter and a polarizer in which the aluminium wires are photolithographically etched on a 12 μm thick Mylar film. The wires are 0.4 μm thick and 2 μm wide with a 4 μm spacing (2500 lines/cm). The efficiency of the beamsplitter and polarizers fall to zero at 700 cm^{-1}. The low frequency region is almost 100% efficient, limited only by the size of mirrors and the lamp power spectrum. The light source is a water-cooled mercury arc lamp. There is a black polyethylene film to protect the polarizer and beamsplitter from the visible and UV radiation. Another black polyethylene film at the output of the spectrometer reduces further the amount of high frequency radiation on the sample.

The amplitude of light is modulated by the fixed linear polarizer at the output of SPS-200. The linearly polarized light from the spectrometer is focused onto the entrance of the 16 mm diameter light pipe. Due to reflections in the light pipe, the polarization state of light is lost. In front of the sample chamber, the polarization state is re-defined by a stepper-motor controlled rotatable polarizer. The sample chamber can be changed depending on the measurement requirements. The Faraday probe is described in Sec. 2.4.1 and Voigt probes in Sec. 2.4.2.

The light from the probe enters a He-bath section, where the filter wheel is situated through a vacuum-tight polypropylene window. The filter wheel is submerged in helium to minimize black body radiation from the filters themselves. The filter wheel is stepper-motor controlled and can hold eight filters, as listed in Table 4. After filters, the light intensity is detected by a 0.3 K bolometer which is situated inside a separate high vacuum chamber with polypropylene windows. The bolometer is a Si chip glued on top of a 5 mm diameter sapphire disk coated with a anti-reflection layer. It is important to note that the bolometer measures light intensity and the phase information of the electromagnetic field is lost. The bolometer signal is amplified by a pre-amplifier and then digitized by the ADC computer board. The signal, measured through filters, is shown in Fig. 14.

The bolometer is cooled with a closed-cycle ^{3}He system which consists of the 1K-capillary, an absorber and the liquid ^{3}He pot, illustrated in the bottom part of Fig. 13. The ^{3}He system

is pre-cooled by the mechanical heat switch that is situated below the bolometer vacuum chamber and connects the helium bath to the ^{3}He system through a metal membrane. When the bolometer reaches 4.2 K, the heat switch is disconnected. The closed cycle-system has a ^{3}He reservoir outside of the cryostat. The 1K-capillary is pumped throughout the experiment and is kept at 1.6 K. The bolometer cooling cycle starts by heating the absorber to 40 K for one hour at which time the ^{3}He gas is released from the charcoal. The warm gas condenses on the portion of the ^{3}He pot neck cooled by the 1K-capillary to form ^{3}He droplets that fall into the ^{3}He pot. After the heater is turned off, the absorber cools to 5 K and starts pumping on the liquid ^{3}He pot, reducing the vapour pressure and by that cooling the pot to 0.3 K. When the temperature 0.3 K is reached, about one hour after switching off the absorber heater, the bolometer is ready for measurements. Compared to the 4.2 K bolometer, the 0.3 K bolometer sensitivity is two orders of magnitude greater.

The TeslaFIR setup is automated using the LabView programming environment and can run automatically following the commands written in the command file. The user is needed to overlook the measurement and provide the setup with liquid helium and nitrogen when needed. In the planning of command file, it's important to consider the times of filling and re-condensation of ^{3}He for the bolometer. For example, by adding liquid helium the magnet may warm above the λ-point, restricting the maximum magnetic field to 15 T for several hours.

Between experiments, the cryostat is warmed up to room temperature. Warming to room temperature without additional heating or breaking the cryostat vacuum can take up to two weeks. An additional week is needed to set up a new run, thus the overall time between experiments could extend to three weeks. This time scale hinders the possibility to do systematic study of samples as was required in the process of this thesis. Therefore, I added a bottom heater to the TeslaFIR cryostat. The bottom heater with maximum power of 50 W, heats the cryostat to room temperature in 48 h. The heater is temperature-controlled in order to minimize the risk of overheating the cryostat which can melt the vax that stabilize the superconducting magnet coils.

It is vital to isolate the experiment from the ambient mechanical vibrations as the interferometer mirrors, beamsplitter and bolometer wires can easily pick up low frequency vibrations. Therefore, in the course of this thesis, I rebuilt the vibration isolators as described next. The cryostat and the spectrometer are supported by a common wooden platform that is not attached to the main wooden frame. Four single convolution air springs "FS 40-6 CI" were placed under the wooden platform, one on each corner. The springs have a natural frequency of 3.3 Hz with the optimal height of 90 mm for vibrational isolation. The air springs are connected to the control hub by PU tubes. The control hub input pressure is regulated by a pressure valve which is fixed at 3.6 bar. The user operates the filling of air springs manually, while monitoring that the platform is levelled as the weight is not equally spread across the platform. Air springs can be deflated by a release valve which relaxes the platform onto wooden cubes.
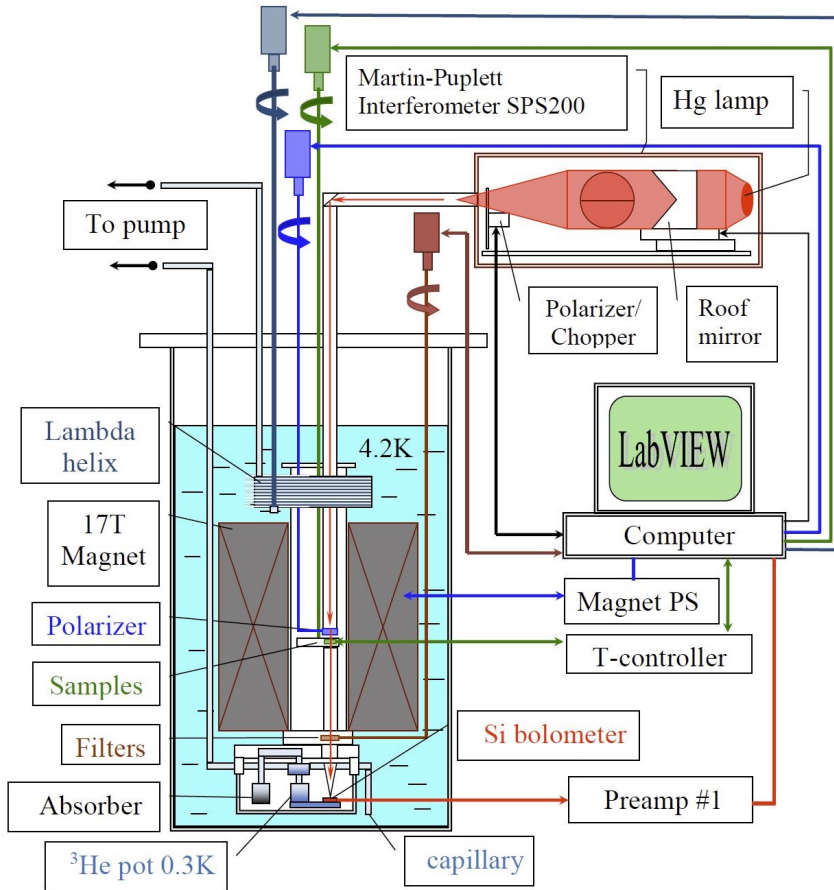
Figure 13: Layout of the TeslaFIR experimental setup with the Faraday probe installed. Sample chamber, superconducting $17\,\mathrm{T}$ solenoid and the $0.3\,\mathrm{K}$ bolometer chamber share the same liquid He bath cryostat. The incident radiation polarization on the sample is selected with the rotatable polarizer. After the sample, the light passes high-frequency cut-off filters mounted on the rotatable filter wheel. The Si bolometer is cooled by the closed $^{3}\mathrm{He}$ system where a charcoal absorber pumps on liquid $^{3}\mathrm{He}$ to cool it to the base temperature of $0.3\,\mathrm{K}$. 1K-capillary at $1.6\,\mathrm{K}$ is in thermal contact with the $^{3}\mathrm{He}$ pot neck and is supplied with liquid helium from the main helium bath. To reach fields above $15\,\mathrm{T}$, the main bath is cooled below $4.2\,\mathrm{K}$ by the λ-helix immersed into liquid He. The sample changer, polarizer and filter wheel, each are controlled by their own stepper motor. Sample chamber, superconducting $17\,\mathrm{T}$ solenoid and the $0.3\,\mathrm{K}$ bolometer chamber share the same liquid He bath cryostat. This figure is reproduced and modified from the TeslaFIR layout created by the members of THz & low temperature physics group in KBFI.
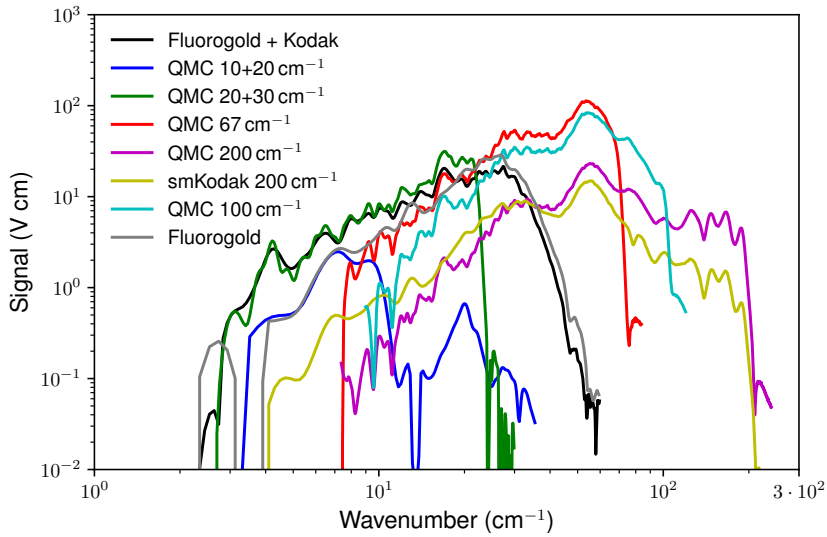
Figure 14: The bolometer signal of TeslaFIR filters through a 3 mm empty hole at 10 K. Using filters to select the frequency range of interest can substantially decrease the noise and speed up measuring time.

Table 4: Filters in the filter wheel, their cut-off frequencies and the recommended mirror scan speeds. There is an additional 200 cm^{-1} cut-off filter attached to the exit window of the sample chamber. Optimal scan speeds of the moving mirror are calculated from the reaction time of the bolometer and the cut-off of the spectrum from the Nyquist criterion.

Position	Filter	Cut-off (cm^{-1})	Scan speed (cm s^{-1})
1	Fluorogold + Kodak	40	0.3
2	QMC 10 + 20 cm^{-1}	10	0.8
3	QMC 20 + 30 cm^{-1}	20	0.45
4	QMC 67 cm^{-1}	67	0.25
5	QMC 200 cm^{-1}	200	0.08
6	Kodak ∅ 4 mm	200	0.08
7	QMC 100 cm^{-1}	100	0.15
8	Fluorogold	40	0.3

2.4.1 Faraday probe

The Faraday configuration states that the light wavevector is parallel to the applied magnetic field, $\mathbf{k} \parallel \mathbf{H}$, Fig. 15 (a). The TeslaFIR Faraday probe has six sample slots in a rotatable sample wheel, see Fig. 16. Each sample can be measured in any linear polarization defined in the plane perpendicular to $\mathbf{H}$. The sample wheel and polarizer are computer-controlled with stepper motors. The accessible temperature range depends on the sample parameters, sample holder hole size and required frequency range. The thermal radiation with 200 cm^{-1} cut-off filter saturates the detector above sample $T = 50$ K. The sample temperature where the detector saturates can be increased by applying extra bias to the bolometer or by applying eccosorb to the light pipe after the heated sample compartment to reduce the bolometer angle of view. However, this reduces the bolometer signal. The Faraday probe is the preferred TeslaFIR experimental probe as it allows to measure several samples in single cool-down.
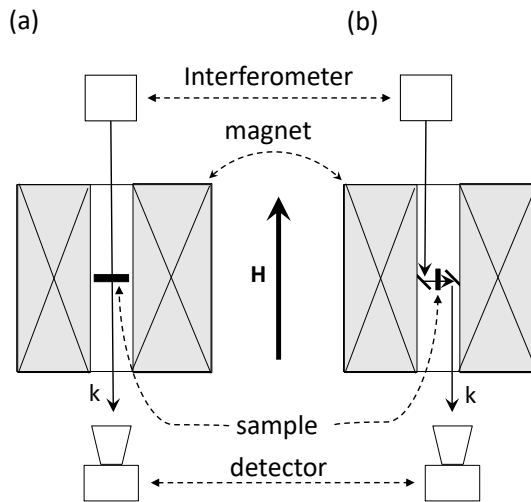

Figure 15: *The Faraday and Voigt configurations shown in panels (a) and (b) respectively. The sample is in the centre of the magnet. In Faraday configuration the light wavevector (arrow) is along the magnetic field, $\mathbf{H}$, the thick arrow. In the Voigt configuration the light wavevector is perpendicular to the magnetic field, $\mathbf{k} \perp \mathbf{H}$. For the Voigt configuration, a two-mirror assembly is needed.*

2.4.2 Voigt probes

The light wavevector in Voigt configuration is perpendicular to the magnetic field, $\mathbf{k} \perp \mathbf{H}$, as shown in Fig. 15(b). The TeslaFIR probe is designed with a interchangeable measurement compartment and a tail which allows easy conversion between the Faraday and Voigt configurations. In the Voigt configuration two mirrors are used to reflect the light to $\mathbf{k} \perp \mathbf{H}$ while passing the sample and back to $\mathbf{k} \parallel \mathbf{H}$. A diagonal light-pipe is used to revert the light back to the initial side where the detector input is located, see Fig. 17(a,b). Because the Voigt configuration acquires more space than the Faraday configuration, the number of samples is limited to one. Next, we will discuss the Voigt probes used in this work.

The static high temperature Voigt probe that also allows high electric field measurements is shown in Fig. 17(a,c). The main advantage of this probe is that the sample holder is isolated from the sample chamber by non-conducting and low heat conductive nylon
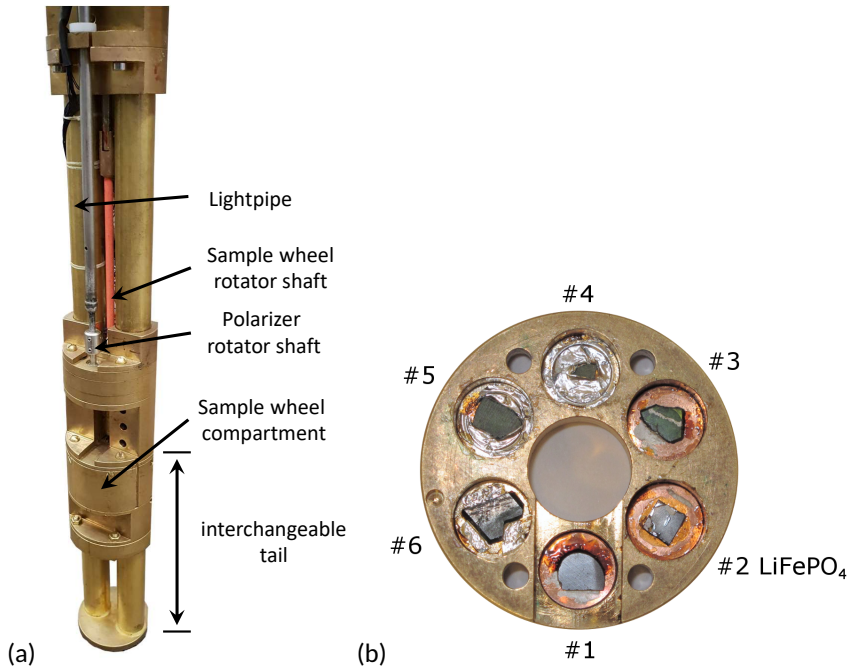
Figure 16: The TeslaFIR Faraday probe on (a) and its sample wheel on (b). The probe tail can be changed to Voigt probes shown in Fig. 17.

line. Both, the thermometer and the heater are attached to the surface of the isolated sample holder. One sample can be mounted at a time and the orientation relative to the magnetic field is fixed. The main flaw of the initial design was that the sample holder – when heated – radiated all the black body radiation toward the detector. This additional heat radiation limited the accessible frequency range above 50 K, therefore the author of this thesis modified the design. A cold metal screen with the hole diameter equal to the sample size was added after the sample holder, see Fig. 17(a). Additionally, eccosorb was glued on the light-pipe walls of the main body extension to collimate the light further. These modifications allowed to obtain spectra up to 200 cm^{-1} above 50 K.

The fixed sample design was not practical for the systematic study of the magnetic field direction dependence of spectra. To change the magnetic field direction relative to the sample the measurements had to be halted, the cryostat warmed up and the sample holder had to be rotated by hand. For this reason the rotatable Voigt probe was designed by J. Viirok and first used in Ref. [140]. In this design the sample wheel could be rotated by a computer controlled stepper motor. This design has three major advantages. Firstly, it allows orienting the sample axes more precise along the magnetic field, as described in Sec. 2.6. Secondly, it allows measuring two field directions in Voigt configuration in one experiment. Thirdly, it allows the systematic study of the sample THz absorption when the magnetic field changes its orientation in the sample plane. The downside of this design was that the heater and thermometer were not attached to the sample wheel, see old heater and old thermometer in Fig. 17(b). The heater was attached to the main brass body of the probe, which resulted in enormous heat radiation. While the design was a great upgrade from the static configuration, the limited frequency and temperature range were not suitable for this work. The rotatable Voigt probe design was upgraded by the author
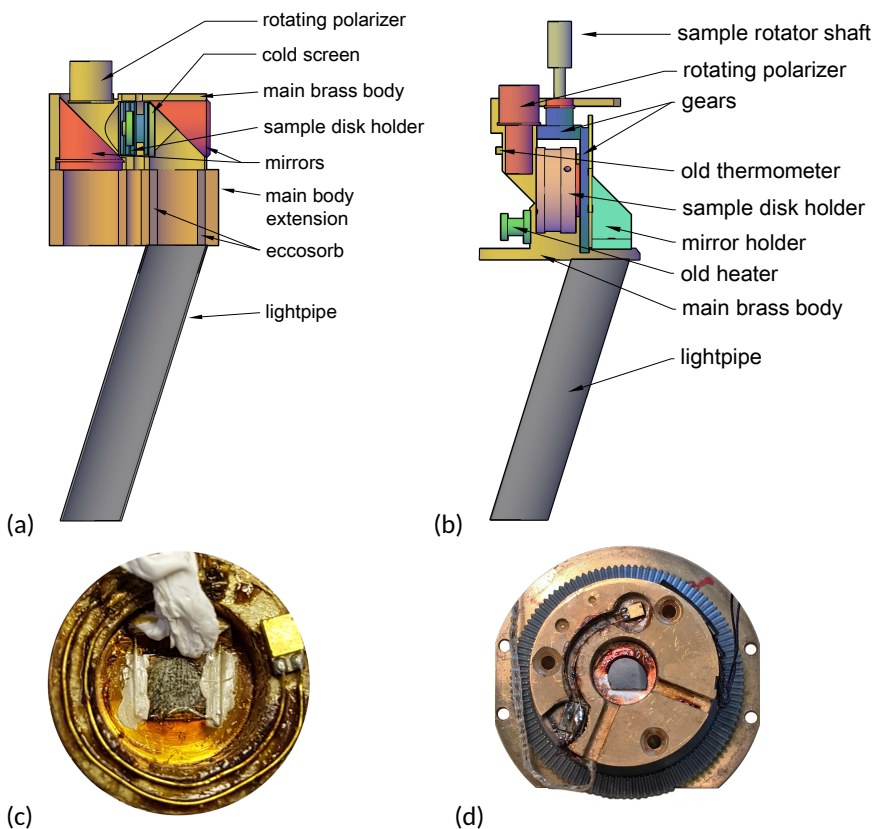
Figure 17: *The TeslaFIR Voigt configuration probes. The static high temperature high voltage Voigt probe scheme (a) with its sample holder on (c). The rotatable high temperature Voigt probe with high-voltage option (b) and its sample holder (d). The schemes (a) and (b) are reproduced and modified from the CAD files created by the members of THz & low temperature physics group in KBFI.*

of this work. The heater and thermometer were moved onto the sample holder and the probe was modified to allow high electric field measurements, Fig. 17(b,d). The sample holder was isolated from the gear by a non-heat-conducting plastic disk. The transfer of the heater onto the sample wheel and additional isolation of sample holder resulted in a significantly lower amount of heat radiation. In this new design the thermometer and heater wires limit the rotation of the sample holder to $\pm 60°$. Therefore, the sample should be mounted in a way that the principal axes within the sample plane are in the accessible $\pm 60°$ range.

2.5 High magnetic field infrared spectroscopy system in Nijmegen

The THz spectroscopy in magnetic fields above 17 T was done at High Field Magnet Laboratory (HFML) in Nijmegen, Netherlands (Fig. 18) [141]. The magnetic fields are produced by resistive Bitter magnet that can reach up to 33 T with 32 mm bore size. The magnet coils are operating at a voltage drop of 500 V and with the maximum current of 40 kA. The enormous amount of heat that is produced by the current flowing in the resistive magnet is removed by deionized cooling water that is pumped through the magnet at the rate of 150 l/s. The cooling system has two 750 m^3 buffers of cold water, a heat exchanger and

three chillers which in total can consume more than 15 MW of power.

The optical system consists of a Genzel-type interferometer Bruker IFS113V, described in Sec. 2.2, a quasi-optical telescope to the cryostat and a 1.6 K bolometer, which is situated at the bottom of the probe. The spectrometer is situated on the upper floor which is connected the cryostat below by a quasi-optical telescope. The accessible spectral range is from 12 cm^{-1} to 700 cm^{-1}. The samples can be measured in Faraday or in Voigt configurations. The polarization of light is selected by a polarizer that is mounted in a fixed position in front of the sample.

Figure 18: Nijmegen Bitter magnet setup at Cell 3. The Bitter magnet is at the centre of the picture under the platform. Four horizontal cooling water pipes are connected to the magnet, two from each side. Above the magnet from the level of the platform there is a cryostat, its tail extends into the 32 mm bore of the magnet. At the top there is a grey pipe, a part of the quasi-optical telescope, coming from the spectrometer that is situated on the upper floor. The two black vertical pipes at the back wall are the power cables. The red light on the left hand side wall shows that the magnet is currently under use.

2.6 Determining the orientation of crystal axes with linearly polarized THz radiation

THz spectroscopy can be used to determine the selection rules of spin-wave excitations. We used linearly polarized light with E-field oriented along selected crystal axes. The orientation of crystal axes of individual pieces was known a priory from the Laue diffraction pattern of X-rays. Although care was taken while mounting the samples to the sample holder a small misalignment of a crystal axis relative to polarizer and dc magnetic field is inevitable. Depending on the probe the misalignment error of the sample can be minimized by carrying out polarization scans or by rotating the sample in magnetic field as

described below. It is important to note here, that principal axes projections can only be determined in the plane of the sample and the tilt of the sample plane cannot be recovered with these methods.

One indicator of the principal axis direction is the absorption strength of the spin-wave excitation. With the polarization scan method, the polarizer is rotated in steps, a few degree at a time and THz spectra are measured at every polarizer angle ϕ. Based on the selection rule of the spin-wave, absorption is modulated as $cos^2(\phi + \phi_0)$ where ϕ_0 is an arbitrary phase shift. From the fit of the intensity with $cos^2(\phi + \phi_0)$ or with parabola around the maximum, the crystal axes in the plane perpendicular to the light propagation direction are determined. The method of rotating the polarizer can be only used in the Faraday configuration and not in the Voigt configuration. In the Voigt configuration there is a mirror between the polarizer and the sample, see Fig. 15. The E-vector must be kept in the plane of incidence or perpendicular to it to preserve the linear polarization. In Voigt configuration the polarizer is aligned with respect to the mirror plane. The trick to use this method in Voigt is to rotate the sample, keeping the polarizer fixed. The polarization scan method was mostly used in the TeslaFIR Faraday experiments shown in Ref. I and Ref. III.

In the second method the principal axis direction is found from the changing spin-wave excitation energies, while rotating the sample in the applied constant magnetic field. For example, an AFM crystal with an easy-axis should have a strong magnetic field dependence of spin-wave excitation energies if the magnetic field is applied along the easy axis. If the magnetic field is applied perpendicular to the easy axis, then the spin-wave excitation energy should have small or negligible field dependence. By rotating the AFM crystal plane that exhibits also the easy axis in constant magnetic field, the field direction alternates between hard- and easy-axis direction. This manifests itself in the THz spectra by the change in spin-wave frequencies. Similarly as mapping the intensities modulation, in this method the modulation of spin-wave excitation energies at different angles relative to the applied constant magnetic field is used. The sample rotation angle, where the mode energy is farthest from the zero field mode position, indicates one of the main principal axis. This method only requires a spin-wave excitation that is sensitive to the magnetic field and therefore a two-spin-wave excitation, which can have a strong magnetic field dependence along the hard axis that can be also used to align the sample. Compared to the polarization scan method, the method of rotating sample in magnetic field gives a better estimate of the orientation of the crystal axes. This method was used to align the crystal in Ref. II and in several Voigt measurements of Ref. I and Ref. III.

3 Data analysis

Data handling and interpretation is a vital part of the experiment as it can resolve or hide important scientific findings. This chapter investigates the delicate nuances of calculating the relative absorption spectra, the handling of the data and offers an overview of the tools developed in order to help the process of data analysis.
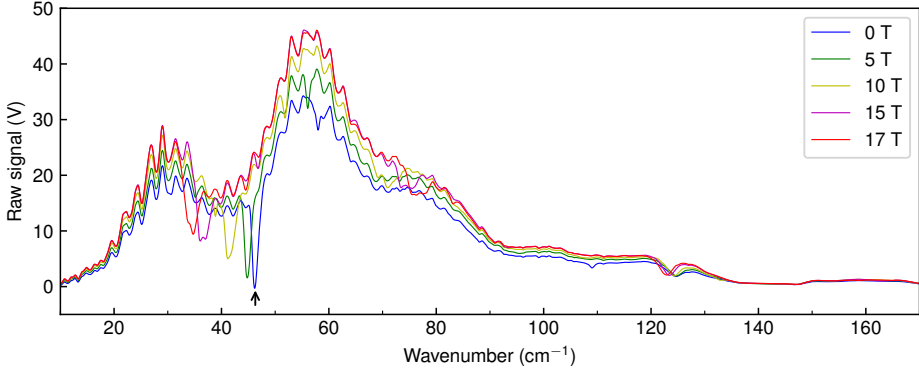
3.1 Absorption calculation methods

Figure 19: Raw spectra of LiFePO$_4$ at $T = 3.5$ K measured with TeslaFIR setup at 0, 5, 10, 15 and 17 T. A strong absorption around 46 cm^{-1}, marked with the arrow, is moving toward lower frequencies with increasing magnetic field.

An intensity spectrum of the radiation transmitted trough the sample as measured with the TeslaFIR setup is shown in Fig. 19. In this spectrum the useful information is not resolved because it is dominated by the characteristics of the whole measurement system. These features can be suppressed by dividing the intensity transmitted through the sample, I_{sample}, with some reference intensity, I_{ref}. The result is transmittance,

$$\mathscr{T} = \frac{I_{sample}}{I_{ref}}, \tag{99}$$

which shows how much light is transmitted through the sample. For quantitative analyses the absorbance is used what shows how much light is absorbed per a unit thickness of the sample. For a plane-parallel sample with thickness d, the absorbance is

$$\alpha = -\frac{1}{d}\ln(s\mathscr{T}), \tag{100}$$

where s is the ratio of reference and sample hole cross sections. $s = 1$ if the sample itself is used for reference under different conditions, like magnetic field H or temperature T. There are three main methods for defining the reference spectrum when calculating absorption. In the first method, the absorption is calculated with respect to an empty hole as

$$\alpha_{abs}(H,T) = -\frac{1}{d}\ln\left(s\frac{I(H,T)}{I_{hole}(0T,T)}\right). \tag{101}$$

The second method uses reference spectra from the paramagnetic phase of the sample

$$\begin{aligned} \Delta\alpha_T(H,T) &= \alpha(H,T) - \alpha(0T,T_{ref}) \\ &= -d^{-1}\ln[I(H,T)/I(0T,T_{ref})], \end{aligned} \tag{102}$$

with $T_{\text{ref}} > T_{\text{N}}$, where T_{N} is the magnetic ordering temperature of the sample. The third method is statistical – there the reference spectrum, H_{ref}, is a spectrum in a specific magnetic field or the average of spectra measured in different magnetic fields. The differential absorption is then calculated as

$$
\begin{aligned}
\Delta\alpha_H(H_i) &= \alpha(H_i) - \alpha(H_{\text{ref}}) \\
&= -d^{-1}\ln\left[I(H_i)/I(H_{\text{ref}})\right].
\end{aligned}
\tag{103}
$$

Here the absorption lines of the reference spectrum $\alpha(H_{\text{ref}})$ are pointing downward and $\alpha(H_{\text{ref}})$ can be recovered by finding the minimum value of $\Delta\alpha_H(H_i)$ at each frequency over the field range of H_i. By adding the calculated $\alpha(H_{\text{ref}})$ to the relative absorption $\Delta\alpha_H(H_i)$, it is possible to recover the absorption spectrum $\alpha_S(H_i)$. Instead of finding the minimum value, the median of all negative values or the median of all values can be used.

The differential absorbance in Fig. 20(a) is calculated with the reference spectrum of 17 T instead of 0 T, which has a region (marked with arrow), where the absorption is above the detection limit. By calculating the $\alpha_S(H_i)$, shown in Fig. 20(b), we can recover the whole magnetic field range, including the 17 T spectrum. The benefit of the statistical method is that it can resolve weaker magnetic field dependent modes than can be resolved by using an empty hole as a reference. The limitation of this method is that it cannot resolve features independent of the magnetic field. For example, the mode at 125 cm^{-1} always retains a derivative-like shape in the differential absorption spectra, Fig. 20(a) . This shows that the 125 cm^{-1} mode does not have a strong enough magnetic field dependence to be moved away from the 0 T position by 17 T field.

Differential absorption spectra calculated with the spectrum $I(T_{\text{ref}})$ measured in the paramagnetic phase or with the empty hole reference spectrum are shown in Fig. 21(a) and (b) correspondingly. As can be seen, both these methods reveal features independent of the magnetic field. From $\Delta\alpha_T(H,T)$, shown in Fig. 21(a), the 125 cm^{-1} mode is fully recovered, which was not possible with the spectra measured in different fields but at constant T. The empty hole reference, shown in Fig. 21(b), can also resolve 125 cm^{-1} mode, but it is not possible to separate it from the phonon background absorption that starts at 120 cm^{-1}. However, the existence of a phonon in that region could only be verified with the empty hole reference spectrum. Thus, in order to quantify the area of the 125 cm^{-1} mode we must use spectra calculated with high T reference, Fig. 21(a).

In conclusion, one measurement protocol and absorption calculation method might not be enough to capture modes of different origin. The experimentalist who evaluates and plans the experiment has to choose the correct experimental plan and the method to interpret the data, in order to fully recover the quantitative data and the absorption spectra of the sample.
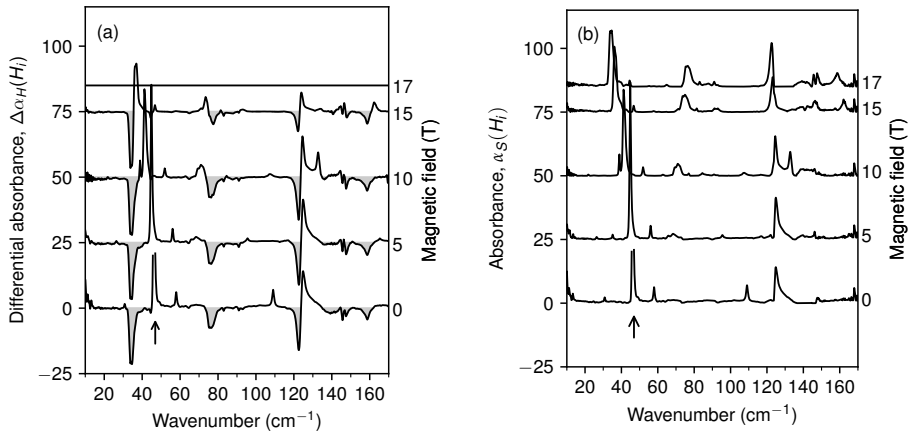
Figure 20: (a) The differential absorption of LiFePO$_4$ at $T = 3.5\,\mathrm{K}$ calculated with $H_{\mathrm{ref}} = 17\,\mathrm{T}$. The reference spectrum lines are pointing downward and the lines in other fields are pointing upward. The negative portions of spectra are coloured grey. The differential $17\,\mathrm{T}$ spectrum is a flat line. (b) The absorption spectra calculated by adding a reference spectrum, the $17\,\mathrm{T}$ spectrum in this panel, to differential absorption spectra shown in panel (a). The arrow on both panels marks the region where the $0\,\mathrm{T}$ spectrum is discontinued because the absorption was above the upper detection limit. Spectra in both panels are shifted to zero around $100\,\mathrm{cm}^{-1}$ and an offset proportional to the magnitude of magnetic field is added.
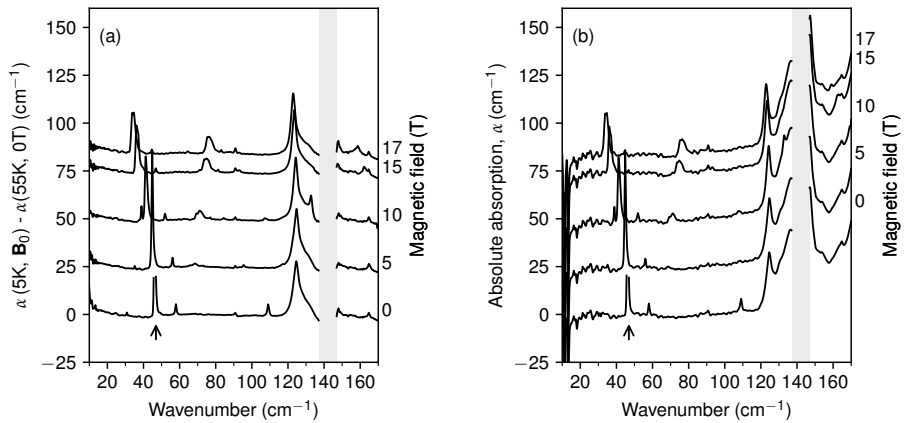
Figure 21: (a) The absorption difference of LiFePO$_4$ at $T = 3.5\,\mathrm{K}$ calculated with $I(T_{\mathrm{ref}})$ measured in the paramagnetic phase at $T = 55\,\mathrm{K}$. (b) The absorption difference calculated with an empty hole reference spectrum. The arrow on both panels marks the region where the $0\,\mathrm{T}$ spectrum is discontinued because the absorption was above the upper detection limit. The grey coloured regions show where the reference spectrum absorption was above the upper detection limit. Spectra in both panels are shifted to zero around $100\,\mathrm{cm}^{-1}$ and an offset proportional to the magnitude of magnetic field is added.

3.2 Measurement history visualization tool

Spectra depend on experimental conditions under which they are measured. In addition, they may depend on the history of crystal treatment by magnetic field, electric field or temperature and even measurements with the same set of parameters can lead to different results. It could happen that the experimental setup faults or user mistakes lead to the realization of a parameter value different from the planned value or it could lead to the wrong sample treatment before the start of the measurement series. The worst of these errors occurs when the program saves the intended parameter value to the measurement log file, called ScanLog in TeslaFIR, and not the actual value. However, there is another log file where the data from different experimental setup controllers is collected and saved.

The measurement history visualization tool was created for showing the TeslaFIR setup experimental parameters next to measurement file numbers, using the information from two log files. The program reads in the ScanLog where the information about the specific measurement files is held and the experimental setup log that holds the logs from the experimental setup controllers. By combining and sorting these two histories through date and time, the measurement is visualized as shown on Fig. 22. The tool allows highlighting the pre-determined parameters by clicking the boxes on the bottom left. The cursor runs over all the panels with a red vertical marker and shows the experiment file number at the given point. The red vertical line values at each panel are printed on the right hand side of panels. This tool was used to sort the experimental results of all three papers involved in this thesis.

3.3 Further development of in-lab Python library BdepTools

Data interpretation should be independent of an individual who handles the data and should enable the reproduction of the same results after periods of time. The main drawback of graphical programs like OriginPro is that the user can unintentionally conduct calculations or copy-paste operations that break the traceability of the data flow. Therefore, the Python programming language for data handling was adopted. Over the course of several years the in-lab Python library named BdepTools has been built in the THz laboratory. It includes tools and programs that allow fast data handling and analysis, including the creation of publication-quality figures. This method allows transparent data handling with clear data flow from the experiment to the final publication figures.

The contribution of this work to BdepTools is following:

1. Creating and formatting multi-panel plots like Fig. 4 in Ref. I and Figs. 4 and S4, in Ref. III.

2. Automatic detection of the measurement configuration from the data file names and the usage of the detected key-word arguments to manipulate and plot the selected configurations (magnetic field directions, polarizations, etc.) in multi-panel figures.

3. Plotting experimental data with symbols where configurations are grouped automatically and plotted by different labels with the symbol size as a function of the fitted area of THz absorption line.

4. Plotting theoretical intensities as lines where the width of the line depends on the parameter, e.g. applied magnetic field.

5. Subtraction of water vapour absorption lines from the spectra (needed only if the spectrometer vacuum was not good).
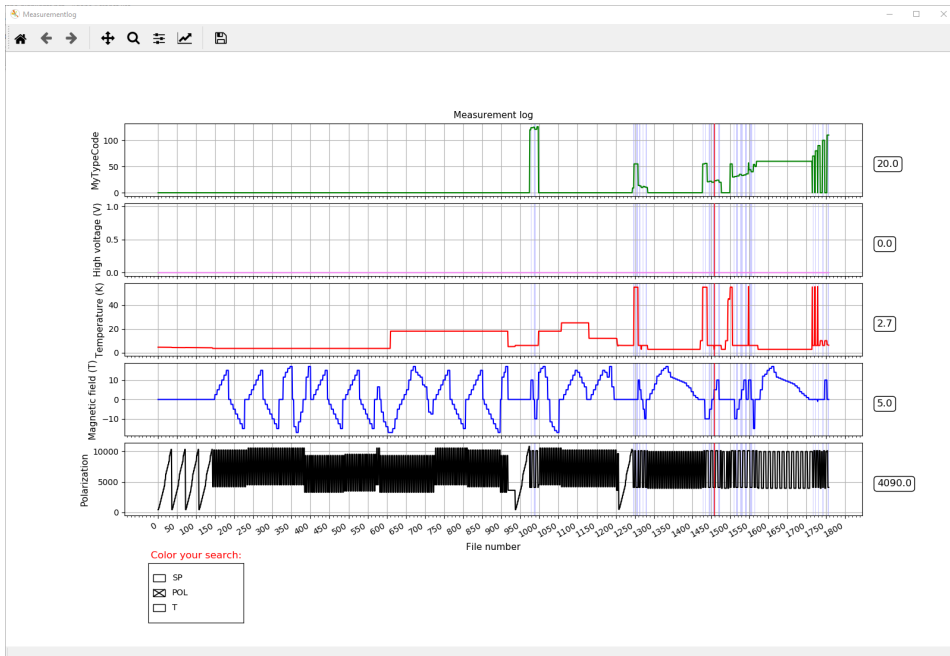
Figure 22: The measurement log visualizer reads in the ScanLog of measured files and the log of the experimental setup controllers combining them in a graphical plot for easier traceability of the measurement history. At the bottom left the three buttons can be used to colour the regions of sample position (SP), polarization (POL) and temperature (T) with predefined values. The blue regions show where the polarization value equals to predefined value of 4090. The red vertical line follows the mouse cursor and its values of it at each panel are printed on the right side. The MyTypeCode is a number that labels different user-defined measurement series.

6. A ME sum rule calculation code which uses excitation energies and full-width half maximum data (obtained from the fit results of spectra) to select the spectral regions where the ME sum rule is calculated, Eq. (39).

The main Python libraries used in this work are NumPy [142], Matplotlib [143], Scipy [144] and Pandas [145].

4 Results and discussion

4.1 THz spectroscopy of orthophosphates in magnetic field

The lithium orthophosphate family with members LMPO_4 ($M =$ Ni, Fe, Co, Mn) have an olivine crystal structure with a space group equal or lower than $Pnma$ with the crystallographic point group D_{2h} [146–150]. The crystal structure of orthophosphates is illustrated in Fig. 23. There are four spins in the unit cell. The long-range antiferromagnetic (AFM) order of these members emerges below the Néel temperature (T_N) in a range from 21.8 K to 50 K [148,149,151,152]. The magnetic dipole moments are almost aligned to a unique crystallographic easy axis in every material: Mn–x, Co–y, Fe–y and Ni–z. The primary C-type spin configurations transform according to irreducible representations of D_{2h} as: Mn–A_u, Co–B_{1u}, Fe–B_{1u} and Ni–B_{2u} [153]. These compounds become ME as their magnetic order breaks the inversion symmetry [149] and they exhibit linear ME effect [154–157]. The ME effect together with strong single-ion anisotropy makes the orthophosphates good candidates for investigating unconventional single-spin-wave or multi-spin-wave excitations with emergent coupling to the electric and magnetic components of THz radiation.
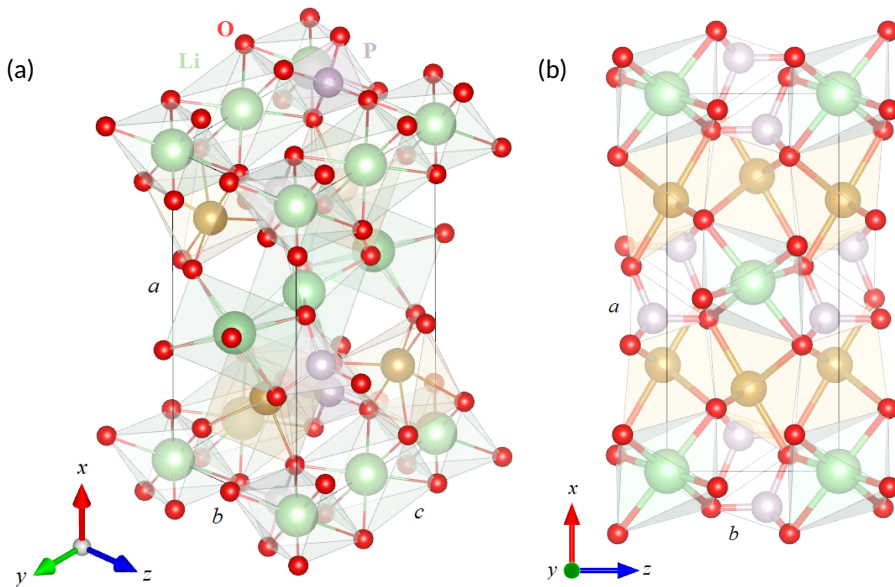

Figure 23: (a) The schematic crystal structure unit cell of orthophosphates LMPO$_4$ (M = Ni, Fe, Co, Mn). (b) The view along y axis. There are four MO$_6$ octahedra and four PO$_4$ tetrahedra in one unit cell. The MO$_6$ form stacked layers along x axis separated by Li$^+$ ions and PO$_4$ tetrahedra. This figure was produced with Vesta [158].

The single crystals of LiNiPO$_4$ and LiFePO$_4$ fall within the scope of this thesis. Samples were grown by the optical floating zone method by V. Kocsis in RIKEN, similarly to the description in Ref. [159]. Both compounds were studied by infrared absorption spectroscopy by applying magnetic field up to 33 T along three principal crystallographic directions in the THz spectral range, see Table 5. The THz absorption study up to 17 T was carried out in NICPB, Tallinn with the TeslaFIR setup described in Sec. 2.4 and the measurements up to 33 T were done in HFML, Nijmegen, as described in Sec. 2.5. Additionally, the magnetization of LiNiPO$_4$ and LiFePO$_4$ was measured up to 32 T and 120 T respectively. Based on

the magnetization and THz absorption study, mean-field models were used by D. Szaller to describe the four magnon modes and the magnetization in both compounds.

Table 5: The measured THz absorption configurations of LiFePO$_4$ and LiNiPO$_4$. The first column shows the experiment configuration of rows. The next columns show the direction of the magnetic field $\mathbf{H}$, light wavevector $\mathbf{k}$ and the orientation of $\mathbf{E}^\omega$ and $\mathbf{H}^\omega$ components of light ($\mathbf{k} \perp \mathbf{E}^\omega \perp \mathbf{H}^\omega$). The last four columns mark the measured configurations and field ranges with check mark.

Configuration	$\mathbf{H}$ dir.	$\mathbf{k}$	$\mathbf{E}^\omega$	$\mathbf{H}^\omega$	LiNiPO$_4$, $\mu_0\mathbf{H}$		LiFePO$_4$, $\mu_0\mathbf{H}$	
					$\leq$17 T	>17 T	$\leq$17 T	>17 T
Faraday	x	x	y	z	✓	✓	✓	✓
Faraday	x	x	z	y	✓	✓	✓	✓
Voigt	x	y	x	z	✓			
Voigt	x	y	z	x	✓			
Voigt	x	z	x	y	✓		✓	
Voigt	x	z	y	x	✓		✓	
Voigt	y	x	z	y			✓	
Voigt	y	x	y	z			✓	
Faraday	y	y	x	z	✓	✓	✓	✓
Faraday	y	y	z	x	✓	✓	✓	✓
Voigt	y	z	y	x	✓		✓	
Voigt	y	z	x	y	✓		✓	
Voigt	z	x	y	z			✓	
Voigt	z	x	z	y			✓	
Voigt	z	y	z	x	✓			
Voigt	z	y	x	z	✓			
Faraday	z	z	x	y	✓	✓	✓	✓
Faraday	z	z	y	x	✓	✓	✓	✓

4.1.1 LiNiPO$_4$, spin $S = 1$

The Ni^{2+} ions in LiNiPO$_4$ with spins $S = 1$ are aligned along z axis with slight canting toward x direction [160], see Fig. 24. In magnetic field along x or z two ME tensor elements χ_{xz}^{me} and χ_{zx}^{me} are finite [156]. Particularly interesting is the delicate balance of the nearest-neighbour J_{yz} and the frustrated next-nearest-neighbour J_y exchange interactions which puts the LiNiPO$_4$ on the verge of commensurate (magnetic unit cell is periodic with crystallographic unit cell) and incommensurate structures (the size of one of the unit cells is not an integer multiple of the other) [37, 38, 160]. Below T_N=20.8 K the strong antiferromagnetic exchange interactions in the yz plane force the crystal into a commensurate antiferromagnetic order. On heating above T_N, the sample enters into a long-range incommensurate magnetic structure. The paramagnetic phase sets in at $T_{IC} = 21.7$ K, with short-range magnetic correlations existing up to 40 K [161]. The application of magnetic field along z direction at low temperature results in an interesting H–T phase diagram, where the commensurate phase (ordering vector (0,0,0)) is stable between 0–12 T and 19–21.5 T. An incommensurate phase is observed at 12–16 T followed by a quintupled commensurate phase (0,1/5,0) in the range 16–19 T. Another incommensurate phase is observed at 21.5–38 T, followed by several other phases in higher fields [39, 45, 65, 162].

The magnetization measurements of single crystal LiNiPO$_4$, Fig. 25, were performed in Nijmegen High Field Magnet Laboratory. The magnetization in $\mathbf{H}\,\|\,\mathbf{x}$ and $\mathbf{H}\,\|\,\mathbf{y}$ changes
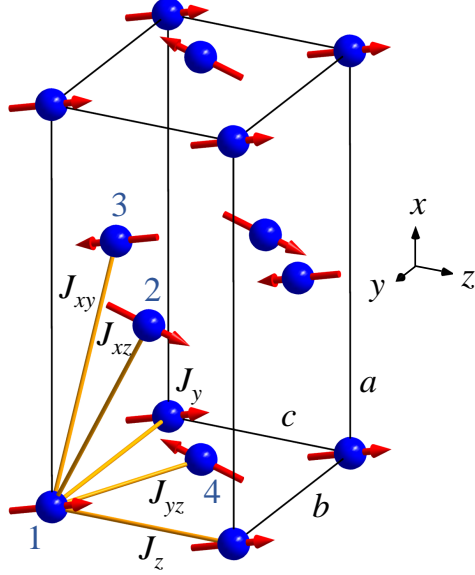
Figure 24: The spin configuration of the antiferromagnetic ground state of LiNiPO$_4$. There are four Ni^{2+} spins, $S = 1$, in the magnetic unit cell drawn as a box. In the primary C-type spin configuration the spins are along the z axis with small canting towards the x axis by $\theta = \pm(7.8° \pm 2.6°)$ [39, 64]. The numbering of spins and the labelling of exchange interactions corresponds to the spin Hamiltonian described by Eq. (104). Figure reproduced from Ref. I.
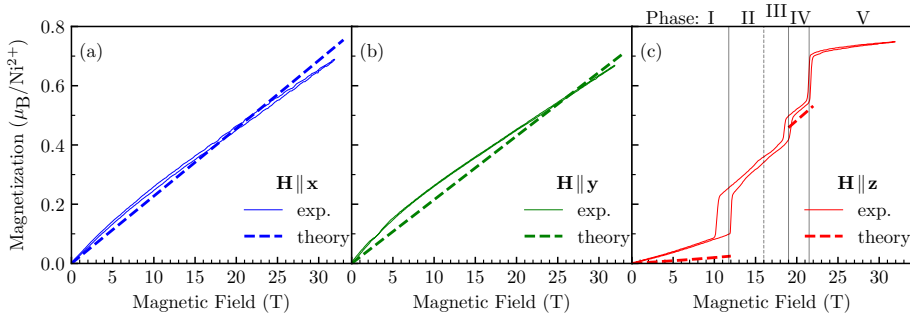

Figure 25: The LiNiPO$_4$ magnetic field **H** dependence of the magnetization **M** parallel to the field at 2.4 K. (a) **H** ∥ **x**, (b) **H** ∥ **y** and (c) **H** ∥ **z**. Solid lines are experimental results and the dashed lines are calculated from the mean-field model with the parameters listed in Table 6. Vertical lines in (c) show the known phase transitions.
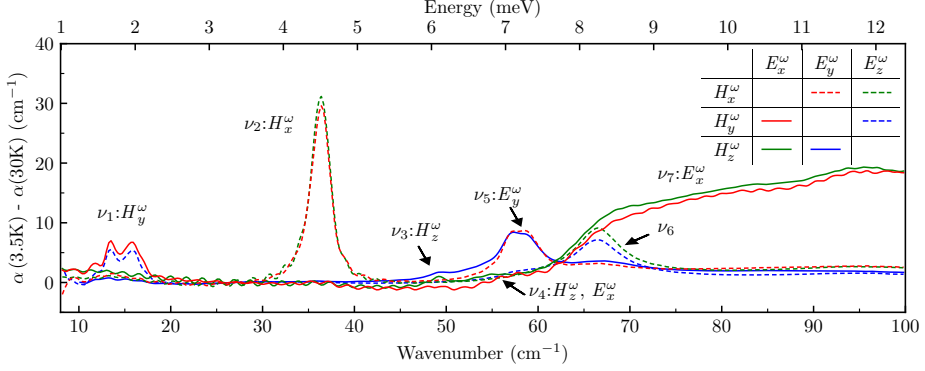
Figure 26: *THz absorption spectra of LiNiPO$_4$ in $H = 0$ T at $T = 3.5$ K relative to spectra measured in the paramagnetic phase at $T = 30$ K. THz radiation propagation directions are **k**∥**x** (blue), **k**∥**y** (green) and **k**∥**z** (red). The two orthogonal polarizations $\{E_i^\omega, H_j^\omega\}$ for a given $k_k \sim E_i^\omega \times H_j^\omega$ are indicated by solid and dashed lines shown in the inset. ν_n labels the modes, $n = 1, \ldots, 7$, with H_j^ω or E_i^ω indicate the magnetic-dipole or electric-dipole activity of the mode respectively.*

continuously, Fig. 25(a,b), while in **H**∥**z**, Fig. 25(c), shows three step-like increases at 12, 19 and 21.5 T that indicate phase transitions, in agreement with previous results. Although magnetization at 16 T hardly changes, the magnetic structure change has been verified by neutron diffraction studies in Ref. [39].

Previous INS measurements [37–39] have identified two magnon branches below 8 meV. We identify seven spin-wave excitations in LiNiPO$_4$ THz absorption spectra measured up to ~12 meV in a zero magnetic field, Fig. 26. All these modes are absent above T_N. Since the neutron diffraction studies did not detect any structural changes at T_N [64] nor were new Raman-active phonons found [32], we assign all 7 modes to spin excitations. We have identified three magnetic-dipole active magnons (ν_1=16 cm^{-1}, ν_2=36.2 cm^{-1}, and ν_3=48.4 cm^{-1}), an electric-dipole active magnon (ν_5=56.4 cm^{-1}), two ME spin excitations (ν_4=54.8 cm^{-1} and ν_6=66.4 cm^{-1}) and a broad absorption band ν_7 that extends from 65 cm^{-1} to 115 cm^{-1}. The electromagnetic field components which excite these modes are ν_1–H_y^ω, ν_2–H_x^ω, ν_3–H_z^ω, ν_4–$\{H_z^\omega, E_x^\omega\}$, ν_5–E_y^ω and ν_7–E_x^ω. The selection rules for ν_6 could not be determined, as it is excited in five different configurations with the strongest activity in E_z^ω, see Table II in Ref. I.

The magnetic field dependence of the modes is presented in Fig. 27 along three magnetic field directions, **H**∥**x**, **H**∥**y** and **H**∥**z**, up to 32 T, see Table 5. From the mean-field model we expect N magnon excitations, where N is limited by the number of spins in the magnetic unit cell if the S_z component of a individual spin is constant [28, I]. In LiNiPO$_4$ $N = 4$, which means that from the seven detected excitations four are magnons. To identify the magnons, we applied a mean-field model with spin dynamics, described in Sec. 1.4.

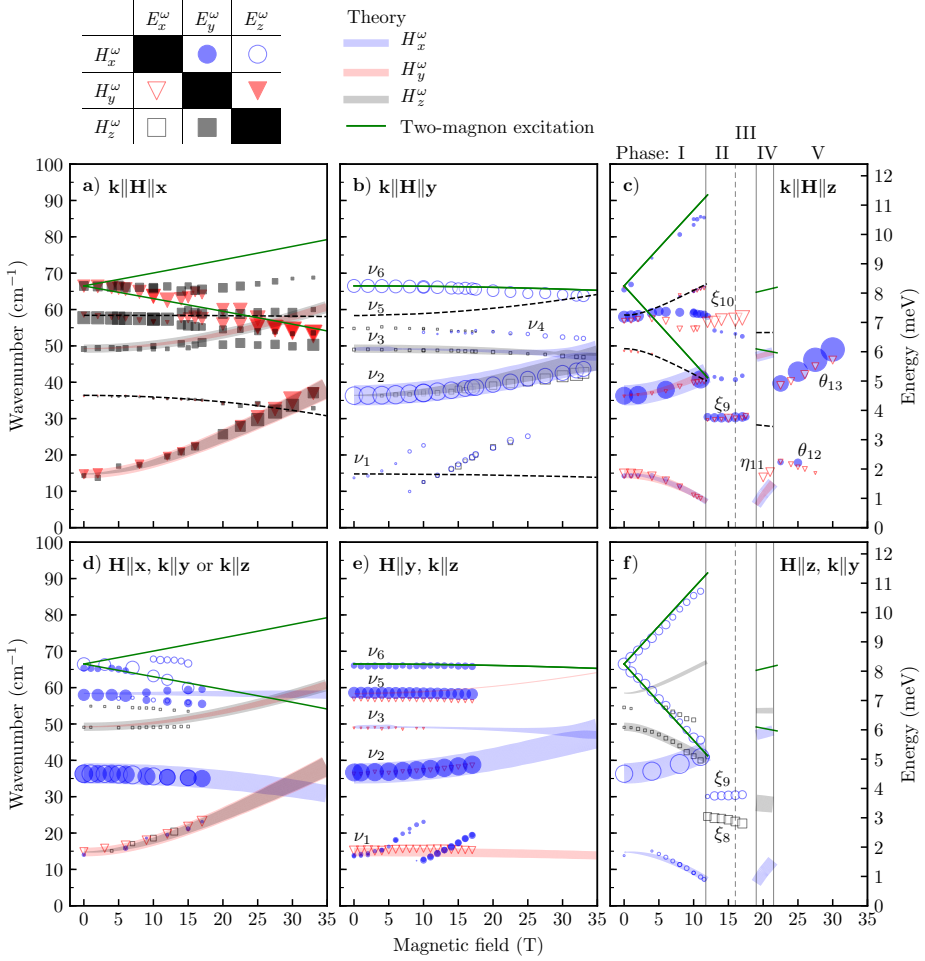LiNiPO$_4$ can be modelled with spin Hamiltonian that includes exchange interactions,

Figure 27: *Magnetic field dependence of the spin-wave resonance frequencies and absorption line areas at $T = 3.5\,\mathrm{K}$ in LiNiPO$_4$. The (a), (b), and (c) panels show the measurements in the Faraday ($\mathbf{k} \parallel \mathbf{B}$), while the (d), (e), and (f) panels correspond to experiments in the Voigt ($\mathbf{k} \perp \mathbf{B}$) configuration. The magnetic field directions are separated in columns as (a), (d) – $\mathbf{H} \parallel \mathbf{x}$, (b), (e) – $\mathbf{H} \parallel \mathbf{y}$, and (c), (f) – $\mathbf{H} \parallel \mathbf{z}$. Symbols are the fit results of experimentally measured modes and correspond to six combinations of $\{E_i^\omega, H_j^\omega\}$ as indicated on top of the figure. The symbol height is proportional to the square root of experimental absorption line area with the same scaling as wavenumber axis. The solid lines are the results of the mean-field model calculations, modes ν_1, ν_2, ν_3 and ν_5. The width of the line is proportional to the square root of the line area calculated in the magnetic dipole approximation. The colour of the symbol and the line is determined by the magnetic component of light, H_x^ω – blue, H_y^ω – red, and H_z^ω – black. The black dashed lines show the modes with vanishing theoretical intensity in all measured configurations of panels (a), (b), and (c). The green solid line is the two-magnon excitation ν_6. The phase boundaries determined from the magnetic field dependence of the THz spectra and magnetization are shown by vertical solid lines in (c) and (f); the phase boundary between II and III, vertical dashed line, is from Refs. [65, 160]. This figure is reproduced from Ref. I.*

single-ion anisotropies, Zeeman energy, and Dzyaloshinskii-Moriya interaction:

$$
\begin{aligned}
\mathcal{H} \;=\; & \sum_{i=1}^{4}\left[\Lambda_x\left(S_i^x\right)^2+\Lambda_y\left(S_i^y\right)^2-g\mu_{\mathrm{B}}\mu_0\mathbf{H}\cdot\mathbf{S}_i\right] \\
+\; & 4\left[J_{xz}\left(\mathbf{S}_1\cdot\mathbf{S}_2+\mathbf{S}_3\cdot\mathbf{S}_4\right)+J_{xy}\left(\mathbf{S}_1\cdot\mathbf{S}_3+\mathbf{S}_2\cdot\mathbf{S}_4\right)\right. \\
+\; & J_{yz}\left(\mathbf{S}_1\cdot\mathbf{S}_4+\mathbf{S}_2\cdot\mathbf{S}_3\right) \\
+\; & \left. D_y\left(S_1^z S_4^x-S_1^x S_4^z+S_3^z S_2^x-S_3^x S_2^z\right)\right].
\end{aligned}
\tag{104}
$$

The model describes spin variables as classical vectors $\{\mathbf{S}_1,\mathbf{S}_2,\mathbf{S}_3,\mathbf{S}_4\}$ which are connected by five different exchange couplings as shown in Fig. 24. We can neglect two exchange couplings, J_y and J_z, as they connect spins at the same crystallographic sites, producing, irrespective of the spin state, a constant energy shift in the Γ point. We use three isotropic Heisenberg exchange interactions J_{xz}, J_{xy}, and J_{yz} in the model. The magnetic ions are located inside a strongly distorted oxygen cage which introduces crystal anisotropy that is taken into account by two single-ion hard-axis anisotropies, $\Lambda_x, \Lambda_y > 0$. The energy change in magnetic field is introduced by the Zeeman term that includes the g factor g, the Bohr magneton μ_{B}, and the vacuum permeability μ_0. The canting of spins out from the easy axis, z, is induced by the Dzyaloshinskii-Moriya interaction proportional to D_y.

In order to describe the experimental results of LiNiPO$_4$, first we calculated the equilibrium orientation of the classical spin vectors by minimizing the energy of the Hamiltonian at each magnetic field with the parameters from Ref. [39]. By comparing the model results with experimental spectra in Fig. 27, we could resolve that the four expected magnon modes are ν_1, ν_2, ν_3 and ν_5. Then, we adjusted the parameters to reproduce the energies of the four modes and the magnetization in Fig. 25. The parameters obtained from the model are shown in the first row of Table 6. The model also predicts the reappearance of the mode ν_1 in phase IV, marked as η_{11}, shown in Fig. 27.

Table 6: The parameters of the mean-field model used to describe the static magnetic properties and single- and two-magnon excitations in LiNiPO$_4$: exchange couplings J_{ij} and J_k, single-ion anisotropy constants Λ_i, Dzyaloshinskii-Moriya coupling D_y, and g factor g. Units are in meV except the dimensionless g. Table is reproduced from Ref. I.

J_y	J_z	J_{xz}	J_{xy}	J_{yz}	Λ_x	Λ_y	D_y	g	Ref.
0.65	0.16	-0.17	0.16	1.24	0.14	0.74	0.41	2.2	Ref. I
0.67	-0.06	-0.11	0.32	1	0.41	1.42	0.32	2.2	[39]
0.67	-0.05	-0.11	0.3	1.04	0.34	1.82			[37]
0.59	-0.11	-0.16	0.26	0.94	0.34	1.92			[38]

The broad absorption band ν_7 has been detected with Raman scattering previously in Ref. [32]. In a sister compound LiMnPO$_4$, a similar broad band absorption was verified as two-magnon excitation with reproducing the line shape using the magnon density of states (DOS) [163]. To identify ν_7 we calculated the magnon DOS of ν_2 numerically on finite-size unit cell of 4 x 4 x 4 with 256 spins, using the Eq. (104) that we extended with Heisenberg exchange couplings J_y and J_z. The two-magnon DOS, seen in Fig. 5 of Ref. I, was obtained by doubling the energy of the magnon ν_2 DOS. Since the calculated DOS overlaps with the broad absorption band ν_7 we concluded that this band is a $\Delta S = 0$ two-magnon continuum.

The frequency of mode ν_6 corresponds to the singularity maximum of the two-magnon DOS, which hints that ν_6 might also be a two-magnon excitation. Furthermore, ν_6 splits

into two resonances in $\mathbf{H} \| \mathbf{z}$ configuration with effective g-factors $g_- = 4.24 \pm 0.07$ and $g_+ = 4.00 \pm 0.04$. These g factors are two times larger than that of a one-magnon excitation. From the two-magnon DOS we could verify that the singular maximum corresponds to the $R - T$ line in the Brillouin zone. By calculating the $R - T$ magnetic field dependence we could reproduce the observed splitting of ν_6 for $\mathbf{H} \| \mathbf{y}$, green solid lines in Fig. 27. The strong absorption with clear splitting of ν_6 was only seen in Voigt configuration, hence this proves that without the systematic study in both the Faraday and the Voigt configurations the ν_6 could not have been identified as a two-magnon excitation.

While magnons at the Γ point do not depend on J_y and J_z, these exchange interactions become relevant for two-magnon excitations near the Brillouin zone edge. While the zero-field frequency of ν_6 depends on J_z, the boundary between phases I and II depend on J_y. Using these dependencies we determined that $J_z = 0.16$ meV and $J_y = 0.65$ meV. The magnitudes J_z and J_y are in agreement with previous INS studies [37–39], while J_z has the opposite sign, see Table 6.

To conclude, we have demonstrated how unconventional modes, like the two-magnon excitation, can open the k-space and the exchange couplings, otherwise silent to THz spectroscopy. We have reported the first electromagnon, a ME resonance and a novel $\Delta S = 2$ ME two-magnon excitation in LiNiPO$_4$. The magnetization together with THz absorption spectra helped us to refine the magnetic interactions parameters that are essential to later in-depth studies of ME effect in LiNiPO$_4$.

4.1.2 LiFePO$_4$, spin $S = 2$

The Fe^{2+} ions in LiFePO$_4$ have spins $S = 2$ which below the T_N at 50 K order antiferromagnetically along the y axis [152] as illustrated in Fig. 28. Weak Bragg peaks detected by neutron diffraction experiments [41] suggest that the ground state features a small spin canting toward the z axis, and a small rotation in the xy plane. LiFePO$_4$ exhibits a linear magnetoelectric effect below T_N with finite ME tensor elements χ_{xy}^{me} and χ_{yx}^{me}, if magnetic field is applied along x or y respectively [41]. Previous magnetization measurements around $T = 10$ K determined that the spins maintain an easy-axis alignment up to 32 T where they flip perpendicular to the magnetic field and start gradually to rotate toward the field at least until 58 T [36, 44]. As the saturation was not reached, we measured the magnetization up to 120 T at $T = 5$ K along the easy-axis y, using ultra-high semidestructive pulses at the Laboratoire National des Champs Magnétiques Intenses in Toulouse [164,165]. Additionally, we measured magnetization using a 14 T PPMS with VSM option (Quantum Design) at $T = 2.4$ K, from where the $\mathbf{H} \| \mathbf{y}$ DC magnetization dependence was used to normalize the pulsed field magnetization. Our measurements concluded that the magnetization grows linearly in magnetic field along $\mathbf{H} \| \mathbf{x}$ and $\mathbf{H} \| \mathbf{z}$, while the weak linear dependence in $\mathbf{H} \| \mathbf{y}$ ends with a jump at (32$\pm$3) T, indicating a spin-flop transition that reaches a saturation plateau at (56$\pm$3) T, extending at least to 120 T, see Fig. 29. The saturation magnetization value in the field polarized state is (4.4$\pm$0.3) μ_B per iron. Our results show that compared to LiNiPO$_4$, the magnetic interactions in LiFePO$_4$ do not lead to more complicated magnetic-field-induced incommensurate nor non-collinear magnetic structures.

The low energy excitations of LiFePO$_4$ have been measured with Raman [33, 34], INS [40–42] and electron spin resonance spectroscopy [35, 36]. The room-temperature Raman measurements found three phonon modes below 175 cm^{-1} at 106 cm^{-1}, 141 cm^{-1} and 147 cm^{-1}. The INS measurements detected two spin-wave branches below 80.7 cm^{-1}
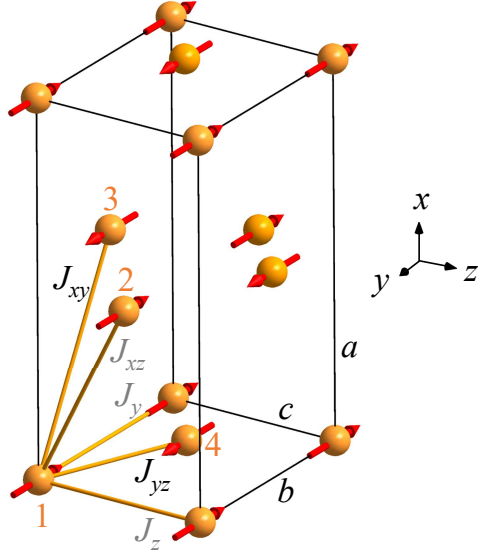
Figure 28: *The LiFePO$_4$ ground state spin configuration in zero magnetic field. There are four Fe^{2+} ions with spin $S = 2$ in the magnetic unit cell drawn as a box. Spins along the y axis form a C-type AFM structure. The counting of spins and the black labels of exchange interactions correspond to the spin Hamiltonian described by Eq. (105). Figure reproduced from Ref. III.*
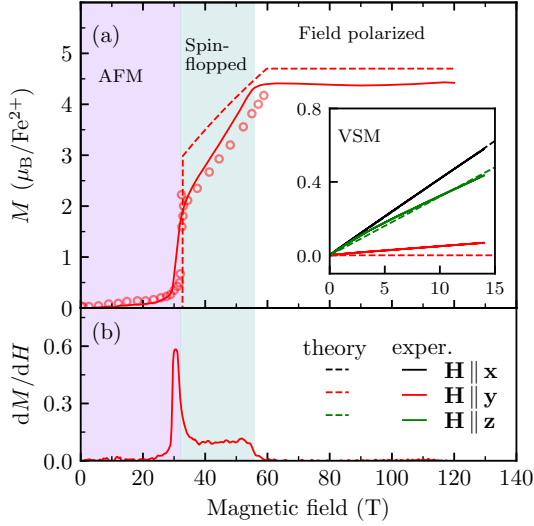

Figure 29: *(a) The LiFePO$_4$ magnetization M (solid, red) and (b) the directly measured $\mathrm{d}M/\mathrm{d}H$ (solid, red) at $T = 5\,\mathrm{K}$ for increasing pulsed field in $\mathbf{H} \parallel \mathbf{y}$. The VSM M-H measurements in quasi-static fields at $T = 2.4\,\mathrm{K}$ are shown in the inset of panel (a), where the magnetic field directions are $\mathbf{H} \parallel \mathbf{x}$ (black), $\mathbf{H} \parallel \mathbf{y}$ (red) and $\mathbf{H} \parallel \mathbf{z}$ (green). The dashed lines in panel (a) are the results of the mean-field calculations with the parameters from Table 8. For comparison, we present the pulsed field magnetization data from Ref. [36] as open red circles. The three state regions, AFM, spin-flopped and spin polarized, are shown for $\mathbf{H} \parallel \mathbf{y}$. Figure reproduced from Ref. III.*

(10 meV) and a nearly dispersionless mode at $36.3\,\mathrm{cm^{-1}}$ (4.5 meV). The electron spin resonance studies have verified two spin-wave excitations near the spin-flop field below $34\,\mathrm{cm^{-1}}$ at 32 T and two excitations from the defects at zero-magnetic field below $14\,\mathrm{cm^{-1}}$. We measured the THz absorption spectra up to $175\,\mathrm{cm^{-1}}$ (22 meV) and detected 17 spin excitations at 3.5 K, and an on-site spin-excitation at 55 K, see Fig. 30. Additionally, we detected a strong mode near $142\,\mathrm{cm^{-1}}$ what we assign to a phonon, because it is present both below and above the magnetic ordering temperature, see Fig. 30(a).

THz spectroscopy in magnetic field was carried out in Faraday and Voigt configurations up to 31.6 T, see Table 5. The mode frequencies and strengths as a function of magnetic field and radiation polarization are presented in Fig. 31 and Fig. 5 in Ref. III. The parameters of spin excitations at 3.5 K are collected in Table 7.
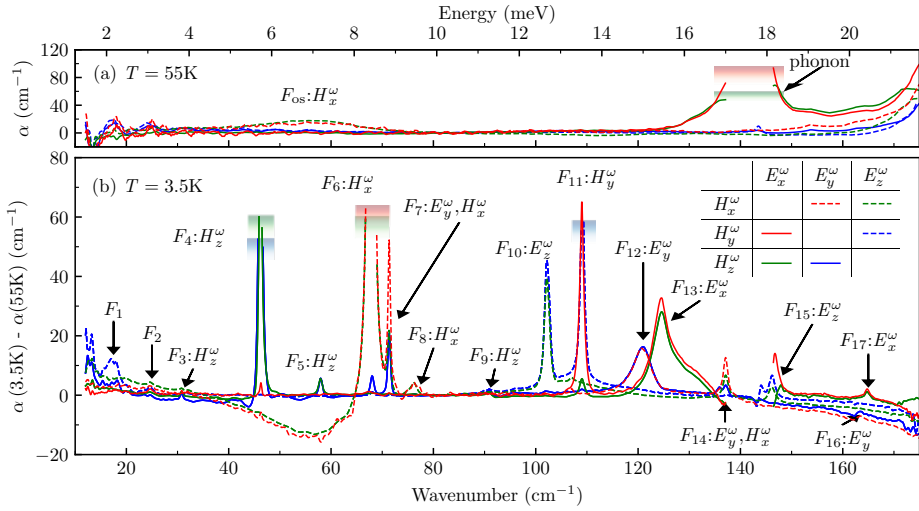

Figure 30: (a) THz absorption spectra of LiFePO$_4$ in the paramagnetic phase at 55 K relative to an open hole, and (b) the spectra at 3.5 K (magnetically ordered phase) relative to 55 K spectra. Line colours correspond to THz radiation propagation direction as k_x (blue), k_y (green) and k_z (red). Two orthogonal THz radiation polarizations $\{E_i^\omega, H_j^\omega\}$ for the given propagation direction, $k_k \sim E_i^\omega \times H_j^\omega$, are shown by the solid and dashed lines, according to the inset of panel (b). The modes in the magnetically ordered state are labelled with F_n where $n = 1, \ldots, 17$. The on-site magnetic excitation in the paramagnetic phase is labelled as F_{os}. The H_j^ω or E_i^ω next to the label indicates the magnetic- or electric-dipole activity of the mode. The blue, green and red rectangles at peaks, F_4, F_6, F_{11}, and phonon, mark the absorption above the upper detection limit. Figure reproduced from Ref. III.

Table 7: *The summary of LiFePO$_4$ mode parameters in the AFM phase including excitation energy, Gaussian fit area, selection rule, field dependence with slope and $|\Delta m_s|$. The selection rules were found by measuring the polarization dependence of spin excitations in three principal directions in the zero magnetic field. The absorption line energy and area without magnetic field were obtained from a Gaussian lineshape fit, except F_{13} where the sum of two Gaussians was used. The slopes were estimated from the linear magnetic field dependence between 15 and 17 T or from lower field range if mode was not visible there. The $|\Delta m_s|$ values are proposed assuming $g \approx 2$ from the slope b_1. Table reproduced from Ref. III.*

Mode	Energy (cm^{-1})	Area (cm^{-2})	Selection rules	Magnetic field direction	Slope b_1 (cm^{-1}T^{-1})	$|\Delta m_s|$
F_1	18.3	4		z	$+1.4$	
F_2	24.7	2		z	$+1.5$	
F_3	30.8	2	H_z^ω	y	$-0.9, +0.9$	1
F_4	46.2 (5.7 meV)	>100	H_z^ω	y	-1.1	1
F_5	58.0	6	H_z^ω	y	-1.1	1
F_6	67.9 (8.4 meV)	>200	H_x^ω	y	$+0.9$	1
F_7	71.4	37	H_x^ω, E_y^ω	y	$+1.0$	1
F_8	76.2	9	H_x^ω	y	$-0.8, +1.0$	1
F_9	90.8	2	H_z^ω	x	$+0.1$	
F_{10}	102.2	57	E_z^ω	y	-3.3	3
F_{11}	109.0	74	H_y^ω	y	$+1.8$	2
F_{12}	120.8	50	E_y^ω	y	-1.9	2
F_{13}	124.4, 127.6	185	E_x^ω	y	-0.3	
F_{14}	137.1	17	H_x^ω, E_y^ω	y	$-3.0, +2.8$	3
				z	-0.6	
F_{15}	146.3	30	E_z^ω	y	$-3.7, +3.8$	4
				z	$+0.7$	
F_{16}	163.7	2	E_y^ω	x	-0.3	
F_{17}	164.8	4	E_x^ω	y	0.0	

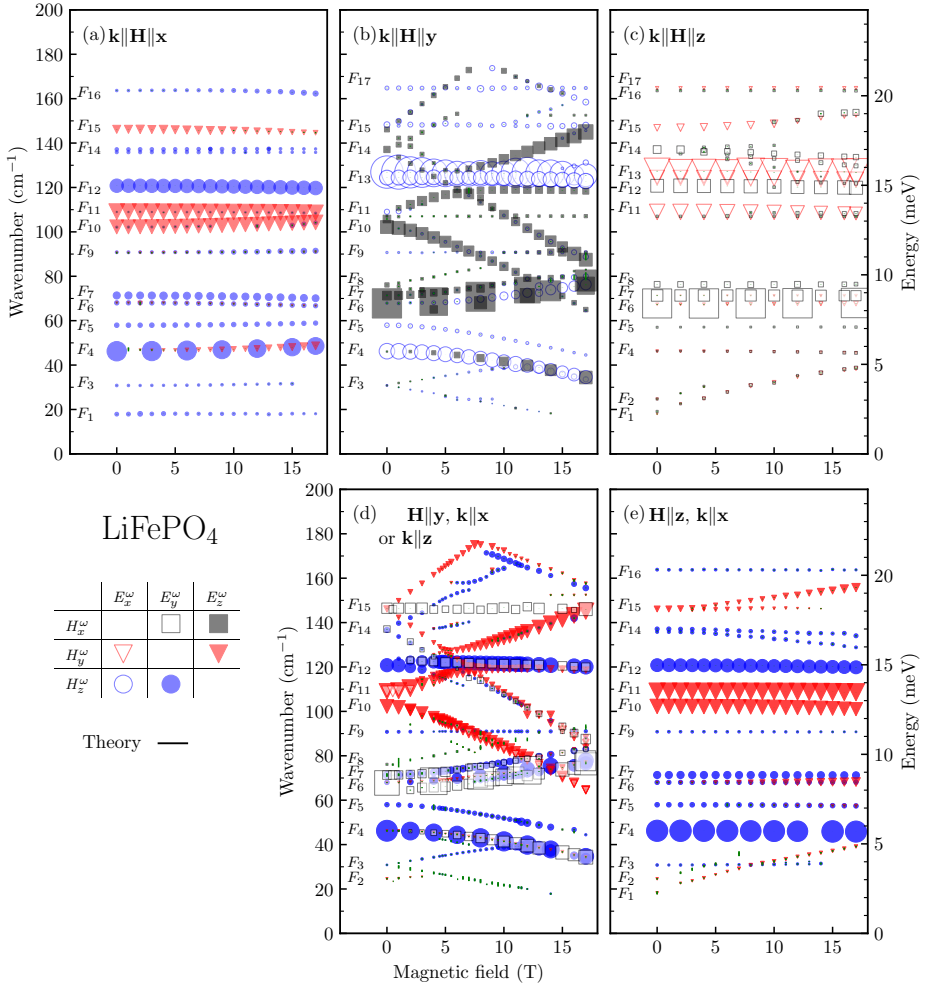*Figure 31: The LiFePO$_4$ magnetic field dependence of the spin-wave resonance frequencies and absorption line areas at $T = 3.5$ K. The first row corresponds to measurements in the Faraday configuration ($\mathbf{k} \parallel \mathbf{H}$), while the second row panels corresponds to experiments in the Voigt ($\mathbf{k} \perp \mathbf{H}$) configuration. Each column of panels corresponds to an individual magnetic field direction as (a) – $\mathbf{H} \parallel \mathbf{x}$, (b), (d) – $\mathbf{H} \parallel \mathbf{y}$, and (c), (e) – $\mathbf{H} \parallel \mathbf{z}$. The symbols are the Gaussian line shape fit results of experimentally measured modes and correspond to six combinations of linear light polarization, $\{E_i^\omega, H_j^\omega\}$, as indicated at bottom left of the figure. The height of symbols is equal to the square root of experimental absorption line area with the same scaling as the wavenumber axis. Larger symbols have been selectively shown, skipping some magnetic field values to simplify the figure. Figure reproduced from Ref. III.*

The spin dynamics of LiFePO$_4$ can be described with a Hamiltonian similar to LiNiPO$_4$, Eq. (104):

$$
\begin{aligned}
\mathscr{H} \;=\; & 4\big[J_{xy}\left(\mathbf{S}_1\cdot\mathbf{S}_3+\mathbf{S}_2\cdot\mathbf{S}_4\right)\\
& +J_{yz}\left(\mathbf{S}_1\cdot\mathbf{S}_4+\mathbf{S}_2\cdot\mathbf{S}_3\right)\\
& +D_y\left(S_1^x S_4^z - S_1^z S_4^x + S_3^x S_2^z - S_3^z S_2^x\right)\big]\\
& +\sum_{i=1}^{4}\Big[\Lambda_x\left(S_i^x\right)^2+\Lambda_z\left(S_i^z\right)^2\\
& -\mu_{\mathrm{B}}\mu_0\left(g_x H_x S_i^x + g_y H_y S_i^y + g_z H_z S_i^z\right)\Big],
\end{aligned}
\tag{105}
$$

where J_{xy} and J_{yz} are exchange interactions, Λ_x and Λ_z are hard-axis single-ion anisotropies, $\mathbf{D}=(0,D_y,0)$ is Dzyaloshinskii-Moriya interaction and the parameters in the Zeeman term are anisotropic g factor $\{g_x,g_y,g_z\}$, the Bohr magneton μ_{B}, and the vacuum permeability μ_0. To use the Landau-Lifshitz-Gilbert equation, Sec. 1.4, for modelling the spin-dynamics we have to know which are the four Brillouin zone centre magnon modes in spectra that can be used as reference for the theory. Previous INS measurements [40–42] in zero-magnetic field have identified two spin dispersion branches. Thus, F_4 and F_6 correspond to the modes observed by INS in the k-space points equivalent the Γ point. There are four remaining $|\Delta m_s|=1$ modes, see Table 7, from which we neglected the F_3 and F_8 as they have a v-type splitting in $\mathbf{H}\,\|\,\mathbf{y}$ that is not expected from mean-field model with two-easy-plane (effective easy-axis is y) magnetic anisotropies, Eq. (105). In summary, we determined that modes F_3, F_4, F_5 and F_6 are the magnons which can be used as the reference for the theory.

Our model in the ground state is a collinear four spin AFM [40] structure in agreement with the *Pnma* crystal symmetry. Therefore in the Hamiltonian, Eq. (105), we omitted the $\Lambda_{xy}S_i^x S_i^y$ anisotropy and $DS_i^y S_j^z$ Dzyaloshinskii-Moriya terms used in earlier works, as they contradict the *Pnma* crystal symmetry. The effective easy axis along y results from two single-ion hard-axis anisotropies, Λ_x and Λ_z. The comparison of the mean-field model results and the measured four magnons are shown in Fig. 32. The obtained parameters are collected and compared to earlier works in Table 8. The theoretical intensities and frequencies of F_4 and F_6 are in good agreement with the experiment, as well the frequencies of F_5 and F_7. The intensity of the ME mode F_7 is not reproduced for configuration E_y^ω as the theory describes only magnetic-dipole activity. The intensity of F_5 is reproduced in configuration H_z^ω, but not in H_x^ω. The reason could be that there exists a small canting or rotation of spins which we cannot determine from THz spectroscopy or the mode has additionally a small electric-dipole activity.

Based on the mean-field results we could unravel the correspondence between the INS magnon dispersion, interpreted in the model of the two-spin unit cell scheme, with our Γ-point optical measurements. F_4 and F_6 are the spin-waves observed in the zone centre at $\mathbf{Q}=(0,2,0)$ [41] or $\mathbf{Q}=(0,0,2)$ [42], whereas F_5 and F_7 correspond to zone-boundary excitations of the two-spin unit cell at $\mathbf{Q}=(0,0,1)$ [42], $\mathbf{Q}=(1,1,0)$ [40, 41] and $\mathbf{Q}=(0,1,1)$ [41].

The mean-field theory uses an assumption that the length of each individual spin is constant [119, I]. This limits the number of spin-waves to N, the number of spins in the magnetic unit cell and these spin-wave excitations are called magnons. If the condition $S=\mathrm{const}$ is relaxed, the number of modes can increase up to $2NS$, as shown by the multiboson spin-wave theory in Refs. [29, 118] and Ref. [119, Ch. 8.3]. Some of the extra modes appearing in the multiboson spin-wave theory may be viewed as "spin-stretching" spin-waves. The four magnon modes described with mean-field model are included in

Table 8: *The parameters of the mean-field model used to describe the static magnetic proper-*
ties and spin-waves in LiFePO$_4$: exchange couplings J_i and J_{ij}, single-ion anisotropies Λ_i and Λ_{ij},
Dzyaloshinskii-Moriya coupling D_y, and anisotropic g-factor g_i. The parameters are in units of meV
except the dimensionless g_i. The Ref. [36] used the exchange interactions and single-ion anisotropies
from Ref. [41] and g factors from Ref. [44]. The Dzyaloshinskii-Moriya parameter J_{DM} from Ref. [36]
is $D_y = J_{\mathrm{DM}}/4$ where 4 is the corresponding coordination number. Table reproduced from Ref. III.

J_{xz}	J_{xy}	J_{yz}	Λ_x	Λ_z	D_y	g	Ref.
-	0.096(6)	0.54(1)	0.51(2)	1.45(3)	0.025(5)	$g_x = 2.10(6)$ $g_y = 2.35(17)$ $g_z = 2.10(6)$	Ref. III
0.05(1)	0.14(2)	0.77(7)	0.62(12)	1.56(3)	0.038	$g_x = 2.24(3)$ $g_y = 2.31(2)$ $g_z = 1.99(3)$	[36]
0.01(1)	0.09(1)	0.46(2)	0.86(2)	2.23(2)	-	-	[42]
0.05(1)	0.14(2)	0.77(7)	0.62(12)	1.56(3)	-	-	[41]

the expected $2NS$ multi-boson modes. The multi-boson spin-wave theory was applied
to LiCoPO$_4$, a $S = 3/2$ spin system [27]. Developing a multi-boson spin-wave theory for
LiFePO$_4$, a $S = 2$ and $N = 4$ spin system, is a mayor task that falls outside the scope of this
thesis. Thus, the origin of remaining $17 - 4 = 13$ modes has to be unravelled by qualitative
arguments.

The modes F_1, F_2 and F_3 are below the lowest magnon mode F_4 and we propose that
they are impurity modes. The linear magnetic field dependence of F_1 and F_2 along $\mathbf{H} \parallel \mathbf{z}$
does not coincide with the easy axis direction of the magnetic structure, supporting the
assignment. Previously, modes with a zero field splitting of 7.3 cm^{-1} (220 GHz) were found
in Ref. [35] and assigned to the anti-site Fe^{2+}–Li$^+$ defects. Our modes in zero field are at
18.3 cm^{-1}, 24.7 cm^{-1} and 30.8 cm^{-1} and therefore can not originate from these anti-site
defects.

We assign the F_{12} and F_{13} to two-magnon excitations. Reasons for this are, firstly, the
spectral shape of modes F_{12} and F_{13} is clearly different from rest of the modes: they are
broader and with an asymmetric line shape that may reflect the high density of magnon
states in certain points of the Brillouin zone. Secondly, they are excited by the electric com-
ponent of light, that usually dominates over magnetic-dipole absorption in a two-magnon
process [114]. The magnon dispersion has a flat region near the Brillouin zone point $[1, 1, 0]$
and also there is a crossing of two dispersion curves at $[0, 1.5, 0]$, which could lead to high
density of states [41, 42]. Since the spin-wave energy in these points is 60 cm^{-1}, the ex-
pected range of a two-spin-wave excitation would be around 120 cm^{-1}. The F_{13} is not
affected by magnetic field and therefore can be $|\Delta m_s| = 0$ two-magnon excitation. The
F_{12} has a two times larger slope than the a one-magnon excitation, suggesting it is a two-
magnon excitation with $|\Delta m_s| = 2$.

The remaining F_9 to F_{11} and F_{14}-F_{17} we assign to multi-boson (quadrupolar) spin-wave
modes. The frequency versus magnetic field slopes for different modes are listed in Ta-
ble 7. We make a note here that the m_s defined in the Table 7 does not strictly define
the field dependence of these modes as there could be mixing of m_s states, see Sec. 1.5.3.
The mixing of states could originate from the large single-ion anisotropy (Λ) that is com-

parable to or stronger than the exchange couplings (J). The wave functions of mixed m_s states were calculated in Ref. [42, Table II] for a single iron spin without magnetic field. Because the mixing of states changes with magnetic field, it was not possible to use their results to calculate the slopes of LiFePO$_4$ mode frequencies in magnetic field. From the calculations of Yiu et al. it is seen that there is a group of excitations around 12.7 meV (100 cm^{-1}) and as well above 16 meV (130 cm^{-1}), consistent with with the frequency span of F_9-F_{11} and F_{14}-F_{17}. We can describe the magnetic field dependence and THz activity of these modes qualitatively as put forward next. Let us assume rotational symmetry about y axis in Eq. (105), therefore $\Lambda_z = \Lambda_x$. The energy levels E_{m_s} of a spin $S = 2$ in the presence of single-ion anisotropy and spin quantization axis y, are E_0, $E_{\pm 1}$ and $E_{\pm 2}$. The energy differences in $\mathbf{H} \| \mathbf{y}$ are $E_0 - E_{+1} \sim 1$ cm^{-1}T^{-1}, $E_0 - E_{+2} \sim 2$ cm^{-1}T^{-1}, $E_{+2} - E_{-1}$ ~ 3 cm^{-1}T^{-1} and $E_{+2} - E_{-2} \sim 4$ cm^{-1}T^{-1}. The similarity of these slopes to the slopes in Table 7 can be recognized. Next, let us unravel how these modes obtain THz activity, hence the electric-dipole moment. The $\Delta m_s = \pm 2$ electric dipole activity originates from the on-site spin-induced polarization which in the lowest order of spin operators is $P \propto \hat{S}_\alpha \hat{S}_\beta$ ($\alpha, \beta = x, y, z$) [27]. If the quantization axis is y, then $P \propto \hat{S}_x^2$ and $\hat{S}_z^2$ couple the states with different $\Delta m_s = \pm 2$. The mixing of E_0 into $E_{\pm 2}$ can happen if $\Lambda_z \neq \Lambda_x$. Indeed, LiFePO$_4$ single ion anisotropies are not equal, see Table 8, and can give a finite electric-dipole moment to the $\Delta m_s = 4$, ($E_{+2} - E_{-2}$), transition. The spin operators $\hat{S}_x \hat{S}_y$ and $\hat{S}_y \hat{S}_z$ can mix the spin states different by $\Delta m_s = \pm 1$, allowing electric-dipole-active $\Delta m_s = \pm 3$ transitions between energy levels $E_{\pm 1}$ and $E_{\mp 2}$.

To conclude, by studying the magnetic field dependence of magnon modes we refined the magnetic interactions and discovered abundance of previously undetected modes that could in future deepen the understanding of the ME effect in LiFePO$_4$ if combined with additional experimental techniques and theoretical calculations.
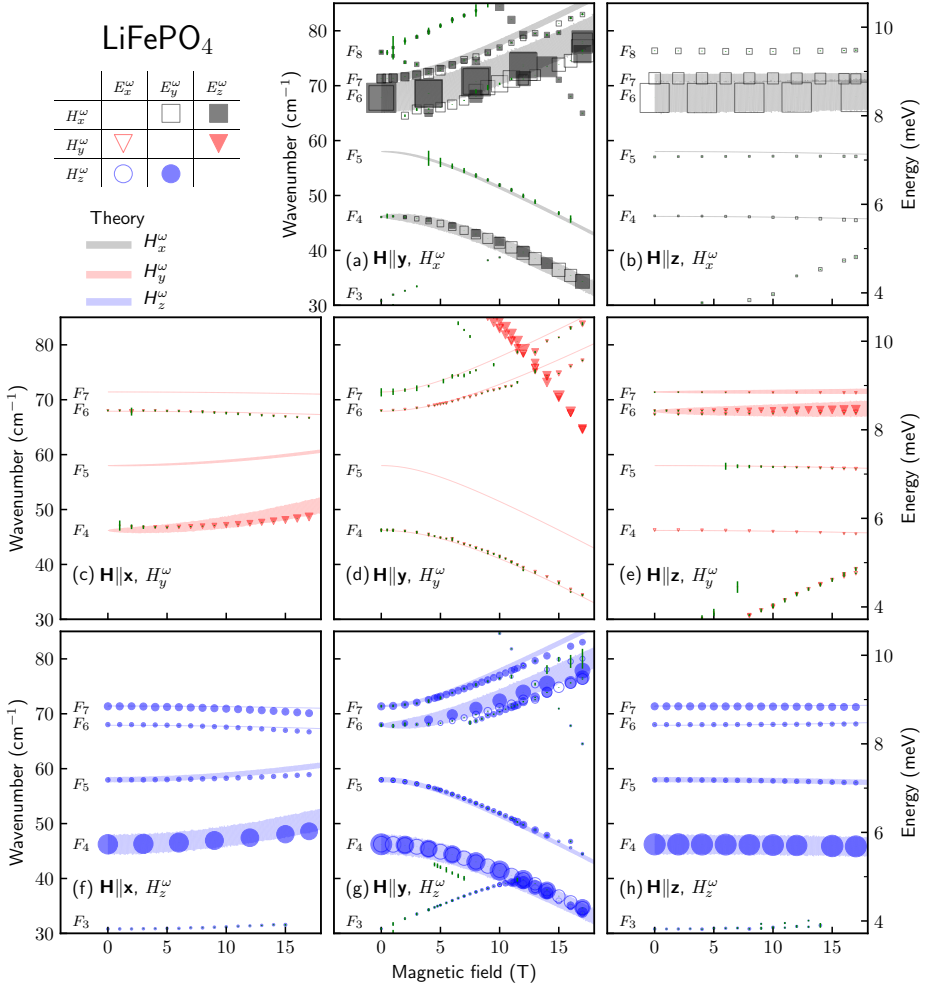
Figure 32: LiFePO$_4$ spin-wave resonance frequencies and absorption line areas magnetic field de-pendence at $T = 3.5$ K. Each column corresponds to individual magnetic field direction as {$\mathbf{H} \| \mathbf{x}$, $\mathbf{H} \| \mathbf{y}$, $\mathbf{H} \| \mathbf{z}$}, while the rows correspond to individual oscillating magnetic field direction of light as {$H_x^\omega, H_y^\omega, H_z^\omega$}. Symbols are the fit results of experimentally measured resonances with Gaussian lines and correspond to six combinations of {E_i^ω, H_j^ω} as shown on top left of the figure. The symbol height is the square root of experimental absorption line area with the same scaling as wavenumber axis. The symbol frequency error bars are indicated with green vertical lines. Wide solid curves are the results of the mean-field calculation in the magnetic dipole approximation. The width of curves is proportional to the square root of the absorption line area with the same scale as wavenumber axis. Figure reproduced from the Supplemental Material of Ref. III.

4.2 Electric-field control of transparent direction in Ba$_2$CoGe$_2$O$_7$

The melilite insulator Ba$_2$CoGe$_2$O$_7$ belongs to the barium based Type-II multiferroic family Ba$_2$XGe$_2$O$_7$ ($X =$ Mn, Co, Cu) [66,94]. Ba$_2$CoGe$_2$O$_7$ crystallizes into non-centrosymmetric tetragonal $P\bar{4}2_1m$ space group [166–168], which crystal structure is shown in Fig. 33. The $P\bar{4}2_1$m space group has a fourth-order rotation-reflection axis perpendicular to the tetragonal plane, two-fold screw axes along [100] and [010] directions and mirror planes (110) and ($1\bar{1}0$). There are two Co^{2+} ions with $S = 3/2$ in one magnetic unit cell, $\mathbf{S_A}$ and $\mathbf{S_B}$ in Fig. 34(a). The spins order into a two-sublattice AFM state below the $T_N =$ 6.7 K [166], where the strong in-plane anisotropy forces the spins into the tetragonal (001) easy-plane [168]. The AFM order reduces the space group symmetry to $P2_1'2_12_1'$, in which the formation of four AFM domains is allowed, Fig. 34(b). The $()'$ denotes the time-reversal operation, e. g. $2'$ consists of two consecutive symmetry operations, $180°$ rotation about the axis and the time reversal. The static and dynamic ME effects of Ba$_2$CoGe$_2$O$_7$ are explained by the spin-dependent $p - d$ hybridization [19, 29, 95, 169, 170], see Sec. 1.2.2. Ba$_2$CoGe$_2$O$_7$ was one of the first materials, where strong NDD was found at THz frequencies [15].
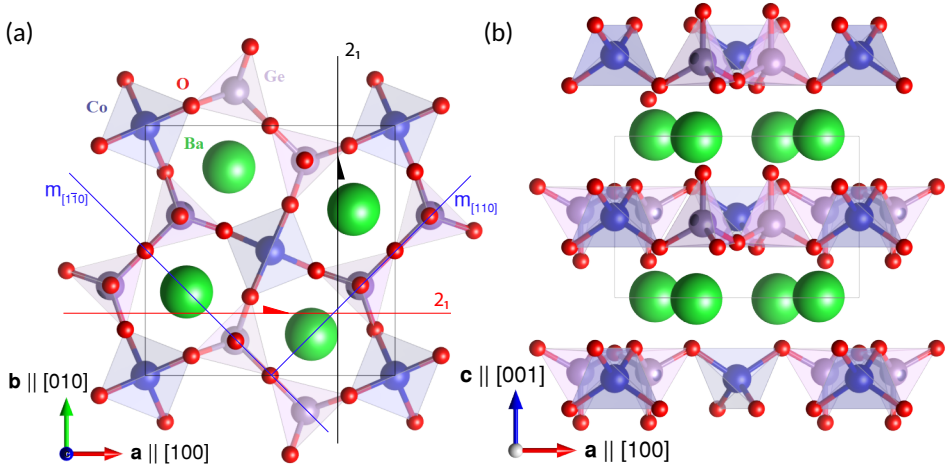

Figure 33: *The crystal structure of Ba$_2$CoGe$_2$O$_7$ along (a)* c *axis and (b)* b *axis. The Co and Ge ions are inside O$_4$ tetrahedra which are connected from corners and form two-dimensional layers. The layers of CoO$_4$ and GeO$_4$ are stacked along* c *having Ba spacer ions between the layers. This figure was produced with Vesta [158].*

The Ba$_2$CoGe$_2$O$_7$ spin dynamics can be described with a Hamiltonian consisting of parameters stated in Ref. II and Refs. [19, 29, 118, 171] as

$$
\begin{aligned}
\mathscr{H} &= J \sum_{(i,j)} \left(S_i^a S_j^a + S_i^b S_j^b \right) + J_c \sum_{(i,j)} \left(S_i^c S_j^c \right) \\
&\quad - D_c \left(S_i^a S_j^b - S_i^b S_j^a \right) + \Lambda \sum_i \left(S_i^c \right)^2 - \sum_i E_a P_i^a \\
&\quad - \mu_B \mu_0 \left(g_a H_a S_i^a + g_b H_b S_i^b + g_c H_c S_i^c \right),
\end{aligned}
\tag{106}
$$

where (i, j) pairs index the nearest-neighbour sites, J and J_c are anisotropic Heisenberg exchange interactions, D^c is the Dzyaloshinskii-Moriya interaction, Λ is single-ion anisotropy,

E_a is external electric field and P^a is the spin-induced polarization. The values of parameters are listed in Table 9. The cobalt spins are directly coupled to the induced polarization P_j^a through spin-quadrupole operators as

$$P_j^a \propto -\cos\left(2\kappa_j\right)\left(S_j^b S_j^c + S_j^c S_j^b\right) + \sin\left(2\kappa_j\right)\left(S_j^a S_j^c + S_j^c S_j^a\right),$$

$$P_j^b \propto -\cos\left(2\kappa_j\right)\left(S_j^a S_j^c + S_j^c S_j^a\right) - \sin\left(2\kappa_j\right)\left(S_j^b S_j^c + S_j^c S_j^b\right), \tag{107}$$

$$P_j^c \propto -\cos\left(2\kappa_j\right)\left(S_j^a S_j^b + S_j^b S_j^a\right) + \sin\left(2\kappa_j\right)\left[\left(S_j^a\right)^2 - \left(S_j^b\right)^2\right],$$

where a, b and c refer to the axes $[100]$, $[010]$ and $[001]$ respectively, $j = A, B$ is site index, κ_j is the orientation angle between Ge and Co tetrahedra where $\kappa_A = -\kappa_B = \kappa$, see Fig. 34(a). The weak Dzyaloshinskii-Moriya interaction was neglected in Ref. II as it is negligible compared to the exchange interactions.
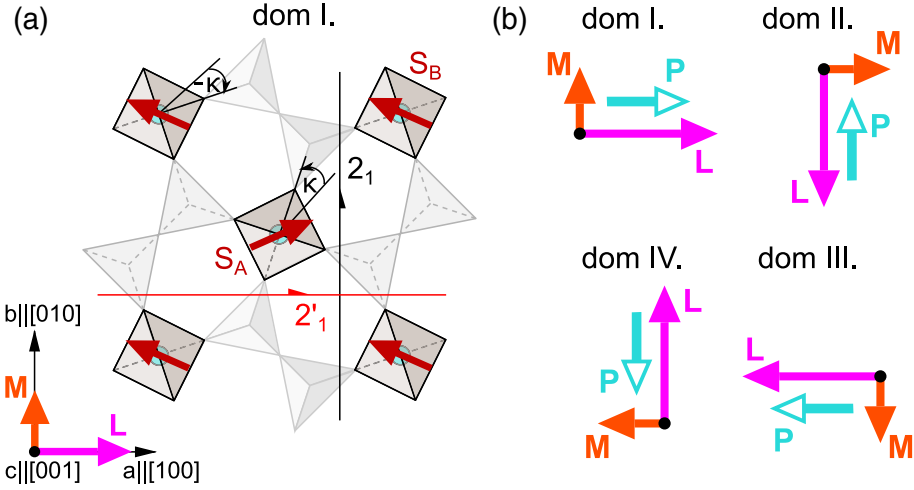
Figure 34: (a) The Ba$_2$CoGe$_2$O$_7$ low temperature canted antiferromagnetic order in domain I without magnetic field. The spins of Co^{2+} ions are shown with dark red arrows. There are two spins in one magnetic unit cell denoted with S_A and S_B. The two symmetry operations are shown with half-arrows, black 2_1 screw axis along b and red $2_1'$ orthogonal screw axis along a axis with the time reversal symmetry. The $M = S_A + S_B$ is uniform magnetization marked with red arrow and $L = S_A - S_B$ is staggered magnetization marked with violet arrow. (b) The four possible domain configurations. Magnetic field applied along c induces electric polarization $P = P_A + P_B$ (light blue arrow) via linear magnetoelectric effect. This figure is reproduced from Ref. II.

The spin-wave excitations of Ba$_2$CoGe$_2$O$_7$ have previously been studied with INS [166, 172–174] and THz spectroscopy [15, 18, 20, 29]. These studies revealed two sharp spin-wave excitations at 18 cm^{-1} (No. 1) and 34 cm^{-1} (No. 2) [15], see Fig. 35(a). No. 1 is only present if excited by H_x^ω or H_y^ω being independent of the E^ω direction, therefore labelled as magnon that can be described with standard spin-wave theory. No. 2 is a ME resonance that in magnetic field normal to the easy plane, $\mathbf{H} \parallel \mathbf{c}$, has strong v-type splitting to modes No. 2-2 and No. 2-3, with an extra mode No. 2-4 emerging from the No. 2-3 branch, see Fig. 35(a). To explain the additional modes the multi-boson spin-wave theory was used in Ref. [29] that revealed the exotic nature originating from $\Delta m_s = 2$ to 3 excitations with

Table 9: The parameters considered in Ref. II and Refs. [19,29,118,171] to describe the static magnetic properties of Ba$_2$CoGe$_2$O$_7$: exchange couplings J and J_c, single-ion anisotropy Λ, Dzyaloshinskii-Moriya coupling D_c and anisotropic g-factor g_i. All parameters are in units of meV except the dimensionless g_i. The Dzyaloshinskii-Moriya parameter was calculated using $D_c = 0.04J$ from Ref. [118].

J	J_c	Λ	D^c	g_a	g_b	g_c	Ref.
0.198	0.155	1.21	0.008	2.24	2.18	2.1	[171]

possible oscillations of the spin length. Additionally, the theory predicts that mode No. 2-4 is present in zero magnetic field just hidden under the degenerate mode No. 2, Fig.1 in Ref. [29].

Magnetic field $\mathbf{H} \parallel \mathbf{c}$ induces an on-site electric polarization $\delta\mathbf{P}$ in the ab plane via the linear magnetoelectric effect. The induced electric polarization is parallel to the staggered sublattice magnetization $\mathbf{L} = \mathbf{S}_A - \mathbf{S}_B$, see Fig. 34(b), and averages out between the domains if the field is perfectly aligned along c. Small tilting of the magnetic field from c will rearrange the domain population [95], which can be detected as NDD of spin waves as described in Sec. 1.3.3. Whereas with $\mathbf{H} \parallel \mathbf{a}$ or $\mathbf{H} \parallel \mathbf{b}$ the ferroelectricity vanishes accompanied with the spin pattern breaking all mirror-plane symmetries of lattice resulting in the material becoming chiral. In this magnetically induced chiral state it was found that modes No. 2 and No. 2-4 exhibit gigantic MChD as well as strong natural circular dichroism (NCD) [20].

In this work, Ref. II, we exploited the NDD effect of different domains by applying in-plane electric field $\mathbf{E} \parallel \mathbf{a}$ which, as the tilting of magnetic field does [95], can break the delicate balance of four domains. By changing the direction of the electric field, we attained control over the absorption of THz radiation with wavevector $\mathbf{k}$ by spin waves in the configuration $\mathbf{k} \parallel (\mathbf{E} \times \mathbf{H})$ where $\mathbf{k} \parallel \mathbf{b}$, $\mathbf{E} \parallel \mathbf{a}$ and $\mathbf{H} \parallel \mathbf{c}$.

The single crystals were grown by the optical floating zone technique by V. Kocsis in RIKEN, following Ref. [95]. The crystal quality and crystallographic axes were verified with the X-ray Laue diffraction. The determined axes were used to cut slabs with edges along crystallographic axes a and c. The thickness of slabs was about 0.7 mm in the b direction. Gold wire electrodes were painted with silver paste on the parallel sides of the rectangular (010) cut to facilitate the application of electric field along the a axis. The THz measurements were performed with the TeslaFIR setup using the rotatable Voigt probe with electric field option, described in Sec. 2.4.2. To determine the sample rotation angle when the c axis is precisely along the magnetic field, we used the No. 2 mode frequency dependence on the magnetic field orientation, as described in Sec. 2.6.

The main results of Ref. II are presented in Fig. 35, showing how the absorption changes depending on the applied $\pm\mathbf{E}$ and $\pm\mathbf{H}$. The measurements were performed in polarization $\{E_c^\omega, H_a^\omega\}$ at $T = 3.5$ K, in electric field $E_a = \pm 3$ kV/cm and in magnetic field up to $\mu_0 H_c = \pm 15$ T. There are two different effects that exist when $\pm\mathbf{E}$ and $\pm\mathbf{H}$ are applied. Firstly, the magnetic field induces absorption difference depending on the magnetic field sign, see Fig. 35(a). Secondly, the applied electric field induces absorption difference depending on the $\mathbf{E}$ sign, see Fig. 35(b). Additionally, the absorption difference in $\pm\mathbf{E}$ has a different sign depending on the magnetic field direction, see Fig. 35(b).

We used multi-boson spin-wave theory following Ref. [29] to calculate the susceptibilities of spin-wave excitations of Ba$_2$CoGe$_2$O$_7$ for the configuration of applied fields $\mathbf{H} \parallel \mathbf{c}$, $\mathbf{E} \parallel \mathbf{a}$, and in polarization $\{\mathbf{H}^\omega \parallel \mathbf{a}, \mathbf{E}^\omega \parallel \mathbf{c}\}$. We considered the Hamiltonian, Eq. (106), with-

out the weak Dzyaloshinskii-Moriya interaction. The magnetic susceptibility χ_{aa}^{mm}, plotted in Fig. 35(c), was calculated using the transition matrix elements of spin operators, $|\langle 0|\hat{S}^{\alpha}|n\rangle|^2$, between the ground state $|0\rangle$ and the excited state $|n\rangle$, where $\alpha = a, b$ or c. The ME susceptibility, $\chi_{ca}^{\mathrm{em}} \propto \langle 0|P^c|n\rangle\langle n|S^a|0\rangle$, where the electric polarization operator $\hat{P}^{\alpha}$ is expressed in spin operators, see Eq. (107). The result of calculation is shown in Fig. 35(d).

The lower energy mode, No. 1, has finite magnetic susceptibility χ_{aa}^{mm} only in domains II and IV, Fig. 35(c). The spin stretching modes No. 2 and No. 4 have finite χ_{aa}^{mm} in domains I and III and as well in II and IV. Both these modes show finite ME susceptibility χ_{ca}^{em} whereas the sign of the χ_{ca}^{em} depends on the sign of electric and magnetic field allowing the switching between domain I and III. These finite dynamic ME susceptibilities predict the NDD of spin wave excitations by ME sum rule Eq. (39) which is also captured by the experiment shown in Fig. 35(b). More comprehensive and detailed analysis of the theory results, symmetry considerations and experimental observations can be found in Ref. II.

We have been one of the first to demonstrate electric-field switching of AFM domain population which we detected as a NDD effect of ME excitations. From the application point of view the results of Ref. II are remarkable for the electric field switching of absorption. However, the NDD effect is present only below 6.7 K and the switching is not ideal. The level of NDD switching depends on the history of electric field sweeps and there is a small remnant finite absorption difference, i.e hysteresis, see Ref. II Fig.3 and Ref. II Supplemental Material. Although these factors hinder the usefulness $Ba_2CoGe_2O_7$, our study is an important step forward in understanding how to design electrically switchable magnetic domains and light diodes.

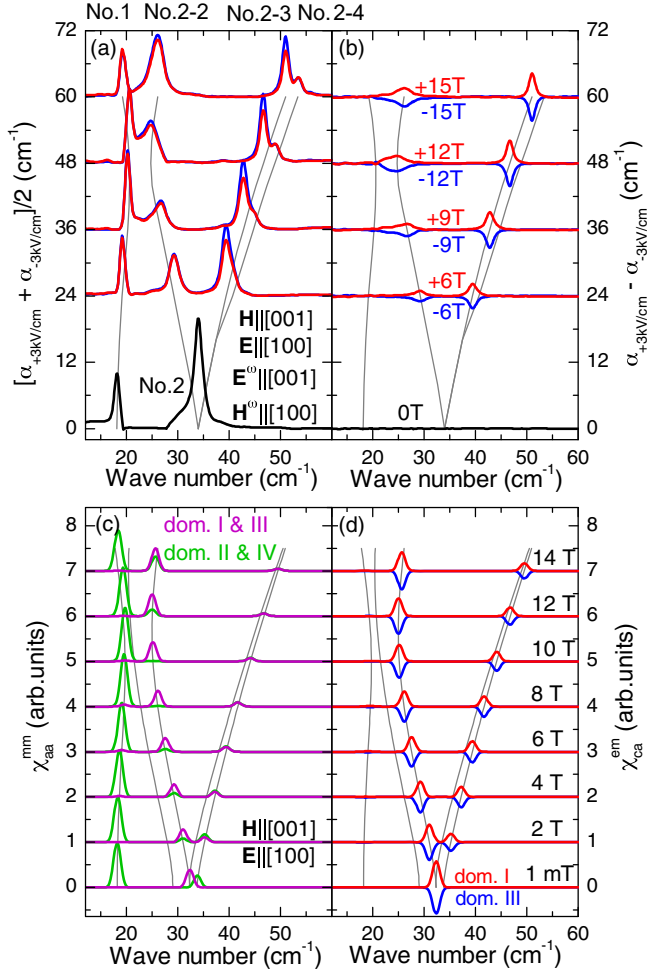Figure 35: Ba$_2$CoGe$_2$O$_7$ NDD effect of spin-wave resonances in $\pm\mathbf{E}$ and $\pm\mathbf{H}$ compared to theory at $T = 3.5$ K. The spectra are recorded in polarization $\{E_c^\omega, H_a^\omega\}$, in electric field $E_a = \pm 3$ kV/cm and in magnetic field up to $\mu_0 H_c = \pm 15$ T. (a) The THz absorption spectra averaged for opposite electric field directions, $(\alpha_{+E} + \alpha_{-E})/2$, in magnetic field $+\mathbf{H}$, red line, and in $-\mathbf{H}$, blue line. (b) The electric-field induced change of absorption spectra in $\pm\mathbf{H}$ presented as the difference of the absorption spectra $(\alpha_{+E} - \alpha_{-E})$. (c) The magnetic susceptibility, χ_{aa}^{mm}, in different domains calculated using the multiboson spin-wave theory. The domains I and III are indicated by violet line while domains II and IV by green line. (d) The ME susceptibility, χ_{ca}^{em}, in domains I (red) and III (blue) calculated using the multiboson spin-wave theory. Grey lines indicate the resonance energies in magnetic field. Spectra on each panel is shifted proportionally to the absolute value of magnetic field. This figure is reproduced from Ref. II.

5 Summary

We fulfilled the goals to investigate the magnetic field dependence of THz absorption spectra and magnetoelectric coupling of the spin-waves in orthophosphates $LiNiPO_4$ and $LiFePO_4$ and to demonstrate the electric field switching of non-reciprocal directional dichroism (NDD) of magnetoelectric resonances in $Ba_2CoGe_2O_7$.

Next, are the main results of this thesis:

1. We measured the THz absorption spectra and magnetization in various magnetically ordered phases in $LiNiPO_4$. With THz absorption spectroscopy we found magnons, a two-magnon continuum, an electromagnon, a magnetoelectric resonance and a two-magnon ME resonance. We constructed a mean-field model to describe the magnetic field dependence of the four magnon modes and the magnetization in the commensurate magnetic phases. With this model we refined the values of exchange couplings, single-ion anisotropies, and Dzyaloshinskii-Moriya interaction. The two-magnon excitations were described by calculating the magnon density of states in magnetic field which revealed additional exchange interactions that are usually silent in THz spectroscopy.

2. We measured the THz absorption spectra in magnetic field up to 32 T and magnetization in pulsed magnetic field up to 130 T in $LiFePO_4$. The spin-wave resonances in THz absorption spectra were identified as magnons, electromagnons and magnetoelectric resonances. With the mean-field model we described the magnetization and the magnetic field dependence of four magnon modes. From the model fit we could adjust the values of exchange couplings, single-ion anisotropies, and Dzyaloshinskii-Moriya interaction. We suggest, based on the magnetic field dependence of spin-wave frequencies and the absorption line shape, that some of the higher energy modes are spin stretching spin-waves or two-magnon excitations.

3. We re-designed the rotational Voigt probe for electric field measurements. With this probe using non-reciprocal light absorption phenomenon of spin-waves we demonstrated novel electric field control of antiferromagnetic domains in $Ba_2CoGe_2O_7$. We confirmed using multi-boson spin-wave theory that the electric-field-induced change of non-reciprocal directional dichroism originates from the change of antiferromagnetic domain population driven by applied electric field.

List of Figures

References

 [1] M. Fiebig, "Revival of magnetoelectric effect," *J. Phys. D: Appl. Phys.*, vol. 38, pp. R123–R152, 2005.

 [2] Y. Tokura, S. Seki, and N. Nagaosa, "Multiferroics of spin origin," *Rep. Progr. Phys.*, vol. 77, no. 7, p. 076501, 2014.

 [3] R. Ramesh and S. Manipatruni, "Electric field control of magnetism," *Proc. R. Soc. A*, vol. 477, p. 20200942, July 2021.

 [4] C. Chappert, A. Fert, and F. N. V. Dau, "The emergence of spin electronics in data storage," *Nat. Mater.*, vol. 6, pp. 813–823, nov 2007.

 [5] M. Gajek, M. Bibes, S. Fusil, K. Bouzehouane, J. Fontcuberta, A. Barthélémy, and A. Fert, "Tunnel junctions with multiferroic barriers," *Nat. Mater.*, vol. 6, pp. 296–302, Apr. 2007.

 [6] K. Wang, J.-M. Liu, and Z. Ren, "Multiferroicity: the coupling between magnetic and polarization orders," *Adv. Phys.*, vol. 58, no. 4, pp. 321–448, 2009.

 [7] A. Brataas, A. D. Kent, and H. Ohno, "Current-induced torques in magnetic materials," *Nat. Mater.*, vol. 11, pp. 372–381, apr 2012.

 [8] A. D. Kent and D. C. Worledge, "A new spin on magnetic memories," *Nat. Nanotechnol.*, vol. 10, pp. 187–191, mar 2015.

 [9] F. Matsukura, Y. Tokura, and H. Ohno, "Control of magnetism by electric fields," *Nat Nano*, vol. 10, pp. 209–220, Mar. 2015.

[10] P. Wadley, B. Howells, J. Železný, C. Andrews, V. Hills, R. P. Campion, V. Novák, K. Olejník, F. Maccherozzi, S. S. Dhesi, S. Y. Martin, T. Wagner, J. Wunderlich, F. Freimuth, Y. Mokrousov, J. Kuneš, J. S. Chauhan, M. J. Grzybowski, A. W. Rushforth, K. W. Edmonds, B. L. Gallagher, and T. Jungwirth, "Electrical switching of an antiferromagnet," *Science*, vol. 351, pp. 587–590, feb 2016.

[11] J. T. Heron, J. L. Bosse, Q. He, Y. Gao, M. Trassin, L. Ye, J. D. Clarkson, C. Wang, J. Liu, S. Salahuddin, D. C. Ralph, D. G. Schlom, J. Iniguez, B. D. Huey, and R. Ramesh, "Deterministic switching of ferromagnetism at room temperature using an electric field," *Nature*, vol. 516, pp. 370–373, Dec. 2014.

[12] E. Parsonnet, L. Caretta, V. Nagarajan, H. Zhang, H. Taghinejad, P. Behera, X. Huang, P. Kavle, A. Fernandez, D. Nikonov, H. Li, I. Young, J. Analytis, and R. Ramesh, "Nonvolatile electric field control of thermal magnons in the absence of an applied magnetic field," *Phys. Rev. Lett.*, vol. 129, p. 087601, aug 2022.

[13] F. Bloch, "Zur theorie des ferromagnetismus," *Z. Für Phys.*, vol. 61, pp. 206–219, mar 1930.

[14] A. Pimenov, A. A. Mukhin, V. Y. Ivanov, V. D. Travkin, A. M. Balbashov, and A. Loidl, "Possible evidence for electromagnons in multiferroic manganites," *Nat. Phys.*, vol. 2, pp. 97–100, 2006.

[15] I. Kézsmárki, N. Kida, H. Murakawa, S. Bordács, Y. Onose, and Y. Tokura, "Enhanced directional dichroism of terahertz light in resonance with magnetic excitations of the multiferroic $Ba_2CoGe_2O_7$ oxide compound," *Phys. Rev. Lett.*, vol. 106, p. 057403, Feb 2011.

[16] Y. Takahashi, R. Shimano, Y. Kaneko, H. Murakawa, and Y. Tokura, "Magnetoelectric resonance with electromagnons in a perovskite helimagnet," *Nat. Phys.*, vol. 8, pp. 121–125, 2012.

[17] T. Arima, "Magneto-electric optics in non-centrosymmetric ferromagnets," *J. Phys.: Condens. Matter*, vol. 20, no. 43, p. 434211, 2008.

[18] I. Kézsmárki, D. Szaller, S. Bordács, V. Kocsis, Y. Tokunaga, Y. Taguchi, H. Murakawa, Y. Tokura, H. Engelkamp, T. Rõõm, and U. Nagel, "One-way transparency of four-coloured spin-wave excitations in multiferroic materials," *Nat Commun*, vol. 5, p. 3203, 2014.

[19] S. Miyahara and N. Furukawa, "Theory of magnetoelectric resonance in two-dimensional $S = 3/2$ antiferromagnet $Ba_2CoGe_2O_7$ via spin-dependent metal-ligand hybridization mechanism," *J. Phys. Soc. Jpn.*, vol. 80, no. 7, p. 073708, 2011.

[20] S. Bordács, I. Kézsmárki, D. Szaller, L. Demkó, N. Kida, H. Murakawa, Y. Onose, R. Shimano, T. Rõõm, U. Nagel, S. Miyahara, N. Furukawa, and Y. Tokura, "Chirality of matter shows up via spin excitations," *Nat. Phys.*, vol. 8, pp. 734–738, 2012.

[21] S. Bordács, V. Kocsis, Y. Tokunaga, U. Nagel, T. Rõõm, Y. Takahashi, Y. Taguchi, and Y. Tokura, "Unidirectional terahertz light absorption in the pyroelectric ferrimagnet $CaBaCo_4O_7$," *Phys. Rev. B*, vol. 92, p. 214441, Dec 2015.

[22] I. Kézsmárki, U. Nagel, S. Bordács, R. S. Fishman, J. H. Lee, H. T. Yi, S.-W. Cheong, and T. Rõõm, "Optical diode effect at spin-wave excitations of the room-temperature multiferroic $BiFeO_3$," *Phys. Rev. Lett.*, vol. 115, p. 127203, Sep 2015.

[23] J. Viirok, U. Nagel, T. Rõõm, D. G. Farkas, P. Balla, D. Szaller, V. Kocsis, Y. Tokunaga, Y. Taguchi, Y. Tokura, B. Bernáth, D. L. Kamenskyi, I. Kézsmárki, S. Bordács, and K. Penc, "Directional dichroism in the paramagnetic state of multiferroics: A case study of infrared light absorption in $Sr_2CoSi_2O_7$ at high temperatures," *Phys. Rev. B*, vol. 99, p. 014410, Jan 2019.

[24] A. M. Kuzmenko, D. Szaller, T. Kain, V. Dziom, L. Weymann, A. Shuvaev, A. Pimenov, A. A. Mukhin, V. Y. Ivanov, I. A. Gudim, L. N. Bezmaternykh, and A. Pimenov, "Switching of magnons by electric and magnetic fields in multiferroic borates," *Phys. Rev. Lett.*, vol. 120, p. 027203, Jan 2018.

[25] S. Kimura, M. Matsumoto, and H. Tanaka, "Electrical switching of the nonreciprocal directional microwave response in a triplon Bose-Einstein condensate," *Phys. Rev. Lett.*, vol. 124, p. 217401, May 2020.

[26] J. Vít, J. Viirok, L. Peedu, T. Rõõm, U. Nagel, V. Kocsis, Y. Tokunaga, Y. Taguchi, Y. Tokura, I. Kézsmárki, P. Balla, K. Penc, J. Romhányi, and S. Bordács, "In situ electric-field control of THz nonreciprocal directional dichroism in the multiferroic $Ba_2CoGe_2O_7$," *Phys. Rev. Lett.*, vol. 127, p. 157201, oct 2021.

[27] V. Kocsis, K. Penc, T. Rõõm, U. Nagel, J. Vít, J. Romhányi, Y. Tokunaga, Y. Taguchi, Y. Tokura, I. Kézsmárki, and S. Bordács, "Identification of antiferromagnetic domains via the optical magnetoelectric effect," *Phys. Rev. Lett.*, vol. 121, p. 057601, Aug 2018.

[28] R. S. Fishman, J. A. Fernandez-Baca, and T. Rõõm, *Spin-Wave Theory and its Applications to Neutron Scattering and THz Spectroscopy*. 1210 Fifth Avenue, Suite 250, San Rafael, CA, 94901, USA: IOP Concise Physics, Morgan and Claypool Publishers, 2018.

[29] K. Penc, J. Romhányi, T. Rõõm, U. Nagel, A. Antal, T. Fehér, A. Jánossy, H. Engelkamp, H. Murakawa, Y. Tokura, D. Szaller, S. Bordács, and I. Kézsmárki, "Spin-stretching modes in anisotropic magnets: Spin-wave excitations in the multiferroic $Ba_2CoGe_2O_7$," *Phys. Rev. Lett.*, vol. 108, p. 257203, Jun 2012.

[30] X. Bai, S.-S. Zhang, Z. Dun, H. Zhang, Q. Huang, H. Zhou, M. B. Stone, A. I. Kolesnikov, F. Ye, C. D. Batista, and M. Mourigal, "Hybridized quadrupolar excitations in the spin-anisotropic frustrated magnet FeI_2," *Nat. Phys.*, vol. 17, pp. 467–472, jan 2021.

[31] A. Legros, S.-S. Zhang, X. Bai, H. Zhang, Z. Dun, W. A. Phelan, C. D. Batista, M. Mourigal, and N. Armitage, "Observation of 4- and 6-magnon bound states in the spin-anisotropic frustrated antiferromagnet FeI_2," *Phys. Rev. Lett.*, vol. 127, p. 267201, dec 2021.

[32] V. I. Fomin, V. P. Gnezdilov, V. S. Kurnosov, A. V. Peschanskii, A. V. Yeremenko, H. Schmid, J.-P. Rivera, and S. Gentil, "Raman scattering in a $LiNiPO_4$ single crystal," *Low Temp. Phys.*, vol. 28, no. 3, pp. 203–209, 2002.

[33] W. Paraguassu, P. T. C. Freire, V. Lemos, S. M. Lala, L. A. Montoro, and J. M. Rosolen, "Phonon calculation on olivine-like $LiMPO_4$ ($M =$ Ni, Co, Fe) and Raman scattering of the iron-containing compound," *J. Raman Spectrosc.*, vol. 36, no. 3, pp. 213–220, 2005.

[34] T. Stanislavchuk, D. S. Middlemiss, J. S. Syzdek, Y. Janssen, R. Basistyy, A. A. Sirenko, P. G. Khalifah, C. Grey, and R. Kostecki, "Infrared-active optical phonons in $LiFePO_4$ single crystals," *J. Appl. Phys.*, vol. 122, p. 045107, 07 2017.

[35] J. Werner, C. Neef, C. Koo, S. Zvyagin, A. Ponomaryov, and R. Klingeler, "Antisite disorder in the battery material $LiFePO_4$," *Phys. Rev. Materials*, vol. 4, p. 115403, nov 2020.

[36] J. Werner, C. Neef, C. Koo, A. Ponomaryov, S. Zvyagin, and R. Klingeler, "Exceptional field dependence of antiferromagnetic magnons in $LiFePO_4$," *Phys. Rev. B*, vol. 103, p. 174406, may 2021.

[37] T. B. S. Jensen, N. B. Christensen, M. Kenzelmann, H. M. Rønnow, C. Niedermayer, N. H. Andersen, K. Lefmann, M. Jiménez-Ruiz, F. Demmel, J. Li, J. L. Zarestky, and D. Vaknin, "Anomalous spin waves and the commensurate-incommensurate magnetic phase transition in $LiNiPO_4$," *Phys. Rev. B*, vol. 79, p. 092413, Mar 2009.

[38] J. Li, T. B. S. Jensen, N. H. Andersen, J. L. Zarestky, R. W. McCallum, J.-H. Chung, J. W. Lynn, and D. Vaknin, "Tweaking the spin-wave dispersion and suppressing the incommensurate phase in $LiNiPO_4$ by iron substitution," *Phys. Rev. B*, vol. 79, no. 17, p. 174435, 2009.

[39] R. Toft-Petersen, J. Jensen, T. B. S. Jensen, N. H. Andersen, N. B. Christensen, C. Niedermayer, M. Kenzelmann, M. Skoulatos, M. D. Le, K. Lefmann, S. R. Hansen, J. Li, J. L. Zarestky, and D. Vaknin, "High-field magnetic phase transitions and spin excitations in magnetoelectric $LiNiPO_4$," *Phys. Rev. B*, vol. 84, p. 054408, Aug 2011.

[40] J. Li, V. O. Garlea, J. L. Zarestky, and D. Vaknin, "Spin-waves in antiferromagnetic single-crystal $LiFePO_4$," *Phys. Rev. B*, vol. 73, p. 024410, Jan 2006.

[41] R. Toft-Petersen, M. Reehuis, T. B. S. Jensen, N. H. Andersen, J. Li, M. D. Le, M. Laver, C. Niedermayer, B. Klemke, K. Lefmann, and D. Vaknin, "Anomalous magnetic structure and spin dynamics in magnetoelectric $LiFePO_4$," *Phys. Rev. B*, vol. 92, p. 024404, Jul 2015.

[42] Y. Yiu, M. D. Le, R. Toft-Petersen, G. Ehlers, R. J. McQueeney, and D. Vaknin, "Hybrid excitations due to crystal field, spin-orbit coupling, and spin waves in $LiFePO_4$," *Phys. Rev. B*, vol. 95, p. 104409, Mar 2017.

[43] V. Kocsis, S. Bordács, Y. Tokunaga, J. Viirok, L. Peedu, T. Rõõm, U. Nagel, Y. Taguchi, Y. Tokura, and I. Kézsmárki, "Magnetoelectric spectroscopy of spin excitations in $LiCoPO_4$," *Phys. Rev. B*, vol. 100, p. 155124, Oct 2019.

[44] J. Werner, S. Sauerland, C. Koo, C. Neef, A. Pollithy, Y. Skourski, and R. Klingeler, "High magnetic field phase diagram and failure of the magnetic Grüneisen scaling in $LiFePO_4$," *Phys. Rev. B*, vol. 99, p. 214432, Jun 2019.

[45] E. Fogh, T. Kihara, R. Toft-Petersen, M. Bartkowiak, Y. Narumi, O. Prokhnenko, A. Miyake, M. Tokunaga, K. Oikawa, M. K. Sørensen, J. C. Dyrnum, H. Grimmer, H. Nojiri, and N. B. Christensen, "Magnetic structures and quadratic magnetoelectric effect in $LiNiPO_4$ beyond 30T," *Phys. Rev. B*, vol. 101, p. 024403, Jan 2020.

[46] S. Reschke, D. G. Farkas, A. Strinić, S. Ghara, K. Guratinder, O. Zaharko, L. Prodan, V. Tsurkan, D. Szaller, S. Bordács, J. Deisenhofer, and I. Kézsmárki, "Confirming the trilinear form of the optical magnetoelectric effect in the polar honeycomb antiferromagnet $Co_2Mo_3O_8$," *npj Quantum Materials*, vol. 7, jan 2022.

[47] H. Schmid, "Multi-ferroic magnetoelectrics," *Ferroelectrics*, vol. 162, no. 1, p. 317, 1994.

[48] N. A. Spaldin, S.-W. Cheong, and R. Ramesh, "Multiferroics: Past, present, and future," *Phys. Today*, vol. 63, no. 10, pp. 38–43, 2010.

[49] M. Fiebig, "Condensed-matter physics: Multitasking materials from atomic templates," *Nature*, vol. 537, pp. 499–500, Sept. 2016.

[50] N. Hur, S. Park, P. A. Sharma, J. S. Ahn, S. Guha, and S.-W. Cheong, "Electric polarization reversal and memory in a multiferroic material induced by magnetic fields," *Nature*, vol. 429, pp. 392–395, may 2004.

[51] S.-W. Cheong and M. Mostovoy, "Multiferroics: a magnetic twist for ferroelectricity," *Nature Mater.*, vol. 6, pp. 13–20, 2007.

[52] R. Ramesh, R. and N. A. Spaldin, "Multiferroics: progress and prospects in thin films," *Nat. Mater.*, vol. 6, p. 21, 2007.

[53] C.-W. Nan, M. I. Bichurin, S. Dong, D. Viehland, and G. Srinivasan, "Multiferroic magnetoelectric composites: Historical perspective, status, and future directions," *J Appl Phys*, vol. 103, p. 031101, feb 2008.

[54] S. Manipatruni, D. E. Nikonov, and I. A. Young, "Beyond CMOS computing with spin and polarization," *Nat. Phys.*, vol. 14, pp. 338–343, Apr. 2018.

[55] S. Manipatruni, D. E. Nikonov, C.-C. Lin, T. A. Gosavi, H. Liu, B. Prasad, Y.-L. Huang, E. Bonturim, R. Ramesh, and I. A. Young, "Scalable energy-efficient magnetoelectric spin-orbit logic," *Nature*, vol. 565, pp. 35–42, Jan. 2019.

[56] N. A. Spaldin and R. Ramesh, "Advances in magnetoelectric multiferroics," *Nat. Mater.*, vol. 18, pp. 203–212, Mar. 2019.

[57] B. R. Cooper, "Spin waves and magnetic resonance in rare-earth metals: Thermal, applied-field, and magnetoelastic effects," *Phys. Rev.*, vol. 169, pp. 281–294, May 1968.

[58] W. Eerenstein, N. D. Mathur, and J. F. Scott, "Multiferroic and magnetoelectric materials," *Nature*, vol. 442, pp. 759–765, 2006.

[59] N. A. Hill, "Why are there so few magnetic ferroelectrics?," *J. Phys. Chem. B*, vol. 104, pp. 6694–6709, 2000.

[60] D. Khomskii, "Classifying multiferroics: Mechanisms and effects," *Physics*, vol. 2, p. 20, Mar 2009.

[61] N. A. Spaldin and M. Fiebig, "The origin of ferroelectricity in magnetoelctric $YMnO_3$," *Science*, vol. 309, pp. 391–392, 2005.

[62] K. Buschow, *Handbook of Magnetic Materials*, vol. 19 of *Handbook of Magnetic Materials*. Elsevier Science, 2011.

[63] B. B. Van Aken, J.-P. Rivera, H. Schmid, and M. Fiebig, "Observation of ferrotoroidic domains," *Nature*, vol. 449, pp. 702–705, 2007.

[64] T. B. S. Jensen, N. B. Christensen, M. Kenzelmann, H. M. Rønnow, C. Niedermayer, N. H. Andersen, K. Lefmann, J. Schefer, M. Zimmermann, J. Li, J. L. Zarestky, and D. Vaknin, "Field-induced magnetic phases and electric polarization in $LiNiPO_4$," *Phys. Rev. B*, vol. 79, p. 092412, Mar 2009.

[65] R. Toft-Petersen, E. Fogh, T. Kihara, J. Jensen, K. Fritsch, J. Lee, G. E. Granroth, M. B. Stone, D. Vaknin, H. Nojiri, and N. B. Christensen, "Field-induced reentrant magnetoelectric phase in $LiNiPO_4$," *Phys. Rev. B*, vol. 95, p. 064421, Feb 2017.

[66] H. Murakawa, Y. Onose, S. Miyahara, N. Furukawa, and Y. Tokura, "Comprehensive study of the ferroelectricity induced by the spin-dependent d-p hybridization mechanism in $Ba_2XGe_2O_7$ ($X =$ Mn, Co, and Cu)," *Phys. Rev. B*, vol. 85, p. 174106, May 2012.

[67] B. B. van Aken, T. T. M. Palstra, A. Filippetti, and N. A. Spaldin, "The origin of ferroelectricity in magnetoelctric $YMnO_3$," *Nat. Mater.*, vol. 3, pp. 164–170, feb 2004.

[68] I. A. Sergienko and E. Dagotto, "Role of the Dzyaloshinskii-Moriya interaction in multiferroic perovskites," *Phys. Rev. B*, vol. 73, no. 9, p. 094434, 2006.

[69] M. Fiebig, T. Lottermoser, D. Meier, and M. Trassin, "The evolution of multiferroics," *Nat. Rev. Mater.*, vol. 1, p. 16046, July 2016.

[70] D. Lebeugle, D. Colson, A. Forget, and M. Viret, "Very large spontaneous electric polarization in $BiFeO_3$ single crystals at room temperature and its evolution under cycling fields," *Appl. Phys. Lett.*, vol. 91, p. 022907, 2007.

[71] J. Moreau, C. Michel, R. Gerson, and W. James, "Ferroelectric $BiFeO_3$ X-ray and neutron diffraction study," *J. Phys. Chem. Solids*, vol. 32, no. 6, pp. 1315 – 1320, 1971.

[72] T. Ito, T. Ushiyama, Y. Yanagisawa, R. Kumai, and Y. Tomioka, "Growth of highly insulating bulk single crystals of multiferroic $BiFeO_3$ and their inherent internal strains in the domain-switching process," *Cryst. Growth Des.*, vol. 11, no. 11, pp. 5139–5143, 2011.

[73] W. Koehler, H. Yakel, E. Wollan, and J. Cable, "A note on the magnetic structures of rare earth manganese oxides," *Phys. Lett.*, vol. 9, pp. 93–95, apr 1964.

[74] T. Kimura, S. Ishihara, H. Shintani, T. Arima, K. T. Takahashi, K. Ishizaka, and Y. Tokura, "Distorted perovskite with e_g^1 configuration as a frustrated spin system," *Phys. Rev. B*, vol. 68, no. 6, p. 060403, 2003.

[75] M. Eibschütz, H. Guggenheim, S. Wemple, I. Camlibel, and M. DiDomenico, "Ferroelectricity in $BaM^{2+}F_4$," *Phys. Lett. A*, vol. 29, pp. 409–410, jun 1969.

[76] L. Holmes, M. Eibschütz, and H. Guggenheim, "Spin-flop transition in $BaMnF_4$," *Solid State Commun.*, vol. 7, pp. 973–976, jul 1969.

[77] D. E. Cox, M. Eibschütz, H. J. Guggenheim, and L. Holmes, "Neutron diffraction study of the magnetic structure of $BaNiF_4$," *J. Appl. Phys.*, vol. 41, pp. 943–945, mar 1970.

[78] N. Ikeda, K. Kohn, N. Myouga, E. Takahashi, H. Kitôh, and S. Takekawa, "Charge frustration and dielectric dispersion in $LuFe_2O_4$," *J. Phys. Soc. Jpn.*, vol. 69, pp. 1526–1532, may 2000.

[79] N. Ikeda, H. Ohsumi, K. Ohwada, K. Ishii, T. Inami, K. Kakurai, Y. Murakami, K. Yoshii, S. Mori, Y. Horibe, and H. Kitô, "Ferroelectricity from iron valence ordering in the charge-frustrated system $LuFe_2O_4$," *Nature*, vol. 436, pp. 1136–1138, aug 2005.

[80] C. Jooss, L. Wu, T. Beetz, R. F. Klie, M. Beleggia, M. A. Schofield, S. Schramm, J. Hoffmann, and Y. Zhu, "Polaron melting and ordering as key mechanisms for colossal resistance effects in manganites," *Proc. Natl. Acad. Sci.*, vol. 104, pp. 13597–13602, aug 2007.

[81] M. Angst, "Ferroelectricity from iron valence ordering in rare earth ferrites?," *physica status solidi (RRL) - Rapid Research Letters*, vol. 7, pp. 383–400, apr 2013.

[82] S. M. Gaw, H. J. Lewtas, D. F. McMorrow, J. Kulda, R. A. Ewings, T. G. Perring, R. A. McKinnon, G. Balakrishnan, D. Prabhakaran, and A. T. Boothroyd, "Magnetic excitation spectrum of $LuFe_2O_4$ measured with inelastic neutron scattering," *Phys. Rev. B*, vol. 91, p. 035103, Jan 2015.

[83] I. A. Sergienko, C. Şen, and E. Dagotto, "Ferroelectricity in the magnetic E-phase of orthorhombic perovskites," *Phys. Rev. Lett.*, vol. 97, no. 22, p. 227204, 2006.

[84] S. Dong, H. Xiang, and E. Dagotto, "Magnetoelectricity in multiferroics: a theoretical perspective," *Natl. Sci. Rev.*, vol. 6, pp. 629–641, 02 2019.

[85] S. Ishiwata, Y. Kaneko, Y. Tokunaga, Y. Taguchi, T.-h. Arima, and Y. Tokura, "Perovskite manganites hosting versatile multiferroic phases with symmetric and antisymmetric exchange strictions," *Phys. Rev. B*, vol. 81, p. 100411, Mar 2010.

[86] Y. Noda, H. Kimura, M. Fukunaga, S. Kobayashi, I. Kagomiya, and K. Kohn, "Magnetic and ferroelectric properties of multiferroic RMn_2O_5," *J. Phys.: Condens. Matter*, vol. 20, p. 434206, oct 2008.

[87] R. D. Johnson, K. Cao, F. Giustino, and P. G. Radaelli, "$CaBaCo_4O_7$: A ferrimagnetic pyroelectric," *Phys. Rev. B*, vol. 90, p. 045129, Jul 2014.

[88] H. Katsura, N. Nagaosa, and A. V. Balatsky, "Spin current and magnetoelectric effect in noncollinear magnets," *Phys. Rev. Lett.*, vol. 95, p. 057205, Jul 2005.

[89] T. Kimura, T. Goto, H. Shintani, K. Ishizaka, T. Arima, and Y. Y. Tokura, "Magnetic control of ferroelectric polarization," *Nature*, vol. 426, p. 55, 2003.

[90] T. Goto, T. Kimura, G. Lawes, A. P. Ramirez, and Y. Tokura, "Ferroelectricity and giant magnetocapacitance in perovskite rare-earth manganites," *Phys. Rev. Lett.*, vol. 92, p. 257201, Jun 2004.

[91] M. Kenzelmann, A. B. Harris, S. Jonas, C. Broholm, J. Schefer, S. B. Kim, C. L. Zhang, S.-W. Cheong, O. P. Vajk, and J. W. Lynn, "Magnetic inversion symmetry breaking and ferroelectricity in $TbMnO_3$," *Phys. Rev. Lett.*, vol. 95, no. 8, p. 087206, 2005.

[92] M. Akaki, J. Tozawa, D. Akahoshi, and H. Kuwahare, "Gigantic magnetoelectric effect caused by magnetic-field-induced canted antiferromagnetic-paramagnetic transition in quasi-two-dimensional $Ca_2CoSi_2O_7$ crystal," *Appl. Phys. Lett.*, vol. 94, p. 212904, 2009.

[93] M. Akaki, H. Iwamoto, T. Kihara, M. Tokunaga, and H. Kuwahara, "Multiferroic properties of an Åkermanite $Sr_2CoSi_2O_7$ single crystal in high magnetic fields," *Phys. Rev. B*, vol. 86, p. 060413, Aug 2012.

[94] H. T. Yi, Y. J. Choi, S. Lee, and S.-W. Cheong, "Multiferroicity in the square-lattice antiferromagnet of $Ba_2CoGe_2O_7$," *Appl. Phys. Lett.*, vol. 92, p. 212904, may 2008.

[95] H. Murakawa, Y. Onose, S. Miyahara, N. Furukawa, and Y. Tokura, "Ferroelectricity induced by spin-dependent metal-ligand hybridization in $Ba_2CoGe_2O_7$," *Phys. Rev. Lett.*, vol. 105, p. 137202, Sep 2010.

[96] P. Curie, "Sur la symétrie dans les phénomènes physiques, symétrie d'un champ électrique et d'un champ magnétique," *Journal de Physique Théorique et Appliquée*, vol. 3, no. 1, pp. 393–415, 1894.

[97] D. N. Astrov, "The magnetoelectric effect in antiferromagnetics," *JETP*, vol. 38, pp. 984–985, Sept. 1960.

[98] N. Pereira, A. C. Lima, S. Lanceros-Mendez, and P. Martins, "Magnetoelectrics: Three centuries of research heading towards the 4.0 industrial revolution," *Materials*, vol. 13, p. 4033, sep 2020.

[99] J.-P. Rivera, "The linear magnetoelectric effect in $LiCoPO_4$ revisited," *Ferroelectrics*, vol. 161, no. 1, pp. 147–164, 1994.

[100] D. Szaller, S. Bordács, V. Kocsis, T. Rõõm, U. Nagel, and I. Kézsmárki, "Effect of spin excitations with simultaneous magnetic- and electric-dipole character on the static magnetoelectric properties of multiferroic materials," *Phys. Rev. B*, vol. 89, p. 184419, May 2014.

[101] S. Miyahara and N. Furukawa, "Theory of magneto-optical effects in helical multiferroic materials via toroidal magnon excitation," *Phys. Rev. B*, vol. 89, p. 195145, May 2014.

[102] R. Kubo, "Statistical-mechanical theory of irreversible processes. I. General theory and simple applications to magnetic and conduction problems," *J. Phys. Soc. Jpn.*, vol. 12, no. 6, pp. 570–586, 1957.

[103] D. Szaller, "Optical study of spin excitations in multiferroic crystals," 2017.

[104] L. D. Barron, *Molecular Light Scattering and Optical Activity*. Cambridge University Press, 2 ed., 2004.

[105] L. Landau and E. Lifshitz, "On the theory of the dispersion of magnetic permeability in ferromagnetic bodies," *Phys. Z. Sowjetunion*, vol. 8, no. 153, pp. 101–114, 1935.

[106] T. L. Gilbert, "A phenomenological theory of damping in ferromagnetic materials," *IEEE Trans. Magn.*, vol. 40, pp. 3443–3449, Nov 2004.

[107] A. Aharoni, *Introduction to the Theory of Ferromagnetism*. International Series of Monographs on Physics, Oxford University Press, 2nd ed., 2001.

[108] J. Mallinson, "On damped gyromagnetic precession," *IEEE Trans. Magn.*, vol. 23, pp. 2003–2004, jul 1987.

[109] F. J. Dyson, "General theory of spin-wave interactions," *Phys. Rev.*, vol. 102, pp. 1217–1230, jun 1956.

[110] F. Bass and M. Kaganov, "Raman scattering of electromagnetic waves in ferromagnetic dielectrics," *JETP*, vol. 10, no. 5, p. 986, 1960.

[111] R. Elliott and R. Loudon, "The possible observation of electronic Raman transitions in crystals," *Phys. Lett. A*, vol. 3, pp. 189–191, jan 1963.

[112] J. V. KRANENDONK and J. H. V. VLECK, "Spin waves," *Rev. Mod. Phys.*, vol. 30, pp. 1–23, jan 1958.

[113] R. Silberglitt and J. B. Torrance, "Effect of single-ion anisotropy on two-spin-wave bound state in a Heisenberg ferromagnet," *Phys. Rev. B*, vol. 2, pp. 772–778, Aug 1970.

[114] P. L. Richards, "Far infrared absorption by two magnon excitations in antiferromagnets," *J. Appl. Phys.*, vol. 38, no. 3, pp. 1500–1504, 1967.

[115] P. A. Fleury and R. Loudon, "Scattering of light by one- and two-magnon excitations," *Phys. Rev.*, vol. 166, pp. 514–530, Feb 1968.

[116] W. H. Weber and R. Merlin, eds., *Raman Scattering in Materials Science*. Springer Berlin Heidelberg, 2000.

[117] R. Loudon, "Theory of infra-red and optical spectra of antiferromagnets," *Adv. Phys.*, vol. 17, no. 66, pp. 243–280, 1968.

[118] J. Romhányi and K. Penc, "Multiboson spin-wave theory for $Ba_2CoGe_2O_7$: A spin-3/2 easy-plane Néel antiferromagnet with strong single-ion anisotropy," *Phys. Rev. B*, vol. 86, p. 174428, Nov 2012.

[119] R. S. Fishman, "Pinning, rotation, and metastability of $BiFeO_3$ cycloidal domains in a magnetic field," *Phys. Rev. B*, vol. 97, p. 014405, Jan 2018.

[120] K. Katsumata, H. Yamaguchi, M. Hagiwara, M. Tokunaga, H.-J. Mikeska, P. Goy, and M. Gross, "Single-ion magnon bound states in an antiferromagnet with strong uniaxial anisotropy," *Phys. Rev. B*, vol. 61, pp. 11632–11636, May 2000.

[121] A. Fert, D. Bertrand, J. Leotin, J. Ousset, J. Magariño, and J. Tuchendler, "Excitation of two spin deviations by far infrared absorption in FeI_2," *Solid State Commun.*, vol. 26, no. 11, pp. 693 – 696, 1978.

[122] D. Petitgrand, A. Brun, and P. Meyer, "Magnetic field dependence of spin waves and two magnon bound states in FeI_2," *J. Magn. Magn. Mater.*, vol. 15, pp. 381 – 382, 1980.

[123] D. Petitgrand, B. Hennion, and C. Escribe, "Neutron inelastic scattering from magnetic excitations of FeI_2," *J Magn Magn Mater*, vol. 14, pp. 275–276, dec 1979.

[124] M. Orendáč, S. Zvyagin, A. Orendáčová, M. Sieling, B. Lüthi, A. Feher, and M. W. Meisel, "Single-ion bound states in S= 1 Heisenberg antiferromagnetic chains with planar anisotropy and subcritical exchange coupling," *Phys Rev B*, vol. 60, pp. 4170–4175, aug 1999.

[125] M. Akaki, D. Yoshizawa, A. Okutani, T. Kida, J. Romhányi, K. Penc, and M. Hagiwara, "Direct observation of spin-quadrupolar excitations in $Sr_2CoSi_2O_7$ by high-field electron spin resonance," *Phys. Rev. B*, vol. 96, p. 214406, Dec 2017.

[126] A. A. Michelson, "XXVIII. visibility of interference-fringes in the focus of a telescope," *The London, Edinburgh, and Dublin Philosophical Magazine and Journal of Science*, vol. 31, pp. 256–259, mar 1891.

[127] A. Michelson, *Light Waves and Their Uses*. Decennial publications, University of Chicago Press, 1902.

[128] P. Griffiths, J. De Haseth, and J. Winefordner, *Fourier Transform Infrared Spectrometry*. Chemical Analysis: A Series of Monographs on Analytical Chemistry and Its Applications, Wiley, 2007.

[129] C. C. Homes, G. L. Carr, R. P. S. M. Lobo, J. D. LaVeigne, and D. B. Tanner, "Silicon beam splitter for far-infrared and terahertz spectroscopy," *Appl Optics*, vol. 46, p. 7884, nov 2007.

[130] Sciencetech, *Sciencetech SPS-200 Polarizing Roof Mirror Interferometer*, v3.0 ed., 1998.

[131] P. R. Griffiths and C. C. Homes, *Instrumentation for Far-Infrared Spectroscopy*. John Wiley & Sons, Ltd, 2006.

[132] D. Martin and E. Puplett, "Polarised interferometric spectrometry for the millimetre and submillimetre spectrum," *Infrared Phys.*, vol. 10, no. 2, pp. 105 – 109, 1969.

[133] P. Ade, A. Costley, C. Cunningham, C. Mok, G. Neill, and T. Parker, "Free-standing grids wound from 5 μm diameter wire for spectroscopy at far-infrared wavelengths," *Infrared Phys*, vol. 19, pp. 599–601, oct 1979.

[134] C. Mok, W. Chambers, T. Parker, and A. Costley, "The far-infrared performance and application of free-standing grids wound from 5 μm diameter tungsten wire," *Infrared Phys*, vol. 19, pp. 437–442, aug 1979.

[135] J. A. Beunen, A. E. Costley, G. F. Neill, C. L. Mok, T. J. Parker, and G. Tait, "Performance of free-standing grids wound from 10-μm-diameter tungsten wire at submillimeter wavelengths: computation and measurement," *J. Opt. Soc. Am.*, vol. 71, pp. 184–188, Feb 1981.

[136] C. Porter and D. Tanner, "Correction of phase errors in Fourier spectroscopy," *Int. J. Infrared Millimeter Waves*, vol. 4, no. 2, pp. 273–298, 1983.

[137] B. C. Smith, *Fundamentals of Fourier Transform Infrared Spectroscopy*. CRC Press, mar 2011.

[138] L. Mertz, "Auxiliary computation for Fourier spectrometry," *Infrared Phys*, vol. 7, no. 1, pp. 17–23, 1967.

[139] M. L. Forman, "Fast Fourier-transform technique and its application to Fourier spectroscopy," *J. Opt. Soc. Am.*, vol. 56, p. 978, jul 1966.

[140] R. S. Fishman, S. Bordács, V. Kocsis, I. Kézsmárki, J. Viirok, U. Nagel, T. Rõõm, A. Puri, U. Zeitler, Y. Tokunaga, Y. Taguchi, and Y. Tokura, "Competing exchange interactions in multiferroic and ferrimagnetic $CaBaCo_4O_7$," *Phys. Rev. B*, vol. 95, p. 024423, Jan 2017.

[141] S. Wiegers, P. Christianen, H. Engelkamp, A. den Ouden, J. A. Perenboom, U. Zeitler, and J. Maan, "The High Field Magnet Laboratory at Radboud University Nijmegen," *J Low Temp Phys*, vol. 159, pp. 389–393, dec 2009.

[142] C. R. Harris, K. J. Millman, S. J. van der Walt, R. Gommers, P. Virtanen, D. Cournapeau, E. Wieser, J. Taylor, S. Berg, N. J. Smith, R. Kern, M. Picus, S. Hoyer, M. H. van Kerkwijk, M. Brett, A. Haldane, J. Fernández del Río, M. Wiebe, P. Peterson, P. Gérard-Marchant, K. Sheppard, T. Reddy, W. Weckesser, H. Abbasi, C. Gohlke, and T. E. Oliphant, "Array programming with NumPy," *Nature*, vol. 585, p. 357–362, 2020.

[143] J. D. Hunter, "Matplotlib: A 2D graphics environment," *Computing in Science Engineering*, vol. 9, no. 3, pp. 90–95, 2007.

[144] P. Virtanen, R. Gommers, T. E. Oliphant, M. Haberland, T. Reddy, D. Cournapeau, E. Burovski, P. Peterson, W. Weckesser, J. Bright, S. J. van der Walt, M. Brett, J. Wilson, K. J. Millman, N. Mayorov, A. R. J. Nelson, E. Jones, R. Kern, E. Larson, C. J. Carey, İ. Polat, Y. Feng, E. W. Moore, J. VanderPlas, D. Laxalde, J. Perktold, R. Cimrman,

I. Henriksen, E. A. Quintero, C. R. Harris, A. M. Archibald, A. H. Ribeiro, F. Pedregosa, P. van Mulbregt, and SciPy 1.0 Contributors, "SciPy 1.0: Fundamental algorithms for scientific computing in Python," *Nat. Methods*, vol. 17, pp. 261–272, 2020.

[145] Wes McKinney, "Data structures for statistical computing in Python," in *Proceedings of the 9th Python in Science Conference* (Stéfan van der Walt and Jarrod Millman, eds.), pp. 56 – 61, 2010.

[146] S. Geller and J. L. Durand, "Refinement of the structure of $LiMnPO_4$," *Acta Cryst. Sect. A*, vol. 13, pp. 325–331, Apr 1960.

[147] R. Newnham, R. Santoro, and M. Redman, "Neutron-diffraction study of $LiMnPO_4$," *J. Phys. Chem. Solids*, vol. 26, no. 2, pp. 445–447, 1965.

[148] R. Santoro, D. Segal, and R. Newnham, "Magnetic properties of $LiCoPO_4$ and $LiNiPO_4$," *J. Phys. Chem. Solids*, vol. 27, no. 6, pp. 1192 – 1193, 1966.

[149] R. P. Santoro and R. E. Newnham, "Antiferromagnetism in $LiFePO_4$," *Acta Cryst. Sect. A*, vol. 22, pp. 344–347, Mar 1967.

[150] I. Abrahams and K. S. Easson, "Structure of lithium nickel phosphate," *Acta Cryst. Sect. C*, vol. 49, pp. 925–926, May 1993.

[151] J. M. Mays, "Nuclear magnetic resonances and Mn-O-P-O-Mn superexchange linkages in paramagnetic and antiferromagnetic $LiMnPO_4$," *Phys. Rev.*, vol. 131, pp. 38–53, Jul 1963.

[152] J. Creer and G. Troup, "The magnetic susceptibility of $LiFePO_4$ and $LiCoPO_4$," *Phys. Lett. A*, vol. 32, no. 6, pp. 439–440, 1970.

[153] N. A. Spaldin, M. Fechner, E. Bousquet, A. Balatsky, and L. Nordström, "Monopole-based formalism for the diagonal magnetoelectric response," *Phys Rev B*, vol. 88, p. 094429, sep 2013.

[154] M. Mercier, E. Bertaut, G. Quézel, and P. Bauer, "Interpretation de l'effet magneto-electrique dans $LiMnPO_4$," *Solid State Commun.*, vol. 7, pp. 149–154, jan 1969.

[155] M. Mercier and J. Gareyte, "Un nouveau corps magneto-electrique: $LiMnPO_4$," *Solid State Commun.*, vol. 5, p. 139–142, 02 1967.

[156] M. Mercier, J. Gareyte, and E. F. Bertaut, "Une nouvelle famille de corps magnétoélectriques: $LiMPO_4$ (M = Mn, Co, Ni)," *C. R. Acad. Sc. Paris*, vol. 264, pp. 979–982, Mar. 1967.

[157] M. Mercier and P. Bauer, "L'effet magnétoélectrique dans $LiNiPO_4$," *C. R. Acad. Sc. Paris*, vol. 267, pp. 465–468, Aug. 1968.

[158] K. Momma and F. Izumi, "VESTA 3 for three-dimensional visualization of crystal, volumetric and morphology data," *J. Appl. Cryst.*, vol. 44, pp. 1272–1276, 2011.

[159] P. J. Baker, I. Franke, F. L. Pratt, T. Lancaster, D. Prabhakaran, W. Hayes, and S. J. Blundell, "Probing magnetic order in $LiMPO_4$ (M = Ni, Co, Fe) and lithium diffusion in Li_xFePO_4," *Phys. Rev. B*, vol. 84, p. 174403, Nov 2011.

[160] V. Khrustalyov, V. Savitsky, and N. Kharchenko, "Multi-step-like magnetization of $LiNiPO_4$ in a pulse magnetic field," *Czech. J. Phys.*, vol. 54, pp. 27–30, 12 2004.

[161] D. Vaknin, J. L. Zarestky, J.-P. Rivera, and H. Schmid, "Commensurate-incommensurate magnetic phase transition in magnetoelectric single crystal LiNiPO$_4$," *Phys. Rev. Lett.*, vol. 92, p. 207201, May 2004.

[162] V. M. Khrustalyov, V. M. Savytsky, and M. F. Kharchenko, "Magnetoelectric effect in antiferromagnetic LiNiPO$_4$ in pulsed magnetic fields," *Low Temp. Phys.*, vol. 42, no. 12, pp. 1126–1129, 2016.

[163] C. C. Filho, P. Gomes, A. García-Flores, G. Barberis, and E. Granado, "Two-magnon Raman scattering in LiMnPO$_4$," *J. Magn. Magn. Mater.*, vol. 377, no. Supplement C, pp. 430 – 435, 2015.

[164] O. Portugall, N. Puhlmann, H. U. Müller, M. Barczewski, I. Stolpe, and M. von Ortenberg, "Megagauss magnetic field generation in single-turn coils: new frontiers for scientific experiments," *J. Phys. D: Appl. Phys.*, vol. 32, pp. 2354–2366, sep 1999.

[165] S. Takeyama, R. Sakakura, Y. H. Matsuda, A. Miyata, and M. Tokunaga, "Precise magnetization measurements by parallel self-compensated induction coils in a vertical single-turn coil up to 103T," *J. Phys. Soc. Japan*, vol. 81, p. 014702, jan 2012.

[166] A. Zheludev, T. Sato, T. Masuda, K. Uchinokura, G. Shirane, and B. Roessli, "Spin waves and the origin of commensurate magnetism in Ba$_2$CoGe$_2$O$_7$," *Phys. Rev. B*, vol. 68, p. 024428, Jul 2003.

[167] V. Hutanu, A. Sazonov, H. Murakawa, Y. Tokura, B. Náfrádi, and D. Chernyshov, "Symmetry and structure of multiferroic Ba$_2$CoGe$_2$O$_7$," *Phys Rev B*, vol. 84, p. 212101, dec 2011.

[168] V. Hutanu, A. Sazonov, M. Meven, H. Murakawa, Y. Tokura, S. Bordács, I. Kézsmárki, and B. Náfrádi, "Determination of the magnetic order and the crystal symmetry in the multiferroic ground state of Ba$_2$CoGe$_2$O$_7$," *Phys. Rev. B*, vol. 86, p. 104401, Sep 2012.

[169] T. Arima, "Ferroelectricity induced by proper-screw type magnetic order," *J. Phys. Soc. Jpn.*, vol. 76, no. 7, p. 073702, 2007.

[170] K. Yamauchi, P. Barone, and S. Picozzi, "Theoretical investigation of magnetoelectric effects in Ba$_2$CoGe$_2$O$_7$," *Phys. Rev. B*, vol. 84, p. 165137, Oct 2011.

[171] V. Hutanu, A. P. Sazonov, M. Meven, G. Roth, A. Gukasov, H. Murakawa, Y. Tokura, D. Szaller, S. Bordács, I. Kézsmárki, V. K. Guduru, L. C. J. M. Peters, U. Zeitler, J. Romhányi, and B. Náfrádi, "Evolution of two-dimensional antiferromagnetism with temperature and magnetic field in multiferroic Ba$_2$CoGe$_2$O$_7$," *Phys Rev B*, vol. 89, p. 064403, feb 2014.

[172] M. Soda, M. Matsumoto, M. Månsson, S. Ohira-Kawamura, K. Nakajima, R. Shiina, and T. Masuda, "Spin-nematic interaction in the multiferroic compound Ba$_2$CoGe$_2$O$_7$," *Phys. Rev. Lett.*, vol. 112, p. 127205, Mar 2014.

[173] M. Soda, L.-J. Chang, M. Matsumoto, V. O. Garlea, B. Roessli, J. S. White, H. Kawano-Furukawa, and T. Masuda, "Polarization analysis of magnetic excitation in multiferroic Ba$_2$CoGe$_2$O$_7$," *Phys Rev B*, vol. 97, p. 214437, jun 2018.

[174] R. Dutta, H. Thoma, I. Radelytskyi, A. Schneidewind, V. Kocsis, Y. Tokunaga, Y. Taguchi, Y. Tokura, and V. Hutanu, "Spin dynamics study and experimental realization of tunable single-ion anisotropy in multiferroic $Ba_2CoGe_2O_7$ under external magnetic fields," *Phys Rev B*, vol. 104, p. l020403, jul 2021.

Acknowledgements

Foremost, I am thankful to Karmen Saat who continued to patiently and unconditionally support me as I was working on finishing my seemingly unending PhD journey. She motivated me when I was struggling, pushed me out of my comfort zone when needed and had faith in me even when I had sometimes run out of it. Also, I want to sincerely thank my family, their enduring support made it possible for me to focus on the pursuit of knowledge above all.

In addition, I am just as much thankful to my supervisors Toomas Rõõm and Urmas Nagel, who guided me through the years, showing how the science community works and what kind of focus and dedication research acquires. I could not imagine better lab mates than Johan Viirok and Kirill Amelin. The scientific discoveries we made together combined with the adventurous conference trips were some of the highlights of this journey and I am grateful that I have had this chance. I want to thank all other group members and people in KBFI as well, it was a pleasure working aside you all and to have such smart people at coffee breaks is remarkable. Special thanks goes to Tõnu Tolk ja Ain Toim for providing the enormous amount of liquid helium that my systematic study of materials needed.

This work included many collaborators, I thank you all. In particular I would like to thank everybody from the physics department in BUTE, Budapest where I had pleasure to stay more then 6 months during PhD studies. Especially I would like to thank Vilmos Kocsis, David Szaller and Jakub Vit. Without your work and effort this would not have reached to this high level. I am grateful to István Kézsmárki and Sandor Bordács, while you were not my supervisors, at times your support and guidance in untangling the mysteries of the magnetoelectric world was indispensable. Discussions in Hungary would not have been the same without the geniuses of Karlo Penc, Péter Balla and Laszlo Mihály.

In addition I am indebted to the members of the Nijmegen High Field Magnet Laboratory who made the high field measurements possible: Hans Engelkamp, Dmytro Kamenskyi, Bence Bernáth and others at HFML with whom I had the pleasure to meet while my visits.

Dear kitesurfing friends, I thank you for your tolerance of not inviting me to kitesurf sessions when I needed to focus on the science work. I thank my childhood friends for keeping the relaxing sauna warm until I had finished my experiment or had left it running for the night. All other friends, I acknowledge you and I am grateful to have such wonderful people around me.

Abstract
Spin-waves in magnetoelectric materials with strong single-ion anisotropy

Directing electromagnetic radiation upon magnetically ordered matter can force electron spins to deviate from their ground state by exciting low-energy magnetic waves called spin-waves. The properties of these waves are defined by the interactions of magnetic ions. By characterizing these waves, it is possible to quantify magnetic exchange interactions between the spins and their coupling to the lattice and electric charges. Conventionally, the spin-waves are excited by the magnetic component of light. However, recently it was found that the electric component can excite the spin-wave (electromagnons) and there are spin-waves that are excited by magnetic and electric components simultaneously (magneto-electric resonances). Such sensitivity of the spin-waves to the electric field is inherent to multiferroic materials where the magneto-electric (ME) coupling links the spin and charge degrees of freedom. This dynamic ME coupling extends to zero frequency and makes it possible to control magnetization by electric field or electric polarization by magnetic field. The dynamic ME coupling can give rise to numerous novel phenomena, such as the refractive index inequality for the counter-propagating light beams, termed as non-reciprocal directional dichroism (NDD). The practical realization of ME effect is an optical diode with switchable transmittance direction or a ME memory with optical read-out. Thus, the spin-waves can provide valuable information not only about the magnetic properties, but they can also offer insight into the ME nature of materials and in addition support the development of new applications that take advantage from the ME effect.

Another interesting aspect of ME materials is that their low symmetry, in addition to broken space and time inversion symmetry, and strong single-ion anisotropies, makes it possible to observe unconventional multi-spin and spin-stretching excitations with THz spectroscopy. The best known multi-spin excitation is a two-magnon excitation where one absorbed photon creates two magnons with wavevectors $\mathbf{k}_1$ and $\mathbf{k}_2$. While the long wavelength radiation excites one magnon, $\mathbf{k} \approx 0$, in the Brillouin zone centre, the two-magnon pair is excited if $\mathbf{k}_1 + \mathbf{k}_2 \approx 0$. Observation of two-magnon excitations allows THz spectroscopy to access exchange interactions connecting spins in the neighbouring unit cells. In addition, spin-stretching modes and two-magnon excitations can be ME resonances and usually are excited at higher frequencies than magnons. Studying these excitations is important as they can shed light on exchange interactions that are usually not accessible by spectroscopy and in terms of applications, they can extend the frequency range of NDD effect based devices.

In this work three ME compounds, $LiNiPO_4$, $LiFePO_4$ and $Ba_2CoGe_2O_7$, were studied in THz frequency range at the National Institute of Chemical Physics and Biophysics, using the Martin-Puplett interferometer with liquid-helium-bath cryostat and a 17 T superconducting magnet. Additionally, $Ba_2CoGe_2O_7$ measurements included the application of an external electric field. The magnetic field range of THz spectroscopy measurements of $LiNiPO_4$ and $LiFePO_4$ was extended up to 33 T in High Field Magnet Laboratory (HFML) in Nijmegen with Genzel type interferometer and resistive Bitter magnet. The $LiNiPO_4$ and $LiFePO_4$ low field magnetization measurements were done by using a 14 T PPMS with VSM option. The magnetization of $LiNiPO_4$ was measured in HFML, Nijmegen up 33 T and the magnetization of $LiFePO_4$ was measured up to 120 T using ultra-high semidestructive pulses at the Laboratoire National des Champs Magnétiques Intenses in Toulouse.

$LiFePO_4$ and $LiNiPO_4$ belong to the orthophosphate family $LiMPO_4$ ($M =$ Fe, Ni, Co, Mn)

showing linear ME effect. Orthophosphates have gained attention because a ferrotoroidal order and a dynamic ME effect with remnant NDD were found in LiCoPO$_4$. Compared to LiCoPO$_4$, where Co^{2+} ions have spin $S = 3/2$, the LiFePO$_4$ with $S = 2$ and LiNiPO$_4$ with $S = 1$ offers ideal ground to investigate the peculiarities of this family ME effect even further. As spectroscopic data of spin-waves in low frequency range was limited or did not exist, we focused on the measurements of THz absorption spectra of spin-waves in magnetic field with the aim of identifying the ME spin excitations and determining the magnetic interactions parameters.

Previously, LiFePO$_4$ and LiNiPO$_4$ have been studied with inelastic neutron scattering where two individual magnon dispersion branches were detected. Based on the linear spin-wave theory, the number of magnons in the four-sublattice crystals is four. Our THz spectroscopy measurements yielded far richer spin-wave spectrum with 7 modes in LiNiPO$_4$ and 17 modes in LiFePO$_4$ in the zero magnetic field. This high number of modes could be explained by the multi-boson spin-wave theory, but as it is a rather complex and time-consuming theory to implement, we did not practice it with LiNiPO$_4$ and LiFePO$_4$. In both compounds a systematic study of 14 different configurations of polarization and magnetic field directions was carried out. Through polarization dependence study we determined the selection rules of excitations and identified them as magnons, electro-magnons and ME resonances. These results together with magnetization measurements and combined with the mean-field model enabled us to determine the exchange parameters, anisotropies and Dzyaloshinskii-Moriya at a level of precision not done before in LiNiPO$_4$ and LiFePO$_4$.

The third compound, Ba$_2$CoGe$_2$O$_7$, is a multiferroic with a non-centrosymmetric tetragonal crystal structure. The two-sublattice AFM state is realized below $T_{\mathrm{N}} = 6.7$ K with four anti-ferromagnetic (AFM) domains and two $3/2$-spin Co^{2+} ions in the magnetic unit cell. The previous studies showed that macroscopic electric polarization is zero, if the magnetic field is perfectly aligned along the c axis while small tilting of the field out of the c direction leads to the hysteresis of polarization, suggesting the change of AFM domains population by the magnetic field. In this work we applied electric field along the a axis, in addition to the magnetic field applied along the c axis. We detected the rearrangement of domains by NDD of spin-waves using THz spectroscopy. By switching the polarity of electric field we could attain similar control over the domain population as was done with the tilting of magnetic field alone. The multi-boson spin-wave theory confirmed that the non-reciprocal light absorption by some of the spin-wave excitations depends on the AFM domain type. These results conclude this whole work by showing the practical importance of studying the ME effect and that the novel electric field control of magnetic domains and NDD is possible, promoting the future development of voltage-controlled THz-frequency devices.

Kokkuvõte
Spinn-lained tugeva anisotroopiaga magnetelektrilistes materjalides

Elektromagnetkiirguse neeldumisel magnetiliselt korrastunud materjalides ergastatakse elektroni spinne. Tekkinud ergastused on spinn-lained, mille omadused on määratud spinnidevaheliste vastasmõjudega. Spinn-lainete mõõtmine annab võimaluse uurida magnetmomentide vahelisi vastasmõjusid ja ka spinnide vastasmõju kristallvõre ja elektrilaengutega.

Tavaliselt ergastab spinn-laineid valguse magnetiline komponent. Hiljuti aga avastati, et ka valguse elektriline komponent ergastab spinn-laineid (elektromagnonergastus) ja erandjuhtudel võivad valguse magnetiline ja elektriline komponent korraga spinn-lainet ergastada (magnet-elektriline ergastus). Magnet-elektrilised ergastused on omased multiferroididele, millel esineb magnetelektriline vastasmõju. Dünaamiline magnetelektriline nähtus mõjutab ka materjali staatilisi magnetelektrilisi omadusi nullsagedusel ja seeläbi võimaldab kontrollida magneetuvust elektriväljaga ja elektrilist polarisatsiooni magnetväljaga. Magnetelektriline vastasmõju tekitab murdumisnäitajate erinevuse vastassuunas levivatele valguskiirtele, mida nimetatakse suunadikroismiks. Seeläbi võib magnetelektriline vastamõju leida kasutust optilistes dioodides, kus valguse läbilaskvuse suuna saab lülitada elektri- või magnetväljaga, samuti magnetelektrilistes optiliselt loetavates mäludes. Eelnevat üldistades: spinn-lainetest saab väärtuslikku teavet nii materjali magnetiliste omaduste, kui ka magnetelektrilise vastasmõju kohta ja need uuringud edendavad uudse magnetelektrilise tehnoloogia arendamist.

Üks multiferroidide huvitav omadus on see, et nende madal sümmeetria võimaldab lisaks rikutud ruumi- ja ajainversioonisümmeetriale vaadelda THz-spektroskoopiaga tavatuid mitme-spinni ergastusi ja kvadrupoolseid spinn-laineid. Kõige tuntum mitme-spinni ergastus on kahe-magnoni ergastus, kus ühe footoni neeldumisel tekib kaks magnonit lainevektoritega $\mathbf{k}_1$ ja $\mathbf{k}_2$. THz sagedusel ergastatakse magnon Brillouini tsooni keskel, $\mathbf{k} \approx 0$, aga kahe-magnoni ergastus võib sellist optikanõuet rikkuda, kui erisuunaliste lainevektorite summa on $\mathbf{k}_1 + \mathbf{k}_2 \approx 0$. Kahe-magnoni ergastus võimaldab seeläbi THz spektroskoopiaga mõõta spinnide vahetusvastasmõjusid naaber-ühikrakkude vahel. Kvadrupoolsed spinn-lained esinevad $S > 1/2$ spinniga kristallides ja on magnetilise kvadrupoolmomendi võnkumised, samas kui magnonid on magnetilise dipoolmomendi võnkumised. Kvadrupoolsete spinn-lainete eripära on selles, et nendega kaasnevad elektrilise dipooli võnkumised, mistõttu nad avalduvad THz-kiirguse neeldumisspektrites, samas jäädes nähtamatuteks mitte-elastse neutronhajumise spektrites, sest neutroni magnetmoment ei interakteeru elektridipoolmomendiga. Nii kvadrupoolne spinn-laine kui ka kahe-magnoni ergastus võivad mõlemad olla magnetelektrilised resonantsid, enamasti esinedes kõrgematel sagedustel. Kokkuvõtvalt võib öelda, et nende ergastuste mõõtmine annab võimaluse määrata vastasmõjusid, mis ühe-magnoni ergastustes ei avaldu ja võimaldab arendada suunadikroismil põhinevaid seadmeid veel kõrgematel sagedustel.

Antud töös uuriti kolme magnetelektrilist materjali, $LiNiPO_4$, $LiFePO_4$ ja $Ba_2CoGe_2O_7$, THz spektroskoopiaga Keemilise ja Bioloogilise Füüsika Instituudis, kasutades Martin-Puplett'i tüüpi spektromeetrit, heeliumiga jahutatavat krüostaati ja 17 Teslast ülijuhtivat magnetit. $Ba_2CoGe_2O_7$ mõõtmistel kasutati lisaks magnetväljale ka alaliselektrivälja. Täiendavad THz spektroskoopia mõõtmised $LiNiPO_4$ ja $LiFePO_4$ kristallidega kuni 33 Teslani viidi läbi Kõrgete Magnetväljade Laboris (HFML) Hollandis, Nijmegenis, kus kasutati Genzeli tüüpi spektromeetrit ja Bitteri elektromagnetit. Uuritavate kristallide magneetuvust mõõdeti kuni 14 Teslani füüsikaliste omaduste mõõteseadmega PPMS (Physical Property Me-

asurement System), kasutades VSM (Vibrating Sample Magnetometer) magnetomeetrit. $LiNiPO_4$ magneetuvust mõõdeti kuni 33 Teslani Hollandis, Nijmegenis ja $LiFePO_4$ magneetuvust mõõdeti kuni 120 Teslani kasutades impulssmagnetvälja Riiklikus Intensiivsete Magnetväljade Laboris Prantsusmaal, Toulouses.

$LiNiPO_4$ ja $LiFePO_4$ kristallid kuuluvad lineaarsete magnetelektrikute ortofosfaatide perekonda $LiMPO_4$ (M = Fe, Ni, Co, Mn). Antud isolaatorite perekond on saanud tähelepanu tänu $LiCoPO_4$ kristallis avastatud ferrotoroidaalsele korrale ja suunadikroismile, mis säilib pärast polariseerivate väljade nulli viimist. Sarnaselt $LiCoPO_4$-ga ($S = 3/2$), on Ni ja Fe spinnid suuremad kui $1/2$, vastavalt $S = 1$ ja $S = 2$, mis tähendab kvadrupoolsete spinn-lainete ja magnetelektriliste ergastuste olemasolu võimalikkust. Kuna peamine teave spinn-lainete kohta pärines mitte-elastse neutronhajumise spektritest, siis suunasime peamise tähelepanu THz kiirguse neeldumisspektrite mõõtmisele magnetväljas. Täiendavaks eesmärgiks oli leida magnetelektrilisi ergastusi, millel võiks olla suunadikroism ja määrata magnetiliste vastamõjude parameetrid.

Eelnevalt on $LiFePO_4$ ja $LiNiPO_4$ kristalle mõõdetud mitteelastse neutronhajumise meetodil, kus ülekantud impulsi energia dispersioonikõverate alusel tuvastati kaks magnonit. Lineaarse spinnlaine teooria kohaselt on nelja magnetilise alamvõrega $LiMPO_4$ kristallides oodatav magnonite arv neli. Meie THz spektroskoopia mõõtmised näitasid aga palju rikkalikumat spektrit, kus oli 7 erinevat spinn-ergastust $LiNiPO_4$ kristallis ja 17 spinnergastust $LiFePO_4$ kristallis. Varasemast on teada, et sedavõrd kõrget ergastuste hulka saab seletada multi-boson spinn-laine teooriaga, mille rakendamist $LiNiPO_4$ ja $LiFePO_4$ kristallides ei võimaldanud doktoritöö maht ja eesmärgid. Uurides leitud ergastuste sõltuvust THz kiirguse polarisatsioonist määrasime spinn-lainete valikureeglid, mis võimaldasid grupeerida ergastused magnoniteks, elektromagnoniteks ja magnetelektrilisteks ergastusteks. Mõlemas ühendis mõõtsime THz spektreid 14 erinevas magnetvälja ja polarisatsiooni konfiguratsioonis. Ühendades antud tulemused magneetuvuse mõõtmistega ja spinn-laine teooriaga, määrasime magnetiliste ioonide vastamõjud, ühe iooni anisotroopia ja Dzyaloshinskii-Moriya vastamõju parameetrid täpsemini kui kunagi varem.

Kolmas uuritud ühend $Ba_2CoGe_2O_7$ on multiferroid millel on inversioonisümmetriata tetragonaalne kristallstruktuur. Antud kristallis tekib antiferromagnetiline korrapära allpool 6.7 K, kus ühes magnetilises ühikrakus on kaks Co^{2+} iooni spinniga $S = 3/2$ ning esineb neli antiferromagnetilist domeeni. Varasemad uuringud on näidanud, et makroskoopiline elektriline polarisatsioon on null, kui magnetväli on rakendatud täpselt kristalli tetragonaalse c telje suunas. Samas, väike magnetvälja kõrvalekaldumine c teljest tekitab elektrilise polarisatsiooni ja selle hüstereesi, mis viitab antiferromagnetiliste domeenide ümberjaotumisele. Selles töös, lisaks magnetväljale ($\mu_0\mathbf{H}$) c telje suunas, rakendasime elektrivälja ($\mathbf{E}$) piki a telge. Kuna spinn-lainetest põhjustatud suunadikroism sõltub domeenist, siis kasutasime THz spektroskoopiat domeenide asustatuse mõõtmiseks. Elektrivälja polaarsuse vahetamisega muutsime antiferromagnetiliste domeenide vahekorda, nagu eelnevalt tehti kristalli c telje ja magnetvälja vahelise nurga muutmisega. Multibosonite spinn-laine teooria kinnitas, et magnetelektriliste ergastuste suunadikroism sõltub antiferromagnetilise domeeni tüübist.

$Ba_2CoGe_2O_7$ katsetes saadud tulemus võtab kokku kogu doktoritöö, näidates magnetelektrilise efekti uurimise praktilist tähtsust ja demonstreerides uudset magnetelektrilise nähtuse kontrollimist elektriväljaga, millest on kasu elektriväljaga juhitavate THz-sagedusseadmete arendamisel.

Appendix 1

I

L. Peedu, V. Kocsis, D. Szaller, J. Viirok, U. Nagel, T. Rõõm, D. G. Farkas, S. Bordács, D. L. Kamenskyi, U. Zeitler, Y. Tokunaga, Y. Taguchi, Y. Tokura, and I. Kézsmárki, "Spin excitations of magnetoelectric LiNiPO$_4$ in multiple magnetic phases," *Phys. Rev. B*, vol. 100, p. 024406, Apr 2019

Spin excitations of magnetoelectric LiNiPO₄ in multiple magnetic phases

L. Peedu,[1] V. Kocsis,[2] D. Szaller,[3] J. Viirok,[1] U. Nagel,[1] T. Rõõm,[1] D. G. Farkas,[4] S. Bordács,[4,5] D. L. Kamenskyi,[6]
U. Zeitler,[6] Y. Tokunaga,[2,7] Y. Taguchi,[2] Y. Tokura,[2,8] and I. Kézsmárki[4,9]

[1]*National Institute of Chemical Physics and Biophysics, Akadeemia tee 23, 12618 Tallinn, Estonia*
[2]*RIKEN Center for Emergent Matter Science (CEMS), Wako, Saitama 351-0198, Japan*
[3]*Institute of Solid State Physics, Vienna University of Technology, 1040 Vienna, Austria*
[4]*Department of Physics, Budapest University of Technology and Economics, 1111 Budapest, Hungary*
[5]*Hungarian Academy of Sciences, Premium Postdoctor Program, 1051 Budapest, Hungary*
[6]*High Field Magnet Laboratory (HFML-EMFL), Radboud University, Toernooiveld 7, 6525 ED Nijmegen, The Netherlands*
[7]*Department of Advanced Materials Science, University of Tokyo, Kashiwa 277-8561, Japan*
[8]*Department of Applied Physics, University of Tokyo, Hongo, Tokyo 113-8656, Japan*
[9]*Experimental Physics 5, Center for Electronic Correlations and Magnetism, Institute of Physics,
University of Augsburg, 86159 Augsburg, Germany*

Spin excitations of magnetoelectric LiNiPO₄ are studied by infrared absorption spectroscopy in the THz spectral range as a function of magnetic field through various commensurate and incommensurate magnetically ordered phases up to 33 T. Six spin resonances and a strong two-magnon continuum are observed in zero magnetic field. Our systematic polarization study reveals that some of the excitations are usual magnetic-dipole active magnon modes, while others are either electromagnons, being only electric-dipole active, or magnetoelectric, that is both electric- and magnetic-dipole active spin excitations. Field-induced shifts of the modes for all three orientations of the field along the orthorhombic axes allow us to refine the values of the relevant exchange couplings, single-ion anisotropies, and the Dzyaloshinskii-Moriya interaction on the level of a four-sublattice mean-field spin model. This model also reproduces the spectral shape of the two-magnon absorption continuum, found to be electric-dipole active in the experiment.

I. INTRODUCTION

Potential of magnetoelectric (ME) materials in applications relies on the entanglement of magnetic moments and electric polarization [1–8]. Such an entanglement leads not only to the static ME effect but also to the optical ME effect. One manifestation of the optical ME effect is the nonreciprocal directional dichroism, a difference in the absorption with respect to the reversal of light propagation direction [9–12]. The spectrum of nonreciprocal directional dichroism and the linear static ME susceptibility are related via a ME sum rule [13]. According to this sum rule the contribution of simultaneously magnetic- and electric-dipole active spin excitations to the linear ME susceptibility grows as ω^{-2} with $\omega \rightarrow 0$. Indeed, strong nonreciprocal directional dichroism has been observed at low frequencies, typically in the GHz-THz range, at spin excitations in several ME materials [14–26]. Besides the interest in the nonreciprocal effect, the knowledge of the spin excitation spectrum and selection rules, i.e., whether the excitations are ordinary magnetic-dipole active magnons, electromagnons (electric-dipole active magnons [27]), or ME spin excitations (simultaneously magnetic- and electric-dipole active spin excitations), is crucial in understanding the origin of static ME effect.

It is well established that the static ME effect is present in several olivine-type LiMPO₄ (M = Mn, Fe, Co, Ni) compounds [28–35]. LiNiPO₄ is particularly interesting due to

many magnetic-field-induced phases, some with incommensurate magnetic order, which is unique in the olivine lithium-orthophosphate family [36]. However, little is known about the spectrum of spin excitations and their selection rules.

THz absorption spectroscopy offers an excellent tool to investigate spin excitation spectra over a broad magnetic field range. As compared to the inelastic neutron scattering (INS), only spin excitations with zero linear momentum are probed, but with a better energy resolution. In addition to excitation frequencies, THz spectroscopy can determine whether the spin excitations are magnetic-dipole active magnons, electromagnons, or ME spin excitations. This information is essential for developing a spin model that would describe the ground and the low-lying excited states of the material.

We studied the spin excitation spectra of LiNiPO₄ in magnetic field using THz absorption spectroscopy. In the previous INS works two magnon branches were observed below 8 meV [36–38]. Here we broaden the spectral range up to 24 meV, which allows us to observe additional spin excitations and to identify the polarization selection rules for the spin excitations. Using a mean-field model we describe the field dependence of the magnetization and the magnon energies in commensurate phases, from where we refine the values of exchange couplings, single-ion anisotropies, and the Dzyaloshinskii-Moriya interaction. Besides magnons described by the mean-field model, few other spin excitations, including two-magnon excitations, are observed.
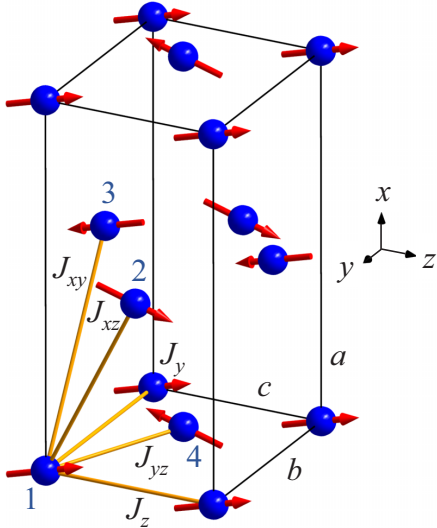
FIG. 1. The ground-state spin configuration of LiNiPO$_4$ in zero magnetic field. There are four Ni^{2+} spins, $S = 1$, in the magnetic unit cell drawn as a box. The spins are canted away from the z axis towards the x axis by $\theta = \pm(7.8° \pm 2.6°)$ [36,39]. The numbering of spins and the labeling of exchange interactions corresponds to the spin Hamiltonian described by Eq. (1).

LiNiPO$_4$ has orthorhombic symmetry with space group *Pnma*. The magnetic Ni^{2+} ion with spin $S = 1$ is inside a distorted O$_6$ octahedron. There are four Ni^{2+} ions in the structural unit cell forming buckled planes perpendicular to the crystal x axis, as shown in Fig. 1. The nearest-neighbor spins in the yz plane are coupled by strong AF exchange interaction which results in a commensurate AF order below $T_N = 20.8$ K [40,41]. The ordered magnetic moments are almost parallel to the crystallographic z axis with slight canting towards the x direction [42]. On heating above T_N the material undergoes a first-order phase transition into a long-range incommensurate magnetic structure. Further heating results in a second-order phase transition into the paramagnetic state at $T_{IC} = 21.7$ K, while short-range magnetic correlations persist up to 40 K [41]. Owing to the competing magnetic interactions LiNiPO$_4$ has a very rich H-T phase diagram with transitions appearing as multiple steps in the field dependence of the magnetization [43,44]. The delicate balance of the nearest-neighbor and the frustrated next-nearest-neighbor exchange interactions puts the material on the verge of commensurate and incommensurate structures, which alternate in increasing the magnetic field applied along the z axis as shown in Fig. 2(a) [37,38,42].

II. EXPERIMENTAL DETAILS

LiNiPO$_4$ single crystals were grown by the floating zone method, similarly as described in Ref. [45]. Crystal quality was tested by 2-θ and Laue x-ray diffraction, which reconfirmed the orthorhombic structure with the same lattice constants as reported in Ref. [46]. Three samples each with a large face normal to one of the principal axes were cut
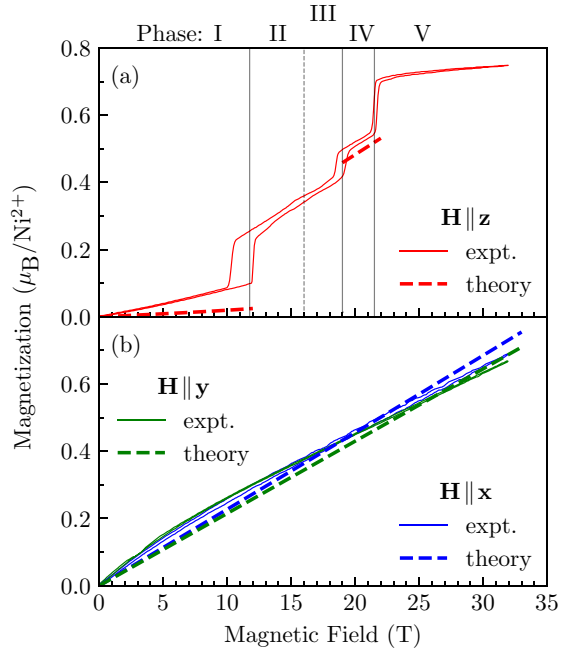

FIG. 2. Magnetic field **H** dependence of the magnetization **M** parallel to the field at 2.4 K. (a) **H** ∥ **z**, (b) **H** ∥ **y** (green) and **H** ∥ **x** (blue). Solid lines are experimental results and the dashed lines are calculated from the mean-field model with the parameters of this work listed in Table I.

from the same ingot. For optical measurements the slabs with thicknesses from 0.87 to 1.09 mm had an approximately 2° wedge to suppress interference caused by internal reflections. Samples were mounted on metal discs where the hole depending on the sample size limited the THz beam cross section to 8–16 mm^2.

THz measurements up to 17 T were performed in Tallinn with a Martin-Puplett interferometer and a 0.3-K silicon bolometer. High-field spectra from 17 T up to 33 T were measured in the Nijmegen High Field Magnet Laboratory using a Bruker IFS 113v spectrometer and a 1.6-K silicon bolometer. The experiments above 17 T were done in the Faraday configuration (**k** ∥ **H**), while below 17 T both the Faraday and the Voigt (**k** ⊥ **H**) configuration experiments were performed. All spectra were measured with an apodized spectral resolution of 0.5 cm^{-1}. A linear polarizer was mounted in front of the sample to control the polarization state of the incoming light.

Absorption was determined by using a reference spectrum. The reference spectrum was obtained on the sample in zero magnetic field in the paramagnetic state at $T = 30$ K or by measuring a reference hole with the area equal to the sample hole area. In the former case the relative absorption is calculated as $\alpha(H, T) - \alpha(0\,T, 30\,K) = -d^{-1} \ln [I(H, T)/I(0\,T, 30\,K)]$ where d is the sample thickness and I is the measured intensity. In the latter case the

absolute absorption is calculated as $\alpha = -d^{-1} \ln(I/I_r)$ where I_r is the intensity through the reference hole.

Magnetization up to 32 T was measured in the Nijmegen High Field Magnet Laboratory on a Bitter magnet with a vibrating-sample magnetometer (VSM) and additional low-field measurements were done using a 14-T PPMS with VSM option (Quantum Design).

III. MEAN-FIELD MODEL AND MAGNONS

The terms included in the spin Hamiltonian, exchange interactions, single-ion anisotropy terms, and the Zeeman energy correspond to those also considered in earlier works on LiNiPO$_4$ [36–38]. The model contains four spin variables as classical vectors $\{\mathbf{S}_1, \mathbf{S}_2, \mathbf{S}_3, \mathbf{S}_4\}$ in accordance with the four crystallographically nonequivalent positions of the spin $S = 1$ Ni^{2+} ions in LiNiPO$_4$. The four spins of the magnetic unit cell are connected by five different exchange couplings as presented in Fig. 1. Two of these couplings, J_y and J_z, connect spins at the same crystallographic sites producing, irrespective of the spin state, a constant energy shift in the Γ point within the four-sublattice model. Although these terms are omitted in the analysis of single-magnon excitations, they become relevant in the analysis of two-magnon excitations as discussed in Sec. B. The spin Hamiltonian of the magnetic unit cell in the four-sublattice model reads

$$
\mathcal{H} = \sum_{i=1}^{4} \left[\Lambda_x \left(S_i^x\right)^2 + \Lambda_y \left(S_i^y\right)^2 - g\mu_B \mu_0 \mathbf{H} \cdot \mathbf{S}_i \right]
$$
$$
+ 4 \big[J_{xz}(\mathbf{S}_1 \cdot \mathbf{S}_2 + \mathbf{S}_3 \cdot \mathbf{S}_4) + J_{xy}(\mathbf{S}_1 \cdot \mathbf{S}_3 + \mathbf{S}_2 \cdot \mathbf{S}_4)
$$
$$
+ J_{yz}(\mathbf{S}_1 \cdot \mathbf{S}_4 + \mathbf{S}_2 \cdot \mathbf{S}_3)
$$
$$
+ D_y \left(S_1^z S_4^x - S_1^x S_4^z + S_3^z S_2^x - S_3^x S_2^z \right) \big]. \quad (1)
$$

Due to the strongly distorted ligand cage of the magnetic ion, the orthorhombic anisotropy of the crystal is taken into account by two single-ion hard-axis anisotropies, $\Lambda_x, \Lambda_y > 0$. The parameters in the Zeeman term are the g factor g, the Bohr magneton μ_B, and the vacuum permeability μ_0. Parameters J_{xz}, J_{xy}, and J_{yz} are the isotropic Heisenberg exchange couplings as shown in Fig. 1, while D_y is the Dzyaloshinskii-Moriya interaction.

According to the neutron-diffraction studies [47,48] the ground-state spin configuration of LiNiPO$_4$ in zero magnetic field is a predominantly collinear AF order, where $\mathbf{S}_1$ and $\mathbf{S}_2$ point in $+z$, while $\mathbf{S}_3$ and $\mathbf{S}_4$ in the $-z$ direction, shown in Fig. 1. Thus, the dominant exchange interaction is the AF $J_{yz} > 0$ coupling, while z is an easy axis as $\Lambda_x, \Lambda_y > 0$. On top of the collinear order a small alternating canting of spins with net spin along x is superimposed [39]. Canting is induced by the Dzyaloshinskii-Moriya coupling D_y and breaks the equivalence of $\mathbf{S}_1$ and $\mathbf{S}_2$ as well as $\mathbf{S}_3$ and $\mathbf{S}_4$. The canting angle θ measured from the z axis is approximately

$$
\tan\theta \approx \frac{2D_y}{\Lambda_x - 4(J_{xz} - J_{yz})}. \quad (2)
$$

At each magnetic field, the ground-state spin configuration is obtained by minimizing the energy corresponding to Eq. (1).

The resonance frequencies and amplitudes of modes are calculated using the Landau-Lifshitz equation [49]

$$
\dot{\mathbf{S}}_i = -\frac{1}{\hbar} \mathbf{S}_i \times \frac{\partial \mathcal{H}}{\partial \mathbf{S}_i}, \quad (3)
$$

where $\dot{\mathbf{S}}_i \equiv d\mathbf{S}_i / dt$.

We solve Eq. (3) for small spin deviations $\{\delta\mathbf{S}\} \equiv \{\delta\mathbf{S}_1, \dots \delta\mathbf{S}_N\}$ from the equilibrium $\{\mathbf{S}^0\} \equiv \{\mathbf{S}_1^0, \dots \mathbf{S}_N^0\}$, where $\{\mathbf{S}\} = \{\mathbf{S}^0\} + \{\delta\mathbf{S}\}$, with N spins in the magnetic unit cell. It follows from Eq. (3) that $\delta\mathbf{S}_i \perp \mathbf{S}_i$, leaving the spin length constant in the first order of $\delta\mathbf{S}_i$. Inserting $\{\mathbf{S}\}$ into Landau-Lifshitz Eq. (3) and keeping only terms linear in $\delta\mathbf{S}_i$ (terms zero order in $\delta\mathbf{S}_i$ add up to zero) we get

$$
\delta\dot{\mathbf{S}}_i = -\frac{1}{\hbar} \mathbf{S}_i^0 \times \frac{\partial \mathcal{H}_\delta}{\partial \mathbf{S}_i}, \quad (4)
$$

where the effective field is

$$
\frac{\partial \mathcal{H}_\delta}{\partial \mathbf{S}_i} = \frac{\partial \mathcal{H}}{\partial \mathbf{S}_i} \bigg|_{\{\mathbf{S}^0\} + \{\delta\mathbf{S}\}}. \quad (5)
$$

We solve Eq. (4) by assuming harmonic time dependence $\delta\mathbf{S}_i(t) = \delta\mathbf{S}_i \exp(i\omega t)$. The number of modes is equal to the number of spins in the unit cell.

To calculate the absorption of electromagnetic waves by the magnons we introduce damping. The Landau-Lifshitz-Gilbert equation [50] for the ith spin is

$$
\dot{\mathbf{S}}_i = -\frac{1}{\hbar} \mathbf{S}_i \times \frac{\partial \mathcal{H}_\delta}{\partial \mathbf{S}_i} + \frac{\alpha}{\hbar S_i} \mathbf{S}_i \times \mathbf{S}_i \times \frac{\partial \mathcal{H}_\delta}{\partial \mathbf{S}_i}, \quad (6)
$$

where α is a positive dimensionless damping parameter and small, $\alpha \ll 1$. Using $\mathbf{A} \times \mathbf{B} \times \mathbf{C} = \mathbf{B}(\mathbf{A} \cdot \mathbf{C}) - \mathbf{C}(\mathbf{A} \cdot \mathbf{B})$, and adding a weak harmonic alternating magnetic field, $\mathbf{H}^\omega(t) = \mathbf{H}^\omega \exp(i\omega t)$, to the effective field yields the following form of the equation of motion up to terms linear in $\delta\mathbf{S}_i$ and $\mathbf{H}^\omega$:

$$
\delta\dot{\mathbf{S}}_i = -\frac{1}{\hbar} \mathbf{S}_i^0 \times \left[\frac{\partial \mathcal{H}_\delta}{\partial \mathbf{S}_i} - \mu_0 \mathbf{H}^\omega(t) \right]
$$
$$
+ \frac{\alpha}{\hbar} \frac{\mathbf{S}_i^0}{S_i^0} \mathbf{S}_i^0 \cdot \left[\frac{\partial \mathcal{H}_\delta}{\partial \mathbf{S}_i} - \mu_0 \mathbf{H}^\omega(t) \right]
$$
$$
- \frac{\alpha}{\hbar} S_i^0 \left[\frac{\partial \mathcal{H}_\delta}{\partial \mathbf{S}_i} - \mu_0 \mathbf{H}^\omega(t) \right]. \quad (7)
$$

The absorption of electromagnetic waves by the spin system related to magnetic dipole excitations is calculated from Eq. (7) by inserting $\delta\mathbf{S}_i(t) = \delta\mathbf{S}_i \exp(i\omega t)$ and $\mathbf{H}^\omega(t) = \mathbf{H}^\omega \exp(i\omega t)$. The frequency-dependent magnetic susceptibility tensor $\hat{\chi}(\omega)$ is obtained by summing up all the magnetic moments in the unit cell, $\mathbf{M} = \gamma\hbar \sum_{i=1}^{N} \mathbf{S}_i$ in Eq. (7), and making a transformation into form

$$
\gamma\hbar \left[\sum_{i=1}^{M} \delta\mathbf{S}_i(t) \right] = \hat{\chi}(\omega) \mu_0 \mathbf{H}^\omega(t). \quad (8)
$$

The absorption coefficient is $\alpha_{i,j} = 2\omega c_0^{-1} \mathrm{Im}\, \mathcal{N}_{i,j}$, where the complex index of refraction is $\mathcal{N}_{i,j} = \sqrt{\epsilon_{ii} \mu_{jj}}$ assuming small polarization rotation and negligible linear magnetoelectric susceptibilities χ_{ij}^{em}, χ_{ji}^{me}. The magnetic permeability is $\mu_{jj}(\omega) = 1 + \chi_{jj}(\omega)$ and the background dielectric permittivity is ϵ_{ii}. The polarization of incident radiation is defined as

TABLE I. The parameters of the mean-field model used to describe the static magnetic properties and single- and two-magnon excitations in LiNiPO$_4$: exchange couplings J_{ij} and J_k, single-ion anisotropy constants Λ_i, Dzyaloshinskii-Moriya coupling D_y, and g factor g. Units are in meV except the dimensionless g.

J_y	J_z	J_{xz}	J_{xy}	J_{yz}	Λ_x	Λ_y	D_y	g	Ref.
0.65	0.16	−0.17	0.16	1.24	0.14	0.74	0.41	2.2	a
0.67	−0.06	−0.11	0.32	1	0.41	1.42	0.32	2.2	[36]
0.67	−0.05	−0.11	0.3	1.04	0.34	1.82			[37]
0.59	−0.11	−0.16	0.26	0.94	0.34	1.92			[38]

aThis work.

$\{E_i^\omega, H_j^\omega\}$ where i and j are x, y, or z. If $\chi_{jj}(\omega) \ll 1$,

$$\mathcal{N}_{i,j} \approx \sqrt{\epsilon_{ii}}\left[1 + \frac{\chi_{jj}(\omega)}{2}\right]. \qquad (9)$$

Thus, for real ϵ_{ii} the absorption is

$$\alpha_{i,j}(\tilde\omega) = 2\pi\tilde\omega\sqrt{\epsilon_{ii}}\,\mathrm{Im}\,\chi_{jj}(\tilde\omega), \qquad (10)$$

where units of wave number are used, $[\tilde\omega_n] = \mathrm{cm}^{-1}$.

The values of magnetic interactions and anisotropies obtained in this work, see Table I, reproduce the magnetic field dependence of the magnetization, canting angle θ, and frequencies of four single-spin excitations and a two-magnon excitation in the I and a single-spin excitation in the IV commensurate magnetic phase of LiNiPO$_4$.

IV. EXPERIMENTAL RESULTS

The LiNiPO$_4$ samples were characterized by measuring the magnetization along the x, y, and z directions, shown in Fig. 2. The magnetization increases continuously for $\mathbf{H}\parallel\mathbf{x}$ and $\mathbf{H}\parallel\mathbf{y}$, while for $\mathbf{H}\parallel\mathbf{z}$ there is step at 12, 19, and 21.5 T. These steps correspond to magnetic-field-induced changes in the ground-state spin structure. Phases I and IV are commensurate, while II, III, and V are incommensurate [36,44]. The boundary between phases II and III at 16 T, where the periodicity of the incommensurate spin structure changes [36], is hardly visible in the magnetization data [42,44]. The size of the magnetic unit cells is the same in phases I and IV [44], i.e., four spins as shown in Fig. 1.

The zero-field THz absorption spectra measured at 3.5 K are shown in Fig. 3. Three absorption lines are identified as magnetic-dipole active magnons: $\nu_1 = 16.1$ cm^{-1}, $\nu_2 = 36.2$ cm^{-1}, and $\nu_3 = 48.4$ cm^{-1}. The excitation $\nu_5 = 56.4$ cm^{-1} is an E_y^ω-active electromagnon. The excitations $\nu_4 = 54.8$ cm^{-1} and $\nu_6 = 66.4$ cm^{-1} are ME spin excitations; ν_4 is $\{E_x^\omega, H_z^\omega\}$ active, while ν_6 is present in five different combinations of oscillating electric and magnetic fields with the strongest intensity in E_z^ω polarization; see Table II. There is an E_x^ω-active broad absorption band ν_7.

All seven modes $\nu_1, \ldots, \nu_7$ are absent above T_N. Since no sign of structural changes has been found in the neutron diffraction [39] and in the spectra of Raman-active phonons at T_N [51], the lattice vibrations can be excluded and all new modes are assigned to spin excitations of LiNiPO$_4$.
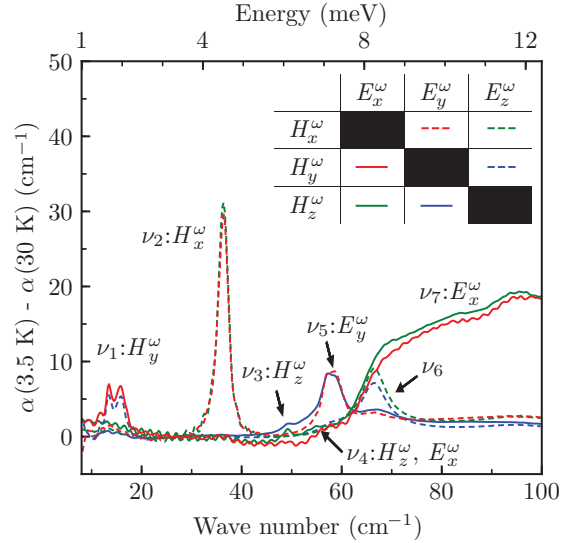

FIG. 3. THz absorption spectra of spin excitations in LiNiPO$_4$ in $H = 0$ at $T = 3.5$ K. Directions of THz radiation propagation are $\mathbf{k}\parallel\mathbf{x}$ (blue), $\mathbf{k}\parallel\mathbf{y}$ (green), and $\mathbf{k}\parallel\mathbf{z}$ (red). Two orthogonal THz radiation polarizations for a given $\mathbf{k}$ vector direction are indicated by solid and dashed lines. Directions of the oscillating THz fields $\{E_i^\omega, H_j^\omega\}$ are indicated in the inset. ν_n labels the modes, $n = 1, \ldots, 7$, with H_j^ω or E_i^ω indicating the magnetic- or electric-dipole activity of the mode, respectively. ν_4 and ν_6 are ME excitations (for the characterization of ν_6 see Table II).

The magnetic field dependence of resonance frequencies and absorption line areas is presented in Fig. 4 as obtained from the fits of the absorption peaks with the Gaussian line shapes. When the magnetic field is applied in $\mathbf{H}\parallel\mathbf{x}$ or $\mathbf{H}\parallel\mathbf{y}$ directions, Fig. 4(a) or 4(b), we found a continuous evolution of modes up to the highest field of 33 T. On the contrary, for $\mathbf{H}\parallel\mathbf{z}$ we observed discontinuities in the spin excitation frequencies, approximately at 12, 19, and 21.5 T. These fields correspond to the field values where the steps are seen in the magnetization in Fig. 2. The boundary between II and III at 16 T is not visible in the THz spectra. Apparently the spin excitation spectra are rather insensitive to the change of the magnetic unit-cell size within the incommensurate phase.

The mean-field model (Sec. III) predicts four magnon modes for a four sublattice system and they are assigned to

TABLE II. The excitation configurations of ME mode ν_6. The area of the symbol is approximately proportional to the absorption line area. The color coding is the same as in Fig. 3.
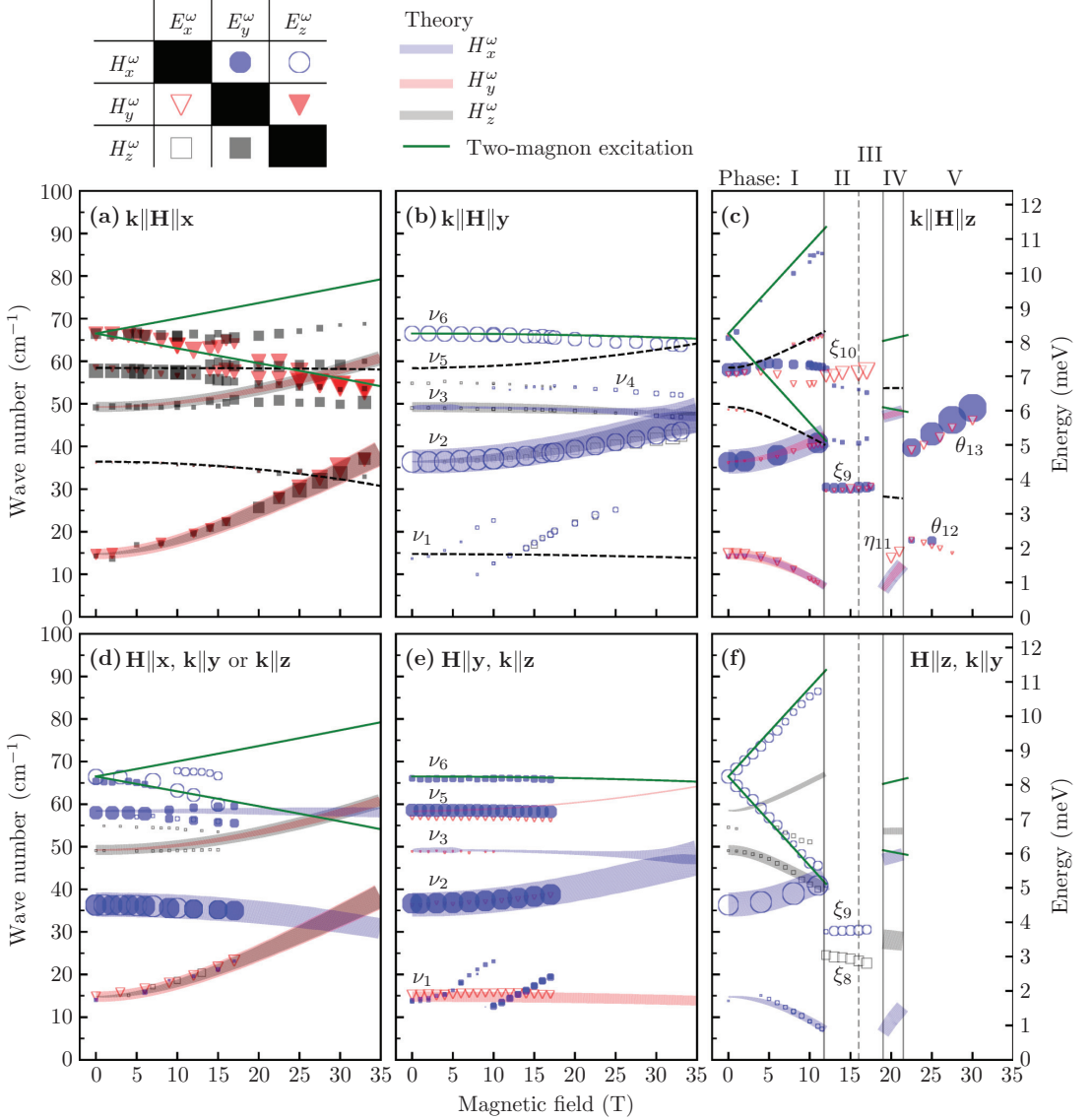
FIG. 4. Magnetic field dependence of the magnon resonance frequencies and absorption line areas at $T = 3.5$ K. Panels (a)–(c) correspond to measurements in the Faraday ($\mathbf{k} \parallel \mathbf{H}$), while panels (d)–(f) correspond to experiments in the Voigt ($\mathbf{k} \perp \mathbf{H}$) configuration. The direction of magnetic field is (a), (d) $\mathbf{H} \parallel \mathbf{x}$, (b), (e) $\mathbf{H} \parallel \mathbf{y}$, and (c), (f) $\mathbf{H} \parallel \mathbf{z}$. Symbols are the fit results of experimentally measured resonances and correspond to six combinations of $\{E_i^\omega, H_j^\omega\}$ as indicated on top of the figure. The symbol area is proportional to the experimental absorption line area. The solid lines are the results of the model calculations based on Eqs. (1)–(7). The width of the line is proportional to the square root of the line area calculated in the magnetic dipole approximation. The color of the symbol and the line is determined by the magnetic component of light: H_x^ω, blue; H_y^ω, red; and H_z^ω, black. The line positions of modes with vanishing theoretical intensity in all measured configurations of panels (a)–(c) are shown by black dashed lines. The green solid line is the two-magnon excitation ν_6. The phase boundaries determined from the magnetic field dependence of the THz spectra are shown by vertical solid lines in (c) and (f); the phase boundary between II and III, vertical dashed line, is from Refs. [42,44].

ν_1, ν_2, ν_3, and ν_5. The magnetic field dependence and the selection rules of the magnetic-dipole active magnons ν_1, ν_2, and ν_3 are reproduced well by the mean-field model, Fig. 4. However, only the energy of the magnon ν_5 is reproduced by

the model and not the intensity as this excitation is found to be an electromagnon in the experiment.

The resonances ν_4, ν_6, and the band ν_7 cannot be described within the four-sublattice mean-field model. The weak ν_4

mode is a ME spin excitation, $\{E_x^\omega, H_z^\omega\}$ active, which might be related to a spin-stretching excitation allowed for $S > 1/2$ [52]. The ν_6 mode is a ME two-magnon excitation and ν_7 is an E_x^ω-active two-magnon excitation band, as will be discussed below. The excitations ξ_8, ξ_9, ξ_{10}, and θ_{12}, θ_{13} are only present in the incommensurate phases II, III, and in phase V with more than four spins per magnetic unit cell and thus cannot be explained by the present four-sublattice model. The field dependence and the selection rules of η_{11}, the only mode found experimentally in the four-sublattice commensurate phase IV, are described by the model, Figs. 4(c) and 4(f).

There are two resonances in the vicinity of the ν_1 mode as indicated by blue symbols in Figs. 4(b) and 4(e). These two modes have a well-defined selection rule, H_x^ω. Because they are at low frequency but not described by the mean-field model we assign them to impurity modes.

The exchange parameters obtained by fitting the mean-field model to THz spectra are presented in Table I. Our model also reproduces the magnetization for commensurate phases I and IV, Fig. 2. The canting angle of spins given by the parameters of the current work, Table I and Eq. (2), is $\pm\theta = 8.1°$ in zero field, in good agreement with the value determined by elastic neutron scattering, $(7.8 \pm 2.6)°$, as reported in Refs. [36,39].

V. DISCUSSION

A. One-magnon excitations

The four sublattice mean-field model describes four magnons ν_1, ν_2, ν_3, and ν_5, among which ν_1 and ν_2 can be identified as Γ-point magnon modes observed in the INS spectra [37], whereas the ν_5 resonance has also been detected by the Raman spectroscopy [51].

The zero-field frequencies of ν_1 and ν_2 are related to the single-ion anisotropies Λ_x and Λ_y, respectively. Furthermore, the selection rules for the ν_1 and ν_2 suggest that they are anisotropy-gapped magnons, since in both cases the magnetic dipole moment oscillates perpendicular to the corresponding anisotropy axis, along y for the ν_1 mode and along x for ν_2 in zero field. Moreover, the mean-field model reproduces the rotation of the magnetic dipole moment of ν_1 (ν_2) towards the z axis in increasing magnetic field $\mathbf{H} \parallel \mathbf{y}$ ($\mathbf{H} \parallel \mathbf{x}$). The reappearance of ν_1 in phase IV, marked as η_{11}, is also predicted by the model.

The frequencies of ν_3 and ν_5 depend strongly on the weak J_{xy} and J_{xz} exchange interactions connecting the two AF systems, $\{\mathbf{S}_1, \mathbf{S}_4\}$ and $\{\mathbf{S}_2, \mathbf{S}_3\}$. While the FM J_{xz} only shifts the average frequency of ν_3 and ν_5, the AF J_{xy} affects the difference frequency. The zero-field selection rules of these excitations—magnetic dipole moment along z for ν_3 and the absence of magnetic-dipole activity of ν_5—are reproduced by the model.

Our model does not describe the incommensurate phases II, III, and V. However, it reproduces the frequency of the lowest η_{11} mode in the commensurate phase IV, Fig. 4(c).

B. Two-magnon excitations

Two-magnon excitations appear in the absorption spectra when one absorbed photon creates two magnons with the total $\mathbf{k}$ vector equal to zero [53]. The two-magnon absorption is the
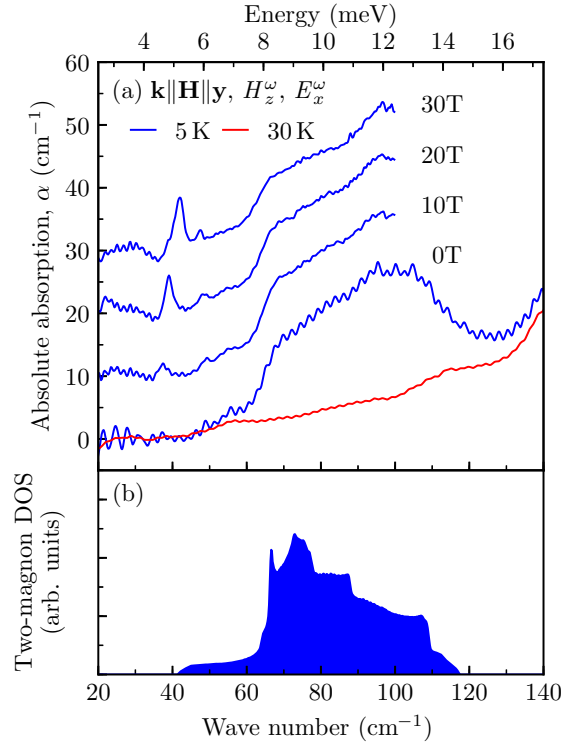

FIG. 5. (a) Two-magnon excitation band ν_7 in LiNiPO$_4$ as observed in the experiment (blue spectra). (b) Calculated two-magnon density of states. The two-magnon absorption is absent in the paramagnetic state, red line in panel (a), measured in 0 T at 30 K. All spectra are first shifted to zero absorption at 20 cm^{-1} and then a constant shift proportional to the field is added. The spectra in magnetic field were measured up to 100 cm^{-1}.

strongest where the density of magnon states is the highest, usually at the Brillouin-zone boundary. Since the product of the two spin operators has the same time-reversal parity as the electric dipole moment, the two-magnon excitation by the electric field is allowed; this mechanism usually dominates over the magnetic-field-induced two-magnon excitation [53].

The broad absorption band between 60 and 115 cm^{-1}, shown in Fig. 5(a), appears below T_N and is E_x^ω active. A similar excitation band observed by Raman scattering was attributed to spin excitations [51]. In another olivine-type crystal LiMnPO$_4$, a broad band in the Raman spectrum was assigned to a two-magnon excitation with the line shape reproduced using the magnon density of states (DOS) [54]. We calculated the magnon DOS numerically on a finite-size sample of $4 \times 4 \times 4$ unit cells with 256 spins using the model represented by Eq. (1) but extended by the J_y and J_z couplings shown in Fig. 1. The two-magnon DOS was obtained by doubling the energy scale of the single-magnon DOS and is shown in Fig. 5(b). Since the observed broad absorption band emerges in the energy range of the high magnon DOS we assign this absorption band to a two-magnon excitation.

There is another dominantly electric-dipole active spin resonance ν_6 at 66.5 cm^{-1} not reproduced by our mean-field model. Since the frequency of the electric-dipole active ν_6 mode is at the maximum of the two-magnon DOS and in a magnetic field, $\mathbf{H} \parallel \mathbf{z}$, splits into a lower and an upper resonances with effective g factors $g_- = 4.24 \pm 0.07$ and $g_+ = 4.00 \pm 0.04$, i.e., two times larger than that expected for one spin-flip excitation, we interpret the ν_6 resonance as a two-magnon excitation. The singular behavior in the DOS coinciding with the ν_6 resonance peak corresponds to the flat magnon dispersion along the R–T line in the Brillouin zone. This mode is weakly magnetic-dipole active as well and is therefore a ME resonance.

The magnetic field dependence of the two-magnon excitation ν_6 was modeled by calculating the field dependence of the magnon DOS. The result is shown in Fig. 4. The splitting of the resonance in magnetic field is observed only for $\mathbf{H} \parallel \mathbf{z}$ and is reproduced by the model calculation. In the calculation J_y was set to 0.65 meV to reproduce the instability of phase I at 12 T, while $J_z = 0.16$ meV was used to reproduce the zero-field frequency of ν_6. The magnitude of J_y and J_z is similar to the ones in INS studies [36–38] but J_z has the opposite sign. In high-symmetry cases the electric-dipole selection rules of two-magnon excitations can be reproduced by group-theoretical analysis [55], but the low magnetic symmetry of LiNiPO$_4$ hinders such an analysis. Nevertheless, it is expected that the $\Delta S = 0$ two-magnon continuum ν_7 has different selection rules than the $\Delta S = 2$ two-magnon excitation ν_6 due to their different symmetry.

VI. CONCLUSIONS

We measured the magnetic field dependence of THz absorption spectra in various magnetically ordered phases of LiNiPO$_4$. We have revealed a variety of spin resonance modes: three magnons, an electromagnon, an electric-dipole active two-magnon excitation band, and a magnetoelectric two-magnon excitation. The abrupt changes in the magnon absorption spectra coincide with the magnetic phase boundaries in LiNiPO$_4$. The magnetic dipole selection rules for magnon absorption and the magnetic field dependence of magnon frequencies in the commensurate magnetic phases are described with a mean-field spin model. With this model the additional information obtained from the magnetic field dependence of mode frequencies allowed us to refine the values of exchange couplings, single-ion anisotropies, and Dzyaloshinskii-Moriya interaction. The significant differences found in magnetic interaction parameters compared to former studies are the opposite sign of J_z exchange coupling, the smaller values of the J_{xy} exchange coupling and the Λ_x and Λ_y anisotropies. The mean-field model did not explain the observed magnetoelectric excitation ν_4 and the spin excitations in the incommensurate phases. In the future, more about the magnetoelectric nature of LiNiPO$_4$ spin excitations can be learned from nonreciprocal directional dichroism studies as in LiCoPO$_4$ [24].

[1] T. Kimura, T. Goto, H. Shintani, K. Ishizaka, T. Arima, and Y. Y. Tokura, Nature (London) **426**, 55 (2003).

[2] M. Fiebig, J. Phys. D: Appl. Phys. **38**, R123 (2005).

[3] N. A. Spaldin and M. Fiebig, Science **309**, 391 (2005).

[4] W. Eerenstein, N. D. Mathur, and J. F. Scott, Nature (London) **442**, 759 (2006).

[5] S.-W. Cheong and M. Mostovoy, Nat. Mater. **6**, 13 (2007).

[6] M. Fiebig and N. A. Spaldin, Eur. Phys. J. B **71**, 293 (2009).

[7] S. Dong, J.-M. Liu, S.-W. Cheong, and Z. Ren, Adv. Phys. **64**, 519 (2015).

[8] M. Fiebig, T. Lottermoser, D. Meier, and M. Trassin, Nat. Rev. Mater. **1**, 16046 (2016).

[9] G. L. J. A. Rikken and E. Raupach, Nature (London) **390**, 493 (1997).

[10] G. L. J. A. Rikken, C. Strohm, and P. Wyder, Phys. Rev. Lett. **89**, 133005 (2002).

[11] L. D. Barron, *Molecular Light Scattering and Optical Activity*, 2nd ed. (Cambridge University Press, Cambridge, UK, 2004).

[12] T. Arima, J. Phys.: Condens. Matter **20**, 434211 (2008).

[13] D. Szaller, S. Bordács, V. Kocsis, T. Rõõm, U. Nagel, and I. Kézsmárki, Phys. Rev. B **89**, 184419 (2014).

[14] I. Kézsmárki, N. Kida, H. Murakawa, S. Bordács, Y. Onose, and Y. Tokura, Phys. Rev. Lett. **106**, 057403 (2011).

[15] S. Bordács, I. Kézsmárki, D. Szaller, L. Demkó, N. Kida, H. Murakawa, Y. Onose, R. Shimano, T. Rõõm, U. Nagel *et al.*, Nat. Phys. **8**, 734 (2012).

[16] Y. Takahashi, R. Shimano, Y. Kaneko, H. Murakawa, and Y. Tokura, Nat. Phys. **8**, 121 (2012).

[17] I. Kézsmárki, D. Szaller, S. Bordács, V. Kocsis, Y. Tokunaga, Y. Taguchi, H. Murakawa, Y. Tokura, H. Engelkamp, T. Rõõm *et al.*, Nat. Commun. **5**, 3203 (2014).

[18] I. Kézsmárki, U. Nagel, S. Bordács, R. S. Fishman, J. H. Lee, H. T. Yi, S.-W. Cheong, and T. Rõõm, Phys. Rev. Lett. **115**, 127203 (2015).

[19] A. M. Kuzmenko, V. Dziom, A. Shuvaev, A. Pimenov, M. Schiebl, A. A. Mukhin, V. Y. Ivanov, I. A. Gudim, L. N.

Bezmaternykh, and A. Pimenov, Phys. Rev. B **92**, 184409 (2015).

[20] S. Bordács, V. Kocsis, Y. Tokunaga, U. Nagel, T. Rõõm, Y. Takahashi, Y. Taguchi, and Y. Tokura, Phys. Rev. B **92**, 214441 (2015).

[21] Y. Okamura, F. Kagawa, S. Seki, M. Kubota, M. Kawasaki, and Y. Tokura, Phys. Rev. Lett. **114**, 197202 (2015).

[22] Y. Nii, R. Sasaki, Y. Iguchi, and Y. Onose, J. Phys. Soc. Jpn. **86**, 024707 (2017).

[23] S. Yu, B. Gao, J. W. Kim, S.-W. Cheong, M. K. L. Man, J. Madéo, K. M. Dani, and D. Talbayev, Phys. Rev. Lett. **120**, 037601 (2018).

[24] V. Kocsis, K. Penc, T. Rõõm, U. Nagel, J. Vít, J. Romhányi, Y. Tokunaga, Y. Taguchi, Y. Tokura, I. Kézsmárki *et al.*, Phys. Rev. Lett. **121**, 057601 (2018).

[25] J. Viirok, U. Nagel, T. Rõõm, D. G. Farkas, P. Balla, D. Szaller, V. Kocsis, Y. Tokunaga, Y. Taguchi, Y. Tokura *et al.*, Phys. Rev. B **99**, 014410 (2019).

[26] Y. Okamura, S. Seki, S. Bordács, A. Butykai, V. Tsurkan, I. Kézsmárki, and Y. Tokura, Phys. Rev. Lett. **122**, 057202 (2019).

[27] A. Pimenov, A. A. Mukhin, V. Y. Ivanov, V. D. Travkin, A. M. Balbashov, and A. Loidl, Nat. Phys. **2**, 97 (2006).

[28] M. Mercier and J. Gareyte, Solid State Commun. **5**, 139 (1967).

[29] M. Mercier, J. Gareyte, and E. F. Bertaut, C. R. Acad. Sci. Paris **264**, 979 (1967).

[30] M. Mercier and P. Bauer, C. R. Acad. Sci. Paris **267**, 465 (1968).

[31] M. Mercier, E. F. Bertaut, G. Quézel, and P. Bauer, Solid State Commun. **7**, 149 (1969).

[32] J.-P. Rivera, Ferroelectrics **161**, 147 (1994).

[33] I. Kornev, M. Bichurin, J.-P. Rivera, S. Gentil, H. Schmid, A. G. M. Jansen, and P. Wyder, Phys. Rev. B **62**, 12247 (2000).

[34] R. Toft-Petersen, M. Reehuis, T. B. S. Jensen, N. H. Andersen, J. Li, M. D. Le, M. Laver, C. Niedermayer, B. Klemke, K. Lefmann *et al.*, Phys. Rev. B **92**, 024404 (2015).

[35] V. M. Khrustalyov, V. N. Savytsky, and M. F. Kharchenko, Low Temp. Phys. **43**, 1332 (2017).

[36] R. Toft-Petersen, J. Jensen, T. B. S. Jensen, N. H. Andersen, N. B. Christensen, C. Niedermayer, M. Kenzelmann, M. Skoulatos, M. D. Le, K. Lefmann, S. R. Hansen, J. Li, J. L. Zaretsky, and D. Vaknin, Phys. Rev. B **84**, 054408 (2011).

[37] T. B. S. Jensen, N. B. Christensen, M. Kenzelmann, H. M. Rønnow, C. Niedermayer, N. H. Andersen, K. Lefmann, M.

Jiménez-Ruiz, F. Demmel, J. Li *et al.*, Phys. Rev. B **79**, 092413 (2009).

[38] J. Li, T. B. S. Jensen, N. H. Andersen, J. L. Zarestky, R. W. McCallum, J.-H. Chung, J. W. Lynn, and D. Vaknin, Phys. Rev. B **79**, 174435 (2009).

[39] T. B. S. Jensen, N. B. Christensen, M. Kenzelmann, H. M. Rønnow, C. Niedermayer, N. H. Andersen, K. Lefmann, J. Schefer, M. Zimmermann, J. Li *et al.*, Phys. Rev. B **79**, 092412 (2009).

[40] Y. N. Kharchenko, N. F. Kharcheno, M. Baran, and R. Szymczak, Low Temp. Phys. **29**, 579 (2003).

[41] D. Vaknin, J. L. Zarestky, J.-P. Rivera, and H. Schmid, Phys. Rev. Lett. **92**, 207201 (2004).

[42] V. Khrustalyov, V. Savitsky, and N. Kharchenko, Czech. J. Phys. **54**, 27 (2004).

[43] V. M. Khrustalyov, V. M. Savytsky, and M. F. Kharchenko, Low Temp. Phys. **42**, 1126 (2016).

[44] R. Toft-Petersen, E. Fogh, T. Kihara, J. Jensen, K. Fritsch, J. Lee, G. E. Granroth, M. B. Stone, D. Vaknin, H. Nojiri *et al.*, Phys. Rev. B **95**, 064421 (2017).

[45] P. J. Baker, I. Franke, F. L. Pratt, T. Lancaster, D. Prabhakaran, W. Hayes, and S. J. Blundell, Phys. Rev. B **84**, 174403 (2011).

[46] O. García-Moreno, M. Alvarez-Vega, J. García-Jaca, J. M. Gallardo-Amores, M. L. Sanjuán, and U. Amador, Chem. Mater. **13**, 1570 (2001).

[47] R. Santoro, D. Segal, and R. Newnham, J. Phys. Chem. Solids **27**, 1192 (1966).

[48] D. Vaknin, J. L. Zarestky, J. E. Ostenson, B. C. Chakoumakos, A. Goñi, P. J. Pagliuso, T. Rojo, and G. E. Barberis, Phys. Rev. B **60**, 1100 (1999).

[49] R. M. White, *Quantum Theory of Magnetism* (Springer-Verlag, Berlin, Heidelberg, 2007).

[50] T. L. Gilbert, IEEE Trans. Magn. **40**, 3443 (2004).

[51] V. I. Fomin, V. P. Gnezdilov, V. S. Kurnosov, A. V. Peschanskii, A. V. Yeremenko, H. Schmid, J.-P. Rivera, and S. Gentil, Low Temp. Phys. **28**, 203 (2002).

[52] K. Penc, J. Romhányi, T. Rõõm, U. Nagel, A. Antal, T. Fehér, A. Jánossy, H. Engelkamp, H. Murakawa, Y. Tokura *et al.*, Phys. Rev. Lett. **108**, 257203 (2012).

[53] P. L. Richards, J. Appl. Phys. **38**, 1500 (1967).

[54] C. C. Filho, P. Gomes, A. García-Flores, G. Barberis, and E. Granado, J. Magn. Magn. Mater. **377**, 430 (2015).

[55] R. Loudon, Adv. Phys. **17**, 243 (1968).

Appendix 2

II

J. Vit, J. Viirok, L. Peedu, T. Rõõm, U. Nagel, V. Kocsis, Y. Tokunaga, Y. Taguchi, Y. Tokura, I. Kézsmárki, P. Balla, K. Penc, J. Romhányi, and S. Bordács, "In situ electric-field control of THz nonreciprocal directional dichroism in the multiferroic $Ba_2CoGe_2O_7$," *Phys. Rev. L*, vol. 127, p. 157201, July 2021

In Situ Electric-Field Control of THz Nonreciprocal Directional Dichroism in the Multiferroic Ba$_2$CoGe$_2$O$_7$

J. Vít,[1,2,3] J. Viirok,[4] L. Peedu,[4] T. Rõõm,[4] U. Nagel,[4] V. Kocsis,[5] Y. Tokunaga,[5,6] Y. Taguchi,[5] Y. Tokura,[5,7] I. Kézsmárki,[1,8] P. Balla,[9] K. Penc,[9] J. Romhányi,[10] and S. Bordács[1,11]

[1]*Department of Physics, Budapest University of Technology and Economics, 1111 Budapest, Hungary*
[2]*Institute of Physics ASCR, Na Slovance 2, 182 21 Prague 8, Czech Republic*
[3]*Faculty of Nuclear Science and Physical Engineering, Czech Technical University, Břehová 7, 115 19 Prague 1, Czech Republic*
[4]*National Institute of Chemical Physics and Biophysics, Akadeemia tee 23, 12618 Tallinn, Estonia*
[5]*RIKEN Center for Emergent Matter Science (CEMS), Wako 351-0198, Japan*
[6]*Department of Advanced Materials Science, University of Tokyo, Kashiwa 277-8561, Japan*
[7]*Department of Applied Physics and Tokyo College, University of Tokyo, Tokyo 113-8656, Japan*
[8]*Experimental Physics V, Center for Electronic Correlations and Magnetism, University of Augsburg, 86135 Augsburg, Germany*
[9]*Institute for Solid State Physics and Optics, Wigner Research Centre for Physics, P.O. Box. 49, H-1525 Budapest, Hungary*
[10]*Department of Physics and Astronomy, University of California, Irvine, 4129 Frederick Reines Hall, Irvine, California 92697, USA*
[11]*Hungarian Academy of Sciences, Premium Postdoctor Program, 1051 Budapest, Hungary*

Nonreciprocal directional dichroism, also called the optical-diode effect, is an appealing functional property inherent to the large class of noncentrosymmetric magnets. However, the *in situ* electric control of this phenomenon is challenging as it requires a set of conditions to be fulfilled: Special symmetries of the magnetic ground state, spin excitations with comparable magnetic- and electric-dipole activity, and switchable electric polarization. We demonstrate the isothermal electric switch between domains of Ba$_2$CoGe$_2$O$_7$ possessing opposite magnetoelectric susceptibilities. Combining THz spectroscopy and multiboson spin-wave analysis, we show that unbalancing the population of antiferromagnetic domains generates the nonreciprocal light absorption of spin excitations.

The interaction between light and matter may produce fascinating phenomena. Among them is the nonreciprocal directional dichroism (NDD), when the absorption differs for the propagation of light along and opposite to a specific direction. In contrast to the magnetic circular dichroism, the absorption difference for NDD is finite even for unpolarized light. The chirality of the light lies at the heart of the phenomenon: the electric ($\mathbf{E}^\omega$) and magnetic ($\mathbf{H}^\omega$) field components of the light and its propagation vector $\mathbf{k} \propto \mathbf{E}^\omega \times \mathbf{H}^\omega$ form a right-handed system. Applying orthogonal static electric ($\mathbf{E}$) and magnetic ($\mathbf{H}$) fields to a material breaks the inversion and time-reversal symmetries, leading to the observation of NDD [1]. Such a symmetry breaking is inherent to magnetoelectric (ME) multiferroics, materials with coexisting electric and magnetic orders. In multiferroics, the ME coupling establishes a connection between responses to electric and magnetic fields: an external electric field generates magnetization $\mathbf{M}$, and a magnetic field induces electric polarization $\mathbf{P}$ in the sample. The NDD is manifested by the refractive index difference $\Delta N = N_+ - N_-$ for counterpropagating ($\pm\mathbf{k}$) linearly polarized beams [2–4]. In the long-wavelength limit,

$$N_\pm = \sqrt{\varepsilon_{\alpha\alpha}\mu_{\beta\beta}} \pm \chi_{\alpha\beta}^{em}, \tag{1}$$

where $\varepsilon_{\alpha\alpha}$ and $\mu_{\beta\beta}$ are the components of the permittivity and the permeability tensors for oscillating fields polarized along E_α^ω and H_β^ω, and $\chi_{\alpha\beta}^{em}$ is the ME susceptibility characterizing the induced polarization $\delta P_\alpha^\omega \propto \chi_{\alpha\beta}^{em} H_\beta^\omega$. The $\chi_{\alpha\beta}^{em}$ becomes resonantly enhanced for spin excitations of multiferroics endowed with a mixed magnetic and electric dipole character giving rise to strong NDD [2–9].

Since $\Delta N \propto \chi_{\alpha\beta}^{em}$, the absorbing and transparent directions are determined by the sign of ME susceptibility, and therefore, they can be interchanged by the sign reversal of the $\chi_{\alpha\beta}^{em}$. The magnetic field can naturally switch between time-reversed magnetic states with opposite signs of ME responses, and allows the control of NDD [2–4]. Can we achieve a similar switch with an electric field, which is a time-reversal even quantity? Apart from being a fundamental question, the voltage control of NDD may promote the application of multiferroics in GHz–THz frequency data transmission and signal processing devices with reduced size and energy consumption. In addition to the

157201-1

NDD, the electric-field-induced switching between time-reversed magnetic states would also provide an efficient way to control other optical ME effects, such as chirality of magnons [3,10,11] or axion-term-induced gyrotropy [12]. The ME coupling may help us to achieve the desired control of magnetic states [5,7,13–16], however, realizing this effect is not at all trivial. It requires a magnetic order permitting NDD and a polarization that is switchable by laboratory electric fields. In the visible spectral range, the realization of this effect has been confirmed for charge excitations [14,15]. However, studies in the THz range of spin-wave excitations are scarce. So far, mostly ME poling was used to select between time-reversed domains by cooling the sample through the ordering temperature in external magnetic and electric fields [5,7,16]. The electric field induced changes in the absorption coefficient were detected only recently [17].

In this Letter, we demonstrate the isothermal electric field control of the THz frequency NDD in $Ba_2CoGe_2O_7$, which provides an ideal model system due to its simple antiferromagnetic (AFM) order. The electric field switches between the transparent and absorbing directions, where the absorption difference between the two is experimentally found as high as 30%. We attribute the observed change of the NDD to the electric-field-induced imbalance in the population of the AFM domains.

The discovery of the ME properties of $Ba_2CoGe_2O_7$ [18], followed by a detection of the gigantic ME effect in $Ca_2CoSi_2O_7$ [19] aroused interest in this family of quasi-two-dimensional compounds. They crystallize in the noncentrosymmetric $P\bar{4}2_1m$ structure, where the unit cell includes two spin-3/2 magnetic Co^{2+} ions, as shown in Fig. 1(a). Below $T_N = 6.7$ K, the spins order in a

FIG. 1. (a) The canted antiferromagnetic order of $Ba_2CoGe_2O_7$ in domain I in zero fields. Cyan circles denote the Co^{2+} ions with $S = 3/2$ (dark red arrows) in the center of the O^{2-} tetrahedra (grey). The symmetry operations are the 2_1 screw axis, (black half-arrow) and the orthogonal $2'_1$ screw axis followed by the time reversal (red half-arrow). **M** and **L** correspond to the uniform and staggered sublattice magnetizations, respectively. (b) The four antiferromagnetic domains. A magnetic field applied along the [001] axis induces a polarization $\delta\mathbf{P}$ (light blue arrows) via linear magnetoelectric effect.

two-sublattice easy-plane AFM structure [20]. A small in-plane anisotropy pins the AFM ordering vector $\mathbf{L} = \mathbf{M}_A - \mathbf{M}_B$ to one of the symmetry-equivalent $\langle 100 \rangle$ directions of the tetragonal plane, as shown in Fig. 1 [21–23]. Applying an external magnetic field $\mathbf{H} \parallel [110]$ rotates the **L** vector to $[1\bar{1}0]$, and gives rise to a sizeable ferroelectric polarization **P** along the tetragonal [001] axis [24]. The same ME interaction leads to NDD for the THz spin excitations of $Ba_2CoGe_2O_7$ [25,26], which has been observed for in-plane magnetic fields: (i) for light propagation **k** along the cross product of the magnetic field $\mathbf{H} \parallel [110]$ and the magnetic-field-induced polarization $\mathbf{P} \parallel [001]$ [2,4], and (ii) for $\mathbf{k} \parallel \mathbf{H} \parallel [100]$ when a chiral state is realized [3].

Both the static and the dynamic ME response of $Ba_2CoGe_2O_7$ are consistently explained by the spin-dependent p–d hybridization [24–28]. In this mechanism, the spin-quadrupole operators of the $S = 3/2$ cobalt spin directly couple to the induced polarization $\mathbf{P}_j$,

$$P_j^a \propto -\cos 2\kappa_j (S_j^b S_j^c + S_j^c S_j^b) + \sin 2\kappa_j (S_j^a S_j^c + S_j^c S_j^a),$$
$$P_j^b \propto -\cos 2\kappa_j (S_j^a S_j^c + S_j^c S_j^a) - \sin 2\kappa_j (S_j^b S_j^c + S_j^c S_j^b),$$
$$P_j^c \propto -\cos 2\kappa_j (S_j^a S_j^b + S_j^b S_j^a) + \sin 2\kappa_j [(S_j^a)^2 - (S_j^b)^2],$$

$$(2)$$

where j is the site index, and a, b, c are parallel to [100], [010], and [001], respectively. $\kappa_j = \kappa$ in A sublattice and $\kappa_j = -\kappa$ in B sublattice account for the different orientation of the tetrahedra [see Fig. 1(a)]. The same mechanism is the source of the multiferroic properties of $Sr_2CoSi_2O_7$ [29], the observation of spin-quadrupolar excitations in $Sr_2CoGe_2O_7$ in the field aligned phase [30], and the microwave non-reciprocity of magnons in $Ba_2MnGe_2O_7$ [31].

The clue how to control the NDD using electric fields comes from the experiment of Murakawa et al. [24]. They showed that a magnetic field applied nearly parallel to the tetragonal axis induces an in-plane electric polarization along one of the $\langle 100 \rangle$ directions. The hysteresis of the polarization observed upon tilting the field away from the [001] axis suggests a rearrangement of the magnetic domain population. The AFM order reduces the space group symmetry from $P\bar{4}2_1m1'$ to $P2'_12_12'$, corresponding to the breaking of the rotoreflection symmetry $\bar{4}$, and the formation of four magnetic domains, shown in Fig. 1(b) [32]. The $P2'_12_12'$ symmetry gives rise to a finite χ^{em}, and in a magnetic field $\mathbf{H} \parallel [001]$, a polarization $\delta\mathbf{P}$ parallel to the **L** develops, as shown in Fig. 1(b). If the field is perfectly aligned $\mathbf{H} \parallel [001]$, the four domains remain equivalent and the field-induced polarizations $\delta\mathbf{P}$ cancel out. However, a small perturbation such as tilting of the magnetic field or applying an in-plane electric field can break the delicate balance between the domains. In our experiments, we exploit this highly susceptible state to
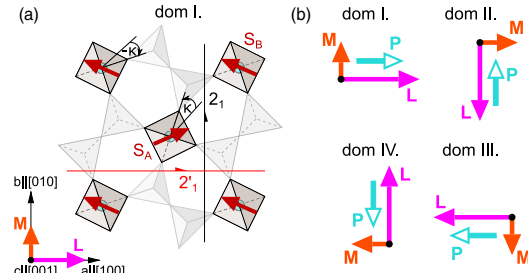
change the relative population of the domains by electric field, $\mathbf{E}\|[100]$, and attain control over the NDD, present for $\mathbf{k}\|\mathbf{E}\times\mathbf{H}$.

$Ba_2CoGe_2O_7$ single crystals were grown by the floating zone technique as described in [24]. Silver paste electrodes were painted on the parallel sides of a $2\times3\times0.7$ mm^3 rectangular (010) cut. The THz spectra were measured in Tallinn with a Martin-Puplett interferometer and a 0.3 K silicon bolometer. We applied the external magnetic and electric fields in the $\mathbf{H}\|[001]$ and $\mathbf{E}\|[100]$ directions, while the THz radiation propagated along the $\mathbf{k}\|[010]$ axis. The crystallographic axes of the sample were oriented by x-ray Laue diffraction and aligned in the THz experiment to, at least, $1°$ precision. The THz absorption spectra were deduced as described in Ref. [33].

Our main experimental results are summarized in Fig. 2. Panel 2(a) displays the average and 2(b) the difference of the THz absorption spectra measured in electric fields with opposite signs ($E=\pm3$ kV/cm) and constant magnetic fields. In agreement with former results [26], we assign the absorption peak around 18 cm^{-1} (mode No. 1) to the optical magnon excitation of the easy-plane AFM ground state, whereas resonances No. 2, No. 3, and No. 4, showing a V shape splitting in magnetic fields, are attributed to the spin stretching modes involving the modulation of the spin length. In a finite magnetic field, the absorption spectra become different for the opposite signs of the electric field as evidenced by Fig. 2(b) for the light polarization $\mathbf{E}^{\omega}\|[001]$ and $\mathbf{H}^{\omega}\|[100]$. The electric field odd component of the signal is the manifestation of the NDD, and it shows that the absorption is different for light propagation along or opposite to the cross product of the static electric and magnetic fields $\mathbf{E}\times\mathbf{H}$. This relation is further supported by the fact that the differential absorption spectra change sign under the reversal of the external magnetic field. The NDD is finite only for the spin stretching modes No. 2 and No. 3 and it increases with magnetic fields up to ~12 T. We note that, for the orthogonal light polarization, $\mathbf{E}^{\omega}\|[100]$ and $\mathbf{H}^{\omega}\|[001]$, we did not find electric-field-induced absorption difference within the accuracy of the experiment.

The electric-field-induced change in the absorption spectra around mode No. 3, measured with respect to the zero-field-cooled state, is displayed in Fig. 3(a). The peak absorption, shown in Fig. 3(b), depends on the electric field history of the sample: the initial and the following upward and downward sweeps are all different, and the absorption difference has a small but finite remanence [34]. Furthermore, the electric field can change the absorption only below T_N as displayed in Fig. 3(c), though the intensity of the spin stretching mode remains finite even above T_N [2]. All of these findings suggest that the observed electric field effect arises only in the magnetically ordered phase, and it is related to switching between domain states possessing different NDD.
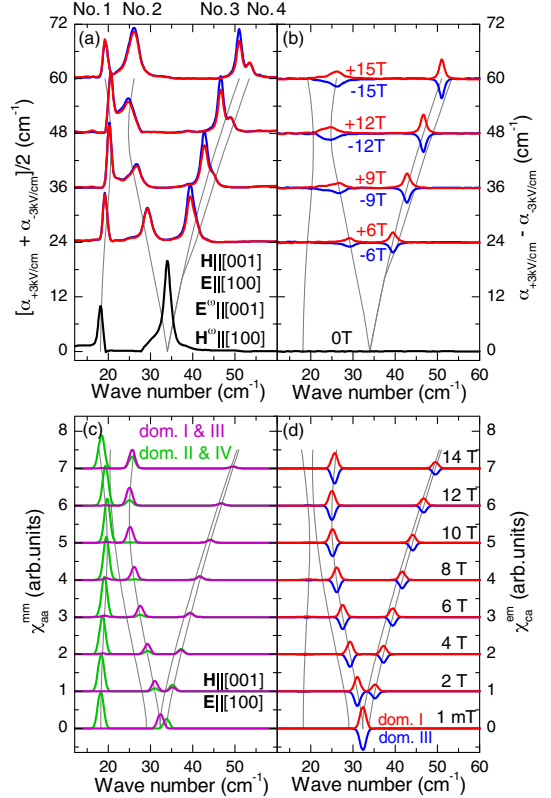

FIG. 2. (a) Magnetic field dependence of the THz absorption spectra averaged for the measurements performed in electric fields with opposite signs, $E=\pm3$ kV/cm at $T=3.5$ K. The light polarization is $\mathbf{E}^{\omega}\|[001]$ and $\mathbf{H}^{\omega}\|[100]$. The spectra measured in positive (red) or negative (blue) magnetic fields $\mathbf{H}\|[001]$ are shifted in proportion with the absolute value of the field. Grey lines indicate the magnetic field dependence of the resonance energies (peak Nos. 1–4). (b) shows the electric field-induced change in the absorption spectra as the difference of the absorption spectra recorded in $E=\pm3$ kV/cm. (c) The magnetic susceptibility calculated from the spin-wave theory in domains I and III (purple) and in domains II and IV (green). (d) The ME susceptibility in domain I (red) and domain III (blue).

Considering the symmetries of the zero-field ground state shown in Fig. 1(a), the (unitary) 2_1 screw axis restricts NDD for light propagation $\mathbf{k}\|\mathbf{c}\times\mathbf{L}$ in a given domain. When a magnetic field is applied along $\mathbf{H}\|[001]$, only the $2_1'$ symmetry remains. The S^b, S^c, P^a operators are even, while S^a, P^b, P^c are odd under $2_1'$ in domain I, depicted in Fig. 1(a). Since time reversal makes this symmetry antiunitary, the operators are either even or odd under conjugation, restricting the transition matrix elements to be either real or imaginary [34,35]. As a consequence, the real part of a ME susceptibility combined from an even and odd

operator vanishes, annulling the time-reversal odd part of χ_{bc}^{em} and χ_{cb}^{em}, thus, forbidding NDD in domain I when $\mathbf{k} \| [100]$. The $2'_1$ does not affect NDD in the other propagation directions, and indeed, this is what we observed for $\mathbf{k} \| [010]$. In finite fields, we also expect NDD for the $\mathbf{k} \| [001]$—but then, the analysis of results would be more complicated as the Faraday effect mixes the polarization states of the light.

In order to interpret the experimental results quantitatively, we considered the microscopic Hamiltonian of interacting $S = 3/2$ Co^{2+} spins following Refs. [25,26]

$$
\begin{aligned}
\mathcal{H} = \sum_{\langle i,j \rangle} [J(\hat{S}_i^a \hat{S}_j^a + \hat{S}_i^b \hat{S}_j^b) + J^c \hat{S}_i^c \hat{S}_j^c] + \sum_i \Lambda(\hat{S}_i^c)^2 \\
- \sum_i [g_{cc} H_c \hat{S}_i^c + E_a \hat{P}_i^a],
\end{aligned} \tag{3}
$$

where summation $\langle i, j \rangle$ runs over the nearest neighbors. Beside the anisotropic exchange coupling (J and J^c), single-ion anisotropy Λ, and the Zeeman term, we introduce the coupling between the external electric field, E_a, and the spin-induced polarization [see Eq. (2)], which breaks the O(2) symmetry of the model.

We calculated the excitations above a variational site-factorized ground state using a multiboson spin-wave theory, following Ref. [26]. The approximate O(2) symmetry of the Hamiltonian (even for finite H_c) is reflected in the ground state manifold, the application of a tiny $E_a > 0$ combined with $H_c > 0$ selects domain I in Fig. 1(b), while $E_a < 0$ selects domain III as the variational ground state. We note that, even in the highest fields, the ME energy [24] is at least an order of magnitude smaller than the in-plane anisotropy [22], thus, the rotation of the AFM vector $\mathbf{L}$ away from the principal axes is negligible (e.g., [23]). The magnetic dipole strengths of the excitations are estimated by the transition matrix elements of the spin operators $|\langle 0|\hat{S}^\alpha|n\rangle|^2$ between the ground state $|0\rangle$ and the excited states $|n\rangle$. The contribution of the magnetic dipole processes to the absorption is shown in Fig. 2(c). The electric dipole matrix elements are evaluated similarly for polarization components $\hat{P}^\beta$. The ME susceptibility, $\chi_{ca}^{em} \propto \langle 0|P_c|n\rangle\langle n|S_a|0\rangle$ is plotted in Fig. 2(d).

For light polarization $\mathbf{E}^\omega \| [001]$ and $\mathbf{H}^\omega \| [100]$, our model predicts that two spin stretching modes have finite ME susceptibility χ_{ca}^{em} and, correspondingly, show NDD with the same sign. The overall sign of the ME response is reversed upon the reversal of either the static electric or the magnetic field related to the switching from domain I to III. All of these findings are in agreement with the experiments and imply that the electric field control of the NDD is realized by influencing the AFM domains. We note that, among modes No. 3 and No. 4, which show a tiny splitting in high fields, resonance No. 3 is NDD active in the experiment, whereas our theory predicts NDD for the higher energy mode. However, we found no obvious way to reproduce the

fine structure of the resonance energies within our model or by including other realistic terms [21,24,25].

Although theory predicts that individual domains possess a finite dichroism as $H_c \to 0$ [see Fig. 3(b)], we observed vanishing NDD in this limit. This suggests that domain walls relax toward their initial positions, and the domain population evens out as fields go to zero. The multidomain state may be favored by: (i) electric dipole-dipole interaction between the ferroelectric domains; (ii) elastic energy, since the AFM domains break the tetragonal symmetry, they can couple to orthorhombic distortion [36]. The finite intensity of mode No. 1 also indicates that domains II and IV coexist with domains I and III. In domains I and III, excitation No. 1 is silent for this light polarization according to the calculation, since it can only be excited by the $\mathbf{H}^\omega \| [010]$, which is perpendicular to $\mathbf{L} \| [100]$. The polarization matrix element is also negligible for this resonance. Therefore, domains II and IV with finite magnetic dipole strength for $\mathbf{H}^\omega \| [100]$ [see Fig. 2(c)] should also be present in the studied sample. Thus, one expects even stronger NDD than observed experimentally here, if the monodomain state of either domain I or domain III can be realized. Finally, we note that the small difference in the averaged absorption [Fig. 2(a)] observed for the reversal of the magnetic field is probably caused by a small misalignment. When the magnetic field is
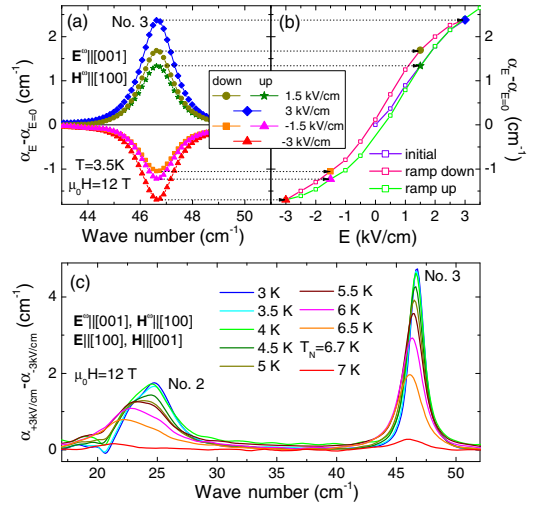
FIG. 3. (a) The electric field induced change in the absorption spectra measured with respect to the zero field cooled state at 3.5 K and in fixed magnetic field 12 T. (b) The hysteresis of the electric field dependence of the peak absorption. The horizontal arrows connect corresponding points of panels (a) and (b). (c) Temperature dependence of the electric field induced change in the absorption spectra measured in 12 T.

slightly tilted toward the light propagation $\mathbf{k}\|[010]$, the balance between domains I and III can be broken.

The absence of the NDD for the orthogonal light polarization, $\mathbf{E}^{\omega}\|[100]$ and $\mathbf{H}^{\omega}\|[001]$, can be explained by the smallness of the χ_{ac}^{em}. Because of the nearly preserved O(2) symmetry of the system, the magnetic matrix element in χ_{ac}^{em} involves the $\hat{S}^c$, which commutes with the terms of the Hamiltonian in Eq. (3) except for the $\mathbf{E} \cdot \mathbf{P}$. Therefore, the dipole oscillator strength for S^c—given by the double commutator [37]—is tiny compared to other matrix elements.

In summary, we demonstrated the isothermal voltage control of the nonreciprocal THz absorption in $Ba_2CoGe_2O_7$. In contrast to former studies applying ME poling, here, the ME polarization is induced by a magnetic field preserving the nearly O(2) symmetric ground states. The degeneracy within this manifold allows efficient voltage control of the magnetic domain population and, so, of the NDD. A similar mechanism may give rise to NDD in ME spin-spiral compounds, e.g., Cu_2OSeO_3 or $CoCr_2O_4$ with multidomain states. Our results can promote the applications of multiferroics in voltage-controlled high-frequency devices and stimulate search for compounds with stronger remanence and higher ordering temperatures.

Note added.—During the preparation of this manuscript, we become aware of the related work of Kimura *et al.*, who study the electric field control of microwave NDD of the triplet Bose-condensate in $TlCuCl_3$ [38].

[1] G. L. J. A. Rikken, C. Strohm, and P. Wyder, Phys. Rev. Lett. **89**, 133005 (2002).

[2] I. Kézsmárki, N. Kida, H. Murakawa, S. Bordács, Y. Onose, and Y. Tokura, Phys. Rev. Lett. **106**, 057403 (2011).

[3] S. Bordács, I. Kézsmárki, D. Szaller, L. Demkó, N. Kida, H. Murakawa, Y. Onose, R. Shimano, T. Rõõm, U. Nagel, S. Miyahara, N. Furukawa, and Y. Tokura, Nat. Phys. **8**, 734 (2012).

[4] I. Kézsmárki, D. Szaller, S. Bordács, V. Kocsis, Y. Tokunaga, Y. Taguchi, H. Murakawa, Y. Tokura, H. Engelkamp, T. Rõõm, and U. Nagel, Nat. Commun. **5**, 3203 (2014).

[5] Y. Takahashi, R. Shimano, Y. Kaneko, H. Murakawa, and Y. Tokura, Nat. Phys. **8**, 121 (2012).

[6] D. Szaller, S. Bordács, V. Kocsis, T. Rõõm, U. Nagel, and I. Kézsmárki, Phys. Rev. B **89**, 184419 (2014).

[7] S. Kibayashi, Y. Takahashi, S. Seki, and Y. Tokura, Nat. Commun. **5**, 4583 (2014).

[8] A. M. Kuzmenko, V. Dziom, A. Shuvaev, A. Pimenov, M. Schiebl, A. A. Mukhin, V. Y. Ivanov, I. A. Gudim, L. N. Bezmaternykh, and A. Pimenov, Phys. Rev. B **92**, 184409 (2015).

[9] S. Yu, B. Gao, J. W. Kim, S.-W. Cheong, M. K. L. Man, J. Madéo, K. M. Dani, and D. Talbayev, Phys. Rev. Lett. **120**, 037601 (2018).

[10] A. M. Kuzmenko, A. Shuvaev, V. Dziom, A. Pimenov, M. Schiebl, A. A. Mukhin, V. Y. Ivanov, L. N. Bezmaternykh, and A. Pimenov, Phys. Rev. B **89**, 174407 (2014).

[11] R. Masuda, Y. Kaneko, Y. Tokura, and Y. Takahashi, Science **372**, 496 (2021).

[12] T. Kurumaji, Y. Takahashi, J. Fujioka, R. Masuda, H. Shishikura, S. Ishiwata, and Y. Tokura, Phys. Rev. Lett. **119**, 077206 (2017).

[13] B. B. Krichevtsov, V. V. Pavlov, and R. V. Pisarev, Pis'ma Zh. Eksp. Teor. Fiz. **44**, 471 (1986) [JETP Lett. **44**, 607 (1986)].

[14] M. Saito, K. Ishikawa, S. Konno, K. Taniguchi, and T. Arima, Nat. Mater. **8**, 634 (2009).

[15] T. Sato, N. Abe, S. Kimura, Y. Tokunaga, and T.-h. Arima, Phys. Rev. Lett. **124**, 217402 (2020).

[16] V. Kocsis, K. Penc, T. Rõõm, U. Nagel, J. Vít, J. Romhányi, Y. Tokunaga, Y. Taguchi, Y. Tokura, I. Kézsmárki, and S. Bordács, Phys. Rev. Lett. **121**, 057601 (2018).

[17] A. M. Kuzmenko, D. Szaller, T. Kain, V. Dziom, L. Weymann, A. Shuvaev, A. Pimenov, A. A. Mukhin, V. Y. Ivanov, I. A. Gudim, L. N. Bezmaternykh, and A. Pimenov, Phys. Rev. Lett. **120**, 027203 (2018).

[18] H. T. Yi, Y. J. Choi, S. Lee, and S.-W. Cheong, Appl. Phys. Lett. **92**, 212904 (2008).

[19] M. Akaki, J. Tozawa, D. Akahoshi, and H. Kuwahara, Appl. Phys. Lett. **94**, 212904 (2009).

[20] A. Zheludev, T. Sato, T. Masuda, K. Uchinokura, G. Shirane, and B. Roessli, Phys. Rev. B **68**, 024428 (2003).

[21] J. Romhányi, M. Lajkó, and K. Penc, Phys. Rev. B **84**, 224419 (2011).

[22] M. Soda, M. Matsumoto, M. Månsson, S. Ohira-Kawamura, K. Nakajima, R. Shiina, and T. Masuda, Phys. Rev. Lett. **112**, 127205 (2014).

[23] M. Soda, S. Hayashida, B. Roessli, M. Månsson, J. S. White, M. Matsumoto, R. Shiina, and T. Masuda, Phys. Rev. B **94**, 094418 (2016).

[24] H. Murakawa, Y. Onose, S. Miyahara, N. Furukawa, and Y. Tokura, Phys. Rev. Lett. **105**, 137202 (2010).

[25] S. Miyahara and N. Furukawa, J. Phys. Soc. Jpn. **80**, 073708 (2011).

[26] K. Penc, J. Romhányi, T. Rõõm, U. Nagel, A. Antal, T. Fehér, A. Jánossy, H. Engelkamp, H. Murakawa, Y. Tokura, D. Szaller, S. Bordács, and I. Kézsmárki, Phys. Rev. Lett. **108**, 257203 (2012).

[27] T. Arima, J. Phys. Soc. Jpn. **76**, 073702 (2007).

[28] K. Yamauchi, P. Barone, and S. Picozzi, Phys. Rev. B **84**, 165137 (2011).

[29] M. Akaki, H. Iwamoto, T. Kihara, M. Tokunaga, and H. Kuwahara, Phys. Rev. B **86**, 060413(R) (2012).

[30] M. Akaki, D. Yoshizawa, A. Okutani, T. Kida, J. Romhányi, K. Penc, and M. Hagiwara, Phys. Rev. B **96**, 214406 (2017).

[31] Y. Iguchi, Y. Nii, M. Kawano, H. Murakawa, N. Hanasaki, and Y. Onose, Phys. Rev. B **98**, 064416 (2018).

[32] The number of the domains is determined by the order of the factor group $S_4 \cong P\bar{4}2_1 m1'/P2_1'2_12'$, which also transforms the domain states among each other.

[33] I. Kézsmárki, U. Nagel, S. Bordács, R. S. Fishman, J. H. Lee, H. T. Yi, S.-W. Cheong, and T. Rõõm, Phys. Rev. Lett. **115**, 127203 (2015).

[34] See Supplemental Material at http://link.aps.org/supplemental/10.1103/PhysRevLett.127.157201 showing that NDD has the same magnitude after ME annealing.

[35] J. Viirok, U. Nagel, T. Rõõm, D. G. Farkas, P. Balla, D. Szaller, V. Kocsis, Y. Tokunaga, Y. Taguchi, Y. Tokura, B. Bernáth, D. L. Kamenskyi, I. Kézsmárki, S. Bordács, and K. Penc, Phys. Rev. B **99**, 014410 (2019).

[36] T. Nakajima, Y. Tokunaga, V. Kocsis, Y. Taguchi, Y. Tokura, and T.-h. Arima, Phys. Rev. Lett. **114**, 067201 (2015).

[37] P. C. Hohenberg and W. F. Brinkman, Phys. Rev. B **10**, 128 (1974).

[38] S. Kimura, M. Matsumoto, and H. Tanaka, Phys. Rev. Lett. **124**, 217401 (2020).

Appendix 3

III

L. Peedu, V. Kocsis, D. Szaller, B. Forrai, S. Bordács, I. Kézsmárki, J. Viirok, U. Nagel, B. Bernáth, D. L. Kamenskyi, A. Miyata, O. Portugall, Y. Tokunaga, Y. Tokura, Y. Taguchi and T. Rõõm, "THz spectroscopy of spin excitations in magnetoelectric LiFePO$_4$ in high magnetic fields," *Phys. Rev. B*, vol. 106, p. 134413, Oct 2022

Terahertz spectroscopy of spin excitations in magnetoelectric LiFePO₄ in high magnetic fields

L. Peedu [1], V. Kocsis,[2] D. Szaller [3], B. Forrai,[4] S. Bordács,[4] I. Kézsmárki,[4,5] J. Viirok,[1] U. Nagel [1], B. Bernáth [6],
D. L. Kamenskyi,[6] A. Miyata,[7] O. Portugall [7], Y. Tokunaga,[2,8] Y. Tokura,[2,9] Y. Taguchi [2], and T. Rõõm [1]

[1]*National Institute of Chemical Physics and Biophysics, Akadeemia tee 23, 12618 Tallinn, Estonia*
[2]*RIKEN Center for Emergent Matter Science (CEMS), Wako, Saitama 351-0198, Japan*
[3]*Institute of Solid State Physics, TU Wien, 1040 Vienna, Austria*
[4]*Department of Physics, Institute of Physics, Budapest University of Technology
and Economics, Műegyetem rkp. 3., H-1111 Budapest, Hungary*
[5]*Experimental Physics 5, Center for Electronic Correlations and Magnetism,
Institute of Physics, University of Augsburg, 86159 Augsburg, Germany*
[6]*High Field Magnet Laboratory (HFML-EMFL),
Radboud University, Toernooiveld 7, 6525 ED Nijmegen, The Netherlands*
[7]*Laboratoire National des Champs Magnétiques Intenses (LNCMI-EMFL),
CNRS-UGA-UT3-INSA,143 Avenue de Rangueil, 31400 Toulouse, France*
[8]*Department of Advanced Materials Science, University of Tokyo, Kashiwa 277-8561, Japan*
[9]*Department of Applied Physics and Tokyo College, University of Tokyo, Tokyo 113-8656, Japan*

We investigated the spin excitations of magnetoelectric LiFePO₄ by THz absorption spectroscopy in magnetic fields up to 33 T. By studying their selection rules, we found not only magnetic-dipole, but also electric-dipole active (electromagnons) and magnetoelectric resonances. The magnetic field dependence of four strong low-energy modes is reproduced well by a four-spin mean-field model for fields applied along the three orthorhombic axes. From the fit of magnetization and magnon frequencies, we refined the exchange couplings, single-ion anisotropies, and the Dzyaloshinskii-Moriya interaction parameters. Additional spin excitations not described by the mean-field model are observed at higher frequencies. Some of them show a strong shift with the magnetic field, up to 4 cm^{-1} T^{-1}, when the field is applied along the easy axis. Based on this field dependence, we attribute these high frequency resonances to the excitation of higher spin multipoles and of two magnons, which become THz-active due to the low symmetry of the magnetically ordered state.

I. INTRODUCTION

Recent optical studies of multiferroic materials have revealed nonreciprocal directional dicroism, which is the light absorption difference for unpolarized counter-propagating beams [1–25]. This unusual phenomenon is the finite-frequency manifestation of the magnetoelectric (ME) effect, which emerges at simultaneously electric- and magnetic-dipole allowed excitations, that we term as ME resonance.[1] For example, materials with ME resonances can be used as

optical diodes where the direction of transparency for the terahertz (THz) radiation can be switched by magnetic fields [3–5,7–9,17], electric fields [20,24,28], or both [13]. From the fundamental science point of view, the THz spectroscopy of the ME excitations promotes the understanding of the static ME response which is linked to the nonreciprocal directional dichroism spectrum via the Kramers-Kronig relations [16,29]. Moreover, a THz absorption study, combined with magnetization, inelastic neutron scattering measurements [30–32], and theoretical modeling [33–36] can resolve realistic spin Hamiltonians of ME compounds.

The relativistic spin-orbit coupling plays an essential role for ME spin excitations. It establishes a coupling between spins and electric dipoles and also introduces single-ion anisotropy for $S > 1/2$. The single-ion anisotropy expands the frequency scale of spin excitations as it separates the $\pm m_s$ doublets from each other in zero field, where m_s is the spin quantum number. In addition to conventional spin waves, spin-quadrupolar excitations corresponding to $\Delta m_s = \pm 2$ may appear in systems with strong single-ion anisotropy and spin $S > 1/2$ [37–41], broadening the frequency range for possible applications of ME materials. In general, if there

---

[1]Usually, magnons couple to the magnetic component of electromagnetic radiation, i.e., they are magnetic-dipole active. If the magnons are electric-dipole active, the term "electromagnon" is often used [26]. Magnetoelectric resonance is a spin wave excited by both components of electromagnetic radiation [3,27]. For the rest of the paper, we classify the spin waves, based on their coupling to the electromagnetic radiation, using magnetic-dipole active, electric-dipole active and magnetoelectric spin wave. We use "magnon" for the spin-wave excitation described by the mean-field model without making a difference in its coupling to the electromagnetic radiation.
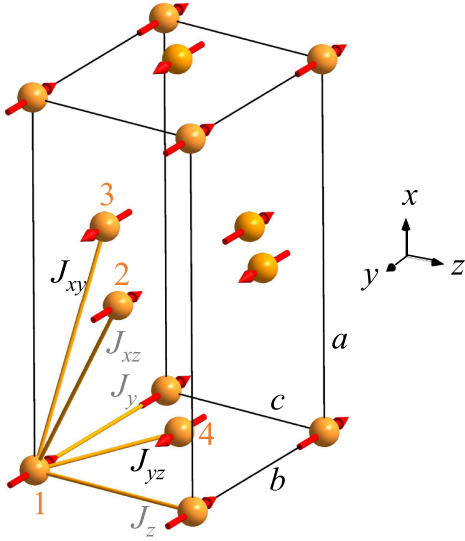
FIG. 1. The ground-state spin configuration of LiFePO$_4$ in zero magnetic field. There are four Fe^{2+} spins, $S = 2$, in the magnetic unit cell drawn as a box. The numbering of spins and exchange interactions J_{xy} and J_{yz} are depicted according to the spin Hamiltonian, Eq. (4).

are N spins in the magnetic unit cell we expect $2NS$ spin excitations, which can be described by the multiboson spin-wave theory [13,37,38,42] or by single-ion spin Hamiltonian with added molecular field to take into account spin-spin interactions [32,43,44].

The LiMPO$_4$ ($M =$ Mn, Co, Fe, Ni) orthophosphate compounds become ME as their magnetic order breaks the inversion symmetry [45]. This, together with their large single-ion anisotropy [31,32,46], makes them appealing candidates to explore unconventional spin excitations. Among these compounds, LiFePO$_4$ has the highest Néel temperature, $T_N = 50$ K below which an antiferromagnetic (AFM) order develops, as depicted in Fig. 1. The spins of the four magnetic ions of the unit cell are nearly parallel to the y axis [47]. Detailed neutron diffraction experiments showed that the spins are slightly rotated in the xy plane and canted toward the z axis [31]. LiFePO$_4$ has one of the largest spins in the orthophosphate family but the number of spin-wave modes detected in the magnetically ordered phase has been substantially less than $2NS = 16$, allowed for a $S = 2$ spin system. In zero-field inelastic neutron scattering (INS) studies, two spin-wave branches [30–32] and a dispersionless mode were observed below 10 meV [32]. Whereas, a recent high-frequency electron spin resonance study detected two modes in the vicinity of the spin-flop field, 32 T [46]. Therefore further experimental data are needed to understand better the spin dynamics and spin Hamiltonian of LiFePO$_4$.

In this work, we studied the magnetic field dependence of the spin excitations using THz absorption spectroscopy in the low temperature AFM phase of LiFePO$_4$. The spectral range of our experiments extending up to 175 cm^{-1} (22 meV)

covers two and five times larger energy window compared to former INS [30–32] and electron spin resonance studies [46,48], respectively. The broader spectral range allowed us to observe 17 spin excitations and to determine their selection rules. The absorption spectra were measured with magnetic field applied along all three principal crystallographic axes up to 33 T in the Faraday configuration (light propagates along the field, $\mathbf{k} \parallel \mathbf{H}$) and up to 17 T in Voigt geometry (light propagates perpendicular to the field, $\mathbf{k} \perp \mathbf{H}$). Beside THz spectroscopy, we measured high-field magnetization up to 120 T along the easy axis from which we determined the spin-flop and the saturation fields. Finally, we successfully employed a mean-field model to describe the field dependence of the magnetization and the resonance frequencies of the four strongest low-frequency spin-wave modes in the AFM state.

II. EXPERIMENTAL

The LiFePO$_4$ single crystals were grown by the floating zone method [49]. The quality of the crystals was verified by powder diffraction and Laue XRD, which confirmed the orthorhombic structure with the same lattice constants as reported in Ref. [50].

The low-field magnetization measurements were done using a 14-T PPMS with VSM option (Quantum Design). High-field magnetization measurements were carried out up to 120 T using ultrahigh semidestructive pulses at the Laboratoire National des Champs Magnétiques Intenses in Toulouse [51,52]. The maximum field of a semidestructive pulse was reached in ∼2.5 μs.

For THz spectroscopy studies the single crystal was cut into three 1 mm thick slabs each with a large face normal to one of the three principal crystallographic directions. The slabs were wedged by two degrees to suppress the fringes in the spectra produced by the internal reflections in the crystal.

The THz measurements up to 17 T were performed with a polarizing Martin-Puplett interferometer and a 0.3 K silicon bolometer in Tallinn. High-field spectra from 17 up to 33 T were measured using a Bruker IFS 113v spectrometer and a 1.6 K silicon bolometer in High Field Magnet Laboratory in Nijmegen. The experiments above 17 T were done in Faraday configuration, while below 17 T both Faraday and Voigt configuration experiments were performed. All spectra were measured with an apodized spectral resolution of 0.3 or 0.5 cm^{-1} which is less than the full width at half maximum (FWHM) of recorded spectral lines. The FWHM of one of the narrowest lines, F_7, is 0.7 cm^{-1}. The polarizer angle with respect to the crystal axes was determined by evaluating the intensity change of the strongest modes in the THz absorption spectra as the function of rotation angle of the polarizer. This information was also used to mount the polarizer in the high field experiments in Nijmegen where the in situ polarizer rotation was not possible. Absorption was determined by using a reference spectrum of an open hole, sample spectrum in the paramagnetic phase or by statistically calculating the baseline from the magnetic field dependence of sample spectra. In the first method, the absorption was calculated as

$$\alpha = -d^{-1}\ln(I/I_r), \qquad (1)$$

where I_r is the intensity through the reference hole with the area equal to the sample hole area and d is the sample thickness. In the second method, the absorption difference was calculated,

$$\Delta\alpha(H, T) = \alpha(H, T) - \alpha(0\,\text{T}, 55\,\text{K})$$
$$= -d^{-1} \ln\left[I(H, T)/I(0\,\text{T}, 55\,\text{K})\right], \quad (2)$$

where $I(0\,\text{T}, 55\,\text{K})$ is the intensity through the sample measured at 0 T and 55 K in the paramagnetic phase. In the third method, the statistically calculated baseline, $\alpha(0\,\text{T})$, was found as a minimum of differential absorption,

$$\Delta\alpha_H(H_i) = \alpha(H_i) - \alpha(0\,\text{T})$$
$$= -d^{-1} \ln\left[I(H_i)/I(0\,\text{T})\right], \quad (3)$$

at each frequency over several magnetic field values H_i. By adding $\alpha(0\,\text{T})$ to the differential absorption we get the dependence of absorption spectra on magnetic field. This method was used to obtain the spectra measured above 17 T.

III. MEAN-FIELD MODEL

The mean-field theory of localized magnetic moments is a widely applied tool to interpret the static and dynamic magnetic properties of systems with periodic magnetic structures [53], e.g., ferro- [54], ferri- [34], and antiferromagnetic [33] insulators. Particularly, the microscopic spin Hamiltonian of LiFePO$_4$ has been discussed by several papers [30–32,46,55,56].

Here we aim to describe the magnetism and the THz-active magnons of LiFePO$_4$. We consider a classical mean-field Hamiltonian of four Fe^{2+} spins represented by classical vectors with length $S = 2$, that occupy crystallographically nonequivalent positions of the unit cell, as shown in Fig. 1. Corresponding to the $Pnma$ paramagnetic crystal symmetry [57], the Hamiltonian consists of orthorhombic single-ion anisotropy and Zeeman terms, and symmetric nearest-neighbor and antisymmetric Dzyaloshinskii-Moriya exchange couplings connecting the four spin sites,

$$\mathcal{H} = 4\big[J_{xy}(\mathbf{S}_1 \cdot \mathbf{S}_3 + \mathbf{S}_2 \cdot \mathbf{S}_4)$$
$$+ J_{yz}(\mathbf{S}_1 \cdot \mathbf{S}_4 + \mathbf{S}_2 \cdot \mathbf{S}_3)$$
$$+ D_y\big(S_1^x S_4^z - S_1^z S_4^x + S_3^x S_2^z - S_3^z S_2^x\big)\big]$$
$$+ \sum_{i=1}^{4}\big[\Lambda_x\big(S_i^x\big)^2 + \Lambda_z\big(S_i^z\big)^2\big]$$
$$- \mu_B\mu_0\big(g_x H_x S_i^x + g_y H_y S_i^y + g_z H_z S_i^z\big)\big]. \quad (4)$$

The two hard-axis anisotropies Λ_x and Λ_z produce the effective easy axis along y. The last term is the interaction of the electron spin with the applied magnetic field taking into account the g factor anisotropy.

In our simplified Hamiltonian, the exchange coupling terms J_y and J_z have been omitted as they connect spins at magnetically equivalent sites, see Fig. 1. While the static magnetic properties and the THz absorption spectrum are insensitive to the identical energy shift of all states at the Γ point of the Brillouin zone produced by J_y and J_z, these couplings are relevant when describing the dispersion of the
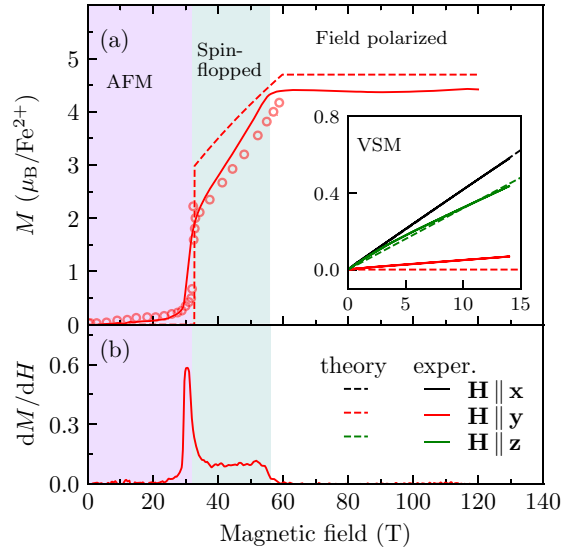

FIG. 2. (a) Magnetic field dependence of the magnetization M (solid, red) and (b) the directly measured dM/dH (solid, red) at $T = 5$ K for increasing pulsed field in $\mathbf{H} \parallel \mathbf{y}$. The inset of panel (a) shows VSM $M - H$ measurements in quasi-static fields at $T = 2.4$ K, where the magnetic field directions are $\mathbf{H} \parallel \mathbf{x}$ (black), $\mathbf{H} \parallel \mathbf{y}$ (red) and $\mathbf{H} \parallel \mathbf{z}$ (green). The dashed lines in panel (a) show the results of the mean-field calculations with the parameters from Table I. For comparison, we show the pulsed field magnetization data from Ref. [46] with open red circles. The AFM, spin-flopped and spin polarized state regions are shown for $\mathbf{H} \parallel \mathbf{y}$.

magnon modes [31]. J_{xz} was set to zero because it does not affect the magnetization and secondly, an equally good fit of magnon frequencies at the Γ point was obtained just with four parameters J_{xy}, J_{yz}, Λ_x and Λ_z. As the antiferromagnetic J_{yz} and J_{xy} couplings connect antiparallel spins of the zero-field ground state, LiFePO$_4$ lacks magnetic frustration, in contrast to the sister compound LiNiPO$_4$ [58].

The Dzyaloshinskii-Moriya interaction obeying the $Pnma$ crystal symmetry is $\mathbf{D} = (0, D_y, 0)$, similarly to the case of LiNiPO$_4$ [58]. Since the energy scale of the single-ion anisotropy preferring spin alignment along y exceeds the Dzyaloshinskii-Moriya interaction, no spin canting is produced in zero field.

However, weak Bragg peaks in neutron diffraction experiments indicate a slight rotation and canting of the spins away from the collinear order by $\sim 1°$, which contradicts the $Pnma$ crystal symmetry [31]. Although spin rotation and canting can be explained by invoking $\Lambda_{xy}S_i^x S_i^y$ anisotropy and $D_x(S_i^y S_j^z - S_i^z S_j^y)$ Dzyaloshinskii-Moriya terms, in this study, we neglect these terms in the Hamiltonian as the spin-wave absorption spectra in the Γ point can be interpreted without assuming the violation of the $Pnma$ symmetry.

We model the spin dynamics using the Landau-Lifshitz-Gilbert equation [59], as used in Ref. [58], by assuming that the spins are oscillating about their equilibrium orientations without changing their lengths. The equilibrium orientation
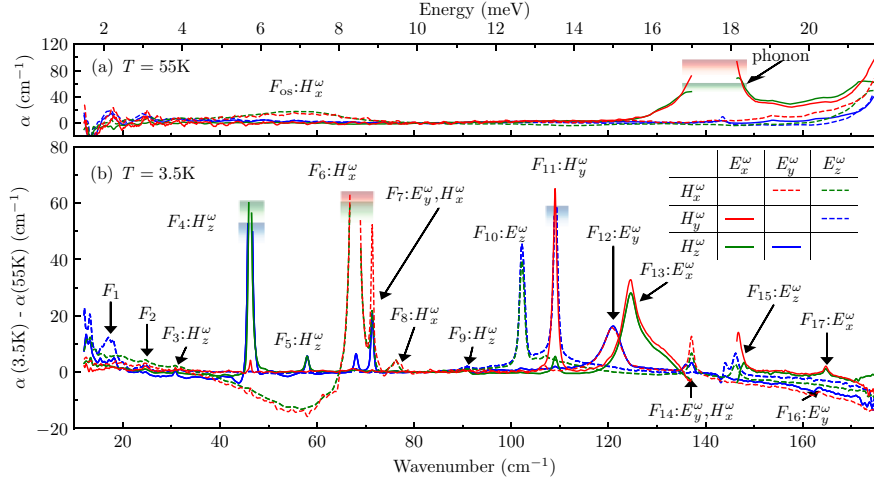
FIG. 3. (a) THz absorption spectra of LiFePO$_4$ at 55 K in the paramagnetic phase, and (b) the difference between the zero-field absorption spectra recorded at 3.5 K (magnetically ordered phase) and 55 K, demonstrating spectral features associated with the onset of magnetic order. Line colors correspond to the propagation direction of the THz radiation: k_x (blue), k_y (green), and k_z (red). Two orthogonal polarizations $\{E_i^\omega, H_j^\omega\}$ for the given propagation direction, $k_k \sim E_i^\omega \times H_j^\omega$, are indicated by the solid and dashed lines, according to the inset of panel (b). F_n with $n = 1, \ldots, 17$ labels the modes in the magnetically ordered phase and F_{os} is an on-site magnetic excitation in the paramagnetic phase. H_j^ω or E_i^ω indicate the magnetic- or electric-dipole activity of the mode, respectively. The blue, green and red rectangles mark the peaks with absorption above the upper detection limit, F_4, F_6, F_{11}, and phonon.

of the spins is found by minimizing the energy described in the Hamiltonian of Eq. (4), with respect to the spin orientations. Then the Landau-Lifshitz equation was solved to get frequencies and oscillating spin components for each magnon mode. The magnetic-dipole absorption of light by spin waves is calculated assuming that the magnetic field $\mathbf{H}^\omega$ of radiation couples to the total magnetic moment of the spins [58]. Dielectric permittivity in the absorption coefficient formula, Eq. (10) in Ref. [58], was assumed to be real and frequency-independent with components $\epsilon_x = 8.1$, $\epsilon_y = 7.3$, and $\epsilon_z = 7.6$ [60].

IV. RESULTS

A. Magnetization

We characterized LiFePO$_4$ samples by measuring the magnetization at 2.4 K along the principal axes up to 14 T. Along $\mathbf{H} \parallel \mathbf{y}$, the measurement is extended up to 120 T at 5 K using pulsed fields, see Fig. 2. The y-axis magnetization determined from the pulsed-field measurements was normalized to the value of static field measurements in the range from 4 to 14 T, neglecting a small hysteresis of magnetization between 0 and 4 T. In the AFM state the spins are predominantly aligned along the easy axis, the y axis in LiFePO$_4$. The magnetization grows approximately linearly in increasing field for $\mathbf{H} \parallel \mathbf{x}$ and $\mathbf{H} \parallel \mathbf{z}$. When $\mathbf{H} \parallel \mathbf{y}$ is applied, the spins maintain easy-axis alignment up to the spin-flop field marked by a jump in the magnetization at (32 ± 3) T. As the field further increases the magnetization grows linearly and reaches saturation at (56 ± 3) T. In the field-polarized state, the saturation magnetization is estimated to (4.4 ± 0.3) μ_B per iron. This value is close to the magnetic moment 4.2 μ_B determined by neutron diffraction measurements in zero field [61]. The spin-flop field

deduced from our measurements is in agreement with former high-field magnetization measurements [46].

B. THz absorption spectra in zero field

The zero-field THz absorption spectra of LiFePO$_4$ are presented in Fig. 3 and the mode parameters are collected in Table II, while Fig. 3(b) features absorption spectra in the AFM phase, relative to the paramagnetic phase.

The spectra in the paramagnetic phase show a broad but weak magnetic-dipole active peak F_{os} at around ~ 55 cm^{-1}, Fig. 3(a). The magnetic on-site excitation F_{os} is H_x^ω active as it is seen in two polarization configurations, $\{E_y^\omega, H_x^\omega\}$ and $\{E_z^\omega, H_x^\omega\}$. The frequency and the selection rules of F_{os} are reproduced by exact diagonalization of a four-spin cluster, see Fig. S6 in Ref. [62]. Other features in the paramagnetic phase spectra are E_x^ω-active phonon at 140 cm^{-1}, with a strong absorption exceeding the detection limit, and absorption rising towards higher frequencies due to the phonons with resonance frequencies above 175 cm^{-1}.

To better resolve spectral features emerging in the magnetically ordered phase we plot the difference spectra, $\alpha(3.5 \text{ K}) - \alpha(55 \text{ K})$, Fig. 3(b). We observe a diminished absorption at the tails of phonons at low T appearing as negative features in the difference spectra between 140 and 175 cm^{-1}. The change of the 140 cm^{-1} phonon mode is obscured by the strong absorption and therefore the E_x^ω spectra, green and red solid lines, are discontinued where the 140 cm^{-1} phonon peaks. The broad peak F_{os} from the high-T paramagnetic phase appears as a negative feature in the difference spectra in H_x^ω polarization.

All sharp modes, labeled $F_1, \ldots, F_{17}$, are absent above T_N and we assign them to spin excitations. The seven excitations, F_3, F_4, F_5, F_6, F_8, F_9, and F_{11}, are identified as magnetic-

TABLE I. The parameters of the mean-field model used to describe the static magnetic properties and spin waves in LiFePO$_4$: Exchange couplings J_i and J_{ij}, single-ion anisotropies Λ_i and Λ_{ij}, Dzyaloshinskii-Moriya coupling D_y, and anisotropic g factor g_i. All parameters are in units of meV except the dimensionless g_i.

J_{xz}	J_{xy}	J_{yz}	Λ_x	Λ_z	D_y	g_x	g_y	g_z	Ref.
-	0.096(6)	0.54(1)	0.51(2)	1.45(3)	0.025(5)	2.10(6)	2.35(17)	2.10(6)	[a]
0.05(1)	0.14(2)	0.77(7)	0.62(12)	1.56(3)	0.038[b]	2.24(3)	2.31(2)	1.99(3)	[46][c]
0.05(1)	0.14(2)	0.77(7)	0.62(12)	1.56(3)	-	-	-	-	[31]
0.01(1)	0.09(1)	0.46(2)	0.86(2)	2.23(2)	-	-	-	-	[32]

[a]This work.

[b]The Dzyaloshinskii-Moriya parameter $D_y = J_{DM}/4$, where J_{DM} is from Ref. [46] and 4 is the corresponding coordination number.

[c]The exchange interactions and single-ion anisotropies are from Ref. [31] and g factors from Ref. [56].

dipole active modes. Six modes, F_{10}, F_{12}, F_{13}, F_{15}, F_{16}, and F_{17}, are identified as electric-dipole active resonances. The mode F_{13} has a shoulder, thus, it was fitted with two Gaussian lines with maxima at 124.4 and 127.6 cm^{-1}. Two modes, F_7 at 71.4 cm^{-1} and F_{14} at 137.1 cm^{-1}, are both electric- and magnetic-dipole allowed, therefore, we identified them as ME resonances. F_7 is the strongest in $\{E_y^\omega, H_x^\omega\}$ polarization, red dashed line in Fig. 3(b), and its intensity is halved if only one of the components, E_y^ω or H_x^ω, is present. Thus F_7 is an example of a ME resonance which couples equally to the magnetic and electric components of radiation. We detected F_{14} in the same three polarization configuration, thus, we also assigned it to a ME resonance with the same selection rule as mode F_7, $\{E_y^\omega, H_x^\omega\}$.

The three strongest magnetic-dipole active modes F_4, F_6, and F_{11} show only weak absorption in polarizations

orthogonal to their main magnetic dipole component. The weak absorption in other polarizations could be explained by the imperfections of the polarizer. However, we can not completely rule out that some of these modes are ME resonances with a weak electric-dipole component which can be tested by further measurements of the nonreciprocal directional dichroism on magnetoelectrically poled samples [13,16]. We can not identify the selection rules for modes F_1 and F_2 as they are too weak.

C. Magnetic field dependence of spin waves

The magnetic field dependence of mode frequencies and intensities between 0 and 17 T is shown in Fig. 4 for Faraday, panels (a)–(c), and Voigt configuration, (d) and (e). The modes mostly stay at constant frequency when the magnetic field

TABLE II. The excitation configurations and field dependence of LiFePO$_4$ modes in the AFM phase. The selection rules were found by measuring polarization dependence of spin excitations in three principal directions without magnetic field. The absorption line energy and area in zero field were obtained from the fit to Gaussian line shape, except F_{13} where the sum of two Gaussians was used. The slopes of the modes were estimated from the linear field dependence between 15 and 17 T; if mode was not visible in this field range, the lower field range was used. From the slopes the $|\Delta m_s|$ values are proposed assuming $g \approx 2$. Modes F_4 to F_7 were observed by INS spectroscopy [31,32] and are fitted to the mean-field model in this work.

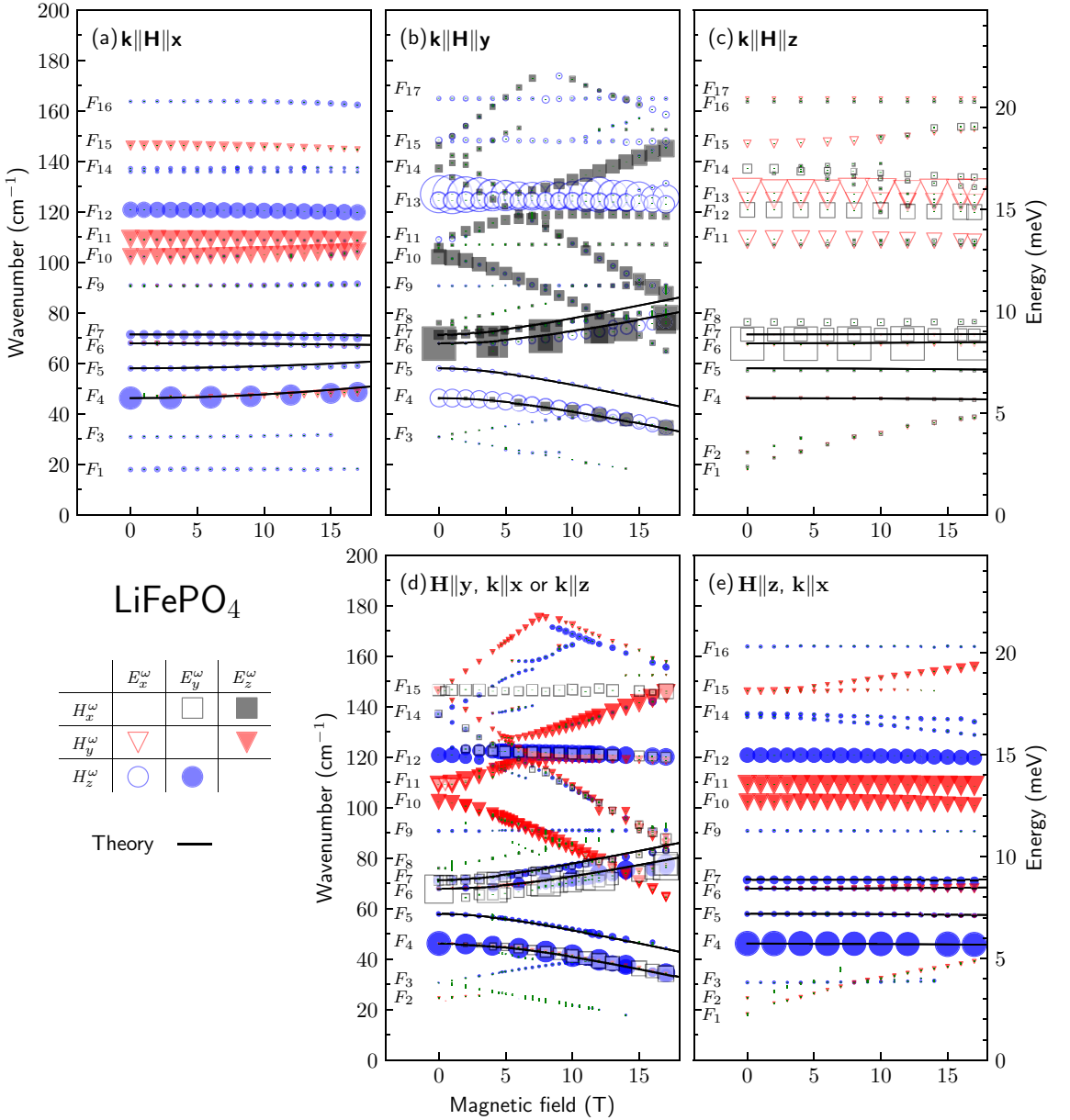| Mode	Energy at 0 T (cm^{-1})	Area at 0 T (cm^{-2})	Selection rules at 0 T	Magnetic field direction	Slope b_1 (cm^{-1} T^{-1})	$|\Delta m_s|$
F_1	18.3	4		z	+1.4	
F_2	24.7	2		z	+1.5	
F_3	30.8	2	H_z^ω	y	−0.9, +0.9	1
F_4	46.2 (5.7 meV)	> 100	H_z^ω	y	−1.1	1
F_5	58.0 (7.2 meV)	6	H_z^ω	y	−1.1	1
F_6	67.9 (8.4 meV)	> 200	H_x^ω	y	+0.9	1
F_7	71.4 (8.9 meV)	37	H_x^ω, E_y^ω	y	+1.0	1
F_8	76.2	9	H_x^ω	y	−0.8, +1.0	1
F_9	90.8	2	H_z^ω	x	+0.1	
F_{10}	102.2	57	E_z^ω	y	−3.3	3
F_{11}	109.0	74	H_y^ω	y	+1.8	2
F_{12}	120.8	50	E_y^ω	y	−1.9	2
F_{13}	124.4, 127.6	185	E_x^ω	y	−0.3	
F_{14}	137.1	17	H_x^ω, E_y^ω	y	−3.0, +2.8	3
				z	−0.6	
F_{15}	146.3	30	E_z^ω	y	−3.7, +3.8	4
				z	+0.7	
F_{16}	163.7	2	E_y^ω	x	−0.3	
F_{17}	164.8	4	E_x^ω	y	0.0	

FIG. 4. Magnetic field dependence of the spin-wave resonance frequencies and absorption line areas at $T = 3.5$ K in LiFePO4. (a)–(c) correspond to measurements in the Faraday ($\mathbf{k} \parallel \mathbf{H}$), while (d) and (e) correspond to experiments in the Voigt ($\mathbf{k} \perp \mathbf{H}$) configuration. The direction of the magnetic field is (a) – $\mathbf{H} \parallel \mathbf{x}$, (b), (d) – $\mathbf{H} \parallel \mathbf{y}$, and (c), (e) – $\mathbf{H} \parallel \mathbf{z}$. The symbols correspond to six combinations of linear light polarization $\{E_i^\omega, H_j^\omega\}$ as indicated at bottom left of the figure. The symbol height is proportional to the square root of experimental absorption line area with the same scaling as wave number axis. To simplify the figure the larger symbols are not shown for every measured field. The error bars (vertical green lines) from fitting the line positions in most cases are too small to be seen in the figure. The black lines are the results of the mean-field model calculations, modes F_4, F_5, F_6, and F_7. Comparison of experimental and calculated intensities is in Ref. [62].

is applied along the hard axes, $\mathbf{H} \parallel \mathbf{x}$, Fig. 4(a) and $\mathbf{H} \parallel \mathbf{z}$, Figs. 4(c) and 4(e). However, most of the resonances shift with the magnetic field for $\mathbf{H} \parallel \mathbf{y}$. We assigned a slope, $b_1 = \Delta E / \Delta B$, calculated between 15 and 17 T in units cm^{-1}T^{-1},

to each of the modes and collected them in Table II. If the mode was not visible in this range, a lower magnetic field range was used. One mode, F_{17}, has zero slope and F_9, F_{13}, and F_{16} have a moderate value, $|b_1| < 0.3$. Modes F_{14} and F_{15}
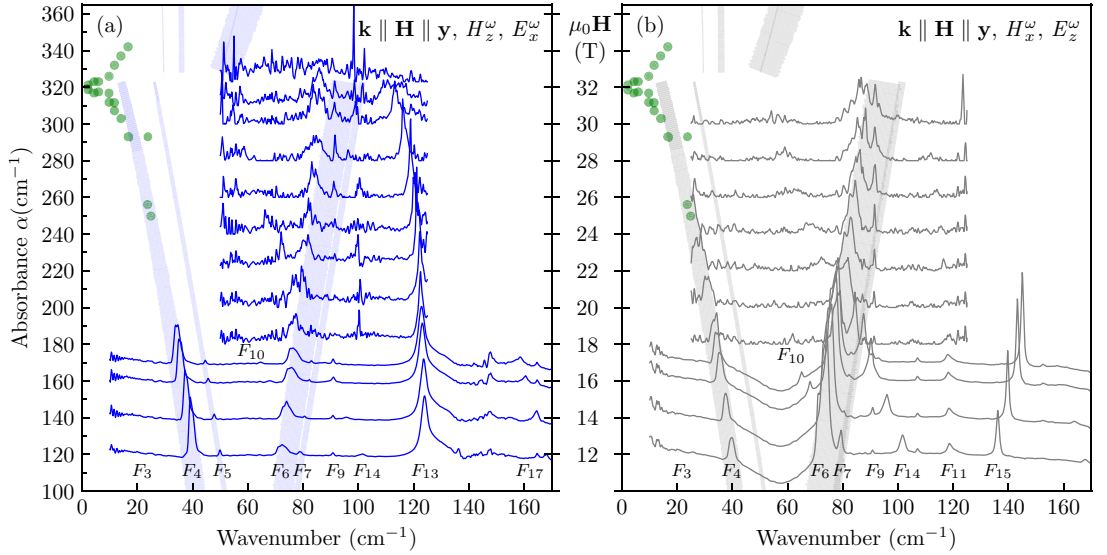
FIG. 5. THz absorption spectra of spin-wave excitations in magnetic field $\mathbf{H} \parallel \mathbf{k} \parallel \mathbf{y}$ at $T = 3.5$ K in two orthogonal polarizations, (a) $\{H_z^\omega, E_x^\omega\}$ and (b) $\{H_x^\omega, E_z^\omega\}$. The broad stripes are the results of the mean-field calculation, F_4, F_5, F_6, and F_7, in order of increasing frequency; the width of the line is proportional to the square root of the line area with the same scale as wave number axis and calculated in the magnetic dipole approximation. The zero-field 55 K spectrum was used as a reference below 17 T and the low-temperature zero-field spectrum above 17 T. Filled circles are the spin-wave excitation energies reproduced from Ref. [46].

have the largest $|b_1|$ for $\mathbf{H} \parallel \mathbf{y}$ but also a substantial $|b_1|$ for $\mathbf{H} \parallel \mathbf{z}$.

Assuming $g = 2$ we estimated from the slopes the change of the spin projection quantum number, Δm_s, upon the excitations. The results are listed in Table II. The spin waves below 80 cm^{-1} (zero-field frequency) have $|\Delta m_s| = 1$ while above 100 cm^{-1} $|\Delta m_s|$ is 2, 3 or 4. $|\Delta m_s|$ was not assigned to F_1 and F_2 where $b_1 \approx 1.5$ cm^{-1} T^{-1} below 8 T, which is between $\Delta m_s = 1$ and 2. We note that b_1 of F_1 changes with field. It is 0.9 cm^{-1} T^{-1} above 8 T. This change of slope could be due to the anti-crossing with F_4 but we do not have evidence for that because the mode was too weak to be detected in the high-field magnet setup above 17 T.

The absorption spectra in high magnetic field $\mathbf{H} \parallel \mathbf{y}$ up to 31.6 T are presented in Fig. 5. The spin-wave excitations, F_6 and F_7, start softening before reaching the spin-flop transition at 32 T, in accordance with the mean-field calculation. Also, F_{13} at about 125 cm^{-1} shows softening close to 30 T. Spectra in other two field directions, $\mathbf{H} \parallel \mathbf{x}$ and $\mathbf{H} \parallel \mathbf{z}$, above 17 T are shown in Ref. [62], Figs. S1 and S3.

D. Mean-field model results

The parameters of the mean-field Hamiltonian [Eq. (4)], listed in Table I, were obtained by fitting the observed field dependence of the magnetization and the frequencies and oscillator strengths of the four magnons, F_4 to F_7.

Neglecting the effect of the weak Dzyaloshinskii-Moriya interaction, the zero-field frequencies of the two strongest spin waves F_4 and F_6 are [2]

$$\nu_{4/6} = 2S\sqrt{\Lambda_{x/z}(4(J_{yz} + J_{xy}) + \Lambda_{z/x})}, \qquad (5)$$

while the zero-field frequencies of the weaker F_5 and F_7 are

$$\nu_{5/7} = 2S\sqrt{(4J_{xy} + \Lambda_{x/z})(4J_{yz} + \Lambda_{z/x})}. \qquad (6)$$

As the measured frequencies of F_4, F_5, F_6, and F_7 have the highest precision among our experimental observables, we used Eqs. (5) and (6) to unambiguously determine the J_{xy}, J_{yz}, Λ_x, and Λ_z parameters.

It follows from the mean-field model that without Dzyaloshinskii-Moriya interaction D_y the intensity of THz absorption of F_5 and F_7 is zero. Thus, we used the observed intensities of F_5 and F_7 in zero field (presented in Table II and in Tables I and II of Ref. [62]) to determine D_y.

The magnetic susceptibilities along the x and z hard axes are obtained from the mean-field model as

$$\chi_{x/z} = \mu_0 \frac{(g_{x/z} \mu_B S)^2}{16(J_{yz} + J_{xy}) + 4\Lambda_{x/z}}, \qquad (7)$$

and was used to obtain the diagonal g_x and g_z components of the g factor from the field-dependent magnetization, $M_\alpha = \chi_\alpha H_\alpha$, shown in Fig. 2.

---

[2]Similar quantum-mechanical formulas but for the spin-wave dispersion were derived in INS studies [30,31,63]. Neglecting the quantum-mechanical 1/2 correction to the spin length introduced in Eq. (7) of Ref. [31], it reduces to Eq. (5) in the Γ point and to Eq. (6) in several other points, e.g., in (0, 0, 1).

In magnetic field along the y easy axis two critical fields appear in the model and in the magnetization measurements (Fig. 2), the spin-flop field ($\mu_0 H_{SF}$) and the saturation field ($\mu_0 H_{Sat}$). The latter can be calculated as

$$\mu_0 H_{Sat} = \frac{2S[4(J_{yz} + J_{xy}) - \Lambda_x]}{\mu_B g_y}. \tag{8}$$

This analytical expression for $\mu_0 H_{Sat}$, the numerical simulation of $\mu_0 H_{SF}$ together with the $\mu_{Sat} = \mu_B g_y S$ relation for the saturation magnetization moment, Fig. 2, and the observed magnetic field dependencies of the mode frequencies F_4 to F_7 [see Figs. 4(b) and 4(d)] were used to fit g_y. The error bar of g_y (Table I) is calculated from the scattering of the g factors obtained from various experimental inputs, from 2.2 to 2.5, and from the error bars of corresponding measurements.

With the parameter set determined above, Table I, the magnetic field dependence of the modes F_4 to F_7 below 17 T is reproduced remarkably well by the model for all three magnetic field directions, Figs. 4 and 5. The anisotropic g factor values improved not only the magnetic field dependence of spin-wave frequencies, but also reproduce the value of the spin-flop field and the saturation field, Fig. 2. In addition, the calculated magnetization as a function of H_x and H_z follows the measured $M(H)$ below 15 T, inset to Fig. 2.

For the easy-axis direction of the magnetic field, **H** ∥ **y**, the agreement of the observed and calculated magnetization curves is only qualitative. Firstly, the classical model produces collinear antiferromagnetic ground state with zero magnetization below the spin-flop field. Thus, the observed small susceptibility can originate from quantum mechanics, where the ground state deviates from the classical Néel state, or from magnetic impurities[48]. Secondly, the saturation value of the magnetization calculated with the mean-field model for **H** ∥ **y** is 6% higher than the experimentally observed, Fig. 2(a). However, the two values still agree within the experimental accuracy. Reason for the failure to reproduce the saturation magnetization and the spin-flop field with the same set of magnetic-field independent parameters could be magnetostriction [56]. Magnetostriction, as was proposed in Ref. [46], could also be the reason why the mean-field model does not reproduce the frequency of F_4 close to the spin-flop field, 32 T in Fig. 5.

V. DISCUSSION

A. Magnons from the mean-field model

We found that the mean-field model quantitatively describes the magnetic field dependence of the frequencies of spin waves F_4, F_5, F_6, and F_7, Fig. 4. These modes have a linear field dependence with the slope close to ± 1 cm^{-1} T^{-1} when the field is along the easy axis y. This slope corresponds to a spin-wave excitation with $\Delta m_s = \pm 1$, assuming $g \approx 2$. Other studies also found a g factor close to 2 [46]. Other candidates for the $\Delta m_s = \pm 1$ spin-wave excitations are F_3 and F_8. However, both of these modes have two branches degenerate in zero field. The magnetization measurements, inset of Fig. 2(a), indicate biaxial magnetic anisotropy in LiFePO$_4$ which lifts the degeneracy of magnetic resonances in

zero field. Therefore F_3 and F_8 cannot be consistently included into the mean-field description.

The magnons of the mean-field model have oscillating spin components, $\delta \mathbf{S}_i = \mathbf{S}_i - \bar{\mathbf{S}}_i$, perpendicular to the equilibrium direction of the i-th spin, $\bar{\mathbf{S}}_i$. The spin wave couples to the magnetic field of radiation if the oscillating spin component of the whole magnetic unit cell is finite, $\mathbf{H}^\omega \cdot (\sum_{i=1}^4 \delta \mathbf{S}_i)$. The equilibrium direction of the spins is aligned to the easy axis y within few degrees in LiFePO$_4$. The selection rules, Table II, show that F_4 and F_5 are excited by the H_z^ω component of radiation and modes F_6 and F_7 by the H_x^ω component, which both are perpendicular to $\bar{\mathbf{S}}_i$. The magnetic field dependence of intensities of the strongest modes F_4 and F_6 is well described by the mean-field model. Firstly, F_4 is H_z^ω- and F_6 is H_x^ω-active in zero field, Table II. Secondly, as H_y increases, F_4 becomes H_x^ω-active and F_6 becomes H_z^ω-active, Fig. S4 in Ref. [62]. Thus, for modes F_4 and F_6 the agreement between theory and experiment is good. The weak $Pnma$-symmetry allowed Dzyaloshinskii-Moriya interaction D_y in LiFePO$_4$ does not affect the collinear antiferromagnetic ground state, but gives to F_5 and F_7 resonances magnetic dipole activity. The experimental and theoretical selection rules of the weaker modes agree – F_5 is H_z^ω-active while F_7 is H_x^ω-active, see Fig. S4 and Tables I and II in Ref. [62]. As observed experimentally, Fig. 3, F_7 is in addition electric-dipole active. This feature is not reproduced by our calculations because the coupling of spins to the electric field was not included in the mean-field model.

The weak Dzyaloshinskii-Moriya interaction in LiFePO$_4$ was experimentally determined earlier by high-frequency-high field electron spin resonance spectroscopy [46]. They also concluded that a Dzyaloshinskii-Moriya interaction is needed to observe additional weak magnetic-dipole active excitation, F_5 in our notation. The Dzyaloshinskii-Moriya interaction used in Ref. [46] was in general form, (D_x, D_y, D_z). Here we show that one Dzyaloshinskii-Moriya component, D_y allowed by the $Pnma$ symmetry, is sufficient to describe the intensities of F_5 and F_7. The Dzyaloshinskii-Moriya strengths derived from two experiments are similar, see Table I.

As follows from Eq. (5) and Eq. (6), if $J_{xy} = 0$, F_4 and F_5 are degenerate in zero field, $\nu_4 = \nu_5$, and also $\nu_6 = \nu_7$. In this case the nearest-neighbor (100) planes of the $\{S_1, S_4\}$ and $\{S_2, S_3\}$ sublattices, separated by $a/2$, are decoupled from each other, thus, their corresponding in-phase ($F_{4,6}$) and out-of-phase excitations ($F_{5,7}$) with respect to each other are degenerate. Consequently, F_4 and F_6 can be considered as the in-phase while F_5 and F_7 as the out-of-phase resonances of the nearest-neighbor (100) planes. Without Dzyaloshinskii-Moriya interaction the total oscillating magnetic dipole moment of the unit cell produced by F_5 and F_7 is zero. This explains the weak intensity of F_5 and F_7 compared to F_4 and F_6 in the THz absorption spectrum. Furthermore, the correspondence between the INS magnon dispersion interpreted in the two-spin unit cell scheme [30–32] and our Γ-point optical experiments can also be formulated based on the mean-field results. Namely, F_4 and F_6 correspond to the magnons observed in the zone center, $\mathbf{Q} = (0, 2, 0)$ [31] or $\mathbf{Q} = (0, 0, 2)$ [32] while F_5 and F_7 are zone-boundary excitations of the two-spin unit cell, seen at $\mathbf{Q} = (0, 0, 1)$ [32], $\mathbf{Q} = (1, 1, 0)$ [30,31], and $\mathbf{Q} = (0, 1, 1)$ [31] in the INS experiments [30–32].

B. Spin excitations beyond the mean-field model

Out of 17 lines appearing below T_N in the THz absorption spectrum only four can be described by the classical four-spin mean-field model. The rest can be (i) spin-stretching excitations captured only by multiboson spin-wave theory or alternatively by crystal-field schemes including exchange fields, (ii) two-magnon excitations (two spin waves with nearly opposite **k** vectors), or can even be (iii) excitations from impurity spins. Assuming that the spins are aligned along the y axis the magnetic symmetry reduces to $Pnma'$ [30]. Since all spatial symmetries of the paramagnetic state remain in the AFM phase, at least in combination with time-reversal operation, we do not expect new optical phonon modes to emerge below T_N.

We assign absorption lines F_1, F_2 and F_3 to impurities because these very weak modes are located below the lowest-frequency magnon mode F_4. In addition, the frequencies of F_1 and F_2 increase linearly in magnetic field $\mathbf{H} \parallel \mathbf{z}$, not coinciding with easy-axis direction y. Previous works have found that Fe^{2+} at Li^+ site has zero-field splitting 7.3 cm^{-1} (220 GHz) [48]. The lowest impurity absorption line in our spectrum is F_1 at 18 cm^{-1} in zero field. This suggests that we are observing different impurities than reported in Ref. [48].

The mean-field model does not describe spin excitations F_8–F_{17}. Several of them are electric-dipole active and have a steep magnetic field dependence of frequency, suggesting $|\Delta m_s| > 1$ change of a spin projection quantum number. This is unusual for a spin-wave excitation but can be explained by a large single-ion anisotropy (Λ) which is comparable or stronger than the exchange coupling (J) [37], see Table I. In that case a suitable approach is a multiboson spin-wave theory, which describes more than four spin-wave excitations in a four-sublattice magnet. Out from the orthophosphate compounds, the multiboson spin-wave theory has been only applied to $LiCoPO_4$, a $S = 3/2$ spin system [13]. Developing a multiboson spin-wave theory for $LiFePO_4$ is a tedious calculation, therefore, it is out of the scope of this paper.

Some of the observed features can be explained qualitatively in the limit of zero exchange and Dzyaloshinskii-Moriya coupling. Assuming rotational symmetry about the y axis in Eq. (4), $\Lambda_z = \Lambda_x$, the spins are parallel to the quantization axis y, and the energy levels E_{m_s} of spin $S = 2$ are E_0, $E_{\pm 1}$ and $E_{\pm 2}$. When the $\mathbf{H} \parallel \mathbf{y}$ field is applied, the energy difference $E_{+2} - E_{-2}$ increases approximately at a rate 4 cm^{-1} T^{-1}, as observed for the spin-wave excitation F_{15}. The electric dipole activity comes from the on-site spin-induced polarization which in the lowest order of spin operators is $P \propto \hat{S}_\alpha \hat{S}_\beta$ (α, $\beta = x, y, z$) [13]. Although $P \propto \hat{S}_x^2$ and $P \propto \hat{S}_z^2$ (quantization axis is y) couple states different by $\Delta m_s = \pm 2$ it does not explain the $|\Delta m_s| \geqslant 3$ transitions, F_{10}, F_{14} and F_{15}. However, in $LiFePO_4$ the single ion anisotropies are not equal, $\Lambda_z \neq \Lambda_x$ and mix E_0 into $E_{\pm 2}$ states, see Table I in Ref. [32]. Therefore, the selection rule for the electric-dipole transition, $\Delta m_s = 2$, and mixing of states gives finite electric-dipole moment to the $\Delta m_s = 4$ transition. In a similar manner, $P \propto \hat{S}_x \hat{S}_y$ and $\hat{S}_y \hat{S}_z$ could give rise to $\Delta m_s = \pm 1$ transitions and if the mixing of states is taken into account, then to the electric-dipole allowed $\Delta m_s = \pm 3$ transitions.

Two spin waves, $\omega_1(\mathbf{q}_1)$ and $\omega_2(\mathbf{q}_2)$, can be excited by THz radiation of frequency $\omega = \omega_1 + \omega_2$ if $\mathbf{q}_1 = -\mathbf{q}_2$, which is termed as two-magnon excitation. The exact frequency dependence of this absorption depends on the coupling mechanism between the radiation and the spin wave and on the density of spin-wave states [64–69]. This leads to broad absorption bands with peaks at the highest density of spin-wave states [58,64–67,70,71], mostly with spin waves from the edge of the magnetic Brillouin zone. Since the product of the two spin operators has the same time-reversal parity as the electric dipole moment, the simultaneous excitation of two spin waves by the electric field is allowed and this mechanism usually dominates over the magnetic-dipole active absorption [72]. A relatively broad electric-dipole active absorption line is F_{13}. If $\omega_1(\mathbf{q}_1) = \omega_2(\mathbf{q}_2)$, the spin-wave frequency should be $\omega_1 \approx 60$ $cm^{-1} = 7.4$ meV. At about the same energy two dispersion curves cross in the [0,1.5,0] Brillouin zone point of the two-spin unit cell [31,32]. The [0,0.5,0] point, equivalent to [0,1.5,0], is the Brillouin zone boundary of the four-spin unit cell and therefore we expect anticrossing of two dispersion curves which leads to increase in the density of magnon states at this point. Thus, considering the linewidths, energy scale, and the electric-dipole activity, F_{13} could be a two-magnon excitation. Another candidate for a two-magnon excitation is the electric-dipole active F_{12}. Although it is relatively broad in zero field, it has a complicated field dependence in $\mathbf{H} \parallel \mathbf{y}$, see Fig. S5 in Ref. [62], what can not be explained within a simple model of two-magnon excitation.

VI. SUMMARY

We studied the magnetic ground state and the spin excitations of the magnetoelectric antiferromagnet $LiFePO_4$ by magnetization measurements in magnetic fields up to 120 T and by THz absorption spectroscopy up to 33 T. Magnetization measurements revealed a spin-flop transition at 32 T before reaching the saturation at 56 T. We found 17 absorption lines below 175 cm^{-1} (5.25 THz) appearing in the magnetically ordered phase. Based on the magnetic field dependence of the resonance frequencies and the intensities, we assigned four of them to magnon modes ($F_4 - F_7$), eight to multiboson spin-wave excitations ($F_8 - F_{11}$, $F_{14} - F_{17}$), two to two-magnon excitations (F_{12}, F_{13}) and the rest to the absorption by impurity spins ($F_1 - F_3$). We applied a mean-field model, which describes well the four magnon modes ($F_4 - F_7$). We attribute the other spin-wave modes to excitations with $|\Delta m_s| > 1$ arising due to the large, $S = 2$, spin of octahedrally coordinated Fe^{2+} ions. Such excitations may become electric-dipole active due to symmetry allowed coupling between spin-quadrupolar fluctuations and electric polarization. Two modes, F_7 and F_{14}, are magneto-electric resonances with significant coupling to both, electric and magnetic field component of radiation. Additional experiments on magneto-electrically poled samples are needed to clarify if these two resonances show nonreciprocal directional dichroism [13,16].

[1] Y. Tokura, Multiferroics—toward strong coupling between magnetization and polarization in a solid, J. Magn. Magn. Mater. **310**, 1145 (2007).

[2] M. Saito, K. Taniguchi, and T. Arima, Gigantic optical magnetoelectric effect in CuB_2O_4, J. Phys. Soc. Jpn. **77**, 013705 (2008).

[3] I. Kézsmárki, N. Kida, H. Murakawa, S. Bordács, Y. Onose, and Y. Tokura, Enhanced Directional Dichroism of Terahertz Light in Resonance with Magnetic Excitations of the Multiferroic $Ba_2CoGe_2O_7$ Oxide Compound, Phys. Rev. Lett. **106**, 057403 (2011).

[4] S. Miyahara and N. Furukawa, Theory of magnetoelectric resonance in two-dimensional $S = 3/2$ antiferromagnet $Ba_2CoGe_2O_7$ via spin-dependent metal-ligand hybridization mechanism, J. Phys. Soc. Jpn. **80**, 073708 (2011).

[5] S. Bordács, I. Kézsmárki, D. Szaller, L. Demkó, N. Kida, H. Murakawa, Y. Onose, R. Shimano, T. Rõõm, U. Nagel, S. Miyahara, N. Furukawa, and Y. Tokura, Chirality of matter shows up via spin excitations, Nat. Phys. **8**, 734 (2012).

[6] Y. Takahashi, Y. Yamasaki, and Y. Tokura, Terahertz Magnetoelectric Resonance Enhanced by Mutual Coupling of Electromagnons, Phys. Rev. Lett. **111**, 037204 (2013).

[7] I. Kézsmárki, D. Szaller, S. Bordács, V. Kocsis, Y. Tokunaga, Y. Taguchi, H. Murakawa, Y. Tokura, H. Engelkamp, T. Rõõm, and U. Nagel, One-way transparency of four-coloured spin-wave excitations in multiferroic materials, Nat. Commun. **5**, 3203 (2014).

[8] I. Kézsmárki, U. Nagel, S. Bordács, R. S. Fishman, J. H. Lee, H. T. Yi, S.-W. Cheong, and T. Rõõm, Optical Diode Effect at Spin-Wave Excitations of the Room-Temperature Multiferroic $BiFeO_3$, Phys. Rev. Lett. **115**, 127203 (2015).

[9] S. Bordács, V. Kocsis, Y. Tokunaga, U. Nagel, T. Rõõm, Y. Takahashi, Y. Taguchi, and Y. Tokura, Unidirectional terahertz light absorption in the pyroelectric ferrimagnet $CaBaCo_4O_7$, Phys. Rev. B **92**, 214441 (2015).

[10] A. M. Kuzmenko, V. Dziom, A. Shuvaev, A. Pimenov, M. Schiebl, A. A. Mukhin, V. Y. Ivanov, I. A. Gudim, L. N. Bezmaternykh, and A. Pimenov, Large directional optical anisotropy in multiferroic ferroborate, Phys. Rev. B **92**, 184409 (2015).

[11] S. Toyoda, N. Abe, S. Kimura, Y. H. Matsuda, T. Nomura, A. Ikeda, S. Takeyama, and T. Arima, One-Way Transparency of Light in Multiferroic CuB_2O_4, Phys. Rev. Lett. **115**, 267207 (2015).

[12] Y. Iguchi, Y. Nii, and Y. Onose, Magnetoelectrical control of nonreciprocal microwave response in a multiferroic helimagnet, Nat. Commun. **8**, 15252 (2017).

[13] V. Kocsis, K. Penc, T. Rõõm, U. Nagel, J. Vít, J. Romhányi, Y. Tokunaga, Y. Taguchi, Y. Tokura, I. Kézsmárki, and S. Bordács, Identification of Antiferromagnetic Domains Via the Optical Magnetoelectric Effect, Phys. Rev. Lett. **121**, 057601 (2018).

[14] S. Yu, B. Gao, J. W. Kim, S.-W. Cheong, M. K. L. Man, J. Madéo, K. M. Dani, and D. Talbayev, High-Temperature Terahertz Optical Diode Effect without Magnetic Order in Polar $FeZnMo_3O_8$, Phys. Rev. Lett. **120**, 037601 (2018).

[15] Y. Tokura and N. Nagaosa, Nonreciprocal responses from noncentrosymmetric quantum materials, Nat. Commun. **9**, 3740 (2018).

[16] V. Kocsis, S. Bordács, Y. Tokunaga, J. Viirok, L. Peedu, T. Rõõm, U. Nagel, Y. Taguchi, Y. Tokura, and I. Kézsmárki, Magnetoelectric spectroscopy of spin excitations in $LiCoPO_4$, Phys. Rev. B **100**, 155124 (2019).

[17] J. Viirok, U. Nagel, T. Rõõm, D. G. Farkas, P. Balla, D. Szaller, V. Kocsis, Y. Tokunaga, Y. Taguchi, Y. Tokura, B. Bernáth, D. L. Kamenskyi, I. Kézsmárki, S. Bordács, and K. Penc, Directional dichroism in the paramagnetic state of multiferroics: A case study of infrared light absorption in $Sr_2CoSi_2O_7$ at high temperatures, Phys. Rev. B **99**, 014410 (2019).

[18] M. O. Yokosuk, H.-S. Kim, K. D. Hughey, J. Kim, A. V. Stier, K. R. O'Neal, J. Yang, S. A. Crooker, K. Haule, S.-W. Cheong, D. Vanderbilt, and J. L. Musfeldt, Nonreciprocal directional dichroism of a chiral magnet in the visible range, npj Quantum Mater. **5**, 20 (2020).

[19] K. Kimura, T. Katsuyoshi, Y. Sawada, S. Kimura, and T. Kimura, Imaging switchable magnetoelectric quadrupole domains via nonreciprocal linear dichroism, Commun. Mater. **1**, 39 (2020).

[20] S. Kimura, M. Matsumoto, and H. Tanaka, Electrical Switching of the Nonreciprocal Directional Microwave Response in a Triplon Bose-Einstein Condensate, Phys. Rev. Lett. **124**, 217401 (2020).

[21] M. Ogino, Y. Kaneko, Y. Tokura, and Y. Takahashi, Gyrotropic birefringence via electromagnon resonance in a multiferroic of spin origin, Phys. Rev. Res. **2**, 023345 (2020).

[22] S. Kimura, N. Terada, M. Hagiwara, M. Matsumoto, and H. Tanaka, Electric dipole active magnetic resonance and nonreciprocal directional dichroism in magnetoelectric multiferroic materials in terahertz and millimeter wave regions, Appl. Magn. Reson. **52**, 363 (2021).

[23] S. Toyoda, M. Fiebig, T. hisa Arima, Y. Tokura, and N. Ogawa, Nonreciprocal second harmonic generation in a magnetoelectric material, Sci. Adv. **7**, eabe2793 (2021).

[24] J. Vít, J. Viirok, L. Peedu, T. Rõõm, U. Nagel, V. Kocsis, Y. Tokunaga, Y. Taguchi, Y. Tokura, I. Kézsmárki, P. Balla, K. Penc, J. Romhányi, and S. Bordács, In Situ Electric-Field Control of THz Nonreciprocal Directional Dichroism in the Multiferroic $Ba_2CoGe_2O_7$, Phys. Rev. Lett. **127**, 157201 (2021).

[25] S. Reschke, D. G. Farkas, A. Strinić, S. Ghara, K. Guratinder, O. Zaharko, L. Prodan, V. Tsurkan, D. Szaller, S. Bordács, J. Deisenhofer, and I. Kézsmárki, Confirming the trilinear form of the optical magnetoelectric effect in the polar honeycomb antiferromagnet $Co_2Mo_3O_8$, npj Quantum Mater. **7**, 1 (2022).

[26] A. Pimenov, A. A. Mukhin, V. Y. Ivanov, V. D. Travkin, A. M. Balbashov, and A. Loidl, Possible evidence for electromagnons in multiferroic manganites, Nat. Phys. **2**, 97 (2006).

[27] Y. Takahashi, R. Shimano, Y. Kaneko, H. Murakawa, and Y. Tokura, Magnetoelectric resonance with electromagnons in a perovskite helimagnet, Nat. Phys. **8**, 121 (2012).

[28] A. M. Kuzmenko, D. Szaller, T. Kain, V. Dziom, L. Weymann, A. Shuvaev, A. Pimenov, A. A. Mukhin, V. Y. Ivanov, I. A. Gudim, L. N. Bezmaternykh, and A. Pimenov, Switching of Magnons by Electric and Magnetic Fields in Multiferroic Borates, Phys. Rev. Lett. **120**, 027203 (2018).

[29] D. Szaller, S. Bordács, V. Kocsis, T. Rõõm, U. Nagel, and I. Kézsmárki, Effect of spin excitations with simultaneous magnetic- and electric-dipole character on the static magnetoelectric properties of multiferroic materials, Phys. Rev. B **89**, 184419 (2014).

[30] J. Li, V. O. Garlea, J. L. Zarestky, and D. Vaknin, Spin waves in antiferromagnetic single-crystal $LiFePO_4$, Phys. Rev. B **73**, 024410 (2006).

[31] R. Toft-Petersen, M. Reehuis, T. B. S. Jensen, N. H. Andersen, J. Li, M. D. Le, M. Laver, C. Niedermayer, B. Klemke, K. Lefmann, and D. Vaknin, Anomalous magnetic structure and spin dynamics in magnetoelectric $LiFePO_4$, Phys. Rev. B **92**, 024404 (2015).

[32] Y. Yiu, M. D. Le, R. Toft-Petersen, G. Ehlers, R. J. McQueeney, and D. Vaknin, Hybrid excitations due to crystal field, spin-orbit coupling, and spin waves in $LiFePO_4$, Phys. Rev. B **95**, 104409 (2017).

[33] D. Szaller, V. Kocsis, S. Bordács, T. Fehér, T. Rõõm, U. Nagel, H. Engelkamp, K. Ohgushi, and I. Kézsmárki, Magnetic resonances of multiferroic $TbFe_3(BO_3)_4$, Phys. Rev. B **95**, 024427 (2017).

[34] D. Szaller, K. Szász, S. Bordács, J. Viirok, T. Rõõm, U. Nagel, A. Shuvaev, L. Weymann, A. Pimenov, A. A. Tsirlin, A. Jesche, L. Prodan, V. Tsurkan, and I. Kézsmárki, Magnetic anisotropy and exchange paths for octahedrally and tetrahedrally coordinated Mn^{2+} ions in the honeycomb multiferroic $Mn_2Mo_3O_8$, Phys. Rev. B **102**, 144410 (2020).

[35] T. Rõõm, J. Viirok, L. Peedu, U. Nagel, D. G. Farkas, D. Szaller, V. Kocsis, S. Bordács, I. Kézsmárki, D. L. Kamenskyi, H. Engelkamp, M. Ozerov, D. Smirnov, J. Krzystek, K.

[36] Thirunavukkuarasu, Y. Ozaki, Y. Tomioka, T. Ito, T. Datta, and R. S. Fishman, Magnetoelastic distortion of multiferroic $BiFeO_3$ in the canted antiferromagnetic state, Phys. Rev. B **102**, 214410 (2020).

[36] D. G. Farkas, D. Szaller, I. Kézsmárki, U. Nagel, T. Rõõm, L. Peedu, J. Viirok, J. S. White, R. Cubitt, T. Ito, R. S. Fishman, and S. Bordács, Selection rules and dynamic magnetoelectric effect of the spin waves in multiferroic $BiFeO_3$, Phys. Rev. B **104**, 174429 (2021).

[37] K. Penc, J. Romhányi, T. Rõõm, U. Nagel, A. Antal, T. Fehér, A. Jánossy, H. Engelkamp, H. Murakawa, Y. Tokura, D. Szaller, S. Bordács, and I. Kézsmárki, Spin-Stretching Modes in Anisotropic Magnets: Spin-Wave Excitations in the Multiferroic $Ba_2CoGe_2O_7$, Phys. Rev. Lett. **108**, 257203 (2012).

[38] J. Romhányi and K. Penc, Multiboson spin-wave theory for $Ba_2CoGe_2O_7$: A spin-3/2 easy-plane Néel antiferromagnet with strong single-ion anisotropy, Phys. Rev. B **86**, 174428 (2012).

[39] M. Akaki, D. Yoshizawa, A. Okutani, T. Kida, J. Romhányi, K. Penc, and M. Hagiwara, Direct observation of spin-quadrupolar excitations in $Sr_2CoSi_2O_7$ by high-field electron spin resonance, Phys. Rev. B **96**, 214406 (2017).

[40] A. Legros, S.-S. Zhang, X. Bai, H. Zhang, Z. Dun, W. A. Phelan, C. D. Batista, M. Mourigal, and N. Armitage, Observation of 4- and 6-Magnon Bound States in the Spin-Anisotropic Frustrated Antiferromagnet FeI_2, Phys. Rev. Lett. **127**, 267201 (2021).

[41] X. Bai, S.-S. Zhang, Z. Dun, H. Zhang, Q. Huang, H. Zhou, M. B. Stone, A. I. Kolesnikov, F. Ye, C. D. Batista, and M. Mourigal, Hybridized quadrupolar excitations in the spin-anisotropic frustrated magnet FeI_2, Nat. Phys. **17**, 467 (2021).

[42] R. S. Fishman, J. A. Fernandez-Baca, and T. Rõõm, *Spin-Wave Theory and its Applications to Neutron Scattering and THz Spectroscopy* (IOP Concise Physics, Morgan and Claypool Publishers, USA, 2018).

[43] L. Chaix, S. de Brion, S. Petit, R. Ballou, L.-P. Regnault, J. Ollivier, J.-B. Brubach, P. Roy, J. Debray, P. Lejay, A. Cano, E. Ressouche, and V. Simonet, Magneto- to Electroactive Transmutation of Spin Waves in $ErMnO_3$, Phys. Rev. Lett. **112**, 137201 (2014).

[44] A. Strinić, S. Reschke, K. V. Vasin, M. Schmidt, A. Loidl, V. Tsurkan, M. V. Eremin, and J. Deisenhofer, Magnetoelectric properties and low-energy excitations of multiferroic $FeCr_2S_4$, Phys. Rev. B **102**, 134409 (2020).

[45] R. P. Santoro and R. E. Newnham, Antiferromagnetism in $LiFePO_4$, Acta Crystallogr. **22**, 344 (1967).

[46] J. Werner, C. Neef, C. Koo, A. Ponomaryov, S. Zvyagin, and R. Klingeler, Exceptional field dependence of antiferromagnetic magnons in $LiFePO_4$, Phys. Rev. B **103**, 174406 (2021).

[47] J. Creer and G. Troup, The magnetic susceptibility of $LiFePO_4$ and $LiCoPO_4$, Phys. Lett. A **32**, 439 (1970).

[48] J. Werner, C. Neef, C. Koo, S. Zvyagin, A. Ponomaryov, and R. Klingeler, Antisite disorder in the battery material $LiFePO_4$, Phys. Rev. Mater. **4**, 115403 (2020).

[49] P. J. Baker, I. Franke, F. L. Pratt, T. Lancaster, D. Prabhakaran, W. Hayes, and S. J. Blundell, Probing magnetic order in $LiMPO_4$ (M = Ni, Co, Fe) and lithium diffusion in Li_xFePO_4, Phys. Rev. B **84**, 174403 (2011).

[50] O. García-Moreno, M. Alvarez-Vega, F. García-Alvarado, J. García-Jaca, J. M. Gallardo-Amores, M. L. Sanjuán, and U. Amador, Influence of the structure on the electrochemical performance of lithium transition metal phosphates as cathodic materials in rechargeable lithium batteries: A new high-pressure form of LiMPO$_4$ (M = Fe and Ni), Chem. Mater. **13**, 1570 (2001).

[51] O. Portugall, N. Puhlmann, H. U. Müller, M. Barczewski, I. Stolpe, and M. von Ortenberg, Megagauss magnetic field generation in single-turn coils: New frontiers for scientific experiments, J. Phys. D: Appl. Phys. **32**, 2354 (1999).

[52] S. Takeyama, R. Sakakura, Y. H. Matsuda, A. Miyata, and M. Tokunaga, Precise magnetization measurements by parallel self-compensated induction coils in a vertical single-turn coil up to 103T, J. Phys. Soc. Jpn. **81**, 014702 (2012).

[53] E. A. Turov, *Physical Properties of Magnetically Ordered Crystals* (Izdat. Acad. Sci. SSSR, Moscow, 1963).

[54] C. Kittel, On the theory of ferromagnetic resonance absorption, Phys. Rev. **73**, 155 (1948).

[55] G. Liang, K. Park, J. Li, R. E. Benson, D. Vaknin, J. T. Markert, and M. C. Croft, Anisotropy in magnetic properties and electronic structure of single-crystal LiFePO$_4$, Phys. Rev. B **77**, 064414 (2008).

[56] J. Werner, S. Sauerland, C. Koo, C. Neef, A. Pollithy, Y. Skourski, and R. Klingeler, High magnetic field phase diagram and failure of the magnetic Grüneisen scaling in LiFePO$_4$, Phys. Rev. B **99**, 214432 (2019).

[57] S. Geller and J. L. Durand, Refinement of the structure of LiMnPO$_4$, Acta Crystallogr. **13**, 325 (1960).

[58] L. Peedu, V. Kocsis, D. Szaller, J. Viirok, U. Nagel, T. Rõõm, D. G. Farkas, S. Bordács, D. L. Kamenskyi, U. Zeitler, Y. Tokunaga, Y. Taguchi, Y. Tokura, and I. Kézsmárki, Spin excitations of magnetoelectric LiNiPO$_4$ in multiple magnetic phases, Phys. Rev. B **100**, 024406 (2019).

[59] T. L. Gilbert, A phenomenological theory of damping in ferromagnetic materials, IEEE Trans. Magn. **40**, 3443 (2004).

[60] T. Stanislavchuk, D. S. Middlemiss, J. S. Syzdek, Y. Janssen, R. Basistyy, A. A. Sirenko, P. G. Khalifah, C. Grey, and R. Kostecki, Infrared-active optical phonons in LiFePO$_4$ single crystals, J. Appl. Phys. **122**, 045107 (2017).

[61] G. Rousse, J. Rodriguez-Carvajal, S. Patoux, and C. Masquelier, Magnetic structures of the triphylite LiFePO$_4$ and of its delithiated form FePO$_4$, Chem. Mater. **15**, 4082 (2003).

[62] See Supplemental Material at http://link.aps.org/supplemental/10.1103/PhysRevB.106.134413 for additional data on magnetization, THz absorption spectra, and mean-field model calculation results.

[63] W. Tian, J. Li, J. W. Lynn, J. L. Zarestky, and D. Vaknin, Spin dynamics in the magnetoelectric effect compound LiCoPO$_4$, Phys. Rev. B **78**, 184429 (2008).

[64] J. W. Halley and I. Silvera, Odd-Exciton Magnon Interaction and Explanation of Anomalous Far-Infrared Absorption in Antiferromagnetic FeF$_2$, Phys. Rev. Lett. **15**, 654 (1965).

[65] S. J. Allen, R. Loudon, and P. L. Richards, Two-Magnon Absorption in Antiferromagnetic MnF$_2$, Phys. Rev. Lett. **16**, 463 (1966).

[66] R. Loudon, Theory of infra-red and optical spectra of antiferromagnets, Adv. Phys. **17**, 243 (1968).

[67] Y. Tanaka and K. Nagasaka, Far infrared activity due to two-magnon excitation in antiferromagnetic MEM(TCNQ)$_2$, Solid State Commun. **73**, 735 (1990).

[68] Y. Tanabe, Y. Fujimaki, K. Kojima, S. Uchida, S. Onari, T. Matsuo, S. Azuma, and E. Hanamura, Direct optical excitation of two and three magnons in α-Fe$_2$O$_3$, Low Temp. Phys. **31**, 780 (2005).

[69] C. C. Filho, P. Gomes, A. García-Flores, G. Barberis, and E. Granado, Two-magnon raman scattering in LiMnPO$_4$, J. Magn. Magn. Mater. **377**, 430 (2015).

[70] A. Fert, D. Bertrand, J. Leotin, J. Ousset, J. Magariño, and J. Tuchendler, Excitation of two spin deviations by far infrared absorption in FeI$_2$, Solid State Commun. **26**, 693 (1978).

[71] M. G. Hildebrand, A. Slepkov, M. Reedyk, G. Amow, J. E. Greedan, and D. A. Crandles, Far-infrared optical properties of antiferromagnetic SmTiO$_3$, Phys. Rev. B **59**, 6938 (1999).

[72] P. L. Richards, Far infrared absorption by two magnon excitations in antiferromagnets, J. Appl. Phys. **38**, 1500 (1967).

[73] C. R. Harris, K. J. Millman, S. J. van der Walt, R. Gommers, P. Virtanen, D. Cournapeau, E. Wieser, J. Taylor, S. Berg, N. J. Smith, R. Kern, M. Picus, S. Hoyer, M. H. van Kerkwijk, M. Brett, A. Haldane, J. Fernández del Río, M. Wiebe, P. Peterson, P. Gérard-Marchant *et al.*, Array programming with NumPy, Nature (London) **585**, 357 (2020).

[74] J. D. Hunter, Matplotlib: A 2D graphics environment, Computing in Science Engineering **9**, 90 (2007).

[75] P. Virtanen, R. Gommers, T. E. Oliphant, M. Haberland, T. Reddy, D. Cournapeau, E. Burovski, P. Peterson, W. Weckesser, J. Bright, S. J. van der Walt, M. Brett, J. Wilson, K. J. Millman, N. Mayorov, A. R. J. Nelson, E. Jones, R. Kern, E. Larson, C. J. Carey *et al.*, SciPy 1.0: Fundamental algorithms for scientific computing in Python, Nat. Methods **17**, 261 (2020).

[76] Wes McKinney, Data structures for statistical computing in Python, in *Proceedings of the 9th Python in Science Conference*, edited by S. van der Walt and J. Millman (SciPy library, 2010), pp. 56–61.

Curriculum Vitae

1. Personal data

Name	Laur Peedu
Date and place of birth	1 April 1989, Tallinn, Estonia
Nationality	Estonian

2. Contact information

Address	National Institute of Chemical Physics and Biophysics
	Akadeemia tee 23, 12618, Tallinn, Estonia
Phone	+372 56272640
E-mail	laurpeedu@gmail.com

3. Education

2014–. . .	Tallinn University of Technology, School of Science, Engineering physics, PhD
2011–2013	Tallinn University of Technology, Faculty of Science, Engineering physics, MSc
2008–2011	Tallinn University of Technology, Faculty of Science, Engineering physics, BSc

4. Language competence

Estonian	native
English	full professional

5. Professional employment

2015– . . .	National Institute of Chemical Physics and Biophysics, Junior Researcher
2012–2015	National Institute of Chemical Physics and Biophysics, Engineer

6. Additional employment

2015–. . .	Saue EPT AS, Advisory Board Member
2016–. . .	FinEst Steel AS, Advisory Board Member
2016–. . .	Urmet OÜ, Advisory Board Member

7. Computer skills

- Operating systems: Windows, Linux

- Document preparation: LaTeX, Microsoft Office

- Programming languages: Python, Javascript, Wolfram Mathematica

- Scientific packages: matplotlib, SciPy, NumPy, Pandas, Origin

8. Defended theses

- 2013, Infrared spectroscopy of molecular hydrogen quantum motion in endohedral fullerene $H_2@C_{70}$, MSc, supervisors PhD Toomas Rõõm and PhD Urmas Nagel, Tallinn University of Technology, Institute of Physics

- 2011, Optical properties of graphene in far infrared, BSc, supervisors PhD Toomas Rõõm and PhD Urmas Nagel, Tallinn University of Technology, Institute of Physics

9. Field of research

- FIELD OF RESEARCH: 4. Natural Sciences and Engineering; 4.10. Physics and Technical Physics; CERCS SPECIALITY: P260 Condensed matter: electronic structure, electrical, magnetic and optical properties, superconductors, magnetic resonance, relaxation, spectroscopy; SPECIALITY: infrared and THz spectrometry of low dimensional and strongly correlated electron and spin systems, directional dichroism, high magnetic fields, low temperatures

10. Scientific work
Papers

1. T. Rõõm, L. Peedu, Min Ge, D. Hüvonen, U. Nagel, Shufeng Ye, Minzhong Xu, Z. Bačić, S. Mamone, M. H. Levitt, M. Carravetta, J. Y. -C. Chen, Xuegong Lei, N. J. Turro, Y. Murata and K. Komatsu, "Infrared spectroscopy of small-molecule endofullerenes," *Phil. Trans. R. Soc. A*, 371:20110631, Jan 2013.

2. V. Kocsis, S. Bordács, Y. Tokunaga, J. Viirok, L. Peedu, T. Rõõm, U. Nagel, Y. Taguchi, Y. Tokura, and I. Kézsmárki, "Magnetoelectric spectroscopy of spin excitations in $LiCoPO_4$," *Phys. Rev. B*, 100:155124, Oct 2019.

3. L. Peedu, V. Kocsis, D. Szaller, J. Viirok, U. Nagel, T. Rõõm, D. G. Farkas, S. Bordács, D. L. Kamenskyi, U. Zeitler, Y. Tokunaga, Y. Taguchi, Y. Tokura, and I. Kézsmárki, "Spin excitations of magnetoelectric $LiNiPO_4$ in multiple magnetic phases," *Phys. Rev. B*, 100:024406, Jul 2019.

4. T. Rõõm, J. Viirok, L. Peedu, U. Nagel, D. G. Farkas, D. Szaller, V. Kocsis, S. Bordács, I. Kézsmárki, D. L. Kamenskyi, H. Engelkamp, M. Ozerov, D. Smirnov, J. Krzystek, K. Thirunavukkuarasu, Y. Ozaki, Y. Tomioka, T. Ito, T. Datta, and R. S. Fishman, "Magnetoelastic distortion of multiferroic $BiFeO_3$ in the canted antiferromagnetic state," *Phys. Rev. B*, 102:214410, Dec 2020.

5. D. G. Farkas, D. Szaller, I. Kézsmárki, U. Nagel, T. Rõõm, L. Peedu, J. Viirok, J. S. White, R. Cubitt, T. Ito, R. S. Fishman, S. Bordács, "Selection rules and dynamic magnetoelectric effect of the spin waves in multiferroic $BiFeO_3$," *Phys. Rev. B*, 104:174429, Nov 2021.

6. J. Vit, J. Viirok, L. Peedu, T. Rõõm, U. Nagel, V. Kocsis, Y. Tokunaga, Y. Taguchi, Y. Tokura, I. Kézsmárki, P. Balla, K. Penc, J. Romhányi, and S. Bordács, "In situ electric-field control of THz nonreciprocal directional dichroism in the multiferroic $Ba_2CoGe_2O_7$," *Phys. Rev. Lett*, 127:157201, Jun 2021.

7. L. Peedu, V. Kocsis, D. Szaller, B. Forrai, S. Bordács, I. Kézsmárki, J. Viirok, U. Nagel, B. Bernáth, D. L. Kamenskyi, A. Miyata, O. Portugall, Y. Tokunaga, Y. Tokura, Y. Taguchi and T. Rõõm, "THz spectroscopy of spin excitations in magnetoelectric $LiFePO_4$ in high magnetic fields," *Phys. Rev. B*, 106:134413, October 2022.

Conference presentations

1. L. Peedu. *Dynamics of endohedral H_2 in C_{70}: infrared study*, IV international Symposium on Strong Nonlinear Vibronic and Electronic Interactions in Solids, 30 April – 03 May 2013, Tartu

2. L. Peedu. *THz spectroscopy in high magnetic fields at mK temperatures*, 2nd Grandmaster PhD Workshop in Physics, 6–11 September 2015, Budapest, Hungary

3. L. Peedu. *Directional dichroism of multiferroic materials at THz frequencies*, 15–21 August, PSI summer school, 2015, Zuoz, Switzerland

4. L. Peedu. *THz spectroscopy of spin waves in multiferroic $LiNiPO_4$ in high magnetic fields*, APS March Meeting, 13–18 March 2017, New Orleans, LA, USA

5. L. Peedu. *Optical spin-wave excitations of multiferroic $LiNiPO_4$ in high magnetic fields,*, 3rd Grandmaster PhD Workshop in Physics: 19–23 February 2018, Vienna, Austria

6. L. Peedu. *THz spectroscopy of spin waves in multiferroic $LiFePO_4$ in high magnetic fields*, APS March Meeting, 5–9 March 2018, Los Angeles, CA, USA

7. L. Peedu. *THz spectroscopy of spin waves in multiferroic $LiNiPO_4$ in high magnetic fields*, Graduate School of Functional Materials and Technologies Conference, 4–5 February 2019, Tartu, Estonia

8. L. Peedu. *THz spectroscopy of Spin Waves in Multiferroic $LiNiPO_4$ in High Magnetic Fields*, APS March Meeting, 4–8 March 2019, Boston, MA, USA

9. L. Peedu. *THz spectroscopy of spin waves in magnetoelectric $LiFePO_4$ in high magnetic fields*, 4th Grandmaster PhD Workshop in Physics, 1–7 September 2019, Split, Croatia

10. L. Peedu. *THz spectroscopy of spin excitations in magnetoelectric $LiCoPO_4$ in high magnetic fields*, American Physics Society March Meeting (CANCELLED), 2–6 March 2020, Denver, USA

Elulookirjeldus

1. Isikuandmed

Nimi	Laur Peedu
Sünniaeg ja -koht	01.04.1989, Tallinn, Eesti
Kodakondsus	Eesti

2. Kontaktandmed

Aadress	Keemilise ja Bioloogilise Füüsika Instituut, Akadeemia tee 23, 12618, Tallinn, Estonia
Telefon	+372 56272640
E-post	laurpeedu@gmail.com

3. Haridus

2014–…	Tallinna Tehnikaülikool, Loodusteaduskond, Tehniline füüsika, doktoriõpe
2011–2013	Tallinna Tehnikaülikool, Matemaatika-loodusteaduskond, Tehniline füüsika, MSc
2008–2011	Tallinna Tehnikaülikool, Matemaatika-loodusteaduskond, Tehniline füüsika, BSc

4. Keelteoskus

eesti keel	emakeel
inglise keel	kõrgtase

5. Teenistuskäik

2014– …	Keemilise ja Bioloogilise Füüsika Instituut, nooremteadur
2011–2013	Keemilise ja Bioloogilise Füüsika Instituut, insener

6. Täiendav teeninstuskïk

2015–…	Saue EPT AS, nõukogu liige
2016–…	FinEst Steel AS, nõukogu liige
2016–…	Urmet OÜ, nõukogu liige

7. Arvutioskused

- Operatsioonisüsteemid: Windows, Linux

- Kontoritarkvara: LaTeX, Microsoft Office

- Programmeerimiskeeled: Python, Javascript, Wolfram Mathematica

- Teadustarkvara paketid: matplotlib, SciPy, NumPy, Pandas, Origin

8. Kaitstud lõputööd

- 2013, Vesiniku molekuli kvantliikumise infrapunaspektroskoopia endoeedrilises fullereenis $H_2@C_{70}$, MSc, juhendajad PhD Toomas Rõõm ja PhD Urmas Nagel, Tallinna Tehnikaülikool, Füüsikainstituut

- 2011, Grafeeni optilised omadused kauge infrapuna piirkonnas, BSc, juhendajad PhD Toomas Rõõm ja PhD Urmas Nagel, Tallinna Tehnikaülikool, Füüsikainstituut

9. Teadustöö põhisuunad

- VALDKOND: 4. Loodusteadused ja tehnika; 4.10. Füüsika; CERCS ERIALA: P260 Tahke aine: elektrooniline struktuur, elektrilised, magneetilised ja optilised omadused, ülijuhtivus, magnetresonants, spektroskoopia; PÕHISUUND: madalamõõduliste ja tugevalt korreleeritud elektron- ja spinnsüsteemide infrapuna ja THz-spektromeetria, suunadikroism, tugevad magnetväljad, madalad temperatuurid

10. Teadustegevus
Teadusartiklite ja konverentsiettekannete loetelu on toodud ingliskeelse elulookirjelduse juures.